Counterion condensation for rigid linear polyelectrolytes

Dissertation

zur Erlangung des Grades

"Doktor der Naturwissenschaften"

am Fachbereich Physik

der Johannes Gutenberg-Universität

in Mainz

Markus Deserno

geb. in Erlangen

Datum der mündlichen Prüfung: 17. Februar 2000

Summary

This thesis studies stiff linear polyelectrolytes within the framework of a cell model. The center of attention is the phenomenon of counterion condensation onto the surface of a charged macroion. Its dependence on parameters such as density, Bjerrum length, valence and ionic strength is investigated, and its effects on important observables such as ion distribution functions and osmotic pressure are discussed. These problems are addressed theoretically by using the nonlinear and linearized Poisson-Boltzmann equation as well as more general density functional theories. Molecular dynamics simulations complement the theoretical findings and demarcate their range of applicability.

Based on the Poisson-Boltzmann theory a novel criterion for measuring counterion condensation is proposed which is in accord with the Manning theory. No prior assumptions about the condensed fraction or the radial extension of the condensed layer are made. The criterion quantifies deviations from the Poisson-Boltzmann theory caused, for instance, by excluded volume interactions and correlations, and it elucidates the crossover from condensation to screening upon addition of salt.

A new correction term to the Poisson-Boltzmann free energy density is derived starting from a modification of the one-component plasma model. A comparison with simulations demonstrates that the proposed correction accurately describes weakly correlated systems. Being convex as a function of density, its thermodynamic stability is ensured even within a local density approximation. The corresponding free energy functionals are minimized by employing a novel Monte-Carlo scheme introduced in this work.

Results from original molecular dynamics simulations complement the theoretical studies. The new criterion for measuring counterion condensation is used to investigate the condensed layer of counterions as a function of density, Bjerrum length, valence and ionic strength. Deviations from the Poisson-Boltzmann predictions for distribution functions and osmotic pressure are determined. They can be removed by including the proposed correlation corrections, provided the ions are only weakly coupled. However, at high ionic strength qualitatively new phenomena, such as charge reversal, negative osmotic pressure, and a non-monotonic zeta-potential appear. In all of these cases the importance of multivalent ions becomes evident. The results are compared with integral equation theories and experiments.

In the simulations, electrostatic interactions are computed with the help of highly efficient Particle Mesh Ewald algorithms. Several variants belonging to this class of routines, which differ in important components, have been previously proposed in the literature. These versions are analyzed within a unified mathematical framework. Based on this study, as well as on extensive numerical tests, an accuracy-optimized algorithm is proposed. In addition, the first analytical error estimate for the most accurate routine is derived. This permits prior knowledge of the algorithmic precision and thereby provides a straightforward method to optimize the tuning parameters.

Zusammenfassung

Die vorliegende Doktorarbeit studiert steife, lineare Polyelektrolyte im Rahmen eines Zellenmodells. Im Mittelpunkt steht dabei das Phänomen der Gegenionenkondensation an der Oberfläche eines geladenen Makroions. Seine Abhängigkeit von Parametern wie Dichte, Bjerrum-Länge, Valenz und Ionenstärke wird untersucht, und seine Auswirkungen auf wichtige Observablen wie Ionenverteilungen und osmotischer Druck werden diskutiert. Von theoretischer Seite werden diese Probleme mit Hilfe der nichtlinearen und linearisierten Poisson-Boltzmann Gleichung sowie allgemeineren Dichtefunktionaltheorien behandelt. Molekulardynamik-Simulationen ergänzen die theoretischen Ergebnisse und grenzen den Bereich ihrer Gültigkeit ab.

Ausgehend von der Poisson-Boltzmann Theorie wird ein neuartiges Kriterium für Gegenionenkondensation vorgeschlagen, welches mit der Manning Theorie verträglich ist. Vorab werden keine Annahmen über den Bruchteil kondensierter Ionen oder die radiale Ausdehnung der kondensierten Schicht gemacht. Das Kriterium quantifiziert Abweichungen von der Poisson-Boltzmann Theorie, wie sie etwa von einer Volumenausschlusswechselwirkung oder von Korrelationen verursacht werden, und klärt den Übergang von Kondensation zu Abschirmung bei Zugabe von Salz.

Ein neuer Korrekturterm für die Dichte der freien Energie in Poisson-Boltzmann Näherung wird hergeleitet, ausgehend vom modifizierten Modell eines einkomponentigen Plasmas. Ein Vergleich mit Simulationen zeigt, dass die vorgeschlagene Korrektur schwach korrelierte Systeme präzise beschreibt. Sie ist konvex in der Dichte, somit ist thermodynamische Stabilität sogar im Rahmen einer lokalen-Dichte-Approximation gewährleistet. Die entsprechenden Funktionale der freien Energie werden mittels einer neuartigen Monte-Carlo Methode minimiert, die in dieser Arbeit vorgestellt wird.

Ergebnisse eigener Molekulardynamik-Simulationen ergänzen die theoretischen Untersuchungen. Das neue Kriterium zur Messung von Gegenionenkondensation wird verwendet, um die kondensierte Schicht als Funktion der Dichte, Bjerrum-Länge, Valenz und Ionenstärke zu studieren. Abweichungen von den Poisson-Boltzmann Vorhersagen über die Verteilungsfunktionen und den osmotischen Druck werden bestimmt. Diese können mittels der vorgeschlagenen Korrelationskorrekturen beseitigt werden, vorausgesetzt die Ionen sind nur schwach gekoppelt. Bei hoher Ionenstärke jedoch treten qualitativ neue Phänomene auf, wie etwa Ladungsumkehr, ein negativer osmotischer Druck oder ein nichtmonotones zeta-Potential. In all diesen Fällen wird die Bedeutung multivalenter Ionen offensichtlich. Die Ergebnisse werden verglichen mit Integralgleichungstheorien und Experimenten.

In den Simulationen werden elektrostatische Wechselwirkungen mittels hocheffizienter Particle-Mesh-Ewald Algorithmen berechnet. Verschiedene Varianten solcher Routinen, welche sich jedoch in wichtigen Komponenten unterscheiden, sind in der Vergangenheit publiziert worden. Diese Versionen werden in einem einheitlichen mathematischen Rahmen analysiert. Basierend auf diesen Untersuchungen sowie ausgedehnten numerischen Tests wird ein auf Genauigkeit optimierter Algorithmus vorgestellt. Für diesen wird auch erstmalig eine analytische Fehlerabschätzung hergeleitet. Diese liefert vorab Information über die zu erwartende Genauigkeit und erlaubt ein optimales Einstellen der Parameter.

Contents

Introduction

"Polyelectrolytes are polymers bearing ionizable groups, which, in polar solvents, can dissociate into charged polymer chains (macroions) and small counterions" [BaJo96], see Fig. 1. The combination of macromolecular properties and long-range electrostatic interactions results in an impressive variety of phenomena. It makes these systems interesting from a fundamental as well as a technological point of view.

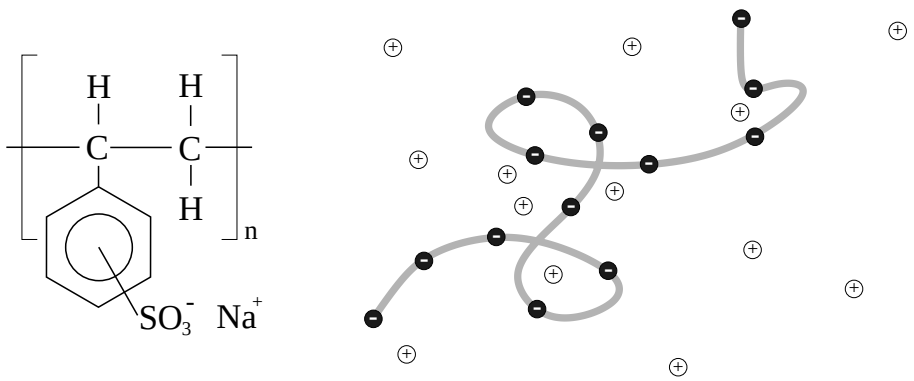

Figure 1: Example of a flexible polyelectrolyte. Constitution formula for sulfonated polystyrene with sodium counterions (left) and a physicist's picture (right).

Some of the relevant questions primarily motivated by scientific interest are the following. How is the size of a polyelectrolyte affected by molecular weight, intrinsic stiffness, solvent quality or ionic strength? Which observables are well characterized by coarse-grained quantities such as a linear charge density, and which depend on chemical details? How are dynamic quantities like viscosity or electrophoretic mobility related to static properties of polyelectrolytes?

Technological questions, on the other hand, are chiefly concerned with the optimization of certain material properties which make polyelectrolytes suitable for numerous applications. For instance, they can function as viscosity modifiers to reduce drag in oil pipelines and to make low-fat milk products creamy. In sewage plants, they are added to the waste water in order to precipitate heavy metal ions. This procedure greatly reduces the amount of remaining sludge. They are also responsible for the tremendous swelling degrees of superabsorbers used in diapers and sanitary napkins, and in precautionary leak protection for deep-sea cables.

A thorough understanding of polyelectrolytes has become increasingly important in biochemistry and molecular biology. This is due to the fact that virtually all proteins, as well as the DNA, are polyelectrolytes. Their interactions with each other and with the charged cell-membrane are still shrouded in mystery to a high degree. For instance, a puzzling question is why two equally charged objects should attract each other in the first place.

Unfortunately, theoretical understanding of polyelectrolytes is less developed than the understanding of the properties of neutral polymers. There are numerous reasons for this. The presence of long-range interactions renders the application of renormalization group techniques and scaling ideas much more difficult than in the neutral case. This is due to the fact that many new length scales appear on the stage.[1] They are not well separated and therefore can influence each other in a complicated manner. The degrees of freedom related to the counterions carry much additional entropy. In contrast, the macroion itself is usually poor in entropy. Hence, there are effects which, despite the strong electrostatic interactions, are in fact entropy driven.[2] For a given chain geometry, the competition between energy minimization and entropy maximization results in a particular equilibrium counterion distribution around the polyelectrolyte. However, this distribution is strongly coupled to the conformation of the macroion itself. In the spirit of John A. Wheelers famous quote on the relation between space and matter in general relativity, one could say: Chain tells ions where to move; ions tell chain how to curve.

Several approaches are conceivable in order to disentangle the intricate coupling between ion distribution and chain conformation. One possibility is to completely integrate out the counterionic degrees of freedom. On a linearized mean-field level this yields a Debye-Hückel-like theory characterized by a screened Coulomb potential between charged monomers. This approach is frequently used in theoretical descriptions, but it suffers from some consistency problems related to the validity of linearization. However, in the complete nonlinear Poisson-Boltzmann equation the superposition principle no longer holds. This excludes the possibility of simply improving the screened pair-potentials.

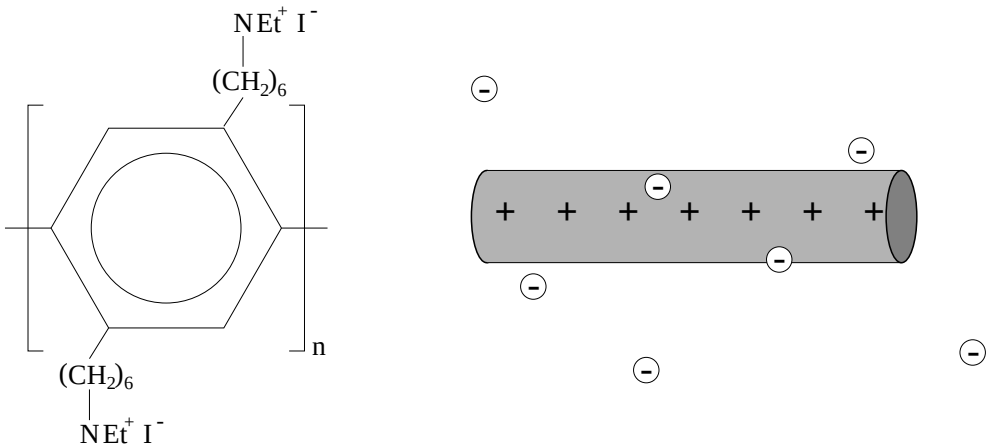

Figure 2: Example of a stiff polyelectrolyte. Constitution formula for poly(paraphenylene) with iodine counterions (left) and a physicist's picture (right).

A complementary approach is to fix the conformation of the chain and to focus on a detailed description of the counterion distribution. Usually polyelectrolytes stretch due to the electrostatic repulsion of their charged groups. Moreover, many important polyelectrolytes have a large intrinsic stiffness (e.g., DNA, actin filaments or microtubules).

[1] A few examples are: Bjerrum length, Debye length, inverse line charge density, Manning radius and mean polyelectrolyte separation. These and various other length scales will be thoroughly discussed later.

[2] A famous example are the superabsorbers mentioned earlier which are actually polyelectrolyte networks. They swell due to the "entropic desire" of the counterions to dilute. This drives the solvent into the network. The seemingly easier alternative in which the ions diffuse out of the network directly into the solution is forbidden by the requirement of macroscopic charge neutrality.

Therefore, a rod-like conformation is an obvious first choice, see Fig. 2. The remaining problem of charged rods immersed into solution is much easier, but is still far from being exactly solvable.

A common further approximation assumes that the investigation of a small sub-volume containing only one rod and its counterions will suffice to unveil much of the interesting physics. The main justification for this approach is that the sub-volume has zero net charge. Moreover, the counterions will also efficiently screen higher order multipoles. Hence, the interactions between two such sub-volumes, which are neglected when focusing on just one rod, will be fairly weak. This approximation is called cylindrical cell model and it provides the framework for all further investigations in this study.

The cell model might seem oversimplified – a reproach which cannot be entirely refuted. Nevertheless, it has several important advantages. Its high symmetry permits the definition of conclusive observables. In addition, the nonlinear Poisson-Boltzmann equation can be solved *exactly* in this geometry. It also displays in a clear fashion the key electrostatic feature of a charged rod, viz, the logarithmic potential. Since the volume dependency of the entropy is logarithmic as well, this gives rise to the fascinating effect of partial counterion condensation. While a charged sphere loses all its counterions upon dilution, a charged plane keeps all of them. For a charged cylinder the fraction of ions, which upon dilution remain in the vicinity of the macroion, can be anywhere between 0 and 100%.

In essence, strongly charged linear polyelectrolytes use their counterions to reduce their line charge density. Although this concept was introduced a long time ago, varying viewpoints persist. Already going beyond the mean-field description many questions arise: How closely condensed and tightly bound is the "condensed layer"? What distinguishes condensed from uncondensed counterions? When is the mean-field Poisson-Boltzmann theory a good approximation for real systems? And how does the presence of salt affect the condensation phenomenon? These are the kind of questions which the present work intends to answer.

This thesis is divided into three main chapters. The first one discusses the cell model from a theoretical point of view. Particular emphasis is given to the nonlinear and linearized Poisson-Boltzmann equation [DeHo00]. An improved theoretical description of correlations [BaDe] is presented, and for the appearing functional minimization problems a convenient Monte-Carlo procedure is proposed [Des00]. Chapter 2 presents original results from molecular dynamics simulations of the cell model, which complement the theoretical findings and demarcate their range of applicability as well. The last chapter is devoted to a thorough discussion of an important class of algorithms for computing electrostatic interactions within periodic boundary conditions: the Particle Mesh Ewald routines [DeHo98^a, DeHo98^b].

1 The cell model within Poisson-Boltzmann approximation

The cylindrical cell model is a commonly used way of reducing the complicated many-body problem of a polyelectrolyte solution to an effective one-particle (i.e., one polyelectrolyte) theory [AlBe51, FuKa51, WeJö82, LeZi84^a, LeZi84^b]. If the individual polyelectrolytes are in a predominantly rod-like conformation, due to their intrinsic stiffness or electrostatic stretching[1] at low densities, each of them can be thought of as being embedded in a fictitious cylinder such that the following requirements hold:

1. Cylinder and polyelectrolyte have the same length.
2. The radius of the cylinder is chosen such that its volume equals the volume per polyelectrolyte in the solution.
3. Counterions and possible salt molecules are distributed equally between these cylinders, thereby leaving each cylinder electrostatically neutral.

Using requirements 1 and 2 the polyelectrolyte density can be mapped to the cell model. Point 3 ensures the electrostatic decoupling of the cells. Particle number is conserved and electrostatic neutrality together with the assumption of a cylindrical distribution of ions demands that the electric field must vanish at the outer cylinder radius.[2] In a further approximation, boundary problems at the end caps of the polyelectrolytes are avoided by assuming them to be infinitely long (at fixed density, i.e., cell radius). It now suffices to investigate just one such cell, the geometry of which is depicted in Fig. 1.1.

This chapter examines theoretical aspects of the cell model, mostly relying on the nonlinear Poisson-Boltzmann (PB) theory. The purpose is to establish a sound base upon which improvements can be built and from which the results of simulations presented in Chapter 2 can be interpreted and understood.

Section 1.1 revisits the famous solution of the nonlinear Poisson-Boltzmann equation within cylindrical geometry and no additional salt. The phenomenon of counterion condensation is shown to be already included in this description. In 1.1.3 a novel criterion for quantifying this effect is introduced. This criterion permits measurement of the condensed fraction and the extension of the condensed layer independently of each other and

[1] This can be seen most intuitively by the following argument going back to Flory: Take a chain consisting of N monomers of size b, a fraction f of which carry a charge e_0. The elastic energy is given by $k_{\mathrm{B}}TR^2/Nb^2$, while the Coulomb energy is just $k_{\mathrm{B}}T(Nf)^2\ell_{\mathrm{B}}/R$, with $\ell_{\mathrm{B}} = e_0^2/4\pi\epsilon k_{\mathrm{B}}T$ being the Bjerrum length. Adding both terms and minimizing with respect to R gives $R \sim f^{2/3}(\ell_{\mathrm{B}}b^2)^{1/3}\,N$, i.e., a size proportional to N. Note, however, that this argument completely neglects the counterions.

[2] An alternative way of arriving at this model is assuming that the surface of zero electric field is *on average* a cylinder enclosing the rod-like polyelectrolyte.

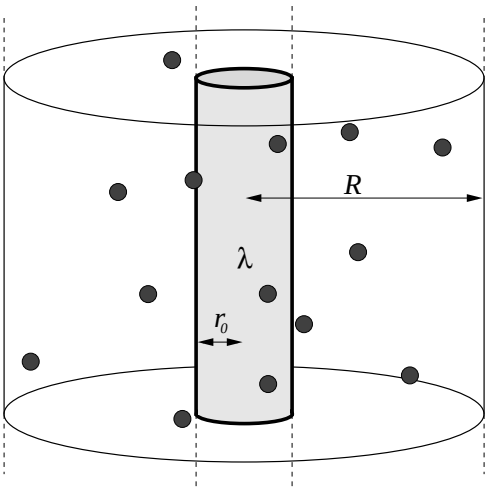

Figure 1.1: Geometry of the cell model. An infinitely long cylinder of radius r_0 and line charge density $\lambda > 0$ is coaxially enclosed in a cylindrical cell of radius R. Global charge neutrality of the system is ensured by adding an appropriate amount of oppositely charged counterions. The outer radius R is used to match the polyelectrolyte density of a solution containing many such macromolecules.

in accord with Poisson-Boltzmann theory. Section 1.1.4 presents a concise derivation of the limiting laws at low density, which shows them to easily follow from a simple sequence of inequalities.

Section 1.2 is devoted to implications resulting from the addition of salt. The importance of the chosen ensemble is pointed out. Furthermore, the new condensation criterion is shown to give a clear and quantitative picture of the crossover from counterion condensation to salt screening upon successive addition of salt.

Section 1.3 addresses the important phenomenon of counterion correlations neglected in Poisson-Boltzmann theory. For the salt-free case the one-component plasma correction to the Poisson-Boltzmann free energy functional is revisited. Its failure within a local density approximation is traced back to the asymptotic concavity of the one-component plasma free energy. Furthermore, this insight permits to precisely demarcate its small region of stability. Based on a more careful treatment of the homogeneous background charge of the one-component plasma, the present work proposes an improved free energy density in 1.3.2. Its analytic zero temperature limit is derived in 1.3.3. Since both resulting free energy densities are convex, they provide a thermodynamically stable way of incorporating correlations even within a local density approximation.

Section 1.4 illustrates how the various free energy functionals encountered up to now can be efficiently "turned" into ionic distribution functions. To this end a novel Monte-Carlo method is suggested. It finds the ion distribution minimizing a fairly general Poisson-Boltzmann like free energy functional. The key advantage is that it avoids falling back upon the differential equation corresponding to this variational problem. Excluded volume interactions and systems consisting of a mixture of different valences are presented as example applications.

Finally, section 1.5 takes one step back and looks at the linearized Poisson-Boltzmann theory within spherical, cylindrical and planar geometry. For the cylindrical case counterion condensation is proved to be absent on this level. Even more, a self-consistent linearized treatment of the cylindrical and planar geometry is shown to be impossible, since the two requirements of low density and small electrostatic potential cannot be fulfilled at the same time. It is emphasized that this is in strong contrast to the spherical case. This result also

acts as a warning: Many theories exploit the superposition principle valid in linear theories and construct polyelectrolytes by giving the charged monomers a Debye-Hückel potential. This may be dangerous.

1.1 Poisson-Boltzmann theory of the salt-free, cylindrical cell model

The nonlinear Poisson-Boltzmann equation for the salt-free cell model can be solved exactly. The analytic properties of the solution shed light on the phenomenon of counterion condensation and suggest a way of quantifying it.

1.1.1 Poisson-Boltzmann solution

Consider an infinitely long cylinder of radius r_0 and line charge density $\lambda > 0$, coaxially enclosed in a cylindrical cell of radius R, as depicted in Fig. 1.1. Global charge neutrality of the system is ensured by adding an appropriate amount of oppositely charged (monovalent) counterions. In the following only the case of no extra salt will be discussed.[3]

Within Poisson-Boltzmann theory the individual counterions are replaced by a cylindrical counterion density $n(r)$, where r denotes the radial distance from the cylinder axis. This gives rise to an electrostatic potential $\psi(r)$ satisfying the Poisson equation

$$\left(\frac{\mathrm{d}^2}{\mathrm{d}r^2} + \frac{1}{r}\frac{\mathrm{d}}{\mathrm{d}r}\right)\psi(r) = \frac{e_0}{\epsilon}\, n(r), \tag{1.1}$$

where ϵ is the dielectric constant outside the cylinder[4] and e_0 the positive unit charge. Conversely, the potential is assumed to influence the counterion density via the Boltzmann factor

$$n(r) = n(R)\, \exp\big\{\beta e_0 \psi(r)\big\}, \tag{1.2}$$

where $\beta := 1/k_\mathrm{B}T$ is the inverse temperature and k_B Boltzmann's constant. This implies the normalization of the potential to be $\psi(R) = 0$.

As usual, it is advantageous to change variables. The following definitions are particularly useful.

1. The strength of the electrostatic interactions is expressed by the Bjerrum length

$$\ell_\mathrm{B} := \beta e_0^2/4\pi\epsilon. \tag{1.3}$$

   It is the distance at which two unit charges have the interaction energy equal to $k_\mathrm{B}T$. For water at room temperature $\ell_\mathrm{B} \approx 7.14\,\text{Å}$.

2. The Bjerrum length suggests a dimensionless way of measuring the line charge density of the rod. For this one defines the so-called Manning parameter as

$$\xi := \lambda \ell_\mathrm{B}/e_0. \tag{1.4}$$

   It counts the number of unit charges on the rod per Bjerrum length. In the following the main focus will be on the strongly charged case characterized by $\xi > 1$.

[3] I.e., apart from the counterions belonging to the rod there are no additional charges in the solution.

[4] Within Poisson-Boltzmann theory the dielectric constant of the cylinder is irrelevant for symmetry reasons. See however Ref. [SkFi78] for the influence on individual particles.

Technical Point 1.1

A constructive solution of Eqn. (1.7) could proceed along the following lines: First transform r and y according to $u(r) := \ln(\kappa r)$ and $f(u) := y(r(u)) + 2u$. In these variables the Poisson-Boltzmann equation reads $f'' = \mathrm{e}^f$ while boundary conditions and normalization become $f'|_{r=r_0} = 2\,(1-\xi)$, $f'|_{r=R} = 2$ and $f|_{r=R} = 2\,\ln(\kappa R)$ respectively. Multiplying the Poisson-Boltzmann equation by f' and integrating over u gives the first integral $(f')^2 = 2\,\mathrm{e}^f - 4\gamma^2$ and Eqn. (1.12). Separating variables gives the second integral, which for $\gamma \in \mathbb{R}$ leads to the solution (1.9). A posteriori the reality of γ can be brought into relation with $\xi_{\min}$ from Rem. 1.1.1.6. See e.g. Ref. [LeZi84^b].

3. A reduced electrostatic potential y and a screening constant $\kappa > 0$ are defined as

$$y(r) := \beta e_0 \psi(r) \qquad \text{and} \tag{1.5}$$

$$\kappa^2 := 4\pi \ell_{\mathrm{B}} n(R). \tag{1.6}$$

Combining the Poisson equation (1.1) with the Boltzmann factor from Eqn. (1.2) gives the Poisson-Boltzmann equation. By further using the abbreviations from Eqns. (1.3–1.6) it can be written as

$$y'' + \frac{y'}{r} = \kappa^2 \mathrm{e}^y. \tag{1.7}$$

Notice that the potential occurring in the exponent on the right hand side makes this a *nonlinear* differential equation. It has to be solved subject to the following boundary conditions for the electric field:

$$y'(r_0) = -2\xi/r_0 \qquad \text{and} \qquad y'(R) = 0. \tag{1.8}$$

A constructive solution of this boundary value problem is outlined in TP 1.1. It is, however, much easier to verify by substitution that the correctly normalized solution to Eqns. (1.7,1.8) can be written as [FuKa51, AlBe51, LeZi84^b, DeHo00]

$$y(r) = -2\,\ln\left\{ \frac{r}{R}\,\sqrt{1+\gamma^{-2}}\,\cos\left(\gamma\,\ln\frac{r}{R_{\mathrm{M}}}\right)\right\}. \tag{1.9}$$

Insertion of the general solution from Eqn. (1.9) into the boundary conditions from Eqn. (1.8) yields two coupled transcendental equations for the two integration constants γ and R_{M}:

$$\gamma\,\ln\frac{r_0}{R_{\mathrm{M}}} = \arctan\frac{1-\xi}{\gamma} \qquad \text{and} \qquad \gamma\,\ln\frac{R}{R_{\mathrm{M}}} = \arctan\frac{1}{\gamma}. \tag{1.10}$$

Subtracting Eqn. (1.10i) from Eqn. (1.10ii) eliminates R_{M} and provides a single equation

$$\gamma\,\ln\frac{R}{r_0} = \arctan\frac{1}{\gamma} + \arctan\frac{\xi-1}{\gamma}, \tag{1.11}$$

from which γ can be obtained numerically. The second integration constant R_{M}, which will be referred to as the Manning radius, can be obtained from either of the Eqns. (1.10i/ii) as soon as γ is known. Note finally that κ and γ are connected via

$$\kappa^2 R^2 = 2\,(1+\gamma^2), \tag{1.12}$$

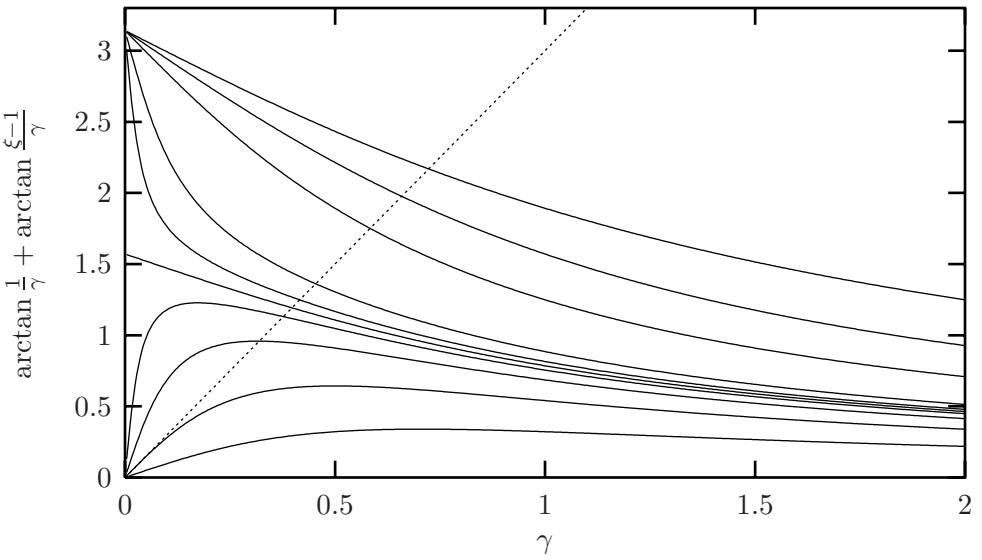

Figure 1.2: Graphical illustration of Eqn. (1.11). The curves indicate the r.h.s. for some exemplary values of ξ (namely: 3, 2, 1.5, 1.1, 1.03, 1, 0.97, 0.9, 0.75, 0.5 from top to bottom) while the dotted line indicates the left hand side with $\ln(R/r_0) = 3$.

thereby ensuring the chosen zero of the potential.

Unfortunately, Eqn. (1.11) has to be solved numerically, see also Fig. (1.2) for illustration. However, several rigorous statements can still be made. A few are summarized in the following.

Remarks 1.1.1

1. The central approximation in Eqn. (1.2) for the counterion density is that the exponential on the right hand side contains the potential instead of the potential of mean force.[5] Hence, Poisson-Boltzmann theory is by construction a low density theory.

2. Eqns. (1.9–1.12) are invariant under the transformation $\gamma \to -\gamma$. Thus, without loss of generality γ can be assumed to be non-negative.

3. The right hand side of Eqn. (1.11) is monotonically increasing with Manning parameter ξ. Hence, γ increases with ξ and decreases with cell radius R. Also, from Eqn. (1.10*ii*) it is seen that R_{M} increases with γ.

4. A general valence v appears as a prefactor on the right hand side of the Poisson equation (1.1) and in the exponent of the Boltzmann factor in Eqn. (1.2), which requires the definitions of the potential y and the screening constant κ to incorporate an additional factor of v. This implies a replacement $\xi \to \xi v$ in Eqns. (1.8*i*, 1.10*i*, 1.11). The remarkable consequence is that within Poisson-Boltzmann theory changing valence or electrostatic interaction strength affects the integration constants γ and R_{M} in the same way.

[5] The potential of mean force between two objects is the effective potential which emerges when integrating out all *other* degrees of freedom. Apart from the limit of zero density it differs from the plain intermolecular potential. "In a sense, one enters the realm of rigorous statistical mechanics when this distinction is clearly appreciated. [McQ76]"

5. At given cell geometry $\{r_0, R\}$ the Manning radius R_M is a unique function of the product of Manning parameter and counterion valence, ξv.

6. Only for $\xi > \xi_\mathrm{min} := \ln(R/r_0)/(1 + \ln(R/r_0))$ does Eqn. (1.11) have a real and nonzero solution for γ, as can easily be seen by determining the slope of the right hand side at $\gamma = 0$.[6]

7. For values $\xi < \xi_\mathrm{min}$ the Poisson-Boltzmann solution can be extended by analytic continuation over the complex numbers. This will not be pursued further, though.[7]

8. The value of κ (or, equivalently, the boundary density $n(R)$) enters the theory only via Eqn. (1.12), i.e., only in the combination κR.

9. Various asymptotics are available in the dilute limit. This will be discussed in more detail in Sec. 1.1.4.

1.1.2 Integrated charge and counterion condensation

Using the formulæ from the last section, the total charge per length, $Q(r)$, within a cylinder of radius $r \in [r_0; R]$ can be determined analytically by integrating the counterion density in Eqn. (1.2):

$$Q(r)/\lambda = 1 - \frac{1}{\lambda}\int_{r_0}^{r} \mathrm{d}\bar{r}\, 2\pi\bar{r}\, e_0\, n(\bar{r}) = 1 - \Big(1 - \frac{1}{\xi}\Big) - \frac{\gamma}{\xi}\tan\Big(\gamma\, \ln\frac{r}{R_\mathrm{M}}\Big). \tag{1.13}$$

Remarks 1.1.2

1. Since $n(r) > 0$, $Q(r)$ decreases monotonically from $Q(r_0) = \lambda$ to $Q(R) = 0$. The latter follows from Eqn. (1.10*ii*) and is in agreement with the requirement of global charge neutrality.

2. It is instructive to use the quantity

$$P(r) := 1 - Q(r)/\lambda, \tag{1.15}$$

   which is the integrated probability distribution of finding a mobile ion at distance r. In other words, it is the fraction of counterions found within a cylinder of radius r, see Fig. 1.3. For simplicity, $Q(r)$ and $P(r)$ will both be referred to as counterion distribution functions.

3. At $r = R_\mathrm{M}$ the last term in Q vanishes, giving a fraction $1 - 1/\xi$ of ions within R_M.

4. Rem. 1.1.1.4 entails that the counterion distribution function depends only on ξv.

5. A numerically convenient connection between P and y is outlined in TP 1.2.

[6] This can also be understood in terms of the Manning radius. For $\xi = 1$ Eqn. (1.10*i*) gives $R_\mathrm{M} = r_0$, i.e. R_M touches the surface of the cylinder. For $\xi > 1$ the Manning radius is outside the cylinder while for $\xi < 1$ it is inside and finally becomes 0 at $\xi = \xi_\mathrm{min}$. For instance, in Fig. 1.2 $\ln(R/r_0) = 3$, such that the curve with $\xi = 0.5$ is below and the curve with $\xi = 0.75$ is at the threshold.

[7] Note that the frequent statement of the Poisson-Boltzmann solution changing its nature at $\xi = 1$ is only true in the limit $R \to \infty$ or $r_0 \downarrow 0$, in which indeed $\xi_\mathrm{min} = 1$.

Technical Point 1.2

The Poisson equation can be used to construct a differential connection between the charge distribution function P and the potential y. First define $x := \ln(r/L)$, $\tilde{P}(x) := P(r)$ and $\tilde{y}(x) := y(r)$, where L is an arbitrary constant with dimension of length. Using these new variables and the Poisson equation, $P(r)$ can be rewritten as:

$$\begin{aligned} P(r) &= \frac{2\pi e_0}{\lambda}\int_{r_0}^{r} \mathrm{d}\bar{r}\,\bar{r}\,n(\bar{r}) \overset{(1.1)}{=} \frac{1}{2\xi}\int_{r_0}^{r}\mathrm{d}\bar{r}\left(\frac{\mathrm{d}^2}{\mathrm{d}\bar{r}^2}+\frac{1}{\bar{r}}\frac{\mathrm{d}}{\mathrm{d}\bar{r}}\right)y(\bar{r}) \\ &= \frac{1}{2\xi}\int_{\ln\frac{r_0}{L}}^{x}\mathrm{d}\bar{x}\,\tilde{y}''(\bar{x}) = \frac{1}{2\xi}\Big[\tilde{y}'(\bar{x})\Big]_{\ln\frac{r_0}{L}}^{x} \qquad \Big\| \;\; \tilde{y}'(\ln\frac{r_0}{L}) \overset{(1.8i)}{=} -2\xi \\ \Longrightarrow \qquad \tilde{P}(x) &= 1+\frac{\tilde{y}'(x)}{2\xi} \end{aligned} \tag{1.14}$$

It is easily verified that Eqns. (1.9) and (1.15) fulfill this relation. However, its range of applicability extends beyond Poisson-Boltzmann theory: Eqn. (1.14) is always true, provided the system is well described by a cylindrically symmetric charge distribution. In particular, it remains true if salt is added to the cell.

The fraction $f_\xi := 1-1/\xi$ of counterions within R_M is a critical threshold in the following sense: For $0<\alpha<1$, $\xi>1$ and the radius r_α defined as

$$r_\alpha := r_0\,\exp\big\{\alpha/(\xi-1)(1-\alpha)\big\} \tag{1.16}$$

it will be shown in section 1.1.4, Eqn. (1.25), that

$$\lim_{R\to\infty} P(r_\alpha) = \alpha\, f_\xi. \tag{1.17}$$

Even in the limit of infinite dilution a fraction α arbitrarily close to 1 of the fraction f_ξ stays within a finite radius r_α. It has thus become common practice to call f_ξ the fraction of condensed counterions or Manning fraction, although $\lim_{\alpha\uparrow 1} r_\alpha = \infty$ (see also Remarks 1.1.3.9 and 10). The phenomenon itself is generally referred to as *Manning condensation* [Man69, Oos70].

1.1.3 A new approach to quantifying counterion condensation

Statements about Manning condensation, as they are made in the literature, are often difficult to compare. This is a consequence of the fact that different authors prefer different ways of measuring this phenomenon. Even worse, some of these approaches are inconsistent with Poisson-Boltzmann theory in the dilute limit, although the theory is known to become exact then.[8] At the risk of enhancing confusion, this thesis proposes a further criterion for quantifying counterion condensation. It is introduced in this section, and its various advantages over the existing methods are outlined. Its extensive applications throughout the rest of this work will further demonstrate that it provides a unified picture of the condensation scenario

[8] The validity of the *cell model* in the dilute limit is in fact a different issue.

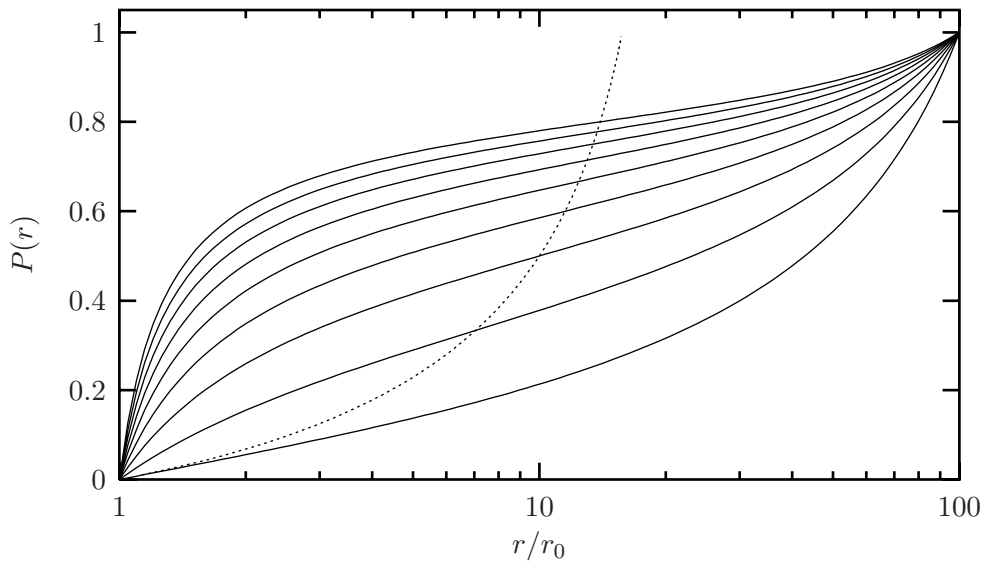

Figure 1.3: Exemplary Poisson-Boltzmann counterion distribution functions from Eqns. (1.13,1.15) for a system with $r_0 = 1$, $R = 100$ and $\xi \in \{1, 1.5, 2, 2.5, 3, 3.5, 4, 4.5, 5\}$ from bottom to top. The dotted line shows the locus of all inflection points, see also Rem. 1.1.1.5. Note the logarithmic horizontal scale.

If the counterion distribution function P is known, the condensed counterion fraction can be characterized in the following "geometric" way: Eqns. (1.13,1.15) show that P viewed as a function of $\ln(r)$ is merely a shifted tangent-function with its center of symmetry at $(\ln(R_\mathrm{M}); f_\xi)$. Since, however, $\tan''(0) = 0$, Manning radius and Manning fraction can be found by plotting P as a function of $\ln(r)$ and localizing the point of inflection, see Fig. 1.3. An alternative but equivalent procedure is outlined in TP 1.3.

This property of P, derived within the framework of Poisson-Boltzmann theory, can in turn be used to *define* the condensed fraction [DeHo00]. It provides a suitable way to quantify counterion condensation beyond the scope of Poisson-Boltzmann theory, and it is exact in the salt-free Poisson-Boltzmann limit. From here on this method will be referred to as the *inflection point criterion*.

To justify the introduction of yet another condensation criterion, it is appropriate to briefly discuss various alternative methods which have been used to measure counterion condensation, and to point out their shortcomings. The notion of a condensed layer closely surrounding the rod suggests that it should be possible to determine the condensed fraction by simply counting the ions within a certain small distance of the rod, e.g., a few Ångströms [LyNo97] or one screening length $1/\kappa$ [Man92]. This amounts to making a prior assumption about the Manning radius. Such a procedure is not only arbitrary, but moreover, the Manning radius from Poisson-Boltzmann theory depends on the polyelectrolyte density and diverges like $\sqrt{R}$ in the dilute limit. If this is not taken into account, the condensed fraction is either underestimated, for fixed condensation distance, or overestimated, for a distance $1/\kappa$, which is proportional to the cell radius R.

Conversely, one could assume that the condensed fraction is always given by $1 - 1/\xi$ and thereby obtain the size of the condensed layer, e.g., when salt is added to the system

Technical Point 1.3

The condensation criterion mentioned in the text can be reformulated in terms of the counterion density $n(r)$: If P has a point of inflection as a function of $\ln r$, $\mathrm{d}P/\mathrm{d}(\ln(r))$ must have a stationary point there. Using Eqns. (1.13,1.15), it follows that $r^2\, n(r)$ must have a stationary point. In the simple salt-free case this is actually a minimum.

[GuWe80]. Although being exact in the salt free Poisson-Boltzmann limit, this criterion excludes by definition the possibility that any effects beyond the mean-field level, like correlations, or the presence of salt also modify the fraction of condensed counterions. In addition, it is not capable of predicting a crossover to a high salt regime where all counterions are condensed solely due to the presence of the salt.

Finally, one could be tempted to use the electrostatic binding energy to distinguish between uncondensed and condensed counterions – the latter having a binding energy to the rod of more than $k_{\mathrm{B}}T$ [PaLa93, LaWo94]. In other words, ions with a distance $r < R_{\mathrm{T}}$ are considered as condensed, with the "thermal" distance R_{T} defined by $y(R_{\mathrm{T}}) = 1$. Within salt-free Poisson-Boltzmann theory, however, this is not a suitable criterion, since the electrostatic potential at the Manning radius asymptotically behaves as $\ln(R/r_0)$ and thus diverges in the limit $R \to \infty$, see Rem. 1.1.3.4. Hence, ions from the Manning layer cannot easily be described by their binding energy. In fact, the particular value $k_{\mathrm{B}}T$ is in no way special.[9] Since furthermore $y(r_0) \sim 2\,\ln(R/r_0)$ in the dilute limit, the potential difference with respect to the rod surface diverges as well.

Figure 1.4 compares the inflection point rule, two energy criteria, the Debye-length approach and a close-distance method with respect to their predictions for the condensed fraction. All five methods quantify condensation differently and – apart from the inflection point rule – are density dependent.[10] This on its own is not a problem; the unsatisfying aspect of the alternative methods is rather that they do not converge to the Manning fraction $1 - 1/\xi$ upon dilution. For the limiting values of $P(\ell_{\mathrm{D}})$, $P(\mathrm{e}\, r_0)$ and $P(R_{\mathrm{T}})$ see Rem. 1.1.3.11, Rem. 1.1.3.12 and Rem. 1.1.3.13, respectively. Observe that those three coincide with the inflection point criterion for $R/r_0 \approx 5$–10 within a few percent. This should, however, not be regarded as anything beyond pure chance.

In conclusion: The inflection point criterion employed in the present work has the advantages of *(i)* not fixing by definition the amount of condensed counterions (f_ξ and R_{M} can be determined independently of each other), *(ii)* reproducing the salt-free Poisson-Boltzmann limit, namely $P(R_{\mathrm{M}}) = 1 - 1/\xi$, and *(iii)* quantifying the breakdown of the coexistence of condensed and uncondensed counterions in the high salt limit, as will be shown in Sec. 1.2.

Notice finally that the appearance of the logarithm in the inflection point criterion is related to $\ln(r)$ being the two-dimensional Coulomb potential, i.e., the Green function of

[9] One might argue that $k_{\mathrm{B}}T$ is the thermal kinetic energy required by an ion for escaping the potential well formed by the macroion [PaLa93]. But this well can easily be much deeper than $k_{\mathrm{B}}T$ also for *spherical* macroions in the dilute limit, although in this case no counterions will be bound. In fact, the phenomenon of Manning condensation – typical for the cylindrical geometry – results from the radial dependence of energy and entropy having the same functional form, viz, logarithmic, and not some particular value.

[10] The inflection point criterion being independent of density is a feature seen on the Poisson-Boltzmann level only.

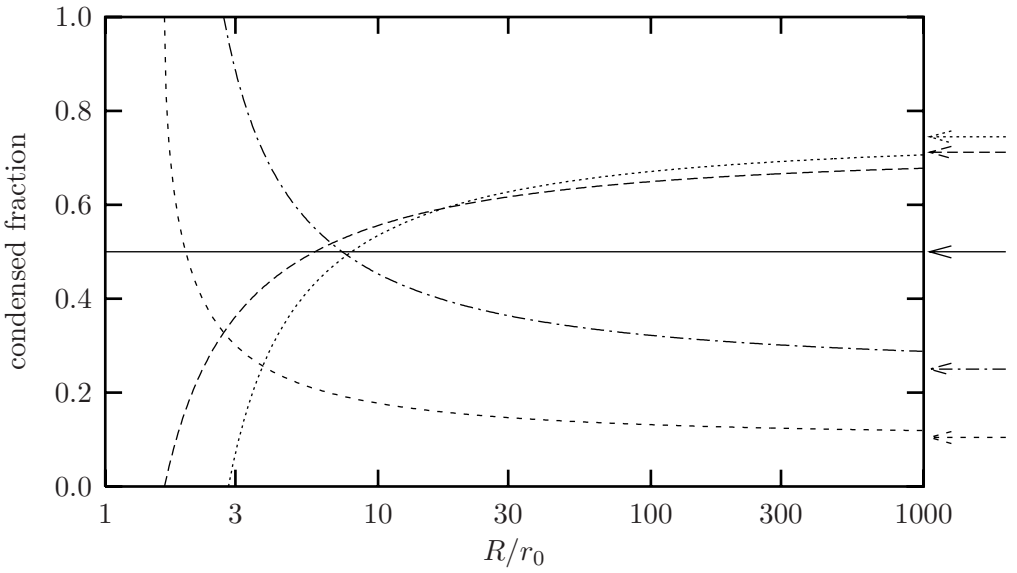

Figure 1.4: Predictions for the condensed fraction from various condensation criteria within Poisson-Boltzmann theory for a system with $\xi = 2$ as a function of cell size R. Solid line: inflection point criterion; long dashed: $y(r) = 1$; short dashed: $y(r_0) - y(r) = 1$; dotted: $P(\ell_\mathrm{D})$; dash-dotted: $P(\mathrm{e}\, r_0)$. The arrows indicate the limiting values at infinite dilution. Note that the inflection point criterion is the only one to give the correct value $1 - 1/\xi = 1/2$ in that limit.

the cylindrically symmetric Laplacian. In the corresponding three-dimensional (spherical) problem of charged colloids the Green function $1/r$ would be the appropriate choice for plotting the radial coordinate [BeDr84, Bel98].

1.1.4 Limiting laws

The only complication with exact results of the Poisson-Boltzmann equation is the transcendental equation (1.11) for the integration constant γ. Since its right hand side is bounded by its zeroth and first order Taylor expansion, this gives an allowed interval for γ. The following considerations only apply to the case of $\xi > 1$:

$$\begin{aligned} \pi \;\geq\; \gamma \ln \frac{R}{r_0} \quad &= \quad \arctan \frac{1}{\gamma} + \arctan \frac{\xi - 1}{\gamma} \;\geq\; \pi - \frac{\xi}{\xi - 1}\,\gamma \qquad \boxed{\xi > 1} \\ &\Rightarrow \quad \underline{\underline{\frac{\pi}{\ln \frac{R}{r_0}} \;\geq\; \gamma \;\geq\; \frac{\pi}{\ln \frac{R}{r_0} + \frac{\xi}{\xi - 1}}}}. \end{aligned} \tag{1.18}$$

In the limit $R \to \infty$ the two bounds and therefore γ converge to zero. Thus, in this limit γ can be approximated by either side of inequality (1.18). Notice, however, that the right hand side originates from the first order expansion and can therefore be assumed to be more accurate. Starting from this it is possible to derive asymptotics or even boundaries for several other observables.

Manning radius:

$$\begin{aligned} R_{\mathrm{M}} &= R\,\exp\left\{-\frac{1}{\gamma}\arctan\frac{1}{\gamma}\right\} \gtrsim R\,\exp\left\{-\underbrace{\frac{\ln\frac{R}{r_0}+\frac{\xi}{\xi-1}}{\pi}}_{\geq 0}\,\underbrace{\operatorname{arccot}\frac{\pi}{\ln\frac{R}{r_0}+\frac{\xi}{\xi-1}}}_{\operatorname{arccot}(x)\lesssim\frac{\pi}{2}-x+\frac{1}{3}x^3}\right\} \\ &\gtrsim R\,\exp\left\{-\frac{\ln\frac{R}{r_0}+\frac{\xi}{\xi-1}}{2}+1-\frac{1}{3}\frac{\pi^2}{\left(\ln\frac{R}{r_0}+\frac{\xi}{\xi-1}\right)^2}\right\} \qquad \Big\| \text{ use } \mathrm{e}^{-x}\geq 1-x \\ &\gtrsim \sqrt{R\,r_0}\,\exp\left\{\frac{1}{2}\frac{\xi-2}{\xi-1}\right\}\times\left\{1-\frac{\pi^2}{3}\Big(\ln\frac{R}{r_0}\Big)^{-2}\right\} \sim \underline{\underline{\sqrt{R\,r_0}\,\exp\left\{\frac{1}{2}\frac{\xi-2}{\xi-1}\right\}}} \end{aligned} \tag{1.19}$$

Contact potential:

$$\begin{aligned} y(r_0) &= -2\,\ln\left\{\frac{r_0}{\gamma\,R}\sqrt{1+\gamma^2}\,\cos\Big(\underbrace{\gamma\,\ln\frac{r_0}{R_{\mathrm{M}}}}_{\arctan\frac{1-\xi}{\gamma}}\Big)\right\} = -2\,\ln\left\{\frac{r_0}{R}\,\underbrace{\sqrt{\frac{\gamma^2+1}{\gamma^2+(\xi-1)^2}}}_{\frac{1}{\xi-1}+\frac{1}{2}\frac{\xi\,(\xi-2)}{(\xi-1)^3}\gamma^2+\mathscr{O}(\gamma^4)}\right\} \\ &\approx 2\,\ln\frac{R}{r_0}+2\,\ln(\xi-1)-\frac{\xi\,(\xi-2)}{(\xi-1)^2}\frac{\pi^2}{\left(\ln\frac{R}{r_0}+\frac{\xi}{\xi-1}\right)^2} \sim \underline{\underline{2\,\ln\frac{R}{r_0}}} \end{aligned} \tag{1.20}$$

Potential at $r=R_{\mathrm{M}}$:

$$\begin{aligned} y(R_{\mathrm{M}}) &= -2\,\ln\left\{\frac{R_{\mathrm{M}}}{R}\frac{1}{\gamma}\sqrt{1+\gamma^2}\right\} = \frac{2}{\gamma}\underbrace{\operatorname{arccot}\gamma}_{\lesssim\frac{\pi}{2}-\gamma+\frac{1}{3}\gamma^3}+2\,\ln\gamma-\underbrace{\ln(1+\gamma^2)}_{\gtrsim 0} \\ &\lesssim \ln\frac{R}{r_0}-2\,\ln\ln\frac{R}{r_0}-\frac{\xi-2}{\xi-1}+2\,\ln\pi+\frac{2}{3}\Big(\frac{\pi}{\ln\frac{R}{r_0}}\Big)^2 \sim \underline{\underline{\ln\frac{R}{r_0}}} \end{aligned} \tag{1.21}$$

Potential, shifted to 0 at r_0:

$$\begin{aligned} y(r)-y(r_0) &= -2\,\ln\frac{\frac{r}{R}\sqrt{1+\gamma^{-2}}\,\cos\left(\gamma\,\ln\frac{r}{R_{\mathrm{M}}}\right)}{\frac{r_0}{R}\sqrt{1+\gamma^{-2}}/\sqrt{1+(1-\xi)^2/\gamma^2}} \\ &= -2\,\ln\left\{\frac{r}{r_0}\sqrt{1+(1-\xi)^2/\gamma^2}\,\cos\Big(\gamma\,\ln\frac{r}{r_0}+\underbrace{\gamma\,\ln\frac{r_0}{R_{\mathrm{M}}}}_{\arctan\frac{1-\xi}{\gamma}}\Big)\right\} \\ &= -2\,\ln\frac{r}{r_0}-2\,\ln\left\{\cos\Big(\gamma\,\ln\frac{r}{r_0}\Big)-\frac{1-\xi}{\gamma}\sin\Big(\gamma\,\ln\frac{r}{r_0}\Big)\right\} \\ &\overset{R\to\infty}{=} \underline{\underline{-2\,\ln\frac{r}{r_0}-2\,\ln\left\{1+(\xi-1)\,\ln\frac{r}{r_0}\right\}}} \end{aligned} \tag{1.22}$$

Boundary density:

$$\begin{aligned} n(R) &= \frac{1+\gamma^2}{2\pi\ell_{\mathrm{B}}R^2} \gtrsim \frac{1+\pi^2/\left(\ln\frac{R}{r_0}+\frac{\xi}{\xi-1}\right)^2}{2\pi\ell_{\mathrm{B}}R^2} \qquad \Big\| \ \overline{\rho}_R := \lambda/\pi R^2 e_0 \\ &= \frac{\overline{\rho}_R}{2\xi}\times\left\{1+\frac{\pi^2}{\left(\ln\frac{R}{r_0}+\frac{\xi}{\xi-1}\right)^2}\right\} \gtrsim \underline{\underline{\frac{\overline{\rho}_R}{2\xi}}} \end{aligned} \tag{1.23}$$

Contact density:

$$\begin{aligned} n(r_0) &= n(R)\,\exp\big\{y(r_0)\big\} \;=\; \frac{1+\gamma^2}{2\pi\ell_{\rm B}R^2}\times\Big(\frac{R^2}{r_0^2}\;\frac{\gamma^2+(\xi-1)^2}{\gamma^2+1}\Big) \qquad \Big\|\; \overline{\rho}_{r_0} := \lambda/\pi r_0^2 e_0 \\ &\gtrsim \frac{\overline{\rho}_{r_0}}{2\xi}\times\left\{(\xi-1)^2+\frac{\pi^2}{\Big(\ln\frac{R}{r_0}+\frac{\xi}{\xi-1}\Big)^2}\right\} \overset{R\to\infty}{=} \underline{\underline{\frac{\overline{\rho}_{r_0}}{2\xi}\,(\xi-1)^2}} \end{aligned} \tag{1.24}$$

Ion fraction within $r_\alpha := r_0\,\exp\big\{\alpha/(\xi-1)(1-\alpha)\big\}$ for $\underline{\alpha<1}$ (see also Eqn. (1.16)):

$$\begin{aligned} P(r_\alpha) &= f_\xi+\frac{\gamma}{\xi}\tan\left\{\gamma\,\ln\frac{r_0\,\exp\big\{\alpha/(\xi-1)(1-\alpha)\big\}}{R_{\rm M}}\right\} \\ &= f_\xi+\frac{\gamma}{\xi}\tan\left\{\arctan\frac{1-\xi}{\gamma}+\frac{\gamma\,\alpha}{(\xi-1)(1-\alpha)}\right\} \\ &= f_\xi+\frac{\gamma}{\xi}\frac{\frac{1-\xi}{\gamma}+\tan\frac{\gamma\,\alpha}{(\xi-1)(1-\alpha)}}{1-\frac{1-\xi}{\gamma}\tan\frac{\gamma\,\alpha}{(\xi-1)(1-\alpha)}} \qquad \Big\|\ \text{expand for small } \gamma \\ &\overset{R\to\infty}{=} f_\xi+\frac{(1-\xi)/\xi}{1+\alpha/(1-\alpha)} \;=\; \underline{\underline{\alpha\,f_\xi}} \end{aligned} \tag{1.25}$$

Ion fraction within $\tilde{r}_\alpha := R\,\exp\big\{(\alpha-1/f_\xi)/(\alpha-1)\big\}$ for $\underline{\alpha>1}$:

$$\begin{aligned} P(\tilde{r}_\alpha) &= f_\xi+\frac{\gamma}{\xi}\tan\left\{\gamma\,\ln\frac{R\,\exp\big\{(\alpha-1/f_\xi)/(\alpha-1)\big\}}{R_{\rm M}}\right\} \\ &= f_\xi+\frac{\gamma}{\xi}\tan\left\{\arctan\frac{1}{\gamma}+\gamma\frac{\alpha-1/f_\xi}{\alpha-1}\right\} \\ &= f_\xi+\frac{\gamma}{\xi}\frac{\frac{1}{\gamma}+\tan\frac{\gamma\,(\alpha-1/f_\xi)}{\alpha-1}}{1-\frac{1}{\gamma}\tan\frac{\gamma\,(\alpha-1/f_\xi)}{\alpha-1}} \qquad \Big\|\ \text{expand for small } \gamma \\ &\overset{R\to\infty}{=} f_\xi+\frac{\alpha-1}{\xi\,(-1+\frac{1}{1-1/\xi})} \;=\; \underline{\underline{\alpha\,f_\xi}} \end{aligned} \tag{1.26}$$

Thermal radius $R_{\rm T}$, defined by $y(R_{\rm T})=1$:

$$\begin{aligned} {\rm e}^{-1/2} &= \frac{R_{\rm T}}{R}\underbrace{\sqrt{1+\gamma^{-2}}}_{\to 1/\gamma}\cos\left\{\gamma\,\ln\frac{R_{\rm T}}{R}+\underbrace{\arctan\frac{1}{\gamma}}_{\to\frac{\pi}{2}-\gamma}\right\} \;\approx\; \frac{R_{\rm T}}{\gamma R}\,\sin\left\{\underbrace{\gamma\Big(1-\ln\frac{R_{\rm T}}{R}\Big)}_{\to 0}\right\} \\ &\approx \frac{R_{\rm T}}{R}\Big(1-\ln\frac{R_{\rm T}}{R}\Big) \qquad\Longrightarrow\qquad \underline{\underline{R_{\rm T}\sim 0.2572577769\ldots\times R}} \end{aligned} \tag{1.27}$$

Thermal fraction $P(R_{\rm T})$:

$$\begin{aligned} P(R_{\rm T}) &= 1-\frac{1}{\xi}+\frac{\gamma}{\xi}\tan\left\{\gamma\,\ln\frac{R_{\rm T}}{R}+\underbrace{\arctan\frac{1}{\gamma}}_{\to\frac{\pi}{2}-\gamma}\right\} \;\approx\; 1-\frac{1}{\xi}+\frac{\gamma}{\xi}\cot\left\{\gamma\Big(1-\ln\frac{R_{\rm T}}{R}\Big)\right\} \\ &\approx 1-\frac{1}{\xi}+\frac{1/\xi}{1-\ln\frac{R_{\rm T}}{R}} \overset{(1.27)}{=} \underline{\underline{1-\frac{0.57585363\ldots}{\xi}}} \;>\; 1-\frac{1}{\xi} \end{aligned} \tag{1.28}$$

Debye fraction $P(\ell_D)$:

$$P(\ell_D) \;=\; P(R/2\sqrt{\xi}) \;\overset{\text{see above}}{\approx}\; \underline{\underline{1-\frac{1}{\xi}+\frac{1/\xi}{1+\ln(2\sqrt{\xi})}}} \;>\; 1-\frac{1}{\xi} \qquad (1.29)$$

Screening fraction $P(\kappa^{-1})$:

$$P(\kappa^{-1}) \;=\; P\big(R/\sqrt{2(1+\gamma^2)}\big) \;\overset{\text{see above}}{\approx}\; \underline{\underline{1-\frac{0.25737441\ldots}{\xi}}} \;>\; 1-\frac{1}{\xi} \qquad (1.30)$$

Remarks 1.1.3

1. All limiting values or asymptotics are reached logarithmically slowly.

2. Estimating the Manning radius by the left hand side of inequality (1.18) yields the upper boundary $R_M \le e\sqrt{R\,r_0}$.[11] Conversely, taking the limit $\xi \to \infty$ at fixed R for the exact expression of the Manning radius gives the lower boundary

$$\lim_{\xi\to\infty} R_M \;\gtrsim\; R\,\exp\left\{-\frac{1+\log\frac{R}{r_0}}{\pi}\arctan\frac{1+\log\frac{R}{r_0}}{\pi}\right\}. \qquad (1.31)$$

   Now taking also $R \to \infty$, the right hand side of this inequality converges towards $\sqrt{eRr_0}$. In this limit the Manning radius is therefore bounded as $\sqrt{eRr_0} \le R_M \le e\sqrt{R\,r_0}$. See also the limiting behavior of the line of inflection points in Fig. 1.3.

3. The $\sqrt{R}$-scaling of the Manning radius leads to the very advantageous separation of length scales $r_0 \ll R_M \ll R$ in the dilute limit. This decouples the Manning condensation both from chemical details important at r_0 as well as from shortcomings of the cell model at the outer boundary, where the mapping of a polyelectrolyte solution to an effective one-particle-theory is most questionable. This partly explains the success of the concept of counterion condensation and the cell model.

4. Both $y(R_M)$ and $y(R_M) - y(r_0)$ diverge in the dilution limit. In other words, the electrostatic energy of an ion at the Manning radius diverges with respect to the cell boundary as "point zero" as well as with respect to the cylinder surface. Hence, deciding upon condensation via some particular electrostatic binding energy is pointless (see also Rem. 1.1.3.13).

5. In Eqns. (1.23,1.24) $\overline{\rho}_R$ and $\overline{\rho}_{r_0}$ can be interpreted as the ion densities resulting from a homogeneous distribution of all counterions within the cell or the cylinder, respectively.

6. Eqn. (1.22) is the exact result for the potential of an isolated cylinder with counterions. Note that up to logarithmic corrections it is identical to the potential of a charged cylinder with charge parameter $\xi = 1$, independent of the *actual* value of ξ. For $\xi > 1$ the counterions effectively "renormalize" the original line charge density λ. Quite contrary, for $\xi < 1$ one would get $y(r) - y(r_0) = -2\xi\,\ln(r/r_0)$ in the dilute limit, which is the same potential as if no counterions were present at all. An explicit derivation of this result can be found in Appendix A of [NeJo98].

[11] The reader should note that here e is Euler's constant 2.71828... and not the unit charge, which is e_0.

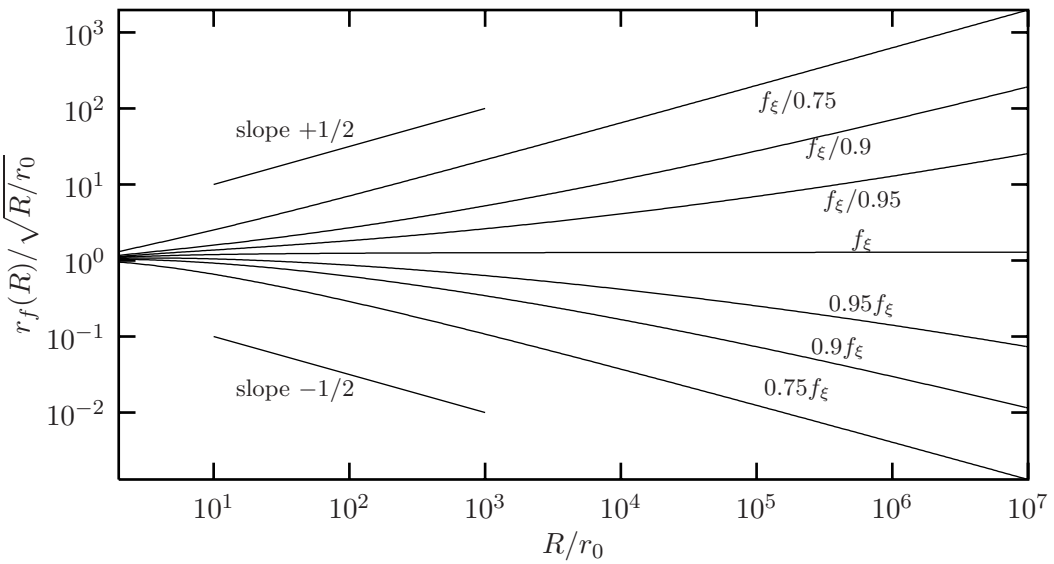

Figure 1.5: Radius $r_f(R)$ which contains a fraction f of ions for a cell model with radius R and Manning parameter $\xi = 3$. Since $r_{f_\xi}(R) \propto \sqrt{R}$, the radius is scaled by $\sqrt{R}$. The criticality at $f = f_\xi$ is clearly visible. See also Rem. 1.1.3.9.

7. Whereas $n(R)$ goes to zero in the limit $R \to \infty$, the contact density $n(r_0)$ converges towards a positive constant for $\xi > 1$. This supports the notion of a condensed layer which cannot be diluted away.

8. A real system need not be able to display a density as large as $n(r_0)$ for excluded volume reasons. If, for instance, the counterions are actually spheres of diameter d, closed packing corresponds to a density $\sqrt{2}/d^3$. Demanding $n(r_0)$ to be smaller than this results in the requirement

$$\frac{r_0^2\,\ell_B}{d^3} \;\geq\; \frac{(\xi-1)^2}{\sqrt{8}\,\pi}. \tag{1.32}$$

   This limits the range of applicability of the Poisson-Boltzmann approximation towards not too large ions, not too small cylinders and not too strong electrostatics (since $\xi \propto \ell_B$).

9. The Manning radius, which contains the critical fraction $f_\xi = 1 - 1/\xi$, diverges like $\sqrt{R}$ in the dilution limit, see Eqn. (1.19). Any radius containing less than f_ξ does not diverge, see Eqn. (1.25), while any radius containing more than f_ξ diverges like R, see Eqn. (1.26) and the definition of $\tilde{r}_\alpha$. It is this property which makes the Manning fraction so special. It is illustrated in Fig. 1.5.

10. Although r_α in Eqn. (1.16) is finite for $\alpha < 1$, it can be quite large for α close to 1. For example, at $\xi = 2$ a fraction of 95% of all "condensed" ions can be found within $r_{0.95} = r_0 \exp\{0.95/(2-1)(1-0.95)\} \approx 1.8 \times 10^8\, r_0$. The idea of a condensed layer closely surrounding the cylinder should be taken with care, particularly if one considers the limit of infinite dilution. On the other hand, for finite densities the

radius within which an arbitrary fraction of ions smaller than 1 can be found is of course bounded by the cell radius R.

11. There is a subtle difference between the Debye length ℓ_D of the system, computed from the average density, and the screening length κ^{-1}, which follows from the boundary conditions and is identical to the local Debye length at the cell boundary. Still, both lengths scale asymptotically like R and will thus enclose more than the Manning fraction – see Eqns. (1.29,1.30). Since $\kappa^{-1} \geq \ell_D$ must hold, one has $P(\kappa^{-1}) \geq P(\ell_D)$.

12. The special case $\alpha = f_\xi$ in Eqn. (1.25) shows that the fraction of ions within a distance $\mathrm{e}\, r_0 = 2.71828\ldots r_0$ is in the dilute limit given by f_ξ^2.

13. The thermal radius R_T is the distance at which the binding energy of a counterion to the rod is $k_B T$. Since for large R it scales linearly with R, the fraction of ions within R_T must be larger than f_ξ, see Rem. 1.1.3.9, as can indeed be seen from Eqn. (1.28). Hence, measuring the condensed fraction in this manner gives results which are incompatible with Manning theory in the dilute limit. However, the relative error becomes small for large ξ.

1.2 The cell model with salt

A moderate addition of salt changes only some quantitative aspects of counterion condensation, but as soon as the Debye length of the salt becomes comparable to the Manning radius, the condensation scenario breaks down.

The amount of analytic knowledge about the Poisson-Boltzmann equation in the case of added salt is much less than in the salt-free case. An exact solution for the cell model described in the last section is still missing. However, rigorous bounds to the solution, as well as error bounds for approximations, have been constructed in Ref. [RaWo85]. A closed expression for the potential of a charged line immersed into a 1:1 and 2:1 bulk electrolyte has recently been derived in Ref. [TrWi97], using exact results from the theory of completely integrable systems of the Painlevé/Toda type. Unfortunately, due to their highly involved mathematical complexity those analytical expression are of much less practical use than the simple analytical result for the salt-free Poisson-Boltzmann equation. This section thus discusses numerical solutions of the Poisson-Boltzmann equations at varying amount of added salt. After emphasizing the importance of the ensemble, the inflection point criterion proposed in Sec. 1.1.3 is used to illustrate the route from counterion condensation at low salt to systems essentially dominated by salt screening at high salt [DeHo00].

1.2.1 Counterion condensation in the presence of salt

The central question to be discussed in this section is the following: Can the concept of counterion condensation be extended to the case of added salt?

First of all: the salt corresponds to a new degree of freedom which comes along with its own length scale, viz, the Debye length $\ell_D = (8\pi\ell_B v^2 n)^{-1/2}$. Here, v is the valence of the for simplicity symmetric salt and n is its bulk density. It is of central importance how this new length relates to the characteristic length R_M of the condensation structure. If ℓ_D

is large compared to R_{M}, this structure is preserved. However, if ℓ_{D} is smaller, it dictates the shape of the charge distribution function and the condensation structure is no longer present.

Counterion condensation becomes apparent in the behavior of the charge distribution function for cell radius $R \to \infty$, hence one should also investigate this limit in the presence of salt. This, however, is crucially dependent on the chosen ensemble, i.e., whether the limit is performed at constant number N of salt molecules or at constant chemical potential μ.

In the constant N case the Debye length is proportional to R and thus diverges faster than the Manning radius, which scales like $\sqrt{R}$, see Eqn. (1.19). For sufficiently large R the condensation structure will therefore be visible and the condensation criterion will be the same as in the salt free case. Conversely, for sufficiently high density, or number of salt molecules, the Debye length will be smaller than the Manning radius, thus modifying the condensation structure. Since the latter is a new mechanism for compensating the rod charge, it is no longer sensible to use the concept of Manning condensation in this limit. The remaining task is to clarify the crossover from counterion condensation to screening, which is subject of the following section.

Side-note: The above line of reasoning needs to be modified if the added salt has a higher valence than the counterions. The reason is that in this case it will be the higher valent salt ions which will condense onto the rod. Two cases have to be distinguished:

1. Already a fraction of the negative salt ions of highest valence could completely neutralize the rod. If these ions are taken to be the "true" counterions and all the rest (including the "original" counterions) is denoted as "salt", one can expect a Manning limiting behavior typical for the high-valent new counterions.

2. There is not enough salt to completely neutralize the rod with the highest valent negative salt ions. This is just as complicated as the case of no salt but different species of counterions and will not be pursued further here. The latter situation will reappear in Sec. 1.4.2 as an exemplary application for a Monte-Carlo Poisson-Boltzmann solver. Some information on systems with mixed-valence counterions can be found there.

Quite differently, in the case of constant chemical potential the Debye length of the salt will remain finite in the limit $R \to \infty$ and consequently be smaller than the diverging Manning radius of salt-free Poisson-Boltzmann theory. The condensation structure will always be wiped out in the dilution limit and it is not possible to produce a condensation criterion as in the salt-free case.

From an experimental point of view, keeping N or μ constant in the limit $R \to \infty$ corresponds to two completely different procedures. In the first case the polyelectrolyte solution is diluted by the addition of pure water. In the second case the dilution is done with a salt solution of the same ionic strength as the one in which the polyelectrolyte originally has been dissolved. One therefore cannot expect these two cases to become equivalent in the thermodynamic limit.

In large systems it is essentially irrelevant whether a certain salt concentration is achieved by choosing a certain number of salt ions or a corresponding chemical potential for them. However, in all systems accessible to computer simulations the number of ions is still rather small, so that the chosen ensemble matters. Since the aim is to eventually compare simulation and theory, and since the most straightforward ensemble for simulations is the one which conserves particle number, the following section derives a Poisson-Boltzmann equation in the presence of salt for this case [DeHo00].

1.2.2 Poisson-Boltzmann equation for constant number of salt molecules

Assume that in addition to the monovalent counterions of the positively charged rod the cell contains K different $v:v$ salts of concentrations $\bar{n}_v$ with $v = 1 \dots K$. The overall concentration of negative monovalent ions is thus $\bar{n}_1 + m$ with $m = \lambda/e\pi R^2$ where m is the contribution due to the counterions of the rod.

The free energy $F = U - TS$ accounts for the internal electrostatic energy U and the translational entropy S of the mobile ions in solution. It can be written in terms of the electrostatic potential ψ and the local ion concentrations n_v and n_{-v} of positive and negative ions of valence v, respectively. Within this mean-field theory F is given by

$$F = \int_V \mathrm{d}^3 r \left[\frac{\epsilon}{2} \big(\nabla\psi\big)^2 + k_\mathrm{B}T \sum_{\substack{v=-K \\ v\neq 0}}^{K} n_v \ln \frac{n_v}{\bar{n}_v} \right], \tag{1.33}$$

where $\bar{n}_{-v} = \bar{n}_v$ (for $v = 2 \dots K$) and $\bar{n}_{-1} = \bar{n}_1 + m$ denote the concentrations of the negatively charged mobile ions.

As discussed in the above section, for each ionic species the number of ions within the cell of volume V should be conserved. With this in mind, the local equilibrium concentrations, n_v, have to be derived under the constraints

$$\langle n_v \rangle \equiv \frac{1}{V} \int_V \mathrm{d}^3 r \; n_v \stackrel{!}{=} \bar{n}_v. \tag{1.34}$$

The variation of F results in the Boltzmann distributions for the local concentrations

$$n_v = \bar{n}_v \mathrm{e}^{-vy-\mu_v}, \tag{1.35}$$

where the (dimensionless) chemical potentials $\mu_v = \ln\langle \mathrm{e}^{-vy} \rangle$ ensure particle conservation (in essence as Lagrange multipliers).

Insertion of the local concentrations n_v into the cylindrically symmetric Poisson equation $\epsilon\,(\psi'' + \psi'/r) = -\sum_v v n_v$ leads to the new Poisson-Boltzmann equation with added salt:

$$y'' + \frac{y'}{r} \;=\; -4\pi\ell_\mathrm{B} \sum_{v=-K}^{K} v\bar{n}_v \frac{\mathrm{e}^{-vy}}{\langle \mathrm{e}^{-vy} \rangle}. \tag{1.36}$$

This equation has to be subjected to the boundary conditions in Eqn. (1.8), which are the same as in the salt free case. Due to the average $\langle \cdots \rangle$ on the right hand side, Eqn. (1.36) is actually an integro-differential equation.

Numerical solutions of Eqn. (1.36) can be found employing a Newton-Raphson iteration scheme in which the chemical potentials μ_v are updated after each iteration step. Once a solution $y(r)$ is found, the integrated charge distribution function of the mobile ions

$$P(r) \;=\; -\frac{e_0}{\lambda} \int_{r_0}^{r} \mathrm{d}r' \, 2\pi r' \sum_{v=-K}^{K} v n_v(r) \tag{1.37}$$

can be calculated via Eqn. (1.14). Eqn. (1.37) is a natural generalization of the distribution function in Eqns. (1.13,1.15), but its interpretation as an integrated probability distribution (or fraction of counterions) is only valid in the salt free case.

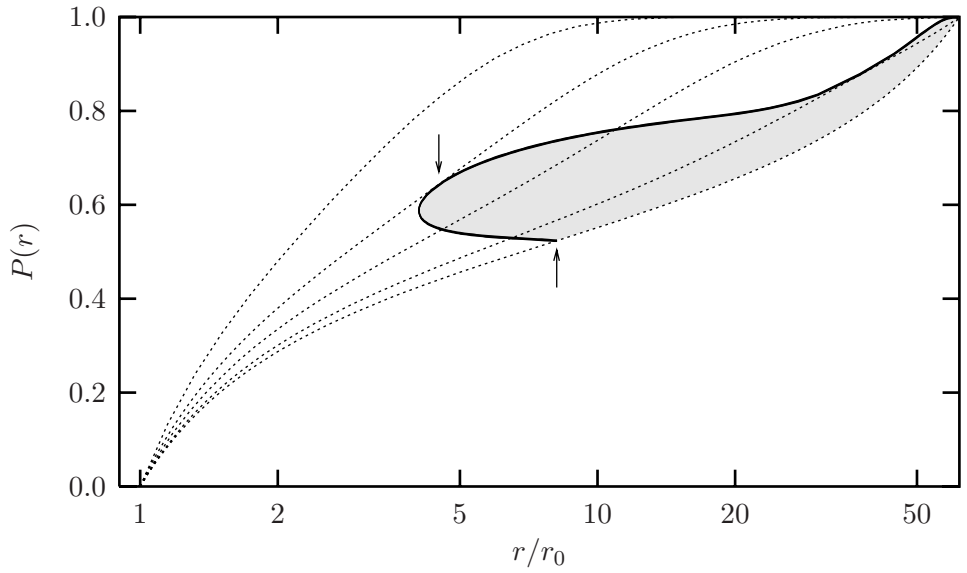

Figure 1.6: Poisson-Boltzmann results (dotted curves) for the integrated charge distribution function $P(r)$ for a system characterized by $R/r_0 = 61.9$, $\xi = 2.1$, $\lambda = 0.96\, e/r_0$, monovalent counterions and different numbers N of 1 : 1 salt molecules per rod segment of length $L = 250\, r_0$: from bottom to top $N \in \{0, 104, 800, 3070, 15\,000\}$. Note that the number of counterions corresponding to L is $M = 240$. The solid curve shows the locus of inflection points, i.e., the union of all inflection points of the functions $P(r)$. The ↑-arrow marks the location of the salt free Manning inflection point and the ↓-arrow shows where it annihilates one of the new salt inflection points. The branch of the locus between these two arrows indicates the range in which the concept of Manning condensation is meaningful. Note that the distribution functions are convex-up within the gray shaded region and convex-down outside.

1.2.3 The crossover scenario within Poisson-Boltzmann theory

To investigate the condensation criterion in the presence of monovalent salt, the potential $y(r)$ is calculated by solving the Poisson-Boltzmann equation for a system characterized by $R/r_0 = 61.92$, $\lambda/e_0 = 0.96/r_0$, $\xi = 2.1$ and a variable number of salt molecules. To facilitate the comparison with computer simulations in the next chapter, the amount of monovalent salt is expressed by the number N of ions belonging to a rod segment of length $L = 250\, r_0$. The corresponding cell volume that contains the mobile ions is then $V = L\pi R^2$ and the Debye length is $\ell_D = (8\pi\ell_B N/V)^{-1/2}$. Note that the line charge density $\lambda = 0.96\, e/r_0$ implies a number $M = 240$ positive charges to be found on the rod segment of length $L = 250\, r_0$.

From the numerical solutions of $y(r)$ all inflection points of $P(r)$ plotted against $\ln r$ are determined. They are solutions of the equation $\mathrm{d}^2P(r)/\mathrm{d}(\ln r)^2 = 0$. Fig. 1.6 presents the inflections points starting from $N = 0$ up to $N = 3070$. For larger values of N no further inflection points are found. In addition, Fig. 1.6 also shows the integrated charge distributions for $N \in \{0, 104, 800, 3070, 15\,000\}$ corresponding to Debye lengths of $\ell_D/r_0 \in \{\infty, 23.0, 8.27, 4.22, 1.91\}$, respectively.

The location of the inflection point for $N = 0$ coincides with R_M, thus indicating a fraction of condensed counterions of $P(R_M) = f_\xi = 1 - 1/\xi$. Increasing N by adding salt

shifts the inflection point to smaller values of r. That is, the layer of condensed counterions contracts, which is in accord with results obtained from other condensation criteria mentioned in Sec. 1.1.3. Importantly, the *amount* of condensation is only marginally increased, as can bee seen from the fairly small slope of the locus of inflection points at $(\ln R_{\mathrm{M}}; f_\xi)$. From a certain N on (in Fig. 1.6 $N = 104$) two more inflection points appear in the region of high r/r_0. This happens typically for a corresponding Debye length being of the order of the cell size itself, indicating the appearance of a characteristic, salt induced, change in the convexity of P (as a function of $\ln r$).

Upon a further increase in N one of the two new inflection points shifts towards smaller values of r/r_0, finally fusing with the Manning inflection point and "annihilating" it. Roughly speaking, the inflection points vanish if the Debye length characterizing the salt content becomes smaller than the radius of the condensed layer. In this case it is no longer meaningful to distinguish between condensed and uncondensed counterions. Indeed, for a very high salt content, where the Debye length is much smaller than the radius of the rod, the solution of the Poisson-Boltzmann equation would be the one of a charged plane and one may consider all excess counterions being condensed – no matter what the charge density of the rod is.

As has been demonstrated, the numerical solutions of the Poisson-Boltzmann equation together with the inflection point criterion from Sec. 1.1.3 describe in detail a route from counterion condensation to salt screening, whose rough direction has become visible earlier in Sec. 1.2.1. Considering the fact that for a quantitative comparison the difficulties sometimes start already with the definition of condensation [GuWe80, Man92, PaLa93, LaWo94, LyNo97, DeHo00], this is indeed a gratifying result.

1.3 Counterion correlations

Some of the ionic correlations neglected in Poisson-Boltzmann theory can be approximately recaptured by including additional contributions to the free energy. One of these corrections is based on an extension of the one-component plasma model.

The classical one-component plasma (OCP) is an idealized model, in which a single species of ions moves in a homogeneous neutralizing background of opposite charge and interacts only via a repulsive Coulomb potential [Sal58, Abe59, LiNa75, LiNa76, BaHa80, Min87]. Apart from its applications in plasma physics [RoDe87, ZeCl92] it is also commonly used in soft matter physics as one of the simplest possible approaches for modeling correlations, e.g., when studying charged planes [StRo90] or charged colloids [AlCh84, KrRo86, PeNo90, Gro91, PeJö93, LeBa98, TaLe98].[12] The general idea is the following: Compute the one-component plasma free energy as a function of bulk density n_{B} and use this expression in the spirit of a local density approximation (LDA) as a correlation correction for the inhomogeneous system (i.e., $n_{\mathrm{B}} \to n(\boldsymbol{r})$). The total excess free energy is the volume integral over the free energy density and thus becomes a functional of $n(\boldsymbol{r})$. There is, however, a fundamental problem: The one-component plasma free energy is not a convex function of

[12] Many alternative and more sophisticated methods based on integral equations [SpPo73, Ng74, Ros96] have been developed for treating this correlation problem. But even though they offer results which are in good agreement with Monte-Carlo simulations, they do not provide any intuitive insight into the physics governing ionic solutions.

density.[13] This implies that it cannot be used in a thermodynamically stable way within a local density approximation, since the system can lower its total free energy by developing local inhomogeneities and increasing its density in one region at the expense of another (disregarding any surface effects) [Cal85, chapter 8.1]. Once started, this continues as a runaway process and the overall system collapses to a point. This feature is already seen on the level of the Debye-Hückel plus hole (DHH) approximation [Nor84], which is an extension of the original Debye-Hückel theory [DeHü23, McQ76] for the special case of the one component plasma, and the instability it gives rise to has been termed "structuring catastrophe" in this context [PeNo90, Gro91].

An alternative approach for avoiding this difficulty is proposed in this work. Instead of modifying the local density approximation, it modifies the one-component plasma model *itself* [BaDe]. Such a procedure should by no means appear suspicious, since it is not the one-component plasma which is under study, and there is no prior reason why this should be the *only* permissible model for describing correlations. Since the necessary changes to it will turn out to be surprisingly small, it is worthwhile to briefly review the way in which Debye-Hückel-hole theory arrives at a free energy for the one-component plasma.

1.3.1 The free energy of the one-component plasma within Debye-Hückel plus hole theory

Consider a system of N identical point-particles of valence v and positive unit charge e_0 inside a volume V with a uniform neutralizing background of charge density $-ve_0n_\mathrm{B}$ and dielectric constant ε. According to the Debye-Hückel approach, the potential created by a central ion, i.e., fixed at the origin, and all its surrounding ions results from solving the spherically symmetric Poisson equation

$$\nabla^2\psi(r) = \psi''(r) + \frac{2}{r}\,\psi'(r) = -\frac{\rho(r)}{\varepsilon} \tag{1.38}$$

under the following requirement: the charge density is $e_0v\delta(\boldsymbol{r})$ at the central ion, and the rest of the mobile ions rearrange themselves in the uniform background in accordance with the Boltzmann distribution $\rho(r) = ve_0n_\mathrm{B}(\exp\left[-\beta ve_0\psi(r)\right] - 1)$. Combining this with Eqn. (1.38) yields the nonlinear Poisson-Boltzmann equation. Linearization[14] of the exponential function in the mobile ion density gives $\rho(r) = -\varepsilon\kappa^2\psi(r)$ and from that the famous Debye-Hückel solution for the potential, $\psi(r) \sim \mathrm{e}^{-\kappa r}/r$. Here, $\kappa \equiv \sqrt{4\pi\ell n_\mathrm{B}}$ is the inverse screening length and $\ell = \ell_\mathrm{B}v^2$. This solution illustrates the rearrangement of the other ions around the central one in order to screen the Coulomb interaction.

The problem with Debye-Hückel theory is that the condition for linearization is obviously not satisfied for small r, where the potential is not small. Indeed, the particle density becomes negative and finally diverges at the origin. This defect was overcome by the Debye-Hückel-hole theory [Nor84], which artificially postulates a correlation hole of radius h around the central ion where no other ions are allowed. In this case the charge

[13] In fact, the thermodynamic limit itself is already a nontrivial issue. Its existence for the free energy, energy, pressure and entropy is established in Refs. [LiNa75, LiNa76], including a proof of the non-convexity of the free energy as a function of density as well as asymptotic scaling relations.

[14] A more detailed account of the linearized Poisson-Boltzmann equation is given in Sec. 1.5.

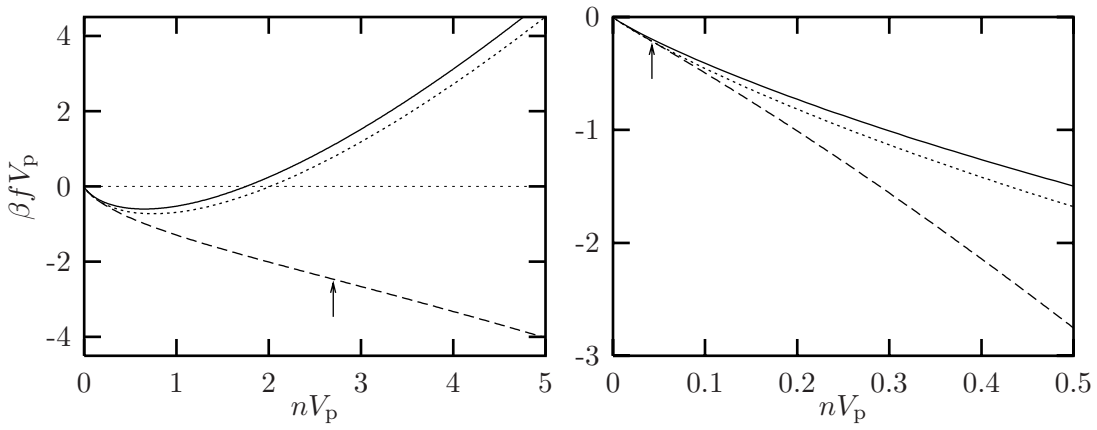

Figure 1.7: Free energy density as a function of density for three different theories: Debye-Hückel-hole [dashed, Eqn. (1.41)], Debye-Hückel-hole-cavity [solid, Eqn. (1.48)] and its zero temperature limit [dotted, Eqn. (1.52)] for Bjerrum length $\ell_\mathrm{B} = 7.14\text{Å}$ and monovalent/divalent ions (left/right). The arrows mark the points at which the Debye-Hückel-hole free energy density changes from convex to concave. A particle volume of $V_\mathrm{p} = (5\text{Å})^3$ was assumed.

density is given by

$$\rho(r) \;=\; \begin{cases} ve_0\left(\delta(\boldsymbol{r}) - n_\mathrm{B}\right) & : \quad r \le h \\ -\varepsilon\kappa^2\psi(r) & : \quad r > h. \end{cases} \tag{1.39}$$

The solution of the linearized Poisson-Boltzmann equation with the appropriate boundary conditions (continuity of electric field and potential) yields the potential for both regions in dependence of h, which has to be fixed on physical grounds. At low temperatures the electrostatic repulsion dominates and the minimum ion separation essentially becomes the mean separation, so $h = (3/4\pi n_\mathrm{B})^{1/3}$. At high temperatures, the hole size can be estimated by balancing Coulombic and thermal energies, leading to $h = \ell$. A systematic way to interpolate between these two limits results from excluding particles from a region where their Coulomb energy is larger than some threshold. A natural choice for the latter is the thermal energy $k_\mathrm{B}T$, which leads to

$$\kappa h = \omega - 1 \qquad \text{with} \qquad \omega = (1 + 3\ell\kappa)^{1/3}. \tag{1.40}$$

Incidentally, this assumption also gives a continuous charge density across the hole boundary.

Once the potential at the position of the central ion is known, the electrostatic contribution to the free energy density can be obtained by the Debye charging process [DeHü23], as was done previously by Penfold *et al.* [PeNo90]:

$$\frac{\beta f_\mathrm{DHH}}{n_\mathrm{B}} \;=\; \frac{1}{4}\left[1 - \omega^2 + \frac{2\pi}{3\sqrt{3}} + \ln\left(\frac{\omega^2+\omega+1}{3}\right) - \frac{2}{\sqrt{3}}\arctan\left(\frac{2\omega+1}{\sqrt{3}}\right)\right]. \tag{1.41}$$

The presented simple Debye-Hückel-hole analysis of the one-component plasma theory offers considerable insight into ionic systems and is in good agreement with Monte-Carlo

Technical Point 1.4 *(convex/concave $f_{\rm DHH}$)*

Consider the total free energy density $\beta f(n) = \beta f_{\rm DHH}(n) + n\ln(nV_{\rm p})$ of a homogeneous one-component plasma system in Debye-Hückel-hole approximation. Using Eqns. (1.40,1.41) and the identities $\mathrm{d}\omega/\mathrm{d}n = (\omega^3-1)/6n\omega^2$ and $\omega^3 - 1 = (\omega^2+\omega+1)(\omega-1)$, one may show

$$\begin{aligned}\beta f'(n) &= \frac{1}{12}\left\{4 + \frac{2\pi}{3\sqrt{3}} - 4\omega^2 + \ln\frac{\omega^2+\omega+1}{3} - 2\sqrt{3}\arctan\frac{2\omega+1}{\sqrt{3}}\right\} + \ln(nV_{\rm p}) + 1\\ \beta f''(n) &= \frac{1 + 39\,\omega - 4\,\omega^3}{36\,\omega\,n}\end{aligned}$$

The condition $f'' = 0$ requires ω to satisfy a cubic equation, whose only positive solution is:

$$\omega^\star \;=\; \sqrt{13}\,\cos\Big(\frac{1}{3}\arctan(6\sqrt{61})\Big) \;\approx\; 3.1352414.$$

One thus obtains the critical density $n^\star$, at which $f_{\rm DHH}$ changes from convex to concave:

$$n^\star \;=\; \frac{(\omega^{\star 3}-1)^2}{36\pi\ell^3} \;\approx\; \frac{7.8618}{\ell^3}. \tag{1.43}$$

Notice the strong dependence on valence, viz., the sixth power (recall that $\ell = \ell_{\rm B}v^2$).

simulations [BrSa66] when fluctuations on the charge density are not relevant [TaLe99]. In principle one can attempt to include such fluctuations by applying the bulk density-functional theory in a local way. The basic idea is to obtain the density distribution via functional minimization of the free energy

$$\beta F_{\rm OCP}[n(\boldsymbol{r})] = \int \mathrm{d}^3r\,\Big\{n(\boldsymbol{r})\ln\big(n(\boldsymbol{r})V_{\rm p}\big) \;+\; \beta f_{\rm DHH}[n(\boldsymbol{r})]\Big\} \tag{1.42}$$

under the constraint of global charge neutrality. Here, $V_{\rm p}$ represents the volume of a particle. Unfortunately, this variational process does not lead to a well defined density profile, since $f_{\rm DHH}(n)$ asymptotically behaves like $-n^{4/3}$ at high densities and therefore is not a convex function[15], with the implications mentioned at the beginning of this section. At small densities, however, the free energy density is convex and changes to a concave form only beyond a critical density $n^\star \approx 7.8618/\ell^3$, see Fig. 1.7 and TP 1.4. Hence, if during the process of actually computing $n(\boldsymbol{r})$ such a density is never met, the theory does not "realize" its asymptotic instability and gives a finite (yet, meta-stable) answer. It has in fact been applied to account for correlations in the case of systems with low ionic strength [StRo90, PeNo90]. For instance, in the case of aqueous solutions and monovalent ions, i.e., $\ell = 7.14$Å, the critical density $n^\star \approx 36\,\mathrm{mol/l}$, which clearly is high enough to prevent a runaway process to set in. However, already for divalent and trivalent ions $n^\star \approx 0.56\,\mathrm{mol/l}$ and $0.049\,\mathrm{mol/l}$, respectively, which are sufficiently low to be realized and trigger a collapse. Notice the strong dependence of $n^\star$ on valence, namely, on the sixth power.

[15] Observe that this is not just a bug of the Debye-Hückel approximation but rather a feature of the one-component plasma. In fact, not only the non-convexity but even the scaling $-n^{4/3}$ is in accord with rigorous results [LiNa75, LiNa76].

1.3.2 Excluding the background: The DHHC theory

To circumvent the instabilities occurring at high densities sometimes misleadingly attributed to the local density approach alone, a number of nonlocal free energies have been proposed [StRo90, Gro91, PaYe99]. In these weighted density approximations (WDA) the local density is replaced by a spatially averaged quantity. The main problem with these methods is that the choice of the weighting function is somewhat arbitrary. In most cases it is obtained by relating the second variation of the free energy with the direct correlation function. At this point the weighted density approximation requires prior information about this function, which is not yet available and thus has to be calculated using different approaches, e.g., integral equation theories. Whatever choice one takes, it is still *(i)* quite arbitrary and *(ii)* leads to a series of approximations which *(iii)* instead of clarifying the physics tend to obscure it.

The instabilities present in the Debye-Hückel-hole approach can be properly overcome by recognizing that the failure of this model is due to the too strong requirement of local charge neutrality imposed by the local density approximation: A local fluctuation leading to an increase of particle density implies a corresponding increase in background density. Therefore the fluctuation is not suppressed by an increase in repulsive Coulomb interactions but quite on the contrary favored by its decrease. A natural solution for that problem is to decouple the particle density from the background density and to apply the local density approximation just to the former one. This, however, leads to nonlinearities in the solution of the differential equation spoiling the simplicity of the Debye-Hückel and Debye-Hückel-hole approximations. The most simple solution is to exclude the neutralizing background from a cavity of radius a placed around the central ion *only*, which is already sufficient to control the unphysical divergence of the particle density. Even though it does not account for excluded-volume effects [PeJö93, NeOr99], the parameter a can in principle be identified with the diameter of the particles. In addition, the exclusion hole for $a \le r \le h$ is retained. The charge density, which for the usual Debye-Hückel-hole theory is given by Eqn. (1.39), has now three regions:

$$\rho(r) \;=\; \begin{cases} ve_0\delta(\boldsymbol{r}) & : \quad 0 \le r < a \\ -e_0 v n_{\mathrm{B}} & : \quad a \le r < h \\ -\varepsilon\kappa^2\psi(r) & : \quad h \le r. \end{cases} \tag{1.44}$$

The solution of the linearized Poisson-Boltzmann equation together with appropriate boundary conditions gives the potential in those regions:

$$\psi(r) = \frac{ve_0}{4\pi\varepsilon r} \times \begin{cases} 1 - \dfrac{r}{2\ell}\left[(\kappa h)^2 - (\kappa a)^2\right] - \kappa r C_h & : \quad 0 \le r < a \\ 1 - \dfrac{r}{2\ell}\left[(\kappa h)^2 - (\kappa r)^2\right] - \dfrac{1}{3\ell\kappa}\left[(\kappa r)^3 - (\kappa a)^3\right] - \kappa r C_h & : \quad a \le r < h \\ C_h\, \mathrm{e}^{-\kappa(r-h)} & : \quad h \le r, \end{cases} \tag{1.45}$$

where

$$C_h \;=\; \frac{1}{1+\kappa h}\left(1 - \frac{(\kappa h)^3 - (\kappa a)^3}{3\ell\kappa}\right). \tag{1.46}$$

In order to obtain the old theory in the limit $a \to 0$, the hole size h is chosen such as to yield the same screening (i.e., the same amount of charge within h) as the Debye-Hückel-hole

theory, which results in

$$\kappa h = \left[(\omega-1)^3 + (\kappa a)^3\right]^{1/3}. \tag{1.47}$$

This expression has four important physical limits: zero/infinite temperature and low/high density. At low temperature the exclusion hole has maximum size and behaves as $h = (3/4\pi n_{\mathrm{B}} + a^3)^{1/3}$. As the temperature is increased, the hole size shrinks, but contrary to Debye-Hückel-hole theory it does not vanishes and $h \to a$ as $T \to \infty$. At low densities, entropic effects compete with the Coulombic repulsion, and therefore $h = \ell + a$; for high densities, the exclusion hole decreases but is again limited below and gives $h \to a$. Using this prescription for h, the free energy can be obtained by Debye-charging the fluid:

$$\frac{\beta f_{\mathrm{DHHC}}}{n_{\mathrm{B}}} \;=\; \frac{(\kappa a)^2}{4} - \int_1^{\omega} \mathrm{d}\overline{\omega} \left\{ \frac{\overline{\omega}^2}{2(\overline{\omega}^3-1)} \Omega(\overline{\omega})^{2/3} + \frac{\overline{\omega}^3}{(1+\Omega(\overline{\omega})^{1/3})(\overline{\omega}^2+\overline{\omega}+1)} \right\} \tag{1.48}$$

where

$$\Omega(\overline{\omega}) = (\overline{\omega}-1)^3 + \frac{(\kappa a)^3}{3\ell\kappa}\,(\overline{\omega}^3-1) \tag{1.49}$$

and where the definition of ω is the same as in Eqn. (1.40). The integral can be solved numerically for given values of ℓ_{B}, v and a. As in the Debye-Hückel-hole approach fluctuations are taken into account by allowing the density to become local. Thus, $n(\boldsymbol{r})$ is obtained by minimizing the free energy from Eqn. (1.42) with f_{DHH} replaced by f_{DHHC} as given by Eqn. (1.48). But differently from the Debye-Hückel-hole theory, the Debye-Hückel-hole-cavity free energy is a convex function of density and can thus be used within a local density approximation. This situation is depicted in Fig. 1.7, which shows the free energy of the Debye-Hückel-hole theory together with the modified expression of the Debye-Hückel-hole-cavity approach.

1.3.3 The limit of zero temperature

The fact that the integral in Eqn. (1.48) has to be solved numerically obstructs a direct view on how thermodynamic stability is actually restored. Luckily, the crucial point can already be seen by focusing on the limit of zero temperature. In this case Eqn. (1.47) gives the expression $h = (3/4\pi n_{\mathrm{B}} + a^3)^{1/3}$ for the correlation hole of Debye-Hückel-hole-cavity theory. This conveniently implies the constant C_h in Eqn. (1.46) to be zero, and thus the potential to vanish outside h. In other words, the region $a < r < h$ contains the right amount of background charge to exactly neutralize the central ion, and it is appropriate to refer to this limit as "complete screening" (CS). The potential in the two other regions then simplifies considerably, i.e.,

$$\psi(r) \;=\; \frac{v\,e_0}{4\pi\epsilon r} \times \begin{cases} 1 \;+\; \dfrac{3r}{2a}\Big(\widehat{n}_{\mathrm{B}} - \dfrac{a}{h}(1+\widehat{n}_{\mathrm{B}})\Big) & : \quad 0 \le r < a \\[2ex] 1 \;+\; \widehat{n}_{\mathrm{B}}\Big(1+\dfrac{r^3}{2a^3}\Big) \;-\; \dfrac{3r}{2h}\Big(1+\widehat{n}_{\mathrm{B}}\Big) & : \quad a \le r < h \end{cases} \tag{1.50}$$

with the dimensionless scaled density $\widehat{n}_{\mathrm{B}}$ given by

$$\widehat{n}_{\mathrm{B}} \;=\; \frac{4}{3}\pi a^3\, n_{\mathrm{B}}. \tag{1.51}$$

After the Debye charging process one obtains the following closed expression for the excess free energy density:

$$\frac{\beta f_{\mathrm{CS}}}{n_{\mathrm{B}}} \;=\; \frac{3\ell}{4a}\left\{\widehat{n}_{\mathrm{B}} - (1+\widehat{n}_{\mathrm{B}})^{2/3}\,\widehat{n}_{\mathrm{B}}^{1/3}\right\}, \tag{1.52}$$

see also Fig. 1.7. For high densities βf_{CS} scales asymptotically like $-\ell n_{\mathrm{B}}/2a$, i.e., linear with density. However, in the limit $a \downarrow 0$ Eqn. (1.52) becomes

$$\lim_{a\downarrow 0} \beta f_{\mathrm{CS}} \;=\; -\ell \left(\frac{9\pi}{16}\right)^{1/3} n^{4/3}, \tag{1.53}$$

so in this case βf_{CS} scales like $-n^{4/3}$, which due to its concavity prevents it from being used within a local density approximation. The zero temperature limit thus demonstrates in a clear way the key role played by the cavity of size a, which excludes the uniform background from the vicinity of the central ion. Incidentally, Fig. 1.7 shows that for the case of aqueous solutions the difference between the full expression βf_{DHHC} and the zero temperature limit βf_{CS} is not very large. Therefore, the latter may in fact be of some practical use as well.

1.3.4 Application to the cylindrical cell model

This section demonstrates that the new free energies derived above can be applied as a correlation correction within a density functional description of the cell model. As has been discussed earlier, a simple way to improve Poisson-Boltzmann theory is to extend its free energy by a term to account for correlations. The configurational free energy for the screened macroion solution can be partitioned into two parts, given by

$$F[n(\boldsymbol{r})] = F_{\mathrm{PB}}[n(\boldsymbol{r})] + \int \mathrm{d}^3 r \; f_{\mathrm{DHHC}}[n(\boldsymbol{r})]. \tag{1.54}$$

The first contribution

$$\beta F_{\mathrm{PB}}[n(\boldsymbol{r})] = \int \mathrm{d}^3 r \left\{ n(\boldsymbol{r}) \ln\left(n(\boldsymbol{r}) V_{\mathrm{p}}\right) + \frac{1}{2}\beta\, v e_0\, n(\boldsymbol{r}) \psi[n(\boldsymbol{r})] \right\} \tag{1.55}$$

contains the entropy of the small ions, the interaction with the macroion potential and the mean-field interaction between the counterions. Minimization of this expression under the constraint of global charge neutrality gives – together with the Poisson equation – the Poisson-Boltzmann equation. The inter-particle correlations are now approximately accounted for by adding an excess free energy, which is the second term in Eqn. (1.54) – the Debye-Hückel-hole-cavity free energy in local density approximation. The equilibrium ion distribution minimizing the functional in Eqn. (1.54) can conveniently be determined by means of a Monte-Carlo solver, which will be described in more detail in Sec. 1.4.

The model system comprises a rod of radius r_0 and line charge density $\lambda = 0.959\, e_0/r_0$ embedded in a cell of outer radius $R = 123.8\, r_0$. The complementary values $\ell_{\mathrm{B}}/r_0 = 3$, $v = 1$ and $\ell_{\mathrm{B}}/r_0 = 1$, $v = 3$ have been investigated, which on the plain Poisson-Boltzmann level give identical distribution functions $P(r)$, see Eqn. (1.15) and Rem. 1.1.1.4. This is, however, no longer the case in the correlation corrected system. The Poisson-Boltzmann

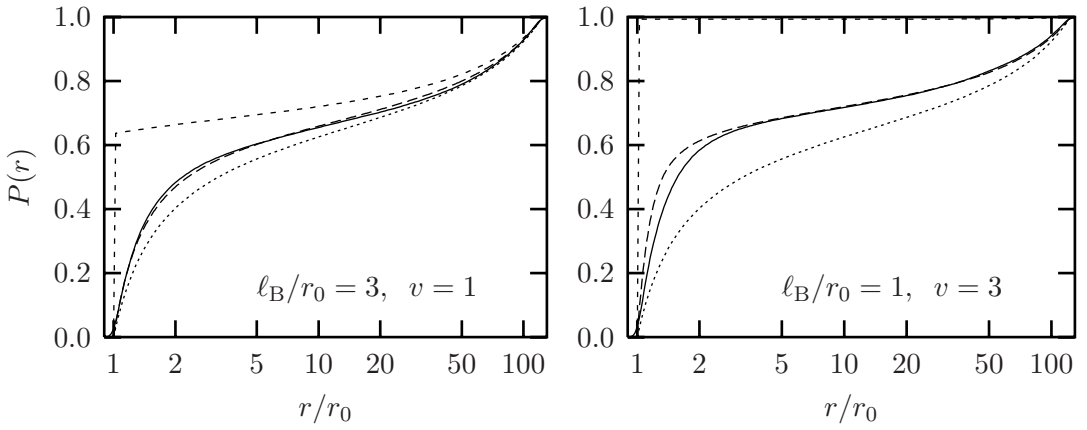

Figure 1.8: Counterion distribution function $P(r)$ from Eqn. (1.15) for two cylindrical cell models with $R/r_0 = 123.8$, $\lambda = 0.959\, e_0/r_0$ and the values for Bjerrum length and valence as indicated in the plots. The solid line is the result of a molecular dynamics simulation while the dotted line is the prediction from Poisson-Boltzmann theory. The increased counterion condensation visible in the simulation is accurately captured by the Debye-Hückel-hole-cavity extended Poisson-Boltzmann theory [long-dashed line, Eqn. (1.48)]. A corresponding curve based on the complete screening expression in Eqn. (1.52) would hardly be distinguishable from the Debye-Hückel-hole-cavity prediction on this scale. The complete failure of the plain one-component plasma correction [short-dashed line, Eqn. (1.41)] is obvious.

distribution functions, the correlation corrected ones obtained via Eqn. (1.54) and the results of molecular dynamics simulations[16] on that system are shown in Fig. 1.8. Compared to the plain Poisson-Boltzmann result the simulation shows a stronger condensation of ions in the vicinity of the rod. This effect is more pronounced in the trivalent system, disproving the prediction of Poisson-Boltzmann theory that $P(r)$ depends only on the product ξv. In both cases the increased condensation is reproduced by the correlation corrected functional from Eqn. (1.54). While in the case $\ell_B/r_0 = 3$, $v = 1$ the theoretical prediction practically overlaps the simulation, it somewhat overestimates correlations in the complementary case $\ell_B/r_0 = 1$, $v = 3$. It must, however, be noted that in the simulation the ions also interacted via a repulsive Lennard-Jones potential giving them a diameter of roughly r_0. The expected reduction of particle density resulting from the additional hard core is not accounted for in the presented theory.

In conclusion, it has been demonstrated that the new free energy correction proposed in this work and based on an extension of the one-component plasma model is able to recapture ionic correlation effects neglected in the plain Poisson-Boltzmann theory. The difficulties of the existing Debye-Hückel-hole approach have been traced back to its thermodynamically unstable free energy, and it has been shown that the creation of a background-free cavity around the central ion is sufficient to yield a convex free energy, applicable within a local density approximation.

[16] A detailed account is given in chapter 2.

1.4 Monte-Carlo simulation of a free energy functional

The Poisson-Boltzmann equation is the differential equation corresponding to the variational problem of minimizing the Poisson-Boltzmann free energy functional F_{PB}. This suggests an alternative numerical procedure of solving it: A Monte-Carlo simulation using the Metropolis factor $\exp\{-\beta F_{\mathrm{PB}}\}$.

Once a free energy functional has been decided on, it remains the task of finding the ion distribution minimizing it. The usual procedure is to transform this variational problem into a differential equation and solve the latter.[17] However, solving the boundary value problem of the resulting nonlinear differential equation is usually a formidable task, even numerically. Moreover, tiny changes in the free energy functional can render all approaches futile, which had been successful before – analytically or numerically. To circumvent this problem, a completely different numerical approach is suggested in this work, which makes direct use of the free energy functional *only* [Des00].

Imagine the cell being subdivided into M concentric cylindrical shells of volume V_i, each containing a certain fraction of ions. If the charge within the shells is replaced by a density $n_i = N_i/V_i$, the total electrostatic energy $\mathscr{E}_{\mathrm{el}}$ of this configuration can be computed exactly by piecewise integrating the cylindrical Poisson equation, as is demonstrated in TP 1.5. On this level of description the state of the system is specified by the number N_i of ions within shell i. Note that extensive quantities are given per unit length of the rod.

The idea now is to perform a Markov process by randomly moving particles between the shells and accepting the moves using the Metropolis-Boltzmann factor. At this point, however, care is called for. The states between which the process moves are *not* equally probable, since *(i)* each of them comprises a different number of microstates for distributing $N = \sum_i N_i$ indistinguishable ions between M shells in a prescribed way, and *(ii)* the shells may vary in size. Therefore, the probability of a given state is the product of two contributions: The usual Boltzmann factor and a "combinatorial" part accounting for the degeneracy of the states and the variable shell volumes. Denoting the total volume by $V = \sum_i V_i$, the latter contribution is given by:

$$P\big(\{N_i\}\big) \;=\; \Big(\frac{V_1}{V}\Big)^{N_1}\Big(\frac{V_2}{V}\Big)^{N_2}\cdots\Big(\frac{V_M}{V}\Big)^{N_M}\,\frac{N!}{N_1!N_2!\cdots N_M!} \;=\; \frac{N!}{V^N}\prod_{i=1}^{M}\frac{V_i^{N_i}}{N_i!}. \quad (1.60)$$

Now generate a new state $\{N_i'\}$ from the old one by moving one particle from shell k to a (not necessarily adjacent) shell l. The ratio of the combinatorial probabilities between these two states is given by

$$\frac{P\big(\{N_i'\}\big)}{P\big(\{N_i\}\big)} \;=\; \frac{N_k}{V_k}\frac{V_l}{N_l+1} \;=\; \frac{n_k^{\mathrm{old}}}{n_l^{\mathrm{new}}}. \quad (1.61)$$

Using the product of P and the Boltzmann-factor as the probability of a state and demanding detailed balance for the transition rates gives the following Metropolis factor for the acceptance probability:

$$\mathrm{Prob}\big(\,k\longrightarrow l\,\big) \;=\; \min\left\{1,\;\exp\Big\{-\beta\big(E^{\mathrm{new}}-E^{\mathrm{old}}\big)\Big\}\times\frac{n_k^{\mathrm{old}}}{n_l^{\mathrm{new}}}\right\}. \quad (1.62)$$

[17] This is quite analogous, e.g., to classical mechanics, where the Euler-Lagrange equations are the differential equations corresponding to the variational problem of least action, called Hamilton's principle.

Technical Point 1.5 *(Poisson's equation, numerically)*

For a cylindrical geometry Gauss' law yields the electric field $E(r) = Q(r)/2\pi\epsilon r$, where $Q(r)$ is the charge within a distance r from the rod axis, see Eqn. (1.13). Integrating this once more gives the potential ψ and the electrostatic energy $\mathscr{E}_{\rm el}$:

$$\psi(r) \;=\; \frac{e_0}{\epsilon}\int_r^R \mathrm{d}\bar{r}\;\bar{r}n(\bar{r})\ln\frac{r}{\bar{r}} \qquad \text{and} \qquad \mathscr{E}_{\rm el} \;=\; \frac{1}{4\pi\epsilon}\int_{r_0}^R \mathrm{d}\bar{r}\;\frac{Q^2(\bar{r})}{\bar{r}}. \tag{1.56}$$

The task is to find the electrostatic energy of a configuration composed of M shells with constant ion density n_i. Eqn. (1.56*ii*) can be decomposed into

$$\mathscr{E}_{\rm el} \;=\; \frac{1}{4\pi\epsilon}\sum_{i=1}^{M}\int_{s_{i-1}}^{s_i}\mathrm{d}r\;\frac{Q^2(r)}{r} \tag{1.57}$$

and $Q(r)$ splits into $Q_{i-1} + \Delta Q_i(r)$, where Q_{i-1} is the total charge up to (but not including) shell i and $\Delta Q_i(r)$ is the contribution between s_{i-1} and $r < s_i$, which is simply given by $e_0 n_i \pi(r^2 - s_{i-1}^2)$.

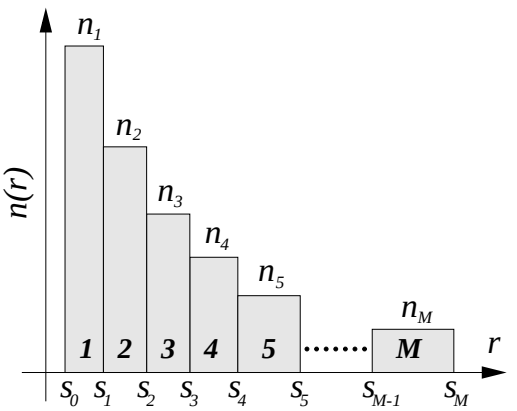

Following this idea, the integrals in Eqn. (1.57) can be evaluated explicitly, giving the following *exact* expression for the total electrostatic energy and the potential in the shell system:

$$\mathscr{E}_{\rm el} \;=\; \frac{1}{4\pi\epsilon}\sum_{i=1}^{M}\left\{\left(Q_{i-1} - \pi s_{i-1}^2 e_0 n_i\right)^2 \ln\frac{s_i}{s_{i-1}} + e_0 N_i\Big(Q_{i-1} + e_0 n_i \pi \frac{s_i^2 - 3s_{i-1}^2}{4}\Big)\right\} \tag{1.58}$$

$$\psi(s_i) \;=\; \frac{1}{2\pi\epsilon}\sum_{j=i+1}^{M}\left\{\left(Q_{j-1} - \pi s_{i-1}^2 e_0 n_i\right)\ln\frac{s_i}{s_{i-1}} + \frac{1}{2}e_0 N_j\right\}. \tag{1.59}$$

These equations give a much better result than an approach which neglects the r dependence of $\Delta Q_i(r)$, i.e., which replaces the densities by delta functions. They are worth implementing.

There is an alternative way of looking at this. Since the entropy of a state is given by[18] $S\big(\{N_i\}\big) = k_{\rm B}\ln\big(P(\{N_i\})\big)$, the Metropolis factor can be written as

$$\begin{aligned}\exp\Big\{-\beta\,\Delta E\Big\} \times \frac{n_k^{\rm old}}{n_l^{\rm new}} \;&=\; \exp\Big\{-\beta\,\Delta E\Big\} \times \exp\Big\{\ln\big(P(\{N_i'\})\big) - \ln\big(P(\{N_i\})\big)\Big\} \\ &=\; \exp\Big\{-\beta\,\Delta E + \beta\,T\,\Delta S\Big\} \;=\; \exp\Big\{-\beta\,\Delta F\Big\}\end{aligned} \tag{1.63}$$

Hence, the multiplicity of the states is automatically taken into account if the Metropolis criterion is tested with the *free* energy. Furthermore, if all N_i are large, the factorials in

[18] Note that the famous formula $S = k\log W$ carved on Boltzmann's tombstone in the Zentralfriedhof of Vienna, which relates the *number* W of microstates compatible with a given state to the entropy of that state, is only correct if all microstates are equally probable. If instead W is taken to be the *probability* of a state, the formula remains valid.

Eqn. (1.60) can be approximated by Stirling's formula. This gives the following expression for the entropy of a state:

$$\begin{aligned} S\big(\{N_i\}\big) &= k_\mathrm{B}\,\ln\left\{\frac{N!}{V^N}\prod_{i=1}^{M}\frac{V_i^{N_i}}{N_i!}\right\} \approx k_\mathrm{B}\left\{N\,\ln N - N + \sum_{i=1}^{M} N_i\Big(\ln\frac{V_i}{V} - \ln N_i + 1\Big)\right\} \\ &= -k_\mathrm{B}\sum_{i=1}^{M} N_i \ln\frac{N_i V}{V_i N} = -k_\mathrm{B}\,V\sum_{i=1}^{M} n_i \ln\frac{n_i}{\bar{n}}. \end{aligned} \tag{1.64}$$

This is the discretized equivalent of the entropy contribution entering into the Poisson-Boltzmann free energy functional in Eqn. 1.33. By performing this Markov process one can thus sample the corresponding ion distribution function, after an initial equilibration time.

Remarks 1.4.1

1. This method can also be applied to other geometries in which the electrostatic energy can be calculated efficiently once the density in the volume elements is known. Two important cases are the spherical and the planar geometry.

2. Addition of salt causes no difficulty. Each species has its own density distribution. A mixture of various kinds of counterions is treated the same way.

3. Eqn. (1.62) is only equivalent to a free energy Metropolis algorithm using Eqn. (1.64) if all N_i are large. E.g., for small particle numbers Eqn. (1.64) does not even yield a constant density for *uncharged* particles, unlike Eqn. (1.62).

4. Still referring to particles within a density functional theory might seem artificial, one could equally well transfer small bits of the density between shells, under conservation of the integral, and employ $\exp\{-\beta F\}$ in the Metropolis criterion with the entropy contribution calculated from Eqn. (1.64). Note, however, that for multiple-ion moves the acceptance probability is more complicated than Eqn. 1.62, since Eqn. 1.61 is no longer valid.

5. In the cylindrical or planar case the total number of particles is irrelevant, since infinite. Only the number of particles per unit length or unit area is significant. This is different in the spherical problem, where the cell is finite.

6. Excluded volume interactions can be taken into account in form of a *virial expansion*. For the free energy it reads [McQ76]

$$F = F_\mathrm{ideal} + N k_\mathrm{B} T\left\{\sum_{j=1}^{\infty}\frac{1}{j}\Big(B_{j+1} + 2T\frac{\mathrm{d}B_{j+1}}{\mathrm{d}T}\Big)\,n^j\right\} \tag{1.65}$$

   In the simple case of hard sphere ions with diameter σ all virial coefficients B_j are independent of temperature, so the second term in the sum in Eqn. 1.65 vanishes. A restriction to the first nontrivial term in the virial expansion gives the following correction for the free energy density:

$$f_{\mathrm{hc},1}(\boldsymbol{r}) = k_\mathrm{B} T B_2\, n^2(\boldsymbol{r}) \qquad \text{with} \quad B_2 = \frac{2}{3}\pi\sigma^3. \tag{1.66}$$

An alternative approach is the *free-volume approximation*, which reduces the total volume by an effective volume V_{eff} for every particle and which derives from a free energy density

$$f_{\text{hc},2}(\boldsymbol{r}) \;=\; -k_{\text{B}}T\, n(\boldsymbol{r}) \ln\Big(1 - V_{\text{eff}} n(\boldsymbol{r})\Big). \tag{1.67}$$

With $V_{\text{eff}} = B_2$, Eqn. (1.67) coincides in lowest order with the virial expansion, but it gives rise to a larger increase in the free energy and thus a "stronger" hard core, even if higher order terms are included in Eqn. (1.66).

7. Various kinds of correlation corrections for the free energy density can be used directly. In fact, the distribution functions in Sec. 1.3 have been calculated in this manner.

8. The approach bears some resemblance to the method of finite elements. There, the transformation from a differential equation to a functional minimization problem is a central idea as well [HeBo96].

The purpose of the next subsections is to illustrate the proposed Monte-Carlo scheme by a few straightforward examples.

1.4.1 Excluded volume

Electrostatic interactions are the only ones which are explicitly described in Poisson-Boltzmann theory. In particular, all effects resulting from an ionic hard core are neglected. These effects range from a suppression of high densities up to a layering (or even crystalline ordering) of particles. A simple way to account for a hard core is the free-volume approximation mentioned in Rem. 1.4.1.6.[19] After including the free energy density (1.67) into the Monte-Carlo simulation, a system with $R/r_0 = 100$, $\lambda = 2\,e_0/r_0$, $\ell_{\text{B}} = r_0$, $v = 3$ and no additional salt has been investigated. The diameter d of the ions has been varied from 0 to $10\,r_0$ in steps of r_0. The results for the density and the distribution function are shown in Fig. 1.9.

Density and distribution function for the system with $d = r_0$ deviate very little[20] from the one with $d = 0$, but for larger values of d the expected changes occur: the contact density is reduced and flattened out. In the vicinity of the rod, the ions cannot exceed a close-packing density and are being pushed outwards, generating a range of constant high density which extends farther out with increasing d. While this decreases the contact density in the shown example by almost three orders of magnitude, the boundary density at the same time rises only by 55%. This indicates that the increase in the osmotic pressure does not mirror the dramatic changes happening at the surface of the rod.

The decrease in contact density shifts the sharp initial rise of $P(r)$, visible in the right frame of Fig. 1.9, to larger values of r and softens it. Surprisingly, though, the amount of condensation is mostly unaffected by the pronounced changes in the ion distribution at small r. This is demonstrated by the straight line fit to the locus of relevant inflection

[19] A related approach has recently been used to incorporate steric repulsion in the Poisson-Boltzmann equation, see Ref. [BoAn97].

[20] Note that the contact density in the absence of a hard core, $n(r_0) = 0.447\,r_0^{-3}$, is of the same order as the maximum density $n_{\max,d=r_0} = 0.477\,r_0^{-3}$ from the free-volume approximation. Recall also Rem. 1.1.3.8.

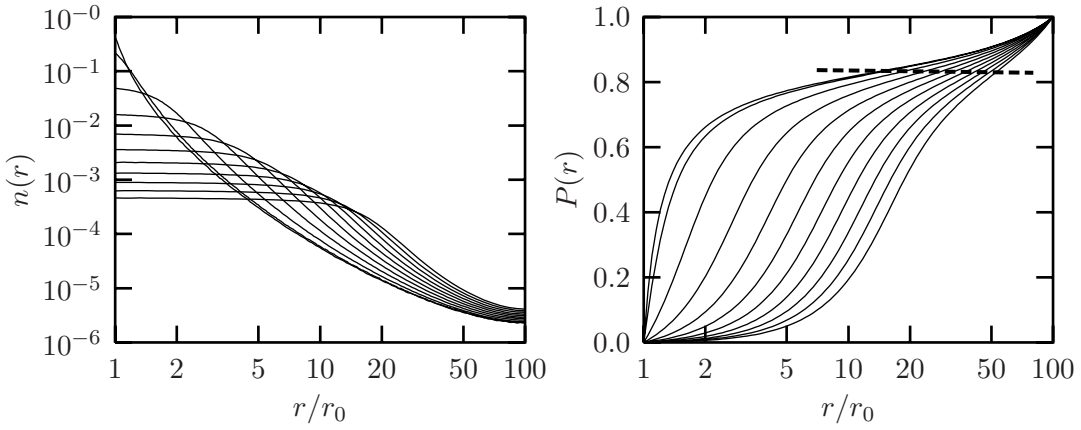

Figure 1.9: Density $n(r)$ (left) and distribution function $P(r)$ (right) for a cylindrical cell model with $R/r_0 = 100$, $\lambda = 2\,e_0/r_0$, $\ell_B = r_0$, $v = 3$ and no additional salt. The diameter d of the ions has been varied in the range $d/r_0 \in \{0, 1, \ldots, 10\}$. For the density this corresponds to a successive lowering of $n(r_0)$, for the distribution function it shifts the initial rise to larger values of r. The straight dashed line in the right frame is a fit to the locus of inflection points relevant for the condensation argument.

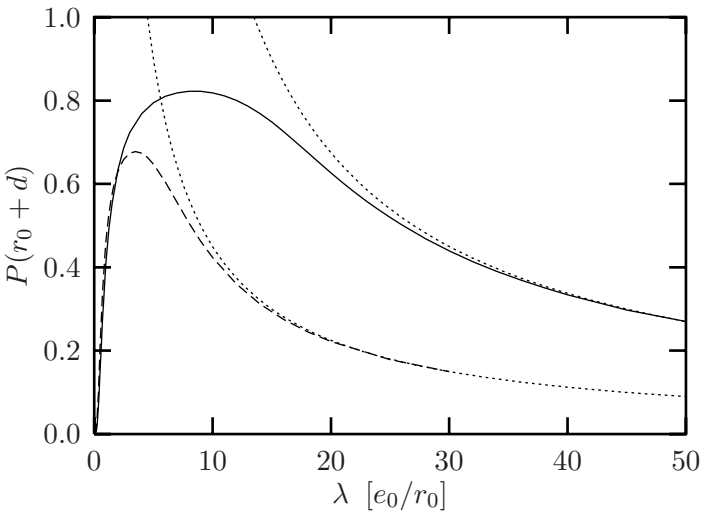

Figure 1.10: Fraction of ions within a distance of one ion diameter d from the rod surface as a function of line charge density λ for two systems with $r_0 = \sigma$, $R/r_0 = 100$, $\ell_B/\sigma = 1$, $v = 3$ and ion diameter $d = \sigma$ (solid line) or $d = 2\sigma$ (dashed line). The two dotted curves are the asymptotics for large λ from Eqn. (1.68).

points. Although the condensed layer increases considerably in size (from $14.3\,r_0$ up to $52.1\,r_0$), the condensed fraction decreases by less than one percent. Incidentally, this is an example of an astonishing effect which would have completely gone unnoticed if the fraction of condensed ions were to be quantified by counting the ions in the immediate vicinity of the rod.

The upper limit to the particle density makes the fraction of charge within the first layer, $P(r_0 + d)$, a non-monotonic function of the line charge density λ, as is shown in Fig. 1.10. While at small λ the fraction first increases due to the onset of ion condensation, the accumulating charges will finally reach a density which cannot be exceeded. But since the total number of counterions keeps on growing proportionally to λ, their fraction within

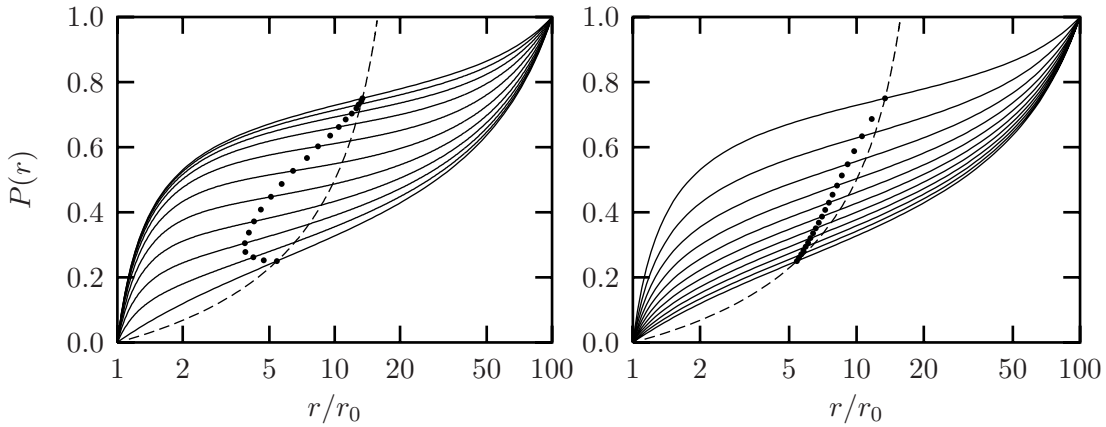

Figure 1.11: Distributions functions $P(r)$ (solid lines) for a valence mixture system with $r_0 = \sigma$, $R/r_0 = 100$ and $\xi = 4/3$. The lowest curve corresponds to 100% monovalent counterions, while for the uppermost curve all ions are trivalent. From bottom to top the monovalent ions are gradually replaced by trivalent ones in steps of 10% of the total charge. The results for the real mixture (left side) are contrasted with distribution functions resulting from convex combinations of the single-valence functions for $v = 1$ and $v = 3$ (right side; see text). The dashed line indicates the locus of inflection points for the single-valence theory (see also Fig. 1.3), whereas the heavy dots mark the *actual* inflection points in the distribution functions.

the densely packed first layer decreases.[21] In the free-volume approximation the highest particle density is given by $1/V_{\text{eff}}$. Thus, for large λ and V_{eff} given by the second virial coefficient for hard spheres, $B_2 = 2\pi d^3/3$, the fraction will asymptotically be given by

$$P(r_0 + d) \;\sim\; \frac{\pi\big((r_0+d)^2 - r_0^2\big)\, e_0 v}{\frac{2}{3}\pi d^3\, \lambda} \;=\; \frac{3 e_0 v \big(2r_0 + d\big)}{2 d^2 \lambda} \;\propto\; \frac{1}{\lambda} \tag{1.68}$$

1.4.2 Valence mixtures

The Poisson-Boltzmann equation in the cylindrical cell model can be solved analytically in the case of no salt and one species of counterions. This was done in Sec. 1.1. However, if the system contains a mixture of different valences, no analytical solution is known.[22] For the Monte-Carlo approach, however, this constitutes no problem, since it can be extended trivially to more than one density histogram. As an example, the left part of Fig. 1.11 shows integrated charge distributions $P(r)$ which represent successive stages of an ion exchange: In a system with $R/r_0 = 100$ and $\xi = 4/3$ the neutralizing monovalent counterions are gradually replaced by trivalent ones, until 100% of the charge is carried by the latter. The corresponding distribution functions are shown in steps of 10% of the monovalent charge.

As expected, the condensed fraction becomes larger as the percentage of high-valent ions increases. Fig. 1.11 shows that the distribution functions are shifted up. In addition, there is also a more subtle effect connected with the screening of the rod. Recall that

[21] The same effect has recently been found by a similar modified Poisson-Boltzmann approach. See, e.g., Fig. 2 in Ref. [BoAn97].

[22] This is related to the appearance of several different Boltzmann factors on the right hand side of the Poisson-Boltzmann equation (1.7), which cannot be removed simultaneously by a simple transformation.

in the single-valence theory the locus of inflection points is solely determined by the cell geometry (cf. Rem. 1.1.1.5). In Fig. 1.11 it can be seen that for the mixtures the actual inflection points are shifted towards smaller radii. Hence, the rod charge is screened more efficiently. This effect must be attributed to global rearrangements of the counterions, as can be deduced from the following argument: Assume that there are N_1 monovalent and N_3 trivalent ions. If each species were to distribute independently of the other, the total distribution function would be a convex combination of the mono- and trivalent single-valence functions. This would imply the relation

$$P(r; N_1, N_3) \stackrel{?}{=} \frac{N_1\, P(r, v=1) + N_3\, P(r, v=3)}{N_1 + N_3}. \tag{1.69}$$

These functions are shown in the right part of Fig. 1.11. Although the points of inflection are also shifted away from the single-valence line, the effect is much more pronounced in the real mixture. Furthermore, the way in which the hypothetical distribution functions from Eqn. (1.69) cross over from the $v = 1$ to the $v = 3$ curve looks qualitatively very different from the true crossover. The distribution of one species clearly depends on the distribution of the other, i.e., different valences are correlated – even on the Poisson-Boltzmann level. In fact, high-valent ions will gather in the vicinity of the rod at the expense of low-valent ones. This process provides a way of decreasing the free energy, and therefore, mixtures can screen the rod charge more efficiently than single-valence solutions.

Note also that the observed shift means that there is no "effective" single-valence v_{eff} such that a fictitious solution of counterions with valence v_{eff} gives the same distribution function as the actual valence mixture. But even if such an effective valence is defined much less demanding, conceptual difficulties remain. This can be seen from the following consideration: Define v_{eff} by the condition that $1 - 1/\xi v_{\text{eff}}$ is the value of P at the actual inflection point. The dependence of this v_{eff} on the percentage p_{m} of charge carried by monovalent ions is shown in Fig. 1.12 for the true mixture (heavy dots) and for the convex-combined functions from Eqn. (1.69) (dashed line)[23]. Another natural way of defining an effective valence is to demand the effective solution to have the same Debye screening constant as the mixture. Neglecting the spatial variation of the densities, the effective valence as a function of the percentage of charge carried by monovalent ions can be readily calculated. Charge neutrality fixes the number of particles with effective valence v_{eff} to $(N_1 + 3N_3)/v_{\text{eff}}$ and the condition of equal screening constant gives

$$N_1 + 3^2 N_3 \;=\; v_{\text{eff}}^2 \frac{N_1 + 3N_3}{v_{\text{eff}}} \qquad \Longrightarrow \qquad v_{\text{eff}} \;=\; \frac{N_1 + 9N_3}{N_1 + 3N_3} \tag{1.70}$$

On the other hand, $p_{\text{m}} = N_1/(N_1 + 3N_3)$. Inserting this into Eqn. (1.70) gives

$$v_{\text{eff}} \;=\; 3 - 2\, p_{\text{m}}, \tag{1.71}$$

i.e., a simple linear relation as indicated by the dotted line in Fig. 1.12. Apart from

[23] The dashed line in Fig.1.12 can quite accurately be obtained by convex combining the condensed fractions:

$$1 - \frac{1}{\xi v_{\text{eff}}} \;=\; \frac{N_1\,(1 - 1/\xi) + N_3\,(1 - 1/3\xi)}{N_1 + N_3} \qquad \Longrightarrow \qquad v_{\text{eff}} \;=\; \frac{6\, p_{\text{m}} + 3}{8\, p_{\text{m}} + 1}.$$

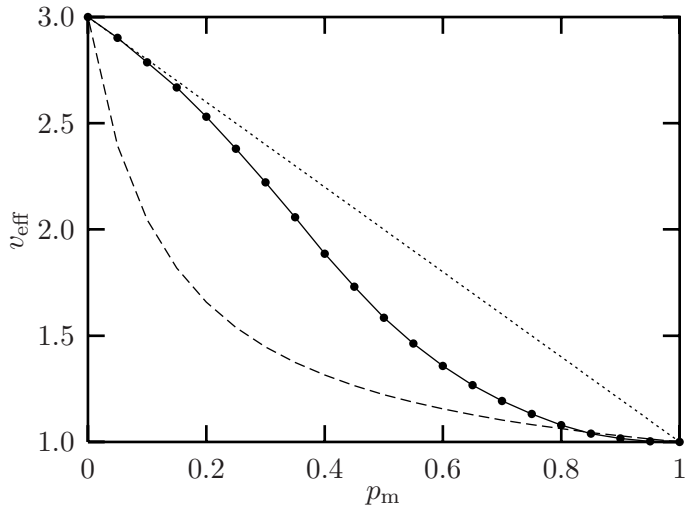

Figure 1.12: Effective valence $v_{\rm eff}$ as a function of the percentage $p_{\rm m}$ of charge carried by monovalent ions. The heavy dots are computed from the measured distributions by demanding the effective solution to give the same amount of condensation. For the dashed line the same is done with the convex combined distribution functions from Eqn. (1.69). Finally, the dotted line gives the effective valence of a solution having the same (bulk) Debye screening constant as the mixture.

the boundaries, these three definitions clearly do not match.[24] Even more surprising, the Debye-approach predicts a larger effective valence than the measured one and hence a stronger screening than observed. All this indicates that a valence mixture behaves qualitatively different from a single-valent solution.

A final note: The "belly" of inflection points in the left part of Fig. 1.11 and the shape of the locus of inflection points in Fig. 1.6 look very similar. However, the underlying physics leading to this feature of $P(r)$ is different. In the valence mixture the screening is enhanced by the polydispersity of ion charges, all of which still have the same sign. In the salt case the size reduction of the condensed layer is driven by the appearance of ions carrying the opposite charge of the counterions, but not necessarily a different valence.

1.5 The linearized Poisson-Boltzmann equation

For the cell model the linearized Poisson-Boltzmann equation can be solved analytically. Yet, linearization turns out to be too strong an approximation: the phenomenon of counterion condensation vanishes. In fact, a self-consistent treatment of the cylindrical and planar case is impossible.

Since the nonlinear Poisson-Boltzmann equation can only be solved analytically in very special cases, its linearized version has always attracted considerable attention.[25] In particular, the cylindrically symmetric problem has been investigated, e.g., by Hill [Hil55] and Stigter [Sti75] for a charged rod immersed into an infinite electrolyte. In this section the linearized solution for the cell model is derived and compared to the full Poisson-Boltzmann result.

[24] At small values of $p_{\rm m}$ the Debye prediction seems to be asymptotically correct. This may be related to the corresponding behavior of the measured locus of inflection points and the single-valence prediction in Fig. 1.11.

[25] Use of the linearized Poisson-Boltzmann equation is frequently referred to as Debye-Hückel theory. The original work of these two authors [DeHü23] is, however, more comprehensive. It is a general theory for calculating the free energy of an electrolyte solution, and not merely the derivation of a screened interaction potential. An excellent account is given in Chapter 15 of Ref. [McQ76] or in Ref. [LeFi96].

Technical Point 1.6 *(Modified Bessel functions)*

The two linearly independent solutions of the second order linear differential equation

$$x^2 \frac{\mathrm{d}^2 f}{\mathrm{d}x^2} + x \frac{\mathrm{d}f}{\mathrm{d}x} - (x^2 + \nu^2) f \;=\; 0$$

are the modified Bessel functions of first and second kind, $\mathrm{I}_\nu(x)$ and $\mathrm{K}_\nu(x)$ respectively. This technical point collects some important facts about these functions; a comprehensive summary can be found in Refs. [AbSt72][Dwi61].

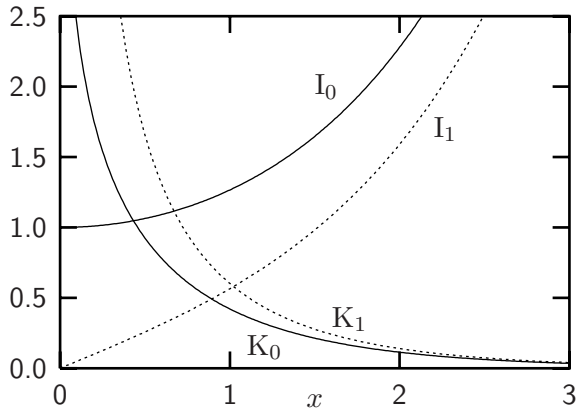

Derivatives	$\mathrm{K}_0'(x) = -\mathrm{K}_1(x)$	$\mathrm{I}_0'(x) = \mathrm{I}_1(x)$
	$\mathrm{K}_1'(x) = -\mathrm{K}_0(x) - \frac{1}{x}\,\mathrm{K}_1(x)$	$\mathrm{I}_1'(x) = \mathrm{I}_0(x) - \frac{1}{x}\,\mathrm{I}_1(x)$
small x	$\mathrm{K}_0(x) \overset{x\ll 1}{\sim} -\{\gamma + \ln\frac{x}{2}\}\,\mathrm{I}_0(x)$	$\mathrm{I}_0(x) \overset{x\ll 1}{\sim} 1 + \frac{1}{4}x^2$
	$\lim_{x\downarrow 0}\, x\,\mathrm{K}_1(x) = 1$	$\lim_{x\downarrow 0}\, \frac{1}{x}\mathrm{I}_1(x) = \frac{1}{2}$
large x	$\mathrm{K}_\nu(x) \overset{x\gg 1}{\sim} \mathrm{e}^{-x}\sqrt{\pi/2x}$	$\mathrm{I}_\nu(x) \overset{x\gg 1}{\sim} \mathrm{e}^{x}/\sqrt{2\pi x}$
Integrals	$\int \mathrm{d}x\; x^\nu\,\mathrm{K}_{\nu-1}(x) = -x^\nu\,\mathrm{K}_\nu(x)$	$\int \mathrm{d}x\; x^\nu\,\mathrm{I}_{\nu-1}(x) = x^\nu\,\mathrm{I}_\nu(x)$
Wronskian	$\mathrm{K}_\nu(x)\,\mathrm{I}_{\nu+1}(x) + \mathrm{K}_{\nu+1}(x)\,\mathrm{I}_\nu(x) = 1/x$	

Starting point for the linearized Poisson-Boltzmann (LPB) theory is an expansion of the exponential function in Eqn. (1.7) up to linear order in the potential. Furthermore, change variables $x := \kappa r$ and $f(x) := y(x/\kappa)$, where the definition of the screening constant κ is taken from Eqn. (1.6). This results in the following inhomogeneous linear differential equation of Bessel type:

$$f'' + \frac{f'}{x} - f \;=\; 1 \tag{1.72}$$

and the unchanged boundary conditions from Eqn. (1.8)

$$f'(x_0) \;=\; -2\xi/x_0 \qquad \text{and} \qquad f'(X) \;=\; 0, \tag{1.73}$$

with $x_0 := \kappa r_0$ and $X := \kappa R$. An obvious particular solution is $f_{\mathrm{part}}(x) = -1$, and the general solution of the homogeneous equation is a linear combination of the zeroth order modified Bessel functions of first and second kind

$$f_{\mathrm{homo}}(x) \;=\; c_{\mathrm{K}}\,\mathrm{K}_0(x) + c_{\mathrm{I}}\,\mathrm{I}_0(x). \tag{1.74}$$

Some important properties of these functions are collected in TP 1.6. The boundary conditions (1.73) yield the following linear system of equations:

$$\begin{pmatrix} -\mathrm{K}_1(x_0) & \mathrm{I}_1(x_0) \\ -\mathrm{K}_1(X) & \mathrm{I}_1(X) \end{pmatrix} \begin{pmatrix} c_{\mathrm{K}} \\ c_{\mathrm{I}} \end{pmatrix} \;=\; \begin{pmatrix} -2\xi/x_0 \\ 0 \end{pmatrix}. \tag{1.75}$$

Its solution is readily found to be

$$\begin{pmatrix} c_{\mathrm{K}} \\ c_{\mathrm{I}} \end{pmatrix} = -\frac{2\xi}{x_0 D} \begin{pmatrix} \mathrm{I}_1(X) \\ \mathrm{K}_1(X) \end{pmatrix} \qquad \text{with} \qquad D := \mathrm{K}_1(X)\,\mathrm{I}_1(x_0) - \mathrm{K}_1(x_0)\,\mathrm{I}_1(X). \tag{1.76}$$

Linearization of the radial density (1.2) gives $n(r) = n(R)\big(1 + y(r)\big)$. Like in the nonlinear case this equation requires the potential to vanish at the outer cell boundary, which together with the full solution $f_{\mathrm{part}} + f_{\mathrm{homo}}$ and the integration constants c_{K} and c_{I} from Eqn. (1.76) gives the condition

$$\begin{aligned} 0 \;\stackrel{!}{=}\; f(X) \;&=\; -\frac{2\xi}{x_0 D}\Big(\underbrace{\mathrm{K}_0(X)\,\mathrm{I}_1(X) + \mathrm{K}_1(X)\,\mathrm{I}_0(X)}_{=1/X,\ \text{see TP 1.6}}\Big) - 1 \\ \Longrightarrow \quad \frac{2\xi}{r_0 R} \;&=\; \kappa^2\Big(\mathrm{K}_1(\kappa r_0)\,\mathrm{I}_1(\kappa R) - \mathrm{K}_1(\kappa R)\,\mathrm{I}_1(\kappa r_0)\Big). \end{aligned} \tag{1.77}$$

This equation fixes the screening constant κ, thereby making the solution unique.[26] Combining all parts finally results in the potential

$$y(r) \;=\; \frac{2\xi}{\kappa r_0}\,\frac{\mathrm{I}_1(\kappa R)\,\mathrm{K}_0(\kappa r) \;+\; \mathrm{K}_1(\kappa R)\,\mathrm{I}_0(\kappa r)}{\mathrm{I}_1(\kappa R)\,\mathrm{K}_1(\kappa r_0) \;-\; \mathrm{K}_1(\kappa R)\,\mathrm{I}_1(\kappa r_0)}. \tag{1.78}$$

Remarks 1.5.1

1. Just like in the nonlinear case the integration can be done analytically up to the numerical determination of the integration constants, here via the value of κ.

2. The nonlinear contact potential $y(r_0)$ diverges in the limit $R \to \infty$, see Eqn. (1.20), as does the linear one. Since the contact potential does not remain small for large R, *the linear approximation is inconsistent*. This is in sharp contrast to the spherical problem, where the range over which the electrostatic potential can vary is bounded in the limit $R \to \infty$, leaving a chance for linearized Poisson-Boltzmann theory to work at least in the weakly charged case.

3. Fig. 1.13 compares the nonlinear and linear (solid/dotted) potential $y(r)$ for systems differing in cell size R (left/right) and Manning parameter ξ. As expected from Rem. 1.5.1.2, deviations are much more pronounced in the dilute system. The value of the contact potential is always too large, particularly for large Manning parameter.

4. Fig. 1.14 compares the radial distribution functions from the systems in Fig. 1.13. The overestimation of $y(r_0)$ in the linear theory translates into a complete failure in describing the high ion concentration around the charged rod due to counterion condensation.

[26] Since $\kappa^2 = 4\pi\ell_{\mathrm{B}} n(R)$, one may interpret $1/\kappa$ as the Debye-length at the outer cell radius. This however has to be distinguished from a Debye length computed from the average ion density in the cell, and the interpretation ceases to be meaningful in the limit $R \to \infty$. It must be emphasized that – unlike in the case of a bulk electrolyte (see TP 1.7) – κ is not given but has to be determined from the boundary conditions.

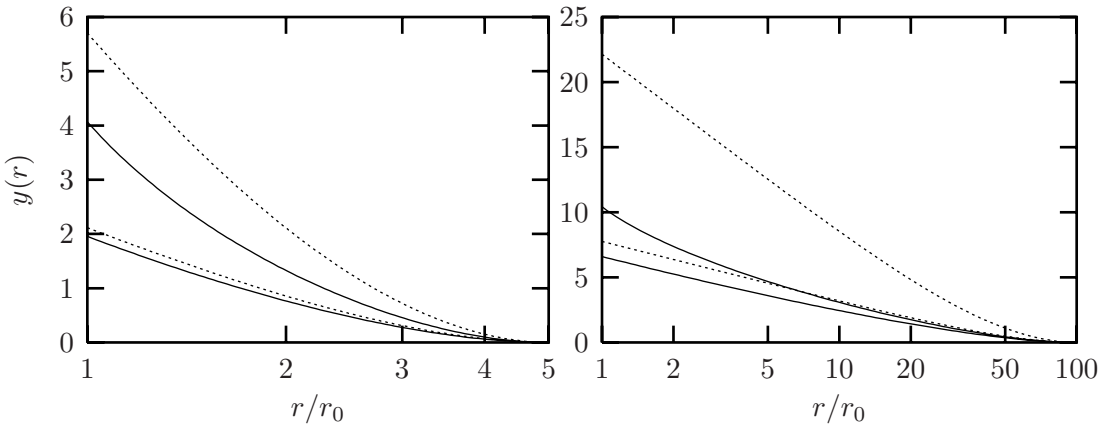

Figure 1.13: Nonlinear (solid) and linearized (dotted) mean electrostatic potential for two cell models with $R/r_0 = 5$ (left) or $R/r_0 = 100$ (right). The upper curves are for $\xi = 3$ and the lower for $\xi = 1$. Note that the linear theory overestimates the contact potential $y(r_0)$ – particularly at large ξ and in dilute systems.

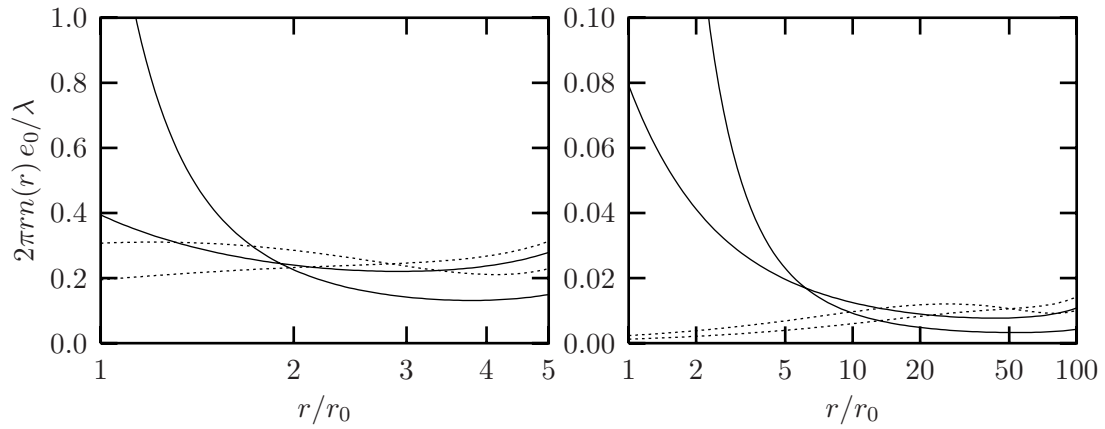

Figure 1.14: Nonlinear (solid) and linearized (dotted) radial distribution function $2\pi r n(r)\, e_0/\lambda$ for the two cells from Fig. 1.13. At small r the upper curve indicates the larger Manning parameter. The differences between the full and the linearized theory are remarkable: The latter completely fails to describe the strong accumulation of counterions at the rod.

The previous remarks suggest that the phenomenon of counterion condensation is absent on the linearized level. In fact, this can be proved rigorously by computing the potential in the limit $R \to \infty$. Eqns. (1.12,1.17) show that in the nonlinear Poisson-Boltzmann equation $\lim_{R\to\infty} \kappa R = \sqrt{2}$. In the linearized case this is no longer true, but it can be verified that κR still converges towards a constant. Using identities from TP 1.6, the

potential can be rewritten in the following way:

$$\begin{aligned} y(r) &= \frac{2\xi}{\kappa r_0}\,\frac{\mathrm{I}_1(\kappa R)\,\mathrm{K}_0(\kappa r) + \mathrm{K}_1(\kappa R)\,\overbrace{\mathrm{I}_0(\kappa r)}^{\to 1}}{\mathrm{I}_1(\kappa R)\,\underbrace{\mathrm{K}_1(\kappa r_0)}_{\to 1/\kappa r_0} - \mathrm{K}_1(\kappa R)\,\underbrace{\mathrm{I}_1(\kappa r_0)}_{\to 0}} = 2\xi\Big(\mathrm{K}_0(\kappa r) + \frac{\mathrm{K}_1(\kappa R)}{\mathrm{I}_1(\kappa R)}\Big) \\ &= 2\xi\left(-\ln(\kappa r/2) - 0.57721566... + \frac{\mathrm{K}_1(\kappa R)}{\mathrm{I}_1(\kappa R)}\right) = \underline{-2\xi\,\ln\frac{r}{r_0} + y(r_0).} \end{aligned} \quad (1.79)$$

Remarks 1.5.2

1. In the dilute limit the electrostatic potential converges towards the potential of a rod with Manning parameter ξ. This implies that all counterions have "receded to infinity". There is no counterion condensation, regardless of the value of ξ.

2. The simple form of the asymptotic potential – a shifted logarithm – is clearly visible in the right frame of Fig. 1.13.

3. In the nonlinear case the potential converges against that of a rod with effective Manning parameter 1 plus a logarithmic correction, see Eqn. (1.22).

4. The solution for the infinite system within a bulk electrolyte is briefly discussed in TP 1.7.

The knowledge of the counterion distribution function $n(r)$ permits the calculation of the fraction of condensed ions within a cylinder of radius r around the charged rod. This is the linearized analogue of the charge distribution functions from Poisson-Boltzmann theory introduced in Eqns. (1.13,1.15). With the help of TP 1.6 the integration yields

$$\begin{aligned} P_{\mathrm{LPB}}(r) &= \frac{1}{\lambda}\int_{r_0}^{r} \mathrm{d}\bar{r}\; 2\pi\bar{r}e_0 n(R)\Big(1+y(r)\Big) \qquad \Big\| \quad x := \kappa r \\ &= \frac{2\pi e_0 n(R)}{\lambda\kappa^2}\int_{x_0}^{x} \mathrm{d}\bar{x}\;\bar{x}\Big(c_{\mathrm{K}}\,\mathrm{K}_0(\bar{x}) + c_{\mathrm{I}}\,\mathrm{I}_0(\bar{x})\Big) \\ &\overset{\text{TP 1.6}}{=} \frac{1}{2\xi}\left(c_{\mathrm{K}}\Big[-\bar{x}\,\mathrm{K}_1(\bar{x})\Big]_{x_0}^{x} + c_{\mathrm{I}}\Big[\bar{x}\,\mathrm{I}_1(\bar{x})\Big]_{x_0}^{x}\right) \\ &= 1 - \frac{r}{r_0}\,\frac{\mathrm{I}_1(\kappa R)\,\mathrm{K}_1(\kappa r) - \mathrm{K}_1(\kappa R)\,\mathrm{I}_1(\kappa r)}{\mathrm{I}_1(\kappa R)\,\mathrm{K}_1(\kappa r_0) - \mathrm{K}_1(\kappa R)\,\mathrm{I}_1(\kappa r_0)}. \end{aligned} \quad (1.83)$$

Remarks 1.5.3

1. The boundary requirements $P_{\mathrm{LPB}}(r_0) = 0$ and $P_{\mathrm{LPB}}(R) = 1$ are easily seen to hold.

2. An alternative derivation of $P_{\mathrm{LPB}}(r)$ could employ Eqn. (1.14), which still holds, since it has been derived without reference to the Boltzmann assumption from Eqn. (1.2).

3. Fig 1.15 shows $P_{\mathrm{LPB}}(r)$ for the systems from Figs. 1.13 and 1.14. The absence of counterion condensation is obvious.

Technical Point 1.7 *(Linearized Poisson-Boltzmann in bulk salt)*

The solution of the linearized Poisson-Boltzmann equation for a charged rod in bulk salt differs from the solution in Eqn. 1.78. For an electrolyte composed of ions with (signed) valence v_i, bulk concentration n_i and corresponding electroneutrality condition $\sum_i v_i n_i = 0$ one has to solve

$$y'' + \frac{y'}{r} \;=\; -\frac{\beta e_0^2}{\epsilon} \sum_i v_i n_i \mathrm{e}^{-v_i y} \;\approx\; 4\pi \ell_\mathrm{B} \sum_i v_i^2 n_i \, y \;=:\; \kappa^2 \, y. \tag{1.80}$$

The natural boundary conditions $y'(r_0) = -2\xi/r_0$ and $\lim_{r\to\infty} y'(r) = 0$ give the solution

$$y(r) \;=\; 2\xi \, \frac{\mathrm{K}_0(\kappa r)}{\kappa r_0 \, \mathrm{K}_1(\kappa r_0)}. \tag{1.81}$$

In the zero salt limit $\kappa \downarrow 0$ and Eqn. (1.81) converges towards Eqn. (1.79), up to a constant. Note that here κ is a measure of the *bulk* salt concentration and not of the counterion concentration at some value of r, e.g., at the cell boundary.
Mathematically, the sphere with charge Q differs from the rod only by the term $2y'/r$ (instead of y'/r) in the Laplacian and the boundary condition $y'(r_0) = -\ell_\mathrm{B} Q/e_0 r_0^2$, which results in the famous Debye-Hückel expression for the electrostatic potential outside the sphere:

$$y(r) \;=\; \ell_B \, \frac{Q/e_0}{1+\kappa r_0} \, \frac{\mathrm{e}^{-\kappa(r-r_0)}}{r}. \tag{1.82}$$

The bare potential $1/r$ is exponentially screened and the charge Q is renormalized. Most frequently it is used for point charges, i.e., $r_0 = 0$. Note that like in the rod-case Eqn. (1.82) converges towards the unscreened potential for $\kappa \downarrow 0$.

4. Taking the limit $R \to \infty$ on P_LPB in the same spirit as on $y(r)$ gives:

$$P_\mathrm{LPB}(r) \;\overset{R\to\infty}{=}\; 1 - \frac{r}{r_0} \, \frac{\mathrm{I}_1(\kappa R) \overbrace{\mathrm{K}_1(\kappa r)}^{\to 1/\kappa r} - \mathrm{K}_1(\kappa R) \overbrace{\mathrm{I}_1(\kappa r)}^{\to 0}}{\mathrm{I}_1(\kappa R) \underbrace{\mathrm{K}_1(\kappa r_0)}_{\to 1/\kappa r_0} - \mathrm{K}_1(\kappa R) \underbrace{\mathrm{I}_1(\kappa r_0)}_{\to 0}} \;=\; 0. \tag{1.84}$$

   In the dilute limit no counterions are found within any finite distance of the rod. This is markedly different to the nonlinear case. There, even the contact density remains positive in the dilute limit, if $\xi > 1$, see Eqn. (1.24).

5. One might hope to improve the linear theory by artificially adding the phenomenon of counterion condensation in the following way: A rod with radius r_0 and Manning parameter ξ is replaced by a rod with effective radius R_M (either to be calculated from the nonlinear theory or simply to be guessed) and effective Manning parameter 1. The charge distribution function is then given by:

$$P_\mathrm{LPB,eff}(r;\xi,r_0) \;=\; 1 - \frac{1}{\xi} + \frac{1}{\xi} \, P_\mathrm{LPB}(r;1,R_\mathrm{M}). \tag{1.85}$$

   This is shown by the dashed lines in Fig. 1.15. Although it improves considerably upon the plain linear version, this procedure also fails upon dilution. The reason is

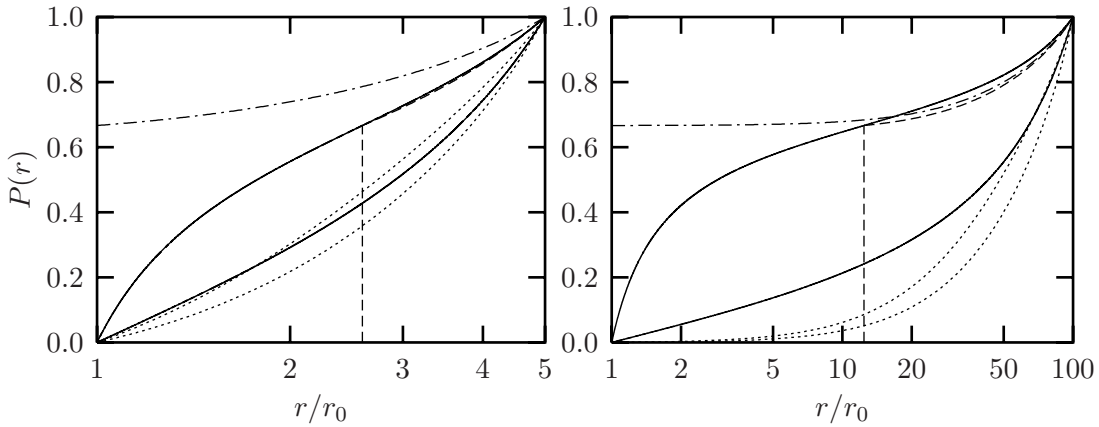

Figure 1.15: Nonlinear (solid) and linearized (dotted) integrated distribution function for the two cells from Fig. 1.13. The upper curves indicate the larger Manning parameter. Again, the complete failure of the linear theory is obvious. The dashed curves are a linearized computation for a charge- and radius-renormalized rod (i.e., with $\xi_{\text{eff}} = 1$ and a radius equal to the Manning radius of the $\xi = 3$ system). In this case $P_{\text{LPB,eff}}(r)$ from Eqn. (1.85) is plotted. The dash-dotted curves show the result of a renormalization which only adjusts the Manning-parameter to 1.

that the potential at the Manning radius will not remain small for $R \to \infty$. In fact, it will diverge, see Eqn. (1.21).

An even less involved renormalization-recipe would merely adjust the Manning parameter to 1. The result, however, is equally dissatisfying as the (ξ,r_0)-renormalization, also at large distances.

6. Counterion condensation can be investigated within the full Debye-Hückel theory by incorporating the assumption of aggregates formed of charged rods and associated counterions, see Ref. [KuLe98].

The linearization can only work if the potential remains small over the *entire* range of relevant distances. It does not suffice that it is small in the regions of interest. Solving a differential equation with given boundary conditions is a global procedure. Note that Poisson-Boltzmann and linearized Poisson-Boltzmann theory for the cylindrical cell model have exactly the same potential and electric field at the outer cell boundary, yet their predictions for the counterion density at that point differ. The gross overestimation of the potential at r_0 and the corresponding underestimation of $n(r_0)$ causes linearized Poisson-Boltzmann theory to overestimate $n(R)$. This is due to the fact that the global requirement of particle conservation couples these densities. This is demonstrated in Fig. 1.16.

A small overall potential can be achieved either by reverting to small R, and hence dense systems, or by the addition of enough salt, which also increases density. In any case, the statement that linearized Poisson-Boltzmann theory becomes valid at sufficiently high dilution (made, e.g., in Ref. [LeZi84^b]) is tempting but wrong for the cylinder. The expressions for the electrostatic potential in the salt-free cell model, Eqn. (1.78), and the potential within bulk electrolyte, Eqn. (1.81), both converge to the bare rod potential in Eqn. (1.79) instead of the renormalized potential in Eqn. (1.22). On the other hand, the electrostatic potential for a *sphere* in bulk electrolyte from linearized Poisson-Boltzmann

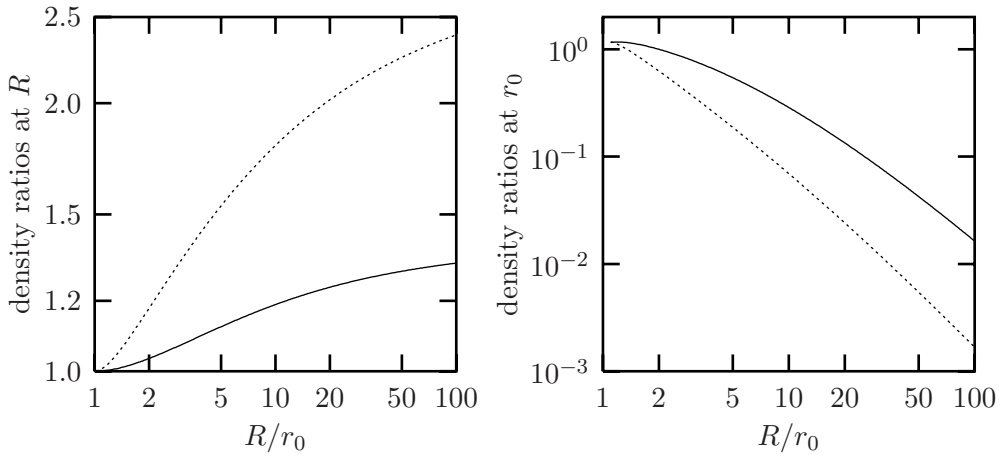

Figure 1.16: Ratio between linear and nonlinear ion density $n(r)$ at the points $r = R$ (left) and $r = r_0$ (right) for Manning parameter $\xi = 1$ (solid lines) and $\xi = 3$ (dotted lines) as a function of cell size R.

theory, Eqn. (1.82), correctly converges towards the unscreened $1/r$ potential. As has been pointed out in Rem. 1.5.1.2, this difference originates from the boundedness of the spherical Green function at large r compared to the unbounded Green function of the cylinder.

Example: within linearized Poisson-Boltzmann theory the reduced contact potential $y(r_0)$ at the surface of a sphere embedded in an electrolyte is according to Eqn. (1.82) given by

$$y(r_0) \;=\; \frac{\ell_B}{r_0}\,\frac{Q/e_0}{1+\kappa r_0} \;\overset{\kappa\downarrow 0}{=}\; \frac{\ell_B}{r_0}\,Q/e_0. \tag{1.86}$$

If this is small compared to 1, the potential is small everywhere.

Remarks 1.5.4

1. Linearized Poisson-Boltzmann theory can in principle work for spheres, but it is still dependent on the conditions *(i)* small Bjerrum length (i.e., high temperature), *(ii)* low charge and *(iii)* sufficiently large sphere radius.

2. In the limit of large spheres, $r_0 \to \infty$, the contact potential will always be small for fixed charge Q, but never for fixed surface charge density ς. As a corollary, linearized Poisson-Boltzmann theory is inconsistent for the charged plane within an electrolyte at arbitrarily small ς.

3. If Eqn. (1.86) is violated due to a large value of Q, a possible remedy is to observe that a considerable number of counterions will be condensed onto the surface of the sphere. Hence, if this layer is added to the sphere, one obtains a new sphere with reduced effective charge and a larger effective radius. Inspection of Eqn. (1.86) shows that both changes reduce the surface potential and thus are desirable.

4. The limit $\kappa \downarrow 0$ is obviously counterproductive, since decreasing κ increases $y(r_0)$. Concerning the validity of linearization, the dilute limit is actually a worst case.

The contact potential $y(r_0)$ in the corresponding cylindrical case diverges in the limit $\kappa \downarrow 0$, see Eqn. (1.81), no matter how small the Bjerrum length or how large the cylinder radius

Technical Point 1.8 *(Gouy-Chapman-layer)*

Within Poisson-Boltzmann theory the infinite plane with surface charge density $\varsigma > 0$ and neutralizing counterions of valence v in one half-space has first been treated by Gouy [Gou10] and Chapman [Cha13]:

$$\psi''(x) \;=\; \frac{ve_0}{\epsilon}\, n(0)\, \mathrm{e}^{\beta e_0 v \psi(x)} \quad ; \quad \psi'(0) \;=\; -\frac{\varsigma}{\epsilon} \quad , \quad \lim_{x\to\infty} \psi'(x) \;=\; 0. \tag{1.87}$$

It is straightforward to verify that the solution to Eqns. (1.87) is

$$y(x) \;=\; \beta e_0 v \psi(x) \;=\; -2\, \ln\left(1 + \frac{x}{\lambda}\right) \qquad \text{with} \quad \lambda \;:=\; \frac{e_0}{2\pi \ell_{\mathrm{B}} v \varsigma}. \tag{1.88}$$

λ is referred to as the *Gouy-Chapman length*. Ion density and distribution are given by

$$n(x) \;=\; \frac{1}{2\pi \ell_{\mathrm{B}} v^2}\, \frac{1}{(x+\lambda)^2} \quad \text{and} \quad P(x) \;=\; \frac{ve_0}{\varsigma} \int_0^x \mathrm{d}\bar{x}\; n(\bar{x}) \;=\; 1 - \left(1 + \frac{x}{\lambda}\right)^{-1}. \tag{1.89}$$

This shows that half of the ions are found within the Gouy-Chapman length, since $P(\lambda) = \frac{1}{2}$. Incidentally, the potential in Eqn. (1.88) can be obtained from the cylindrical solution in Eqn. (1.22) by taking the limit $r_0 \to \infty$ at constant surface charge density $\varsigma = e_0\xi/2\pi r_0 \ell_{\mathrm{B}}$, and by changing to the variable $x := r - r_0$.

In linearized Poisson-Boltzmann approximation Eqn. (1.87) becomes a linear second order differential equation with constant coefficients. Its solution is

$$y(x) = \mathrm{e}^{-2x/\lambda} - 1. \tag{1.90}$$

The ion distribution in the linear case is given by

$$n(x) = \frac{1}{\pi \ell_{\mathrm{B}} v^2 \lambda^2}\, \mathrm{e}^{-2x/\lambda}. \tag{1.91}$$

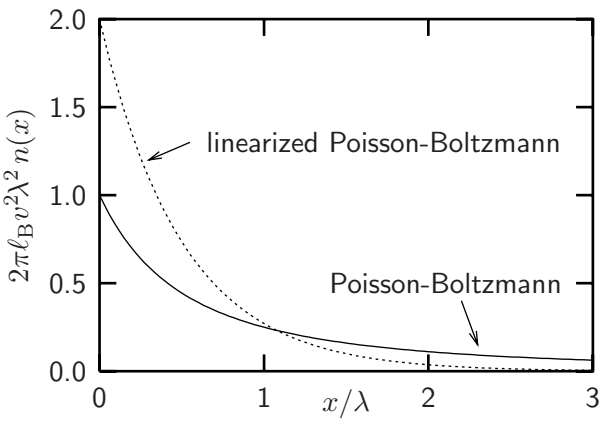

Observe that the potential in Eqn. (1.90) is bounded while the potential from Eqn. (1.88) is not. The ionic density in Eqn. (1.91) shows an exponential rather than algebraic decay. Furthermore, the contact density $n(0)$ is overestimated by a factor of 2 independent of the surface charge density ς. Hence, linearized Poisson-Boltzmann theory fails already at arbitrarily small ς. This is also visible in the picture above.

is. Thus, linearized Poisson-Boltzmann theory can only work – if at all – at sufficiently high concentration. The same caveats apply to the planar case, in which the unscreened and Poisson-Boltzmann screened potential is unbounded as well. See TP 1.8 for a brief discussion.

Linearity implies that the superposition principle holds. While this permits, e.g., the construction of line charges from lined-up spherical charges, it departs at the same time from the limit of small potentials. As a consequence, the applicability of linearized Poisson-Boltzmann theory to polyelectrolytes becomes questionable. The fundamental dilemma is

that nonlinear Poisson-Boltzmann theory is valid in the dilute limit, in which correlations become unimportant. However, its linearized version approaches the Poisson-Boltzmann result only in the dense limit, in which the potentials remain small. It is thus not at all obvious, in which limit linearized Poisson-Boltzmann theory is capable of describing a real system.

2 Computer simulations of the cell model

This chapter presents original results of molecular dynamics simulations of a cell like model for stiff polyelectrolytes. It complements the theoretical findings of Chap. 1 and is aimed to *(i)* demonstrate the applicability of the new condensation criterion from Sec. 1.1.3, *(ii)* validate the proposed correlation corrections for the expected deviations from Poisson-Boltzmann theory and *(iii)* study effects which qualitatively go beyond the mean-field level. The latter include overcharging, charge oscillations, a non-monotonic zeta-potential and attractive interactions.

Section 2.1 briefly discusses general algorithmic prerequisites. The implementation of the dynamics by a Verlet integrator is described within the Liouville formalism. The additional steps necessary for changing from the microcanonical to the canonical ensemble via a Langevin thermostat are outlined. In 2.1.3 the possible complications resulting from the presence of velocity dependent forces are formulated and a simple solution is presented. Based on its Taylor expansion in the discrete time step it is argued that a straightforward approach neglecting those complications is indeed permissible.

Section 2.2 describes the model system used for the simulations. A new method is introduced for constructing a charged rod within a hexagonal cell. It explicitly utilizes periodic boundary conditions and does not require leaving the numerically very convenient simple cubic symmetry. Furthermore, the interaction potentials are specified. The important issue of efficiently computing electrostatic interactions within periodic boundary conditions is deferred to Chap. 3.

Section 2.3 investigates ion distribution functions, based on the theoretical considerations from Chap. 1. The density dependence of deviations from the Poisson-Boltzmann theory are quantified and shown to vanish in the dilute limit. It is demonstrated how to describe real distribution functions by suitably generalized Poisson-Boltzmann curves. This will also be important for modeling experimental data. Multi- and mixed-valent systems are studied and correlation effects are found to become very strong, in accord with the findings in Sec. 1.3. The addition of salt is shown to yield the scenario described in Sec. 1.2. However, at high density and strong coupling overcharging and charge oscillations are found, which the mean-field Poisson-Boltzmann theory is unable to reproduce.

Section 2.4 is devoted to the study of pressure within the cell model. Due to the intrinsic anisotropy of the system and the long-range electrostatic interactions this has to be done via the stress tensor. The Poisson-Boltzmann prediction for the osmotic coefficient is found to be qualitatively correct, but systematically too low at finite densities and high Manning parameter. This has the surprising consequence that the Manning limiting law is often a better description than the full Poisson-Boltzmann theory. For trivalent systems the pressure is found to become negative for a certain region of density. This indicates the presence of attractive interactions between the like-charged rods.

Section 2.5 presents simulations in which the system parameters have been mapped

explicitly to important model systems, viz, DNA and poly(p-phenylene). For DNA-sized rods the distribution functions are measured in the presence of 0.5 mol/l 2:2 salt and as a function of the Manning parameter. Overcharging is again observed at sufficiently high charge. Furthermore, the dependence of the zeta-potential on the Manning parameter is found to be non-monotonic. This is in accord with predictions from integral equation theories. In addition, DNA has been investigated at different bulk ionic strengths. The radius, at which overcharging is observed, is found to increase with decreasing salt and to be in very good agreement with integral equation predictions. For the poly(p-phenylene) simulations the distribution functions and the osmotic coefficients are computed. They are compared to the Poisson-Boltzmann theory and to the Debye-Hückel-hole-cavity correlation correction from Sec. 1.3. The latter is found to give an excellent quantitative description of the simulated data.

Section 2.6 sheds light onto specific ionic correlations in the investigated systems. Two-dimensional correlations on the surface of the rods are found to be present, but weakly developed. No hexatic order is observed. The three-dimensional pair correlation function is shown to exhibit a fairly long-ranged structure. However, this is proven to be imposed by the presence of the rods. This calls into question alternative explanations which assume a three-dimensional Wigner crystal to form on the background of the charged rods.

2.1 General algorithmic prerequisites

Thermostatics via molecular dynamics simulations is the attempt to generate ensemble averages from hopefully ergodic phase space trajectories. The key ingredients are a stable numeric integrator and a mechanism to reach the desired ensemble.

2.1.1 The Verlet propagator

Approximate factorization of the classical Liouville propagator permits the construction of various stepwise but still unitary integration schemes [Spr96, FrSm96]. The standard Verlet integrator is a well known example. Let f be a function depending on the canonically conjugate phase space coordinates p and q, but not explicitly on time. Its time evolution generated by a Hamiltonian H is given by the Hamilton equation

$$\frac{\mathrm{d}f}{\mathrm{d}t} \;=\; \frac{\partial f}{\partial q}\frac{\partial H}{\partial p} - \frac{\partial f}{\partial p}\frac{\partial H}{\partial q} \;=:\; \{f,H\} \;=:\; \mathrm{i}\mathscr{L}f. \tag{2.1}$$

Here $\{\cdot,\cdot\}$ stands for the Poisson bracket and $\mathscr{L} := -\mathrm{i}\{\cdot,H\}$ for the Liouville operator, which is hermitian[1] by virtue of the additional i. The solution to the initial value problem $f(p(0),q(0)) = f(p_0,q_0)$ can be formally written as

$$f(p(t),q(t)) \;=\; e^{\mathrm{i}\mathscr{L}t}\, f(p_0,q_0) \;=:\; U(t)\, f(p_0,q_0). \tag{2.2}$$

For numerical purposes it proves to be advantageous to approximately factorize the propagator for small timesteps δt into exponentials containing only one kind of derivative. This need not spoil unitarity. With the definitions

$$\mathscr{L}_q := -\mathrm{i}\,\frac{\partial H}{\partial p}\frac{\partial}{\partial q} = \mathscr{L}_q^\dagger \qquad \text{and} \qquad \mathscr{L}_p := \mathrm{i}\,\frac{\partial H}{\partial q}\frac{\partial}{\partial p} = \mathscr{L}_p^\dagger \tag{2.3}$$

[1] that is, $\int \mathrm{d}p\,\mathrm{d}q\; f^*(p,q)\big(\mathscr{L}g(p,q)\big) = \int \mathrm{d}p\,\mathrm{d}q\; \big(\mathscr{L}f(p,q)\big)^* g(p,q)$ for a suitable class of phase space functions f and g. With the hermitian operator denoted by $\mathscr{L}^\dagger$, this is shortly expressed as $\mathscr{L} = \mathscr{L}^\dagger$.

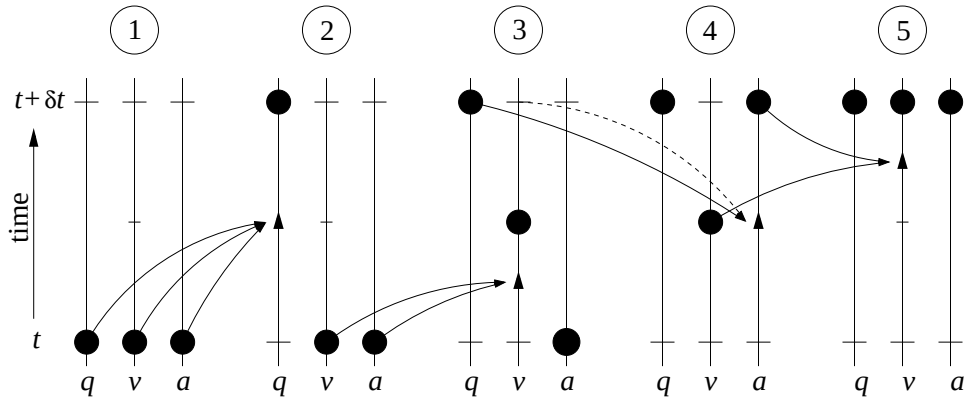

Figure 2.1: Schematic representation of the procedures involved in one timestep of the velocity Verlet integrator. Note that for velocity dependent forces the unknown new velocities are required for the step $3 \to 4$.

the Liouville propagator can for instance be approximated as

$$U(\delta t) \;=\; e^{\mathrm{i}\mathscr{L}\,\delta t} \;=\; e^{\frac{\mathrm{i}}{2}\mathscr{L}_p\,\delta t + \mathrm{i}\mathscr{L}_q\,\delta t + \frac{\mathrm{i}}{2}\mathscr{L}_p\,\delta t} \;\approx\; e^{\frac{\mathrm{i}}{2}\mathscr{L}_p\,\delta t}\, e^{\mathrm{i}\mathscr{L}_q\,\delta t}\, e^{\frac{\mathrm{i}}{2}\mathscr{L}_p\,\delta t} \;=:\; \tilde{U}(\delta t). \quad (2.4)$$

Clearly, $\tilde{U}^\dagger(\delta t) = \tilde{U}(-\delta t) = \tilde{U}^{-1}(\delta t)$, which proves $\tilde{U}$ to be unitary and time reversible. In the case of a force $F = -V'$ and a Hamiltonian $H = p^2/2m + V(q)$, state vectors transform according to

$$e^{\mathrm{i}\mathscr{L}_p\,\delta t}\begin{pmatrix} q_0 \\ p_0 \end{pmatrix} = \begin{pmatrix} q_0 \\ p_0 + F(q_0)\,\delta t \end{pmatrix} \qquad \text{and} \qquad e^{\mathrm{i}\mathscr{L}_q\,\delta t}\begin{pmatrix} q_0 \\ p_0 \end{pmatrix} = \begin{pmatrix} q_0 + \frac{1}{m}\,p_0\,\delta t \\ p_0 \end{pmatrix}. \quad (2.5)$$

(Proof: differentiation with respect to δt). Thus, the following discrete dynamics results:

$$\begin{aligned}
\begin{pmatrix} q(t+\delta t) \\ p(t+\delta t) \end{pmatrix} &= e^{\frac{\mathrm{i}}{2}\mathscr{L}_p\,\delta t}\, e^{\mathrm{i}\mathscr{L}_q\,\delta t}\, e^{\frac{\mathrm{i}}{2}\mathscr{L}_p\,\delta t}\begin{pmatrix} q(t) \\ p(t) \end{pmatrix} \\
&= e^{\frac{\mathrm{i}}{2}\mathscr{L}_p\,\delta t}\, e^{\mathrm{i}\mathscr{L}_q\,\delta t}\begin{pmatrix} q(t) \\ p(t) + \frac{1}{2}F\big(q(t)\big)\,\delta t \end{pmatrix} \\
&= e^{\frac{\mathrm{i}}{2}\mathscr{L}_p\,\delta t}\begin{pmatrix} q(t) + \frac{1}{m}\Big[p(t) + \frac{1}{2}F\big(q(t)\big)\,\delta t\Big]\,\delta t \\ p(t) + \frac{1}{2}F\big(q(t)\big)\,\delta t \end{pmatrix} \\
&= \begin{pmatrix} q(t) + \frac{1}{m}\Big[p(t) + \frac{1}{2}F\big(q(t)\big)\,\delta t\Big]\,\delta t \\ p(t) + \frac{1}{2}F\big(q(t)\big)\,\delta t + \frac{1}{2}F\big(q(t+\delta t)\big)\,\delta t \end{pmatrix}.
\end{aligned} \quad (2.6)$$

This is the *velocity Verlet integration scheme*, which reproduces the originally continuous dynamics from Eqn. (2.2) up to a truncation error of order δt^4 by a stroboscopic process. For practical purposes it is convenient to slightly rewrite the algorithm. With $v := p/m$ being the velocity and $a := F/m$ the acceleration, Eqn. (2.6) can be implemented in the following four steps, which are also illustrated in Fig. 2.1

$$q(t+\delta t) = q(t) + v(t)\,\delta t + \frac{1}{2}\,a(t)\,\delta t^2 \tag{2.7}$$

$$v(t+\frac{1}{2}\,\delta t) = v(t) + \frac{1}{2}\,a(t)\,\delta t \tag{2.8}$$

compute new accelerations $a(t+\delta t)$

$$v(t+\delta t) = v(t+\frac{1}{2}\,\delta t) + \frac{1}{2}\,a(t+\delta t)\,\delta t. \tag{2.9}$$

A direct consequence of the integrator being unitary is that it conserves phase space volume. This is important when during a microcanonical simulation statistical properties are measured according to the motto "ensemble average equals time average". This is due to the fact that ergodicity requires the Liouville measure to be invariant under the applied dynamics [LaMa85]. Furthermore, the notorious long-term energy-updrift of many other discrete integration schemes is strongly suppressed [FrSm96]. This drift would distinguish a direction in time, a fact which is incompatible with a time reversible propagator. In some sense, the energy is "very close" to a constant of motion. A more detailed account is given in [Spr96].

2.1.2 Creating the canonical ensemble: The Langevin thermostat

The basic idea of molecular dynamics (MD) simulations is to create a sufficiently long trajectory of a model system through its phase space and – by appealing to ergodicity – to identify a time average over this trajectory with a suitable statistical ensemble average. The purpose of the present work is to study the thermodynamic properties of specific polyelectrolyte systems within the canonical ensemble. However, the integrator described in the previous section is a Hamiltonian one and can thus by construction at most yield a microcanonical average. To turn the argument on its head, it means that obtaining canonical averages requires going beyond standard Hamiltonian dynamics.

Today a large variety of methods exist, which drive the system into the canonic state, e.g., by introduction of artificial degrees of freedom or by coupling the system to a heat bath via stochastic methods. The reader will find more details in Refs. [AlTi97, FrSm96]. The choice for the present work is a Langevin thermostat [GrKr86]. This means that instead of integrating Newton's equations of motion, one solves a set of Langevin equations

$$m_i \ddot{\boldsymbol{r}}_i = -\nabla U(\{\boldsymbol{r}_i\}) - \Gamma \dot{\boldsymbol{r}}_i + \boldsymbol{\xi}_i(t) \tag{2.10}$$

with $\boldsymbol{\xi}_i(t)$ being a δ-correlated Gaussian noise source with its first and second moments given by

$$\langle \boldsymbol{\xi}_i(t) \rangle = 0 \qquad \text{and} \qquad \langle \boldsymbol{\xi}_i(t) \cdot \boldsymbol{\xi}_j(t') \rangle = 6\, k_{\mathrm{B}} T\, \Gamma \delta_{ij} \delta(t-t'). \tag{2.11}$$

Remarks 2.1.1

1. The friction term $-\Gamma \dot{\boldsymbol{r}}_i$ and the noise $\boldsymbol{\xi}_i(t)$ can be though of as imitating the presence of a surrounding viscous medium responsible for a drag force and random collisions, respectively.

2. The second moment of $\boldsymbol{\xi}_i(t)$ is adjusted via the fluctuation-dissipation theorem such as to reach the canonical state in the limit $t \to \infty$.

3. The dynamics generated by the Langevin equation can alternatively be written as a general Fokker-Planck process. This permits a transparent proof of two important facts: *(i)* the stationary state of the process is the Boltzmann distribution and *(ii)* it actually converges to it [Ris89, Dün93].

4. Since for small times the stochastic part is more important than the deterministic one, roughly because $\sqrt{t} \gg t$ for small t, it is actually not necessary to use Gaussian random variables in the simulation [DüPa91]. It suffices to use equidistributed random variables with first and second moment being identical to the Gaussian deviate and once more appeal to the central limit theorem. For this it is helpful to note that a random variable taken from the distribution

$$\overline{w}(x) \;=\; \frac{1}{\sqrt{12}}\,\chi_{[-\sqrt{3};\sqrt{3}]} \;=\; \begin{cases} \frac{1}{\sqrt{12}} & : \quad -\sqrt{3} \le x \le \sqrt{3} \\ 0 & : \quad \text{otherwise} \end{cases} \tag{2.12}$$

   has zero mean and unit variance.

5. This particular implementation of random forces destroys momentum conservation. However, in reality a "piece" of momentum cannot just vanish but has to be transported away. This gives rise to long-ranged hydrodynamic interactions which are screened by the Langevin thermostat. Hereby, the screening length is inversely proportional to the square root of the friction coefficient [Dün93]. Hence, if one is interested in dynamic quantities and hydrodynamic interactions are potentially important, e.g., in a solution, one has to use a different thermostat. One possible choice is "dissipative particle dynamics", which conserves momentum by adding the noise in a pair-wise fashion [EsWa95].

6. If the inertial term $m_i\ddot{\boldsymbol{r}}_i$ is negligible to the other ones, the dynamics becomes overdamped. However, since thermostatics cannot depend on the masses of the particles, the equilibrium properties must be the same in the limit $m_i \to 0$. This method is referred to as "Brownian dynamics" [AlTi97].

2.1.3 Verlet integration and velocity dependent forces

If the force calculation depends on positions as well as on velocities, the plain Verlet integration scheme in Eqns. (2.7–2.9) is actually incorrect. This is the case in Langevin dynamics simulations, see Eqn. (2.10), and also for a Lorentz force. The problem is that the new velocity required for computing the new acceleration is not known at this stage of the algorithm, see also Fig. 2.1. The usual remedy is to alternatively use the almost new half-step velocity $v(t + \frac{1}{2}\,\delta t)$, which may be called the "naive" approach. However, if the new acceleration depends *linearly* on the velocity, there exists a simple but exact way out. Assume that the new acceleration can be written as

$$a(t + \delta t) = f[q(t + \delta t)] - \Gamma\, v(t + \delta t). \tag{2.13}$$

Since Eqns. (2.9,2.13) can be viewed as two linear equations for the two unknowns $v(t+\delta t)$ and $a(t+\delta t)$, they can readily be solved for them, giving

$$v(t+\delta t) = \frac{v(t+\frac{1}{2}\,\delta t)+\frac{1}{2}\,f[q(t+\delta t)]\,\delta t}{1+\frac{1}{2}\,\Gamma\,\delta t} \tag{2.14}$$

$$a(t+\delta t) = \frac{f[q(t+\delta t)]-\Gamma\,v(t+\frac{1}{2}\,\delta t)}{1+\frac{1}{2}\,\Gamma\,\delta t}. \tag{2.15}$$

Expanding the denominator in these equations in powers of δt reveals that the correct new values for v and a differ from the naive ones by terms of order δt^2 for the velocity and δt for the acceleration. This translates to a non-vanishing difference $\frac{1}{2}\,\delta t^3\,\Gamma\big\{f[q(t+\delta t)]-\Gamma\,v(t+\frac{1}{2}\,\delta t)\big\}$ between the new correct and new naive positions $q(t+2\,\delta t)$. This is one order larger than the original fourth order truncation error of the Verlet integrator. However, the treatment of the Langevin thermostat itself is not correct up to fourth order, so the inaccuracy is not vital in this particular case. Since some test simulations showed no difference between both implementations, the naive approach has been chosen in the present work. Note, however, that for dissipative particle dynamics a self-consistent treatment of the velocity is rewarding [PaHa98].

2.2 Description of the model system

The hexagonal prism is the space filling object most "close" to a cylinder and thus a natural choice for an approximate implementation of the cell model. Still, it can be implemented in simple cubic periodic boundary conditions.

2.2.1 Generating a cell-geometry

Compared to the spherical cell model, the cylindrical one presents one additional but crucial complication: It is infinite along the direction of the charged rod.[2] Several methods have been proposed in the literature to handle this problem [Gul89, NiGu91, LyNo97, LyTa98]. They essentially all use as a unit cell a hexagonal[3] prism with a certain height. This approximates the cylindrical cell treated in Chap. 1 by a space-filling object. They differ in the way of obtaining an infinite system via periodic replications and use various kinds of Ewald-summations adapted to the respective symmetry. The present work takes a different approach, exploiting the fact that a hexagonal cell can also be obtained within a cubic symmetry.

The basic idea is the following: Take a cube and place a rod along the main diagonal. Upon periodically replicating this system two things happen:

1. The diagonal rod becomes infinitely long and

[2] The same obviously applies to the charged plane. Observe also that this is closely related to problems in the context of Rem. 1.4.1.5.

[3] It is sometimes remarked that a hexagonal cell is in fact more reasonable than a cylindrical one, since at high densities packing of rods will take place in a hexagonal fashion [LyNo97]. However, this particular cell will also be used for low densities, in which actual systems show no crystal-like order. Despite the natural high density picture it is therefore more appropriate to regard the cell model – cylindrical or hexagonal – as a simple recipe to map a many polyelectrolyte problem to a one polyelectrolyte theory, and not more.

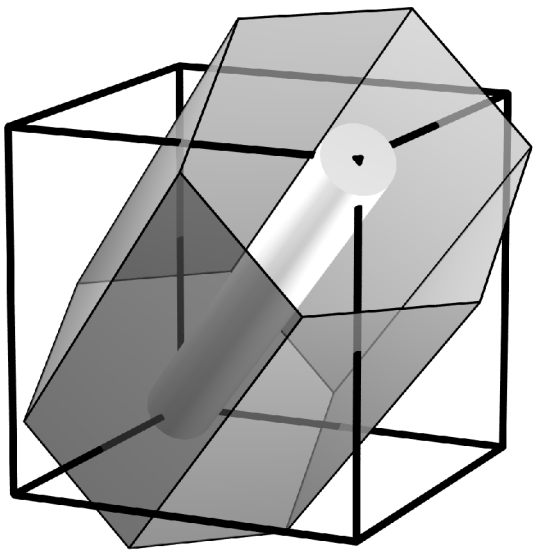

Figure 2.2: Realization of the cell model. A rod placed along the main diagonal of a cube yields an infinite triangular array of infinitely long rods upon periodic replication of the original cube. The Wigner-Seitz cell of this lattice is a regular hexagon enclosing the rod. This therefore provides a way of obtaining a hexagonal cell without abandoning a cubic geometry.

2. an infinite triangular array of such replicated rods appears.

The resulting Wigner-Seitz cell of this lattice is a regular hexagon, which can alternatively be viewed as the unit cell. This is illustrated in Fig. 2.2. Observe that the symmetry of the replicated system is still cubic. A brief summary of important consequences imposed by this geometry is given in TP 2.1.

The main advantage of this approach is that such a system can be treated with the plain cubic Ewald sum or one of its mesh-upgrades, which will be discussed in Chap. 3. This permits a very efficient way for computing the long-range electrostatic interactions.[4] Its main disadvantage is the coupling of counterion number and cell volume, which is responsible for some additional restrictions – the most unusual probably being that decreasing the density entails an increase in counterion number and vice versa, see TP 2.1. While this makes the simulation of low densities rather expensive, it gives at the same time rather small dense systems. The latter problem can be circumvented by combining blocks of $2 \times 2 \times 2$, $3 \times 3 \times 3$ or even more elementary cubes to a big cube and using the latter as the unit box for the periodic boundary conditions.

2.2.2 Interaction potentials

A specification of two interaction potentials is necessary two describe the model system: *(i)* an excluded volume interaction preventing two particles, in particular of opposite charge, from occupying the same position in space and *(ii)* the long-range Coulomb potential.

One of the most widely used choices in molecular dynamics simulations for implement-

[4] A honeycomb lattice can be viewed as a Bravais lattice with a rhombic cell with acute angle 60° and a two point base. This implementation has been chosen, e.g., in Ref. [Gul89]. Although the complexity of the Fourier space part of the Ewald sum is essentially independent of the Bravais symmetry, the lack of orthogonality makes the computation of real space minimum images costly, even for the non-electrostatic interactions.

Technical Point 2.1 *(hexagonal cell)*

Knowledge of the length L_b of the cubic box from Fig. 2.2 is enough to specify the corresponding hexagonal cell model. All other lengths can then be expressed as functions of L_b. The separation between two neighboring rods is $d_\mathrm{rod} = L_\mathrm{b}\sqrt{2/3}$. From that follows the side length of the regular hexagon, which is also the maximum separation from the rod, as $s = L_\mathrm{b}\sqrt{2}/3$ and its area as $A = L_\mathrm{b}^2/\sqrt{3}$. Since the length of the rod segment within the cube is just $L_\mathrm{rod} = L_\mathrm{b}\sqrt{3}$, this immediately shows the hexagonal cell to have the same volume as the cube. The radius R of a circle with the same area A is then given by $R = L_\mathrm{b}/\sqrt{\pi\sqrt{3}}$. This value is most appropriately used for comparing results between the hexagonal and the cylindrical cell model.

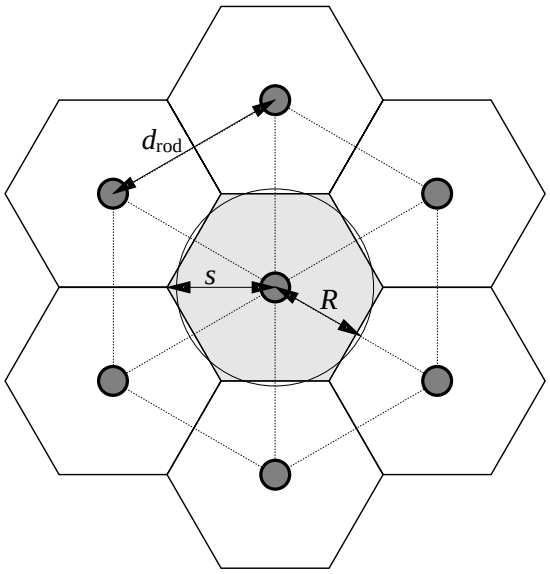

If the line charge density of the rod is λ, electroneutrality requires the number of v-valent counterions to be $N = \sqrt{3}L_\mathrm{b}\lambda/ve_0$. Hence the average counterion density is given by $n = N/L^3 = \sqrt{3}\lambda/ve_0L^2$ and is thus inversely proportional to L^2 instead of L^3. The number of counterions can therefore be written as $N = (\sqrt{3}\lambda/ve_0)^{3/2}n^{-1/2}$. This has the quite unusual implication of a smaller density requiring more particles. This is ultimately a consequence of the fact that the number of counterions cannot be chosen independently of the cell volume. Notice that the ratio between Debye length ℓ_D and rod separation d_rod can be written as

$$\frac{\ell_\mathrm{D}}{d_\mathrm{rod}} \;=\; \frac{\left[4\pi\ell_\mathrm{B}v^2(\sqrt{3}\lambda/ve_0L_\mathrm{b}^2)\right]^{-1/2}}{L_\mathrm{b}\sqrt{2/3}} \;=\; (8\pi\xi v/\sqrt{3})^{-1/2} \;\approx\; 0.2625/\sqrt{\xi v}. \qquad (2.16)$$

For the important strongly charged case, in which the product of Manning parameter ξ and valence v is larger than 1, the Debye length is smaller than the separation of the two rods. Even for $\xi v = 1$ it is only half as large as the distance between rod axis and Wigner-Seitz boundary. Note that this statement is independent of density.

ing a hard core is the purely repulsive Lennard-Jones (LJ) potential:

$$V_\mathrm{LJ}(r) \;=\; \begin{cases} 4\epsilon\left[\left(\dfrac{\sigma}{r}\right)^{12} - \left(\dfrac{\sigma}{r}\right)^{6} + \dfrac{1}{4}\right] & : \quad 0 < r \le r_\mathrm{cut} \equiv 2^{1/6}\sigma \\ 0 & : \quad r_\mathrm{cut} < r. \end{cases} \qquad (2.17)$$

Remarks 2.2.1

1. The energy ϵ and length σ are parameters characterizing the strength and extension of the potential[5]. They are conveniently used as the basic units within simulations, see TP 2.2 or Ref. [FrSm96].

[5]Since (2.17) has dimension energy, it should actually better be referred to as potential energy. However, the corresponding Lennard-Jones charges are dimensionless, such that this distinction does not matter.

Technical Point 2.2 *(Lennard-Jones units)*

For a mechanical system three independent units suffice to define a complete unit system. Dealing with Lennard-Jones particles, it is convenient to choose mass, energy and length. In that case the latter two are identified with the parameters ϵ and σ from Eqn. (2.17), and m is viewed as the mass of the particle. Time is consequently measured in units of $\tau_{\mathrm{LJ}} = \sigma\sqrt{m/\epsilon}$ and temperature in units of ϵ/k_{B}. Additionally treating electrostatic interactions requires a fourth unit, which here is chosen to be the positive elementary charge $e_0 \equiv 1.60219 \times 10^{-19}\,\mathrm{C}$. In this work σ is always used as the unit length and ϵ is always set to the thermal energy $k_{\mathrm{B}}T$, unless stated otherwise. Temperature is implemented via the Bjerrum length $\ell_{\mathrm{B}} = \beta e_0^2/4\pi\varepsilon$. Mass is irrelevant – it would only be needed to translate the Lennard-Jones time τ_{LJ} into "real" time.

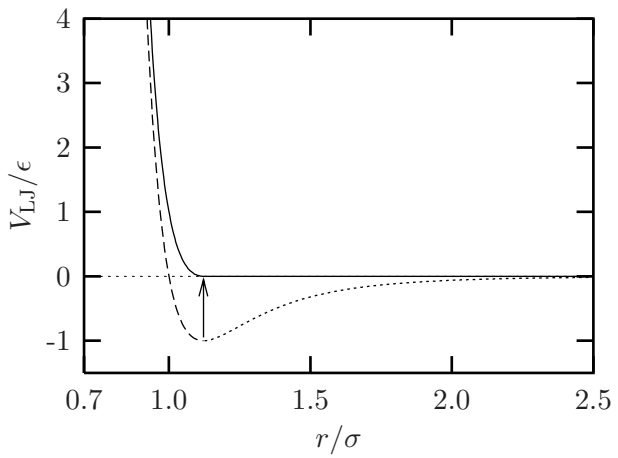

Figure 2.3: Sketch of a truncated and shifted Lennard-Jones potential (solid line). The dashed and dotted line shows the usual Lennard-Jones potential. It is shifted up by ϵ, truncated at the minimum, and set to zero for larger r. Observe that although being smooth, this potential is indeed fairly close to the notion of a hard core.

2. The plain Lennard-Jones potential is shifted up, such that its minimum located at $2^{1/6}\sigma$ has value 0, and set to zero beyond that point.

3. The advantage of including the $-r^{-6}$ contribution instead of merely using the purely repulsive r^{-12} is that Eqn. (2.17) is exactly zero beyond r_{cut} and merges smoothly to this value at r_{cut}.

4. The use of a smooth hard core in molecular dynamics simulations is necessary since the force is the derivative of the potential, therefore, the latter should be differentiable. In fact, the derivative must also be bounded to ensure numerical stability of the discrete integrator.

5. A graphical illustration can be found in Fig. 2.3.

The Coulomb potential of a charge Q is written as

$$\phi(r) \;=\; \frac{Q}{4\pi\varepsilon_0\varepsilon_{\mathrm{r}} r} \tag{2.18}$$

where $\varepsilon_0 = 8.85418 \times 10^{-12}\,\mathrm{C^2\,m^{-2}\,N^{-1}}$ is the dielectric constant of the vacuum and ε_{r} is the dielectric coefficient of the medium. For instance, water at room temperature has $\varepsilon_{\mathrm{r}} \approx 78.5$. The product $\varepsilon_0\varepsilon_{\mathrm{r}}$ will be abbreviated by ε. In the context of thermodynamics

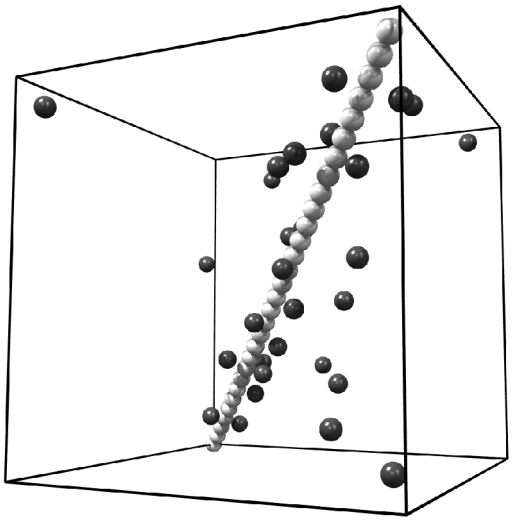

Figure 2.4: Generic version of the cell model. Using the same geometry as illustrated in Fig. 2.2, the rod is realized by a chain of ions lined up along the main diagonal. Concerning excluded volume interactions the particles forming the chain and the particles in solution are identical. Electrostatically, however, they differ by the sign of their charge.
For this particular system the Manning parameter is $\xi = 2.88 > 1$, and the implied condensation of counterions is clearly visible. Note that most of the systems studied in this chapter contain many more particles, but for the purpose of illustration a small system is more informative.

it is more convenient to measure electrostatic interaction strength using the so called Bjerrum length $\ell_B = \beta e_0^2/4\pi\varepsilon$, which already appeared in the first chapter. Recall that the Bjerrum length is the distance at which two unit charges have an interaction energy equal to $k_B T$. The definition of ℓ_B permits the Coulomb potential of a charge Q to be written as

$$\phi(r) \;=\; \ell_B \, k_B T \, \frac{Q/e_0^2}{r}. \tag{2.19}$$

Within the periodic boundary conditions employed during the simulations, the presence of such long-range interactions poses both mathematical and technical difficulties. A thorough discussion of this topic is deferred to Chap. 3.

2.3 Generic ion distribution functions

Poisson-Boltzmann theory systematically underestimates counterion condensation. Particularly its difficulties with high density, rod charge, Bjerrum length and valence indicate the importance of neglected correlations.

On the plain Poisson-Boltzmann level the radius r_0 of the rod is not a completely independent variable, since it enters only in the combination R/r_0, see Eqn. (1.11). This suggests a further simplification of the model system: Instead of explicitly describing the rod as a separate object, one builds it from a sequence of small Lennard-Jones particles lined up along the main diagonal of the simulation cell. This is as shown in Fig. 2.4. No bonding potential is needed to maintain this configuration. Instead, the coordinates of the rod-particles are simply not propagated in time by the integrator. It would be quite natural to identify the distance of closest approach of two Lennard-Jones particles with the radius r_0 of the rod. However, a smooth potential like in Eqn. (2.17) has no clear-cut

			$\ell_B/\sigma = 2$				$\ell_B/\sigma = 3$			
N, p	R/σ	$n\,\sigma^3$	ℓ_D/σ	R_M/σ	$R_M^\star/\sigma$	$f_\xi^\star$	ℓ_D/σ	R_M/σ	$R_M^\star/\sigma$	$f_\xi^\star$
8, 4	2.0641	7.167×10^{-2}	0.7451	1.419	1.530	0.583	0.6084	1.561	1.724	0.793
15, 3	3.8702	2.039×10^{-2}	1.3971	1.929	2.135	0.577	1.1407	2.229	2.443	0.768
30, 3	7.7403	5.097×10^{-3}	2.7941	2.713	3.044	0.564	2.2814	3.247	3.400	0.735
60, 3	15.481	1.274×10^{-3}	5.5882	3.821	4.086	0.537	4.5628	4.681	4.330	0.698
120, 3	30.961	3.185×10^{-4}	11.176	5.389	5.493	0.517	9.1255	6.709	6.019	0.687
240, 1	61.923	7.963×10^{-5}	22.353	7.604	7.513	0.500	18.251	9.577	8.123	0.672
480, 1	123.85	1.991×10^{-5}	44.706	10.74	10.46	0.503	36.502	13.64	11.66	0.668

Table 2.1: Manning radius $R_M^\star$ and condensed fraction $f_\xi^\star = P(R_M^\star)$ determined from the simulation via the inflection point criterion from Sec. 1.1.3. The 14 presented systems differ in density n and Bjerrum length ℓ_B. R, R_M and ℓ_D are the cell radius, Poisson-Boltzmann Manning radius and Debye-length, respectively. N is the number of ions lined up with a distance of $1.04245\,\sigma$ along the main diagonal of a cube like the one from Fig. 2.4, while p is the number of such distinguishable boxes in each space dimensions which together build the periodically replicated simulation box. This gives $Np^3(1+1/v)$ charges in total. Note that the Manning condensed fraction would be 0.479 and 0.653 for $\ell_B/\sigma = 2$ and $\ell_B/\sigma = 3$, respectively.

closest distance, as can be seen in Fig. 2.3. Satisfactory results are nevertheless obtained by alternatively using a "thermal" distance, at which the interaction energy is equal to k_BT. With $\epsilon = k_BT$, the choice in the present study, this yields a thermal distance and thus an effective rod radius of σ.

Upon leaving the Poisson-Boltzmann level, the ratio between counterion diameter σ and rod radius r_0 becomes relevant. This is evident, e.g., from the excluded volume self-consistency condition discussed in Rem. 1.1.3.8, and it is also investigated in Ref. [GrMa97]. Whereas systematic investigations of resulting effects have not been performed in this work, Sec. 2.5 presents results for systems mapped to physically relevant parameters, DNA and two kinds of poly(p-phenylenes), in which the rod has a considerably larger diameter than the counterions.

2.3.1 Density dependence within monovalent systems

At fixed rod radius r_0 the relevant variable R/r_0 is changed by varying the cell size R and therefore the density. Table 2.1 presents results for such a scan for systems with $\ell_B/\sigma \in \{2, 3\}$. The monovalent and positively charged particles forming the rod were placed along the main diagonal with a center-center distance of $1.04245\,\sigma$, giving a line charge density of $\lambda = 0.959279\,e_0/\sigma$. In connection with the two presented values for the Bjerrum length this yields Manning parameters of $\xi \in \{1.919, 2.878\}$ and corresponding Manning fractions of $f_\xi = 1 - 1/\xi \in \{0.4788, 0.6525\}$. The inflection point criterion from Sec. 1.1.3 has been used to determine the radial extension of the condensed layer, $R_M^\star$, and the fraction of ions within it, $f_\xi^\star = P(R_M^\star)$. Recall that P is the integrated counterion distribution function from Eqn. (1.15). Technically, the inflection points were determined by fitting a (2:2) rational polynomial in $\ln(r)$ to $r^2\,n(r)$ in the vicinity of its minimum, where $n(r)$ is the radial counterion density. This procedure follows the alternative formulation of the inflection point criterion given in TP 1.3. The results of these measurements are summarized in Tab. 2.1, and a graphical illustration of the distribution functions is given

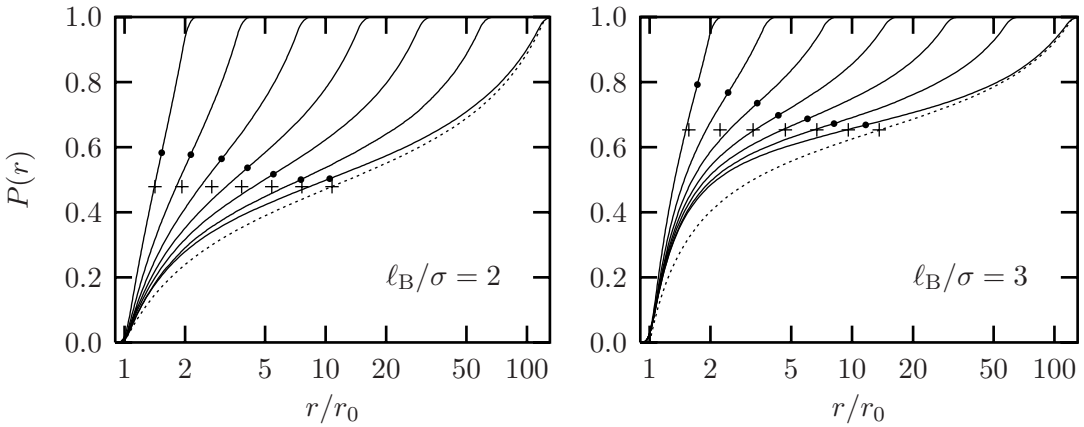

Figure 2.5: Counterion distribution functions $P(r)$, as defined in Eqn. (1.15), for the systems from Table 2.1. Note that an increasing cell radius corresponds to functions extending towards larger values of r. The heavy dots mark the points of inflection in P as a function of $\ln(r)$, while the crosses mark the positions at which those points would be located on the corresponding Poisson-Boltzmann distribution functions. For the sake of clarity such a Poisson-Boltzmann distribution is only plotted for the system with lowest density, i.e., $R = 123.85\,\sigma$ (dotted line).

in Fig. 2.5.

The important things to observe are the following. The measured condensed fraction $f_\xi^\star$ is always larger than the fraction predicted by the Poisson-Boltzmann theory. However, the fraction from the simulation decreases monotonically with decreasing density towards the Manning limit f_ξ. Such a deviation is to be expected, since Poisson-Boltzmann is essentially a low density theory neglecting local ion-ion correlations, see Rem. 1.1.1.1. Furthermore, this finding is in accord with two important features of correlations, which have been discussed in Sec. 1.3:

1. They are more pronounced in dense systems, i.e., the free energy correction describing them goes to zero in the limit of zero density, see Fig.1.7.

2. They lead to an enhanced counterion condensation, see Fig. 1.8.

In contrast to the clear tendency of the measured condensed fraction to decrease upon dilution, the behavior of the condensation radius $R_\mathrm{M}^\star$ appears to be more complicated. There does not seem to exist a simple monotonic convergence of $R_\mathrm{M}^\star$ towards R_M. Rather, for high densities the measured condensation distance is larger than the Manning radius, while for the investigated low densities it is smaller. Unfortunately, a clear-cut statement is difficult since the localization of the point of inflection in P as a function of $\ln(r)$ is only possible with an error estimated to be of the order of 1%.

Table 2.1 does not present values for systems with Bjerrum length $\ell_\mathrm{B} = 1\,\sigma$, since their Manning parameter would be $\xi = 0.9593 < 1$. The implied absence of Manning condensation renders the search for inflection points meaningless. It is more appropriate to compare the complete distribution functions with the Poisson-Boltzmann prediction, as it is done in Fig. 2.6. It can be seen that the measured and Poisson-Boltzmann predicted distributions almost coincide for all cell sizes under investigation. While this is to be expected for low densities, the remarkable agreement at high densities is somewhat surprising. Apparently,

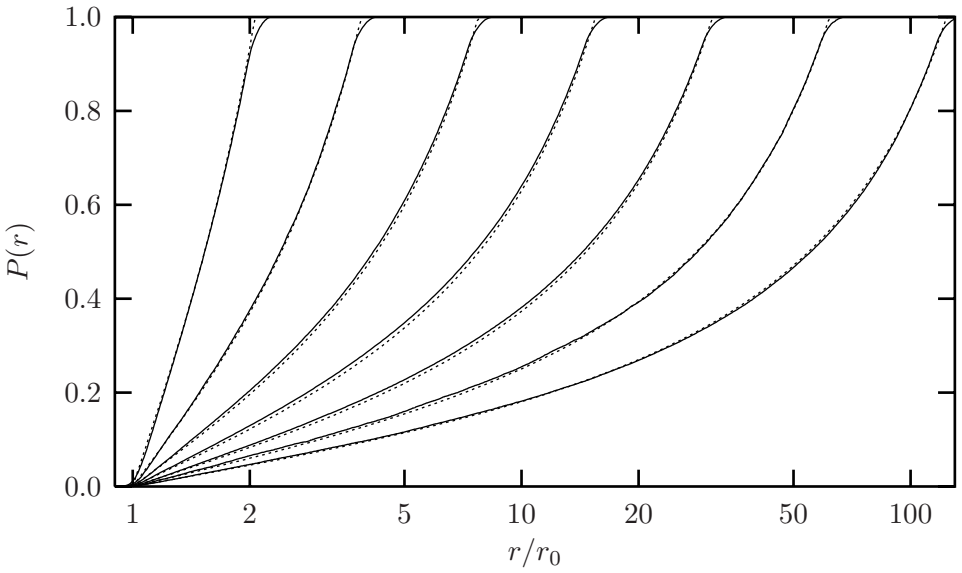

Figure 2.6: Counterion distribution functions $P(r)$ (solid lines) for seven systems with the same dimensions as the ones in Tab. 2.1, but with a Bjerrum length $\ell_B/\sigma = 1$. Since the resulting Manning parameter $\xi = 0.959 < 1$, counterion condensation is not expected to occur. This is borne out by the observation that the functions are convex up already at $r = r_0$. In these weakly charged systems the predictions of Poisson-Boltzmann theory (dotted lines) are excellent and can hardly be distinguished from the simulation results.

Poisson-Boltzmann theory is a fairly good description of weakly charged systems, i.e., ones which are below the Manning threshold. A possible explanation is that upon increasing density two effects neglected within the Poisson-Boltzmann theory start to compete. On one hand, correlations increase and tend to enhance condensation. On the other hand, excluded volume interactions become more relevant and lower the counterion density at rod contact. This is seen in Fig. 1.9.

If the above explanation is accurate, it implies that strongly charged systems deviate from the Poisson-Boltzmann theory mainly due to the neglected correlations, while weakly charged systems deviate mainly due to the neglected hard core. The first statement is supported by the distribution functions of the hard core systems as shown in Fig. 1.9. Despite of the dramatic changes close to the rod, the condensed fraction determined by the inflection point criterion remains largely unchanged. The second statement becomes clear if one recalls that for decreasing Manning parameter the Manning radius approaches the rod, see Rem. 1.1.1.3. Since excluded volume interactions are most relevant at the rod surface, they can interfere more easily with the Manning radius, if the Manning parameter is small, i.e., when the system is weakly charged.

2.3.2 Fitting to a generalized Poisson-Boltzmann distribution

If the measured Manning radius $R_M^\star$ can be smaller than the Poisson-Boltzmann prediction, this has the following consequence. From Rem. 1.1.1.3 and the definition $f_\xi = 1 - 1/\xi$ it follows that within the Poisson-Boltzmann theory f_ξ is monotonically increasing with R_M, see also the locus of inflection points in Fig. 1.3. $f_\xi^\star > f_\xi$ and $R_M^\star < R_M$ is thus

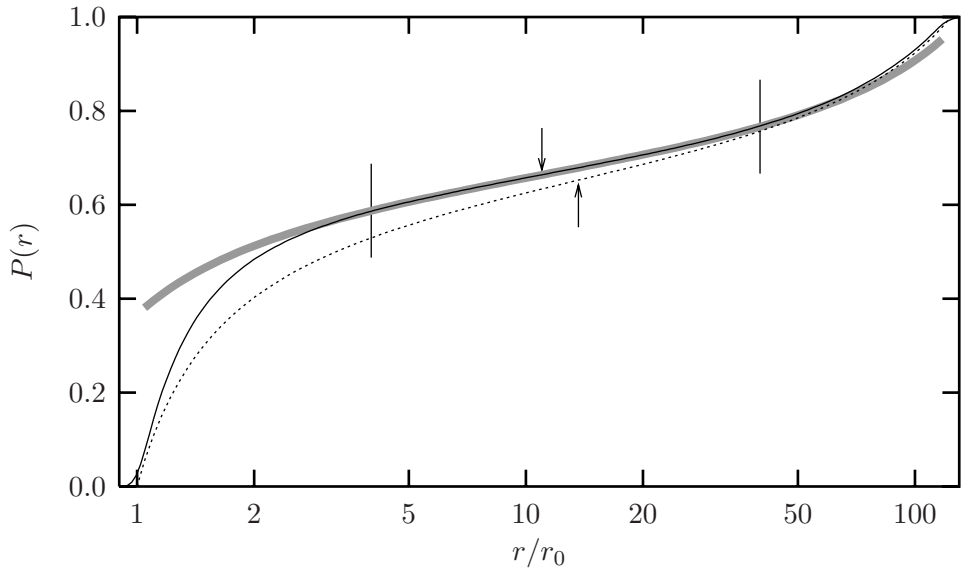

Figure 2.7: The functional form in Eqn. (2.20) has been fitted to the measured distribution function (solid line) of the system with $R = 123.85\,\sigma$ and $\ell_B = 3\,\sigma$ from Tab. 2.1 within the range $[4\,r_0; 40\,r_0]$ between the two vertical bars. The ↑-arrow indicates the inflection point of the Poisson-Boltzmann distribution (dotted line), while the ↓-arrow indicates the corresponding point $(R_M^\star; f_\xi^\star) = (10.989\,\sigma; 0.664)$ of the fit (gray stripe). Note that $R_M^\star < R_M$ although $f_\xi^\star > f_\xi$, in accord with Tab. 2.1, but that the actual values differ. The result of the fit is $\xi^\star = 2.97414$, $\gamma^\star = 0.456611$ and $r_0^\star = 0.579034\,\sigma$.

incompatible with Poisson-Boltzmann theory. It is impossible to describe such a $P(r)$ with a Poisson-Boltzmann distribution function in which a somewhat enlarged effective Manning parameter is used. To the lowest order, e.g., within a two state model, the increase of counterion condensation can be ascribed to such an effective $\xi^\star = 1/(1 - f_\xi^\star)$. Yet, the functional relation is affected upon a closer look. Nevertheless, it would be desirable to use at least some of the knowledge about the ion distribution function from Poisson-Boltzmann theory for evaluating relevant observables in a simulation or in a real experiment. In order to do this, the monotonic connection between f_ξ and R_M has to be broken. This can be done, for instance, by assuming the functional form of P to be given by the Poisson-Boltzmann form in Eqn. (1.13) but neglecting the relation in Eqn. (1.11). Using Eqn. (1.10*i*), this suggests fitting the measured distribution in a region around the inflection point to the form

$$P_{\text{fit}}(r) \;=\; 1 - \frac{1}{\xi^\star} + \frac{\gamma^\star}{\xi^\star} \tan\left(\gamma^\star \,\ln \frac{r}{r_0^\star} + \arctan \frac{1-\xi^\star}{\gamma^\star}\right) \tag{2.20}$$

with the three fit parameters $\xi^\star$, $\gamma^\star$ and $r_0^\star$.[6] The condensed fraction is then given by $f_\xi^\star = 1 - 1/\xi^\star$ and the condensed radius by $R_M^\star = r_0^\star \exp\{\arctan[(\xi^\star - 1)/\gamma^\star]/\gamma^\star\}$. Fig. 2.7

[6] It might seem strange to regard the rod radius as a free parameter, but there are two reasons for this. First, this does not force the fit to coincide with the Poisson-Boltzmann form outside the chosen fitting-region. Second, not even in a real experiment is the radius of a macroion always known in advance. Rather, it is often necessary to obtain this information within the same measurement [GuBl].

		PB		monovalent		multivalent	
R/σ	$v\,\ell_B/\sigma$	R_M/σ	f_ξ	$R^\star_M/\sigma$	$f^\star_\xi$	$R^\star_M/\sigma$	$f^\star_\xi$
7.7403	2	2.71293	0.4788	3.044	0.564	3.290	0.625
	3	3.24690	0.6526	3.400	0.735	3.873	0.846
123.85	2	10.7365	0.4788	10.46	0.503	10.22	0.515
	3	13.6374	0.6526	11.66	0.668	9.076	0.713

Table 2.2: Influence of valence. For the systems from Tab. 2.1 with $R = 7.7403\,\sigma$ and $R = 123.85\,\sigma$ the complementary systems are investigated, in which the values of v and ℓ_B/σ have been interchanged. On the Poisson-Boltzmann level this does not play a role, but in the real system it leads to an even stronger condensation in the multivalent situation.

illustrates this procedure for one system. While this approach might seem to be very powerful, it suffers from the drawback that the actual numbers depend on the chosen fitting region. Nevertheless, it provides an independent way of quantifying condensation and can even be applied to very noisy data, for which the localization of an inflection point in P as a function of $\ln(r)$ is otherwise virtually impossible.

2.3.3 Multivalent ions

Up to now only monovalent ions have been investigated. For multivalent ions the prediction of the Poisson-Boltzmann theory is that for the distribution function $P(r)$ only the product of Manning parameter ξ and counterion valence v matters, see Rem 1.1.2.4. Therefore, a system of monovalent ions at $\ell_B = 3\,\sigma$ is claimed to have the same distribution function as a system of trivalent ions at $\ell_B = 1\sigma$. It will now be shown that this statement is an artifact of the Poisson-Boltzmann approximation. Table 2.2 and Fig. 2.8 show examples of systems which are "complementary" in the described sense. Not only is the condensation enhanced as compared to Poisson-Boltzmann theory, but the enhancement is stronger for the case involving multivalent ions. Two different reasons may be suggested to explain this effect:

1. At given charge density multivalent systems have a lower number density and thus fewer particles. This lowers any kind of excluded volume interactions.

2. Sec. 1.3 demonstrates that the relevant variable for describing the strength of correlation effects is $\ell = \ell_B v^2$ – irrespective of the actual correlational free energy used. Hence, an increase in valence is more important than an increase in Bjerrum length.

However, the first point must be taken with great care for the following reason: The extension of the limiting expression for the contact density $n(r_0)$ in Eqn. 1.24 to general valence v is

$$\lim_{r\to\infty} n(r_0) = \frac{\overline{\rho}_{r_0}}{2\xi v^2}\,(\xi v - 1)^2. \tag{2.21}$$

For high rod charge, i.e., large ξ, this expression becomes independent of valence. Hence, replacing monovalent counterions by multivalent ones reduces their total number in the

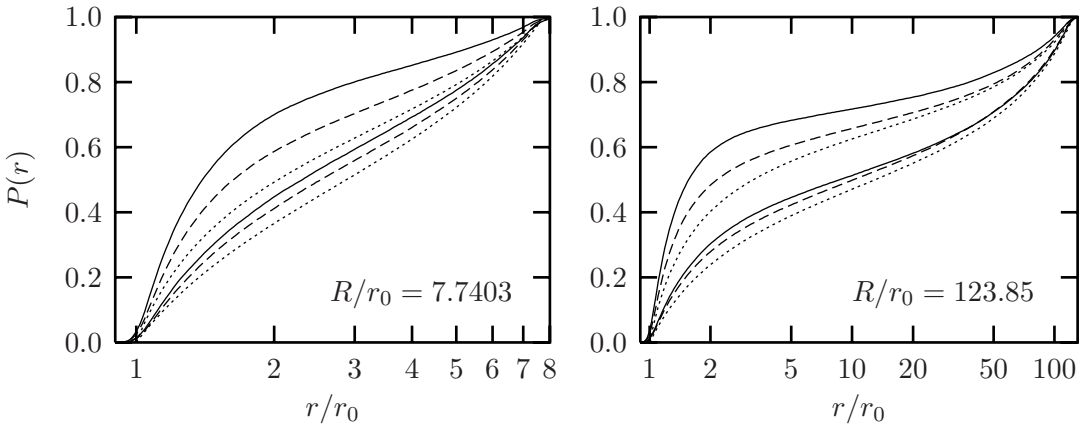

Figure 2.8: Counterion distribution functions $P(r)$ for the complementary systems from Tab. 2.2. The high (low) density situation is shown in the left (right) frame. The lower three curves are for $v\,\ell_B/\sigma = 2$, while the upper three correspond to $v\,\ell_B/\sigma = 3$. The systems with multivalent counterions (solid lines) always show a stronger condensation than the complementary systems with monovalent ions (dashed lines), which themselves show a stronger condensation than Poisson-Boltzmann theory (dotted lines).

cell, but for a highly charged rod not their density at the rod surface.[7]

Taking this into account, the increased condensation must essentially be attributed to correlation effects. From an intuitive point of view one may argue like this: The continuous charge density from the Poisson-Boltzmann theory is actually represented by individual charge carriers, and this discretization is clearly more pronounced for highvalent ions. Increasing valence is a route away from density functional theory towards a situation in which strongly interacting individual particles correlate with each other. Particularly at high densities these correlations become very important. For instance, in the dense trivalent system from Tab. 2.2 the condensation is enhanced by 30% with respect to the Poisson-Boltzmann prediction.

2.3.4 Addition of salt

The influence of salt on the distribution functions has been discussed within the Poisson-Boltzmann theory in Sec. 1.2. The general finding was that a low salt content leaves the picture of Manning condensation qualitatively unchanged, while at increasing salt concentration a crossover between Manning condensation and simple salt-screening occurs. This can be seen in Fig. 1.6. For three systems from that figure – number of salt molecules $N \in \{0, 104, 3070\}$ – a simulation has been performed and compared to the Poisson-Boltzmann prediction in Fig. 2.9. As in the salt-free case the computer simulations show a more pronounced condensation effect towards the rod. Nevertheless, the shape of the distribution functions remains qualitatively the same. Note in particular that the appearance and disappearance of two points of inflection at $N = 104$ and $N = 3070$ respectively, which leads to extremely small curvatures in the Poisson-Boltzmann distribution functions, also

[7] This statement is in fact an *exact* result and not a feature seen in the Poisson-Boltzmann approximation only [WeJö82].

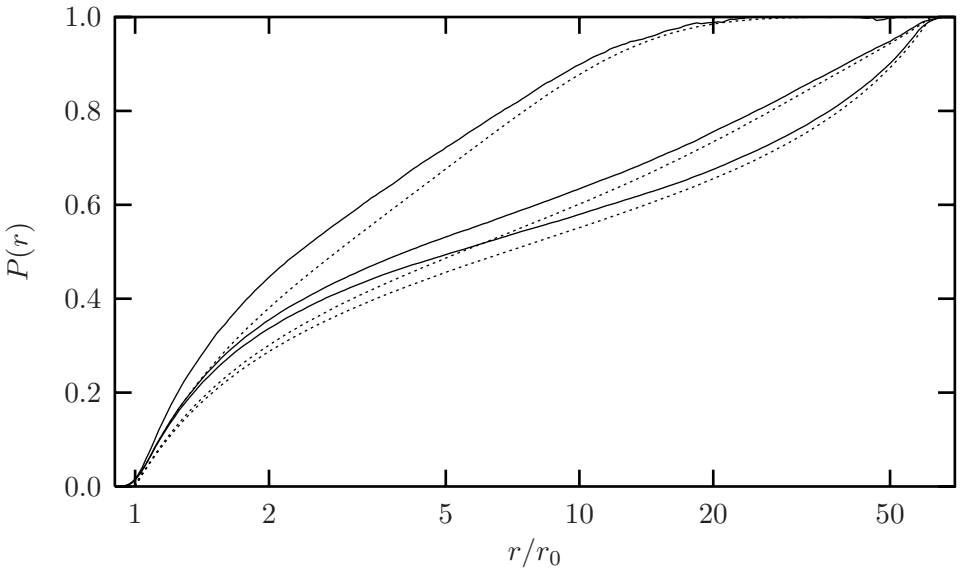

Figure 2.9: Distribution functions $P(r)$ for the system from Fig. 1.6 which has $R/\sigma = 61.923$, $\ell_B/\sigma = 2.189$, $\xi = 2.1$ and monovalent ions. From bottom to top the number of salt molecules added to the simulation box of length $L_b = 144.446\,\sigma$ is 0, 104 and 3070, which corresponds to a salt Debye length of ∞, $22.9\,\sigma$ and $4.2\,\sigma$, respectively. The solid lines are the result of a simulation while the dotted lines are the predictions of Poisson-Boltzmann theory.

leads to very straight regions in the measured distribution functions. The crossover from Manning condensation to screening, as described within the Poisson-Boltzmann theory, can be expected to be essentially correct.

It should not be overlooked, however, that the addition of salt ions will affect the distribution function much more dramatically if their[8] valence is larger than the valence of the counterions. In this case, the salt counterions will accumulate in the vicinity of the rod at the expense of the lower valent "real" counterions as has previously been demonstrated in the valence mixture systems from Sec. 1.4.2, see Fig. 1.11.[9] As an example, Fig. 2.10 illustrates the distribution functions of a system, in which the monovalent ions are accompanied by *(i)* the same number of 1:1 salt molecules or *(ii)* half as many 2:2 salt molecules. Although the charge density of the salt counter- or coions is the same in both cases[10], the charge distribution function of the second system is much more reminiscent of a divalent system, particularly close to the rod. The Poisson-Boltzmann predictions for the 2:2 salt system and – for comparison – a salt-free system of divalent ions almost coincide for small r. The simulated distribution function differs only by the correlation induced enhancement of condensation. At large r, however, the larger total number of ions in the salt system and the consequently smaller Debye length leads to stronger screening than in the salt-free system having divalent ions. Therefore, the distribution function of

[8] To be precise: The valence of the ions having the same charge as the counterions. The valence of the other ones – usually termed coions – is normally much less relevant, since they are repelled from the rod, which deprives them of a mechanism to form a high density and thereby becoming correlated.

[9] From a perturbational point of view it would in fact be advisable to regard the highest valent ions of a charge opposite to the rod as "counterions" and all the rest as potentially asymmetric salt.

[10] The salt Debye length is, however, smaller by a factor $\sqrt{2}$ in the 2:2 system.

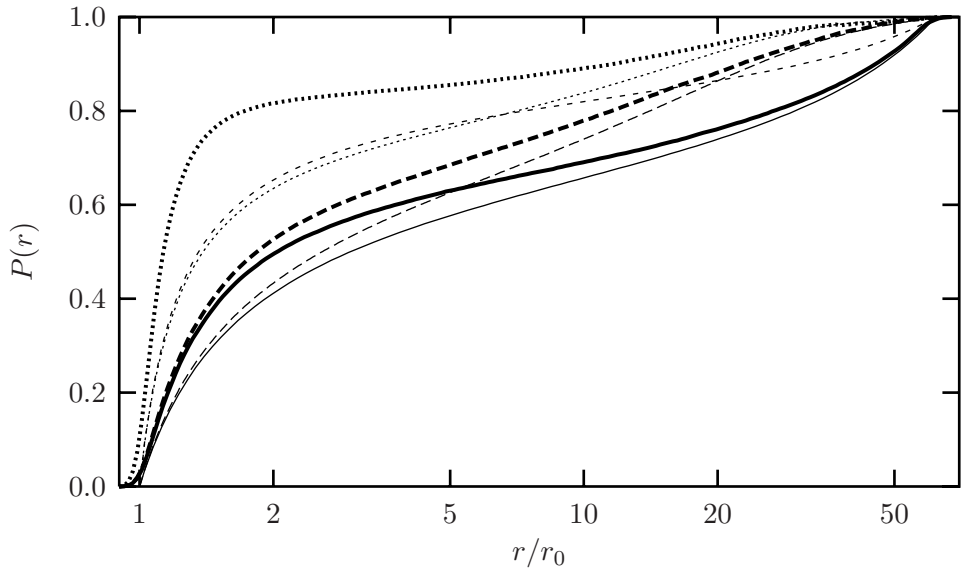

Figure 2.10: To a system with $L_b/\sigma = 144.44$, i.e., 240 monovalent counterions and cell size $R/\sigma = 61.923$, and $\ell_B/\sigma = 3$ (solid lines) the same number of 1:1 salt molecules (long dashed lines) or half as many 2:2 salt molecules (dotted lines) have been added. Heavy lines correspond to a simulation, thin lines to the Poisson-Boltzmann theory. The short dashed line is the Poisson-Boltzmann prediction for such a system containing only divalent counterions. Clearly the charge distribution of the 2:2 system is most appropriately be characterized by a perturbed divalent system.

the former approaches the value 1 more quickly.

The Poisson-Boltzmann approach fails to describe the physical situation if one or more of the following conditions apply: *(i)* the electrostatic interactions are strong, *(ii)* the counterions are multivalent or *(iii)* the density is high. Results of a simulation under such conditions can be seen in Figure 2.11. Here, a system with box length $L_b/\sigma = 36.112$, i.e., 60 monovalent counterions and a cell size of $R/\sigma = 15.481$, and $\ell_B/\sigma = 4.1698$, i.e., $\xi = 4$, has been investigated after adding 1000 molecules of a 2:2 salt. Since this gives almost 17 times as much salt as counterions and a salt Debye length of $\ell_D/\sigma = 0.33 \ll R$, this can essentially be viewed as a charged rod in a bulk 2:2 electrolyte. The most characteristic feature of the charge distribution function is that it overshoots unity, showing a charge reversal of the rod at distances around $r \approx 1.5\,\sigma$, while the simple Poisson-Boltzmann prediction is clearly qualitatively off. This phenomenon is usually referred to as overcharging and has been predicted for the primitive cell model first from hypernetted chain calculations [GoLo85] and later by a modified Poisson-Boltzmann approach [DaBr95, DaBr97]. Since $P(R) = 1$ for the reason of global electroneutrality, the overshooting above 1 at small distances implies the existence of a range of r-values at which the mobile ion system is locally positively charged, i.e., with the same charge as the rod, such that $P(r)$ can eventually decay to 1. This is seen in the right frame of Fig. 2.11, which shows that $n_{+2}(r) > n_{-2}(r)$ at $r \approx 2\,\sigma$. Since $P(1.5\,\sigma) \approx 1.45$, the rod and its innermost layer of condensed ions could be viewed as an effective rod of radius $1.5\,\sigma$ which is negatively charged with Manning parameter $\xi = 1.8$. Since this value is again larger than 1, it entails ion condensation, but this time of positive ions. In fact, it even leads to a second

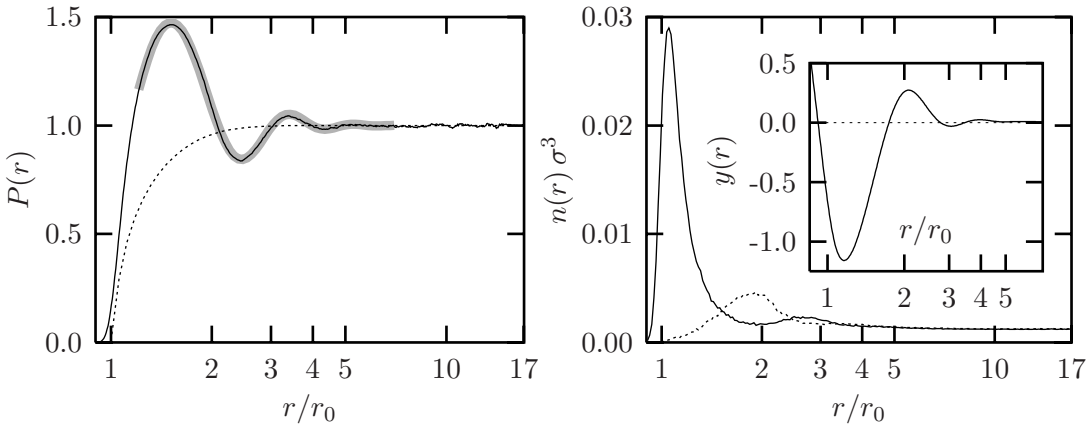

Figure 2.11: Charge distribution for a system characterized by $L_b/\sigma = 36.112$, i.e., 60 monovalent counterions and a cell size of $R/\sigma = 15.481$, $\ell_B/\sigma = 4.1698$, i.e., $\xi = 4$, and 1000 molecules of a 2:2 salt within the box volume. The simulation shows a pronounced overcharging-effect in $P(r)$ (solid curve, left frame), in contrast to Poisson-Boltzmann-theory (dotted curve). The charge oscillations can be described quite accurately by an exponentially damped sine function with period $1.89\,\sigma$ and decay length $0.85\,\sigma$ (gray stripe). The densities $n_{-2}(r)$ (solid line, right frame) and $n_{+2}(r)$ (dotted line) of negative and positive salt ions, respectively, demonstrate the effect of charge layering and local charge reversal, and the inlay shows the dimensionless electrostatic potential $y(r) = \beta e_0 \psi(r)$, which is also oscillating.

overcharging, as can clearly be seen in Fig. 2.11, where $P(r)$ – in decaying from 1.45 – overshoots the value of 1 again. Overcharging can thus give rise to layering. In the presented example no less than three layers can clearly be made out. These local charge oscillations also reflect themselves in oscillations of the electrostatic potential, as demonstrated in the inset in the right frame of Fig. 2.11. Notice that these oscillating potentials will also have pronounced effects on the interaction between such rigid polyelectrolytes.

2.4 Pressure

Within the anisotropic cell model the pressure is related to volume changes leaving the direction along the rod invariant. Simulations constantly yield a smaller osmotic coefficient than predicted by Poisson-Boltzmann theory. For multivalent systems it can even become negative.

2.4.1 Defining and computing the pressure

In a simulation, the pressure for the primitive cell model is a nontrivial variable to compute for two reasons:

1. The long-range attractions have to be properly taken into account.

2. The system is inherently anisotropic. Hence the relevant observable is the stress tensor.

Neglecting for a moment the second problem, the thermodynamic definition of the isotropic pressure within the canonical ensemble is

$$p \;=\; -\left(\frac{\partial F}{\partial V}\right)_{N,T}. \tag{2.22}$$

Together with the statistical definition of the free energy

$$F \;=\; -\frac{1}{\beta}\ln\,\mathrm{Tr}\,\mathrm{e}^{-\beta H} \tag{2.23}$$

belonging to a system with standard Hamiltonian

$$H \;=\; \sum_{i=1}^{N}\frac{\boldsymbol{p}_i^2}{2m_i} + U(\boldsymbol{r}_1,\ldots,\boldsymbol{r}_N) \tag{2.24}$$

with potential energy U this gives the pressure equation

$$p\,V \;=\; Nk_{\mathrm{B}}T - V\left\langle\frac{\partial U}{\partial V}\right\rangle. \tag{2.25}$$

The angular brackets $\langle\cdots\rangle$ denote a canonical average. For the case of short-range interactions the contribution from U can be further simplified by using

$$\frac{\partial U}{\partial V} \;=\; \sum_i \frac{\partial U}{\partial \boldsymbol{r}_i}\cdot\frac{\partial \boldsymbol{r}_i}{\partial V} \;=\; \sum_i(-\boldsymbol{F}_i)\cdot\frac{\boldsymbol{r}_i}{3V}. \tag{2.26}$$

Substituting this into the pressure equation (2.25) gives

$$p\,V \;=\; Nk_{\mathrm{B}}T + \frac{1}{3}\sum_i\langle\boldsymbol{r}_i\cdot\boldsymbol{F}_i\rangle. \tag{2.27}$$

The second contribution is the average over the classical virial. Assuming only pair forces to be present, this part can be rewritten in terms of them. Let $\boldsymbol{F}_{ij}$ be the force which particle j acts onto particle i and let $\boldsymbol{r}_{ij} = \boldsymbol{r}_j - \boldsymbol{r}_i$ be the vector pointing from particle i to particle j. Then

$$\begin{aligned}\sum_i \boldsymbol{r}_i\cdot\boldsymbol{F}_i \;&=\; \sum_i \boldsymbol{r}_i\cdot\sum_j\boldsymbol{F}_{ij} \;=\; \frac{1}{2}\times\left[\sum_i\boldsymbol{r}_i\cdot\sum_j\boldsymbol{F}_{ij} + \sum_j\boldsymbol{r}_j\cdot\sum_i\underbrace{\boldsymbol{F}_{ji}}_{=-\boldsymbol{F}_{ij}}\right]\\ &=\; \frac{1}{2}\sum_{i,j}(\boldsymbol{r}_i-\boldsymbol{r}_j)\cdot\boldsymbol{F}_{ij} \;=\; \underline{\underline{-\sum_{i<j}\boldsymbol{r}_{ij}\cdot\boldsymbol{F}_{ij}}}.\end{aligned} \tag{2.28}$$

It is of fundamental importance that these two expressions for the virial do *not* coincide under periodic boundary conditions. The reason is that the expression $\boldsymbol{r}_{ij} = \boldsymbol{r}_j - \boldsymbol{r}_i$ for the distance is no longer valid. In general, it has to be corrected by a suitable lattice shift to obtain the actual minimum image expression. The correct expression to use is the double sum, since it is manifestly translationally invariant, like the pressure. A thorough discussion is given in Appendix B of Ref. [Hai92].

Concerning the electrostatic contribution to the pressure, there is the temptation to use the expression $\boldsymbol{r}_i \cdot \boldsymbol{F}_i$ from the virial also for the Coulomb pressure. The technical reason for this is that the Fourier space part of the Ewald sum does not easily give access to the pair forces.[11] This is, however, not a good idea due to *(i)* the difference between the two virials under periodic boundary conditions[12] and *(ii)* since the electrostatic energy explicitly depends on the box size. The latter is a consequence of the Coulomb potential not being short-ranged. Luckily, there is a very convenient way of computing the electrostatic contribution to the pressure. It can be derived by realizing that the electrostatic energy U^{C} is a homogeneous function of volume with degree $-1/3$, i.e., it can be written as

$$U^{\mathrm{C}}(\boldsymbol{r}_i, \ldots, \boldsymbol{r}_N; V) \;=\; V^{-1/3}\, U^{\mathrm{C}}(\boldsymbol{r}_i V^{-1/3}, \ldots, \boldsymbol{r}_N V^{-1/3}; 1) \;=\; V^{-1/3}\, U^{*}, \qquad (2.29)$$

where U^* is independent of isotropic volume changes. The derivative of the Coulomb energy with respect to the volume is thus given by

$$\frac{\partial U^{\mathrm{C}}}{\partial V} \;=\; \frac{\partial (V^{-1/3}\, U^{*})}{\partial V} \;=\; -\frac{1}{3}\, V^{-4/3}\, U^{*} \;=\; -\frac{U^{\mathrm{C}}}{3V} \qquad (2.30)$$

Combining Eqns. (2.27,2.28,2.30) finally gives the desired pressure equation

$$p\,V \;=\; N k_{\mathrm{B}} T - \frac{1}{3} \sum_{i<j} \left\langle \boldsymbol{r}_{ij} \cdot \boldsymbol{F}_{ij}^{\mathrm{sr}} \right\rangle + \frac{1}{3} \left\langle U^{\mathrm{C}} \right\rangle, \qquad (2.31)$$

where $\boldsymbol{F}_{ij}^{\mathrm{sr}}$ are the short-range pair forces. Note that for a repulsive hard core the virial contribution is positive, while the electrostatic contribution is one third of the energy density, which for neutral systems is usually negative.

For anisotropic systems the stress tensor is the relevant observable to compute. Whereas the ideal gas contribution to the pressure still remains isotropic, the virial must be replaced by

$$\mathsf{p}^{\mathrm{vir}}\, V \;=\; -\frac{1}{3} \sum_{i<j} \left\langle \boldsymbol{r}_{ij} \otimes \boldsymbol{F}_{ij}^{\mathrm{sr}} \right\rangle, \qquad (2.32)$$

where "$\otimes$" denotes the tensor product. For the case of electrostatic interactions the derivation is more complicated and will not be presented here. The reader is referred to Ref. [EsPe95]. The result is that within the framework of Ewald techniques the electrostatic contribution to the stress tensor, p^{C}, can be decomposed additively into a real space contribution $\mathsf{p}^{(r)}$ and a Fourier space contribution $\mathsf{p}^{(k)}$. They are given by

$$\mathsf{p}^{(r)} V \;=\; \frac{1}{2} \sum_{i,j} q_i\, q_j \sum_{\boldsymbol{m} \in \mathbb{Z}^3}{}' \left[\frac{2\alpha}{\sqrt{\pi}}\, \mathrm{e}^{-\alpha^2 \boldsymbol{r}_{ij\boldsymbol{m}}^2} + \frac{\operatorname{erfc}(\alpha |\boldsymbol{r}_{ij\boldsymbol{m}}|)}{|\boldsymbol{r}_{ij\boldsymbol{m}}|} \right] \frac{\boldsymbol{r}_{ij\boldsymbol{m}} \otimes \boldsymbol{r}_{ij\boldsymbol{m}}}{|\boldsymbol{r}_{ij\boldsymbol{m}}|^2} \qquad (2.33)$$

$$\mathsf{p}^{(k)} V \;=\; \frac{1}{2V} \sum_{\boldsymbol{k} \neq \boldsymbol{0}} \frac{4\pi}{k^2}\, \mathrm{e}^{-k^2/4\alpha^2} \left| \tilde{\rho}(\boldsymbol{k}) \right|^2 \left[\mathbb{I} - 2 \left(1 + \frac{k^2}{4\alpha^2} \right) \frac{\boldsymbol{k} \otimes \boldsymbol{k}}{k^2} \right]. \qquad (2.34)$$

[11] This will become clear in Chap. 3.

[12] Notice, however, that it is actually the interplay between periodic boundary conditions and minimum image convention which causes troubles. Since for the long-range Coulomb interactions a minimum image cutoff is usually out of question nowadays, one might hope to use the "simple" $\boldsymbol{r}_i \cdot \boldsymbol{F}_i$ virial. However, in Ref. [HuGr98] the virial expression for the pressure is compared with Eqn. (2.31) and it is found that both expressions differ for finite systems. The latter is found to be much closer to the thermodynamic limit.

Here, $\boldsymbol{r}_{ij\boldsymbol{m}} = \boldsymbol{r}_i - \boldsymbol{r}_j + \boldsymbol{m}L_\mathrm{b}$, and the canonical average has not been denoted explicitly. Also, the reader is referred to Chap. 3, in particular, Sec. 3.2.2, for details of the notation and the Ewald techniques in general. The connection to the isotropic case requires the trace of the pressure tensor to be equal to the mean electrostatic energy density, i.e.,

$$\mathrm{Tr}\,\mathsf{p}^\mathrm{C} \;=\; U^\mathrm{C}/V. \tag{2.35}$$

While analytically this is not easily seen to be true, it has been checked numerically to be correct for all pressure calculations presented in this work.

After computing the electrostatic stress tensor, it can be rotated such that the rod points along the z-axis. The xx- and yy-components of the new tensor then give the pressure perpendicular to the rod, while the zz-component is the contribution parallel to the rod. A more formal but still numerically convenient approach is the following. Let $\mathsf{d}^\perp$ be the projection operator into the plane perpendicular to the diagonal rod, i.e.,

$$\mathsf{d}^\perp \;=\; \mathbb{I} - \frac{1}{3}\begin{pmatrix}1\\1\\1\end{pmatrix}\otimes\begin{pmatrix}1\\1\\1\end{pmatrix} \;=\; \frac{1}{3}\begin{pmatrix}2&-1&-1\\-1&2&-1\\-1&-1&2\end{pmatrix}. \tag{2.36}$$

Then, the pressure perpendicular to the rod is given by

$$p \;=\; \frac{1}{2}\,\mathrm{Tr}\left(\mathsf{d}^\perp\cdot\mathsf{p}\right). \tag{2.37}$$

In fact, the whole purpose of using the stress tensor is to eliminate the pressure component along the stiff rod. After projecting it out, the left hand side in Eqn. (2.37) will then simply be referred to as the "pressure" of the rod system.

Observe finally that the stress tensor of the generic system constructed from a cubic symmetry is nevertheless *cylindrically* symmetric about the rod. The reason for this nice bonus is that the replicated cubic system still has a threefold rotation symmetry about its main diagonal. In fact, looking at the new Wigner-Seitz cell only would even suggest a sixfold symmetry. However, a symmetric second rank tensor cannot have a discrete rotation symmetry larger than twofold without having complete SO(2) symmetry at the same time. This becomes evident by recalling the possible symmetries of quadratic forms described by a symmetric 2×2 matrix.

2.4.2 Pressure measurements within the generic model

This section presents pressure measurements of the generic systems presented in Tab. 2.1 and Tab. 2.2, using Eqns. (2.36,2.37). However, instead of looking at the actual pressure, it is more convenient to look at the dimensionless osmotic coefficient $\widehat{p}$, which is simply the pressure normalized by its ideal gas contribution

$$\widehat{p} \;=\; \frac{p}{p^\mathrm{ig}} \;=\; \frac{p}{nk_\mathrm{B}T}. \tag{2.38}$$

For an *isolated* cell the pressure is given by the particle density at the outer cell boundary. As a corollary, it must then also be positive. This is a rigorous statement, true for the spherical, cylindrical and planar cell model [WeJö82]. It is a merit of the Poisson-Boltzmann equation that it retains the validity of this exact relation. For the extended

Technical Point 2.3 *(pressure within the cell model)*

Assume that for the cell model the free energy density f as a function of density n is given by

$$f(n) \;=\; \frac{\epsilon}{2}(\nabla\psi)^2 + k_{\rm B}T\, n \ln\frac{n}{\bar{n}} + \widetilde{f}(n), \tag{2.39}$$

where potential ψ and density n are as usual related by the Poisson equation and where $\widetilde{f}$ is some additional contribution to be specified later. The total free energy is the volume integral over (2.39) under the constraint of fixed particle number. Since the pressure follows from the free energy density by a Legendre transformation,

$$p \;=\; -f + \mu\, n \qquad \text{with} \qquad \mu \;=\; \frac{\partial f}{\partial n}, \tag{2.40}$$

this results in the following expression

$$p \;=\; n\, k_{\rm B}T - \frac{\epsilon}{2}\,\boldsymbol{E}\cdot\left(\boldsymbol{E} - 2\,n\,\frac{\partial \boldsymbol{E}}{\partial n}\right) + \; n\,\widetilde{f}'(n) - \widetilde{f}(n), \tag{2.41}$$

with $\boldsymbol{E} = -\nabla\psi$ being the electric field. Since this is zero at the cell boundary but its derivative with respect to n must be finite, both field terms vanish there. However, the pressure should be constant throughout the system. Hence, specializing Eqn. (2.41) to the boundary yields

$$p \;=\; n(R)\, k_{\rm B}T + \Big(n(R)\,\widetilde{f}'\big(n(R)\big) - \widetilde{f}\big(n(R)\big)\Big) \tag{2.42}$$

In the plain Poisson-Boltzmann case $\widetilde{f} \equiv 0$ and the pressure turns out to be given by the ideal gas contribution at the boundary. For an additional excluded volume interaction via the free volume approximation from Eqn. 1.67 the excess pressure contribution will be

$$\widetilde{p}_{\rm hc,2} \;=\; n(R)\, k_{\rm B}T\, \frac{n(R)\, V_{\rm eff}}{1 - n(R)\, V_{\rm eff}}, \tag{2.43}$$

which is of course positive. For the zero temperature limit of the Debye-Hückel-hole-cavity correlation correction in Eqn. (1.52), which has been referred to as "complete screening", the excess pressure contribution is

$$\begin{aligned}
\widetilde{p}_{\rm CS} \;&=\; n(R)\, k_{\rm B}T\, \frac{3\,\ell\,\widehat{n}}{4a}\left\{1 - \Big[\,\frac{2}{3}\left(1+\widehat{n}^{-1}\right)^{-1/3} + \frac{1}{3}\left(1+\widehat{n}^{-1}\right)^{2/3}\Big]\right\} \\
&\overset{\widehat{n}\ll 1}{\simeq}\; -n(R)\, k_{\rm B}T\, \frac{\ell\,\widehat{n}^{1/3}}{4a} \times \left\{1 - 3\,\widehat{n}^{2/3} + \frac{8}{3}\,\widehat{n} - \frac{7}{9}\,\widehat{n}^2 + \mathscr{O}\big(\widehat{n}^3\big).\right\}.
\end{aligned} \tag{2.44}$$

Observe that the exact expression in the first line is negative for all densities. The approximation in the second line underestimates $|\widetilde{p}_{\rm CS}|$ and is accurate to 1% for $\widehat{n} < 0.22$. For notation conventions the reader should refer to the relevant sections 1.4 and 1.3.3.

density functional theories discussed in the first chapter this no longer holds and additional terms appear. The reader will find their derivation in a few important cases in TP 2.3.

Going back to the Poisson-Boltzmann theory, the osmotic coefficient can be determined

		$\ell_B/\sigma = 1$		$\ell_B/\sigma = 2$		$\ell_B/\sigma = 3$	
N, p	$n\sigma^3$	$\widehat{p}$	$\widehat{p}^\star$	$\widehat{p}$	$\widehat{p}^\star$	$\widehat{p}$	$\widehat{p}^\star$
8, 4	7.167×10^{-2}	1.0603	1.0207(56)	0.8773	0.6245(69)	0.7413	0.3250(79)
15, 3	2.039×10^{-2}	0.7599	0.7052(40)	0.5622	0.4218(63)	0.4384	0.2493(82)
30, 3	5.097×10^{-3}	0.6520	0.6196(25)	0.4422	0.3664(43)	0.3272	0.2362(62)
60, 3	1.274×10^{-3}	0.6038	0.5856(11)	0.3850	0.3437(25)	0.2758	0.2207(38)
120, 3	3.185×10^{-4}	0.5777	0.5664(10)	0.3521	0.3349(27)	0.2472	0.2169(41)
240, 1	7.963×10^{-5}	0.5620	0.5548(25)	0.3312	0.3040(67)	0.2293	0.188(11)
480, 1	1.991×10^{-5}	0.5518	0.5496(20)	0.3168	0.3063(54)	0.2174	0.1886(93)

Table 2.3: Measured osmotic coefficient $\widehat{p}^\star$ and Poisson-Boltzmann prediction $\widehat{p}$ as a function of density n for cell models with $r_0/\sigma = 1$, $\lambda = 0.9593\, e_0/\sigma$ and monovalent ions. As in Tab. 2.1, the values of N and p give the number of rod-ions lined up along the main diagonal and the number of such distinguishable sub-boxes per coordinate direction forming the replication box, respectively. The numbers in brackets give the error in the last two digits. A graphical illustration can be found in Fig. 2.12.

from Eqn. (1.23) for the boundary density generalized to arbitrary valence

$$\widehat{p} \;=\; \frac{1+\gamma^2}{2\xi v} \;\overset{R\to\infty}{=}\; \frac{1}{2\xi v}, \tag{2.45}$$

where γ is the density dependent integration constant from Eqn. (1.11), in which ξ is replaced by ξv. Table 2.3 summarizes the results for the monovalent systems and Fig. 2.12 illustrates these measurements graphically.

Several things may be noted: The osmotic coefficient from the simulations is always smaller than the Poisson-Boltzmann prediction. In the limit of low density both values converge. This also illustrates that the limiting law from Eqns. (1.23,2.45) becomes asymptotically correct for dilute systems. Upon increasing the density, the osmotic coefficient rises less strongly than the Poisson-Boltzmann prediction. This is more pronounced for systems with higher Bjerrum length, and consequently, higher Manning parameter. Notice that this has a very remarkable side-effect. Over a considerable range of densities the measured osmotic coefficient is much closer to the limiting law than to the actual Poisson-Boltzmann prediction. This makes the Manning limit look much more accurate than it really ought to be. However, the surprising effect should not be over-interpreted, since the underlying reason is nothing but a fortunate cancellation of two errors of approximately the same size.

Those findings can be related to the measurements of the distribution functions presented in Sec 2.3, since the osmotic coefficient is a measure of the free counterions contributing to the osmotic pressure. The investigation of the distribution functions showed that the amount of condensed ions is always larger than the prediction from the Poisson-Boltzmann theory. This entails a smaller osmotic coefficient. In addition, the stronger deviation at higher density, as well as the asymptotic correctness in the dilute limit, is in accord with the corresponding behavior of $\widehat{p}$.

Also for the pressure it is interesting to investigate complementary systems in which the values of Bjerrum length ℓ_B/σ and valence v have been interchanged. However, the dependence on only the product ξv is no longer universally valid, but restricted to the

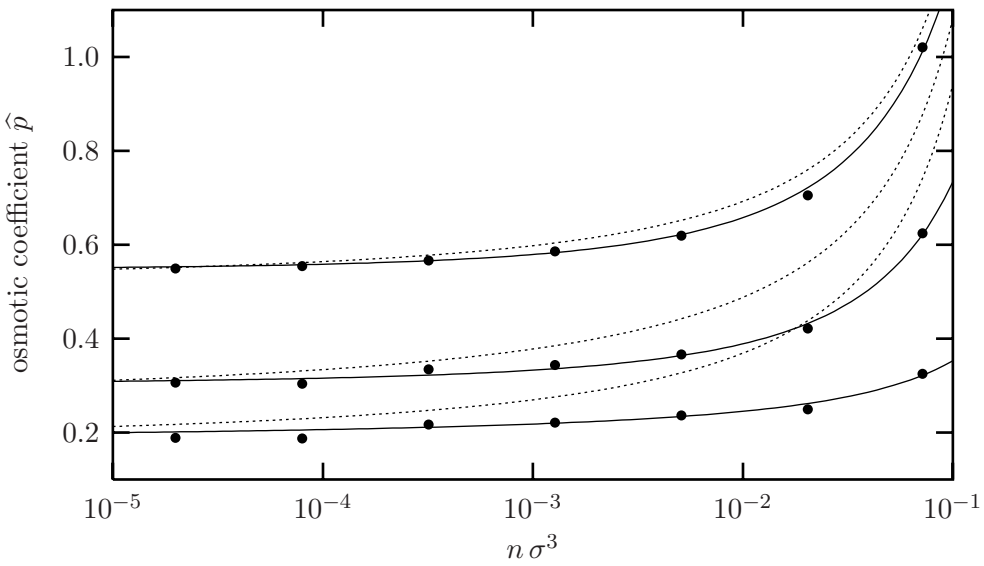

Figure 2.12: Osmotic coefficient $\widehat{p}$ for the systems from Tab. 2.3. Heavy dots mark the measurements, while the solid lines are fits which merely serve to guide the eye. The dotted lines are the prediction of Poisson-Boltzmann theory. From top to bottom the Bjerrum length ℓ_B/σ varies as 1,2,3. The error in the measurement is roughly as big as the dots itself.

dilute limit. In this respect Eqn. (2.45) for the osmotic coefficient is slightly deceiving. From its definition in Eqn. (1.11) γ appears to depend only on ξv. This is true only if two systems with the same cell radius are being investigated. Since the average density $n = \lambda/\pi R^2 e_0 v$ depends on v, two systems of different valence but the same average density differ in cell radius and universality breaks down. In fact, in the high density limit, in which $R = r_0 + \delta r$, the transcendental equation (1.11) defining γ can be solved analytically and yields $\gamma^2 = \xi v\, r_0/\delta r$. Substituting this into Eqn. (2.45) for the osmotic coefficient gives

$$\lim_{R \downarrow r_0} \widehat{p} \;=\; \frac{1}{2}\left(\sqrt{\frac{\lambda}{\pi r_0^2\, e_0 v\, n}} - 1\right)^{-1} . \tag{2.46}$$

In this limit $\widehat{p}$ does no longer depend on Bjerrum length, but it increases with increasing valence. Since in the dilute limit $\widehat{p}$ decreases with increasing valence, this implies the functions $\widehat{p}(n)$ for different valences to intersect at some point.

Table 2.4 summarizes the results of measurements on the multivalent systems corresponding to the monovalent ones investigated before, and Fig. 2.13 visualizes the data. The most striking feature is the appearance of a negative osmotic coefficient in a certain density region of the trivalent case. This implies attractive interactions between the charged rods to be present. If the constraint of a fixed volume in the canonical NVT ensemble suddenly were to be replaced by a constant non-negative pressure, the system would immediately contract, thereby reducing the separation of the rods. Similar observations have been reported in Refs. [NiGu91, GrMa97, LyTa98]. In order to trace back the origin of those attractive interactions, Fig. 2.14 displays the osmotic coefficient in the divalent and trivalent cases, split into two contributions: *(i)* the non-electrostatic part comprising ideal

		$v = 2$				$v = 3$	
N, p	$n\,\sigma^3$	$\widehat{p}$	$\widehat{p}^\star$	N, p	$n\,\sigma^3$	$\widehat{p}$	$\widehat{p}^\star$
4.5, 4	1.133×10^{-1}	3.5302	1.889(19)	4.5, 4	7.550×10^{-2}	3.3765	0.651(23)
5, 4	9.174×10^{-2}	2.1460	0.971(12)	5, 6	6.116×10^{-2}	1.9963	−0.197(11)
6, 4	6.371×10^{-2}	1.3288	0.500(12)	6, 4	4.247×10^{-2}	1.1850	−0.507(17)
7, 4	4.680×10^{-2}	1.0319	0.393(10)	6.5, 6	3.619×10^{-2}	1.0110	−0.4798(81)
8, 3	3.583×10^{-2}	0.8773	0.3379(96)	7, 3	3.120×10^{-2}	0.8926	−0.443(12)
10, 3	2.293×10^{-2}	0.7168	0.3258(86)	8, 3	2.389×10^{-2}	0.7413	−0.299(16)
12, 3	1.593×10^{-2}	0.6333	0.3189(72)	9, 4	1.888×10^{-2}	0.6487	−0.2143(93)
16, 3	8.959×10^{-3}	0.5459	0.3298(49)	15, 3	6.795×10^{-3}	0.4384	0.018(16)
30, 2	2.548×10^{-3}	0.4422	0.3269(75)	30, 3	1.699×10^{-3}	0.3272	0.131(11)
60, 2	6.371×10^{-4}	0.3850	0.3139(68)	60, 3	4.247×10^{-4}	0.2758	0.1663(87)
240, 1	3.982×10^{-5}	0.3312	0.2943(87)	120, 2	1.062×10^{-4}	0.2472	0.1525(96)
				240, 2	2.654×10^{-5}	0.2293	0.1731(70)
				480, 1	6.636×10^{-6}	0.2174	0.171(14)

Table 2.4: Measured osmotic coefficient $\widehat{p}^\star$ and Poisson-Boltzmann prediction $\widehat{p}$ as a function of density n for cell models which are complementary to the ones in Tab. 2.3: $r_0/\sigma = 1$, $\lambda = 0.9593\,e_0/\sigma$ and $\ell_B/\sigma = 1$, but divalent and trivalent counterions have been used. N and p are as before. A graphical illustration can be found in Fig. 2.13.

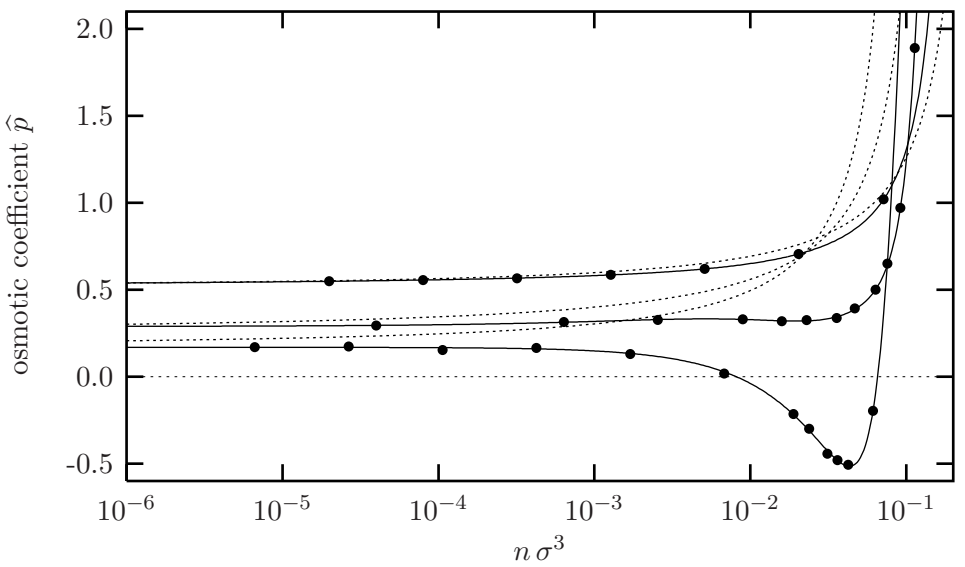

Figure 2.13: Osmotic coefficient $\widehat{p}$ for the systems from Tab. 2.4. Heavy dots mark the measurements, while the solid lines are fits which merely serve to guide the eye. The dotted lines are the prediction of Poisson-Boltzmann theory. From top to bottom the valence v varies like 1,2,3. The error in the measurement is roughly as big as the dots itself.

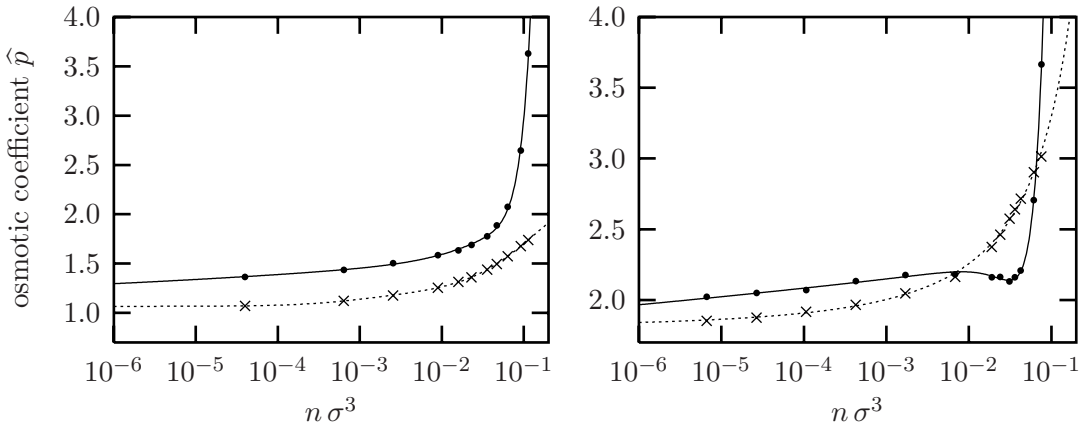

Figure 2.14: Osmotic coefficient $\widehat{p}$ for the divalent (left) and trivalent (right) systems from Fig. 2.13, separated into the non-electrostatic contribution coming from virial and ideal gas (heavy dots on solid lines) and negative electrostatic contribution (crosses on dotted lines). Again, the lines are fits which merely serve to guide the eye.

gas contribution[13] and the short-range virial and *(ii)* the electrostatic part, which for visual convenience is plotted with a reversed sign. Hence, the difference between those two curves gives the curves in Fig. 2.13. Several things should be noted:

1. The electrostatic part leads to a monotonically increasing attraction with increasing density. It is almost twice as strong in the trivalent case.

2. The very strong increase of the osmotic coefficient at large densities is due to the virial, i.e., due to repulsive ion-rod and ion-ion interactions.

3. The negative pressure in the trivalent case is the result of a "sudden" drop in the virial contribution. Nothing particular can be observed in the electrostatic part.

4. The decrease in the virial contribution at high density may be due to the following effect. An important part of the virial results from the force a condensed ion acts onto the rod it is touching. However, this force will be reduced at sufficiently high density when a neighboring rod pulls onto the ion. An alternative explanation suggests that ions condensed on two neighboring rods form a mutually interlocked pattern, which leads to attractions [RoBl96, GrMa97]. However, various investigations of the simulated data have not revealed such a pattern to exist here.

5. From Fig. 2.14 it appears that the curvature of the virial part is larger than that of the electrostatic part. It is therefore conceivable to obtain a negative pressure with both contributions still being monotonic.

6. Even at low density the non-electrostatic contribution to the osmotic coefficient is larger than 1, particularly for the trivalent system. This must originate from the strong repulsive hard-core interactions between condensed ions and the rod, since at those densities inter-ionic repulsions can no longer play a role. This strong repulsion

[13] Observe that the ideal gas contribution to the osmotic coefficient is by definition 1.

is compensated by the electrostatic attraction of the condensed ions. However, since the latter also acts upon the ions which do not touch the rod, the total pressure drops below the ideal gas contribution.

Contrary to the simulations, the osmotic coefficient from the Poisson-Boltzmann theory is always positive. This has led to the general question whether there could be an attraction between like-charged objects within Poisson-Boltzmann theory. Very recently it has been proved that such attractive interactions are absent on the Poisson-Boltzmann level [Neu99]. An extension of this statement to ions of finite size and to a wider class of boundary conditions can be found in Ref. [TrRa]. A fairly general statement in this context is the following: In any local density functional theory, in which the charge density ρ and the electrostatic potential ψ satisfy the inequality $\partial\rho/\partial\psi \leq 0$, the pair interactions are repulsive.
Apart from the phenomenon of a negative osmotic coefficients the remarks which have been made at the monovalent measurements also apply here. The actual $\widehat{p}$ is smaller than the Poisson-Boltzmann prediction, only that this effect is much more pronounced in the multivalent systems. This overestimation of $\widehat{p}$ is again accompanied by an underestimation of counterion condensation, see for instance Tab. 2.2 or Fig. 2.8. The osmotic coefficient converges to the Poisson-Boltzmann result upon dilution, but already at intermediate densities it is surprisingly well described by the Manning limit $1/2\xi v$. Notice finally that contrary to Fig. 2.12 the curves for different valences intersect. The reason for this is the way in which Eqn. (2.46) depends on valence.

Finally it should be noted that the above measurements can not be used to infer that attractive forces between charged rods require the counterions to be at least trivalent. The reason is twofold: First, at given valence one can vary Bjerrum length and line charge density. Increasing the Manning parameter will lead to negative pressure in the divalent system. Second, keeping all interaction potentials fixed, the radius r_0 of the charged rod is a relevant observable, as has been demonstrated in Ref. [GrMa97]. However, a general statement about presence or absence of attractive interactions is difficult, since a five-dimensional parameter space is involved: $\{\lambda, \ell_{\mathrm{B}}, v, r_0, n\}$.

2.5 Realistic examples: DNA and poly(p-phenylene)

Qualitative deviations from Poisson-Boltzmann theory are sometimes very important for real systems. For instance, the zeta potential turns out to be a non-monotonic function of the Manning parameter. This has pronounced influence on the interpretation of electrophoresis experiments.

This section discusses simulations in which the parameters are explicitly mapped to experimental systems. In particular, this mapping affects ion diameter σ, rod radius r_0, Bjerrum length ℓ_{B} and line charge density λ. In order to have a rod radius different from σ this requires the introduction of a new potential for ion-rod interactions, for which a modified truncated and shifted Lennard-Jones potential has been used:

$$V_{\text{ion-rod}}(r) = \begin{cases} 4\epsilon\left[\left(\dfrac{\sigma}{r-r_{\mathrm{s}}}\right)^{12} - \left(\dfrac{\sigma}{r-r_{\mathrm{s}}}\right)^{6} + \dfrac{1}{4}\right] & : \quad 0 < r \leq r_{\mathrm{cut}} \equiv r_{\mathrm{s}} + 2^{1/6}\sigma \\ 0 & : \quad r_{\mathrm{cut}} < r. \end{cases} \tag{2.47}$$

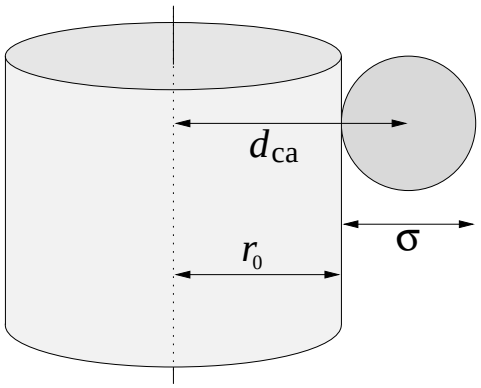

Figure 2.15: Connection between several important length scales. The distance of closest approach, d_{ca}, is the sum of the rod radius r_0 and the ion radius, $\sigma/2$. From Eqn. (2.47) the distance of closest approach, in the sense of the thermal distance already employed for the Lennard-Jones potential, is found to be $d_{\mathrm{ca}} = r_{\mathrm{s}} + \sigma$. Hence, the connection between the translation parameter r_{s} and the rod radius is given by $r_0 = r_{\mathrm{s}} + \sigma/2$.

parameter	symbol	value	value in LJ units
ion diameter	σ	4.25 Å	σ
ion valence	v	2	2
rod radius	r_0	7.86 Å	$1.85\,\sigma$
line charge density (DNA)	λ	$e_0/1.7$ Å	$2.5\,e_0/\sigma$
Bjerrum length (water)	ℓ_{B}	7.14 Å	$1.68\,\sigma$
Manning parameter	ξ	4.2	4.2
box size	L_{b}	122.4 Å	$28.8\,\sigma$
corresponding cell radius	R	69.1 Å	$16.2\,\sigma$
temperature	T	298 K	ϵ/k_{B}

Table 2.5: System parameters for the DNA simulations.

Here, r is the radial distance from the rod axis to the center of the ion and r_{s} is a parameter which shifts the Lennard-Jones potential towards larger r. In Fig. 2.15 its relation to the rod radius is explained. Since these systems have been investigated either in the presence of salt or at rather high Manning parameter, the phenomena happening in the vicinity of the rod are always well decoupled from the cell boundary. Therefore, an even simpler geometry has been chosen for the cell model. The rod has been placed parallel to one of the edges of the cubic simulation cell. This has the advantage that the ion-rod interactions resulting from Eqn. (2.47) can be computed very easily.

2.5.1 Overcharging for DNA-like rods in the presence of salt

The essential parameters used for the DNA-like cell models are summarized in Tab. 2.5. Figure 2.16 shows the distribution functions $P(r)$ and the mean electrostatic potential $\psi(r)$ for six such systems, for which the line charge density, and thereby the Manning parameter, has been successively increased. Two systems have a smaller Manning parameter than DNA and three a larger. Using the classification introduced in Chap. 1.2, all systems are beyond the point up to which the concept of Manning condensation is meaningful. Compared to Fig. 1.6, the distribution functions are already above the gray shaded region. That is, the rod charge is compensated by simple salt screening and no inflection points are present. According to Fig. 1.6, no new remarkable features deep in the salt regime are to be expected. Contrary to that, however, five of the six presented measurements in

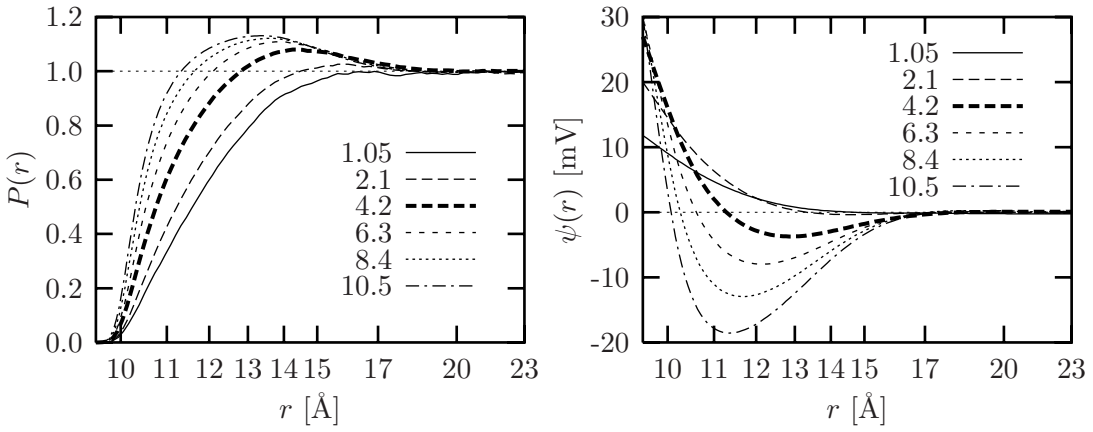

Figure 2.16: Ion distribution function $P(r)$ (left) and mean electrostatic potential $\psi(r)$ (right) for the systems from Tab. 2.5 with 0.49 mol/l added 2:2 salt. The six curves differ in the line charge density of the rod, producing Manning parameters between 1.05 and 10.5 as indicated in the key. The value 4.2 corresponds to DNA. Notice that the radial distance is only plotted up to one third of the cell radius.

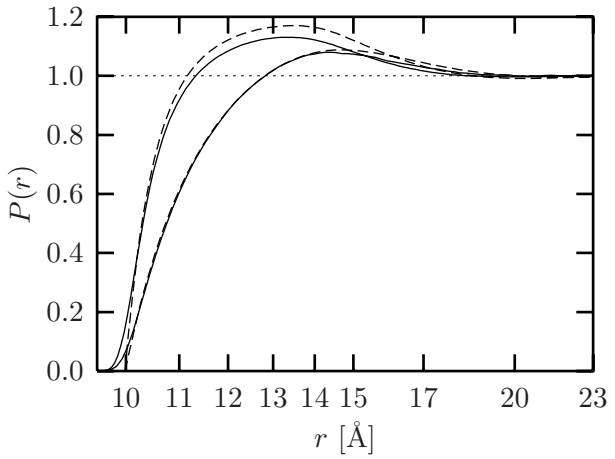

Figure 2.17: Distribution functions $P(r)$ for the systems with Manning parameter 4.2 and 10.5 from Fig. 2.16. The solid lines are the results from the molecular dynamics simulations while the dashed lines are the predictions from hypernetted-chain theory (Felipe Jimenez Angeles, personal communication; see also Ref. [GoLo85]).

Fig. 2.16 show the effect of overcharging, i.e., the rod charge is over-compensated at a certain distance from the rod. Recall the discussion of this phenomenon in the context of generic distribution functions in Sec. 2.3.4. In particular, Fig. 2.11 demonstrates that even in the situation of multiple overcharging the Poisson-Boltzmann theory is unable to account for charge layering.

Integral equation theories give usually much more reliable results at high densities. This is because they appreciate the difference between the potential and the potential of mean force, which is exactly what the Poisson-Boltzmann theory ignores. Figure 2.17 replots two of the distribution functions from Fig. 2.16 together with predictions from hypernetted chain theory in the HNC/MSA approximation[14], as it has been presented in Ref. [GoLo85]. It can be seen that hypernetted-chain theory indeed predicts the occurrence

[14]That is, the ion-cylinder correlations are treated in hypernetted-chain approximation, while the ion-ion correlations are computed within mean spherical approximation.

ξ	ζ_{LPB} [mV]	ζ_{PB} [mV]	ζ_{HNC} [mV]	ζ_{MD} [mV]
0	0	0	0	0
1.05	10.52	10.28	6.262	9.116
2.1	21.04	19.48	10.99	14.62
4.2	42.09	33.32	14.27	16.25
6.3	63.13	42.96	11.08	13.80
8.4	84.17	50.16	3.771	9.263
10.5	105.2	56.03	−6.219	3.675

Table 2.6: ζ-potential of a DNA-sized rod (see Tab. 2.5) immersed into a 0.5 mol/l electrolyte of 2:2 salt as a function of its Manning parameter ξ. The four predictions are from linear Poisson-Boltzmann theory (Eqn. (1.81) in TP 1.7), Poisson-Boltzmann theory (computed with the method introduced in Sec. 1.4), hypernetted-chain theory [GoLo85] and MD simulation. The error in the latter is estimated to be of the order of 2%. Figure 2.18 visualizes the data.

of overcharging, while it slightly overestimates its amount.

Another important phenomenon is indicated by the behavior of the mean electrostatic potential in the right frame of Fig. 2.16. It concerns the value of this potential at the distance of closest approach between ions,

$$\zeta \;=\; \psi(r_0 + \sigma/2), \tag{2.48}$$

which can be identified with the zeta-potential of electrophoresis. This quantity is of importance in the computation of electrophoretic mobilities [Hun87]. Equation (1.81) in TP 1.7 immediately shows that within linearized Poisson-Boltzmann theory of a charged rod within bulk salt ζ depends linearly on ξ. Using the full Poisson-Boltzmann theory leads to the statement that the increase is rather sub-linear but still monotonic. However, Fig. 2.16 suggests the following phenomenon. The presence of overcharging effects shows that the mean electrostatic potential can also decrease upon approaching the rod. This calls the monotonic relation between ζ and ξ into question. Table 2.6 summarized various predictions for the ζ-potential as a function of Manning parameter together with results from the molecular dynamics simulations. A graphical illustration is given in Fig. 2.18. Indeed, ζ is found to first increase with ξ, but from a certain value on it decreases and would finally even become negative. Note that this would reverse the drift direction in electrophoresis measurements. While nonlinear and linearized Poisson-Boltzmann theory coincide with the data and with each other for small Manning parameter, they completely fail to predict the back-bending, which already sets in at comparatively small values of ξ. Hypernetted-chain theory captures this effect, but it underestimates the value of the potential. This is how an overestimated condensation, appears on the level of the potential, see Fig. 2.17. In any case, the success of hypernetted-chain theory indicates that local ionic correlations are responsible for both phenomena.

Finally, one might ask the question how the effect of overcharging depends on salt concentration. Obviously there cannot be any overcharging in the absence of salt, since then even a complete condensation of all ions would merely neutralize the rod. However, it is not clear from the beginning whether an addition of just *some* salt will immediately

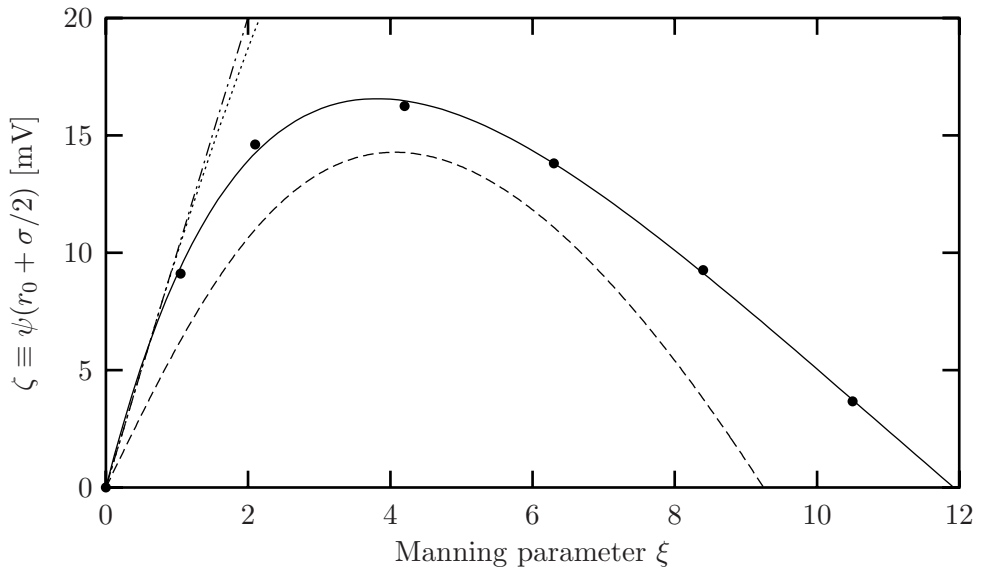

Figure 2.18: Zeta potential $\zeta \equiv \psi(r_0 + \sigma/2)$ as a function of Manning parameter for the DNA like models from Tab. 2.5 with 0.5 mol/l added 2:2 salt. The dotted line is the prediction of Poisson-Boltzmann theory (computed with the method introduced in Sec. 1.4), the dash-dotted line is from bulk Debye-Hückel theory (Eqn. (1.81) in TP 1.7) and the dashed line is the result from a hypernetted-chain calculation [GoLo85]. The solid line is a fit which merely serves to guide the eye.

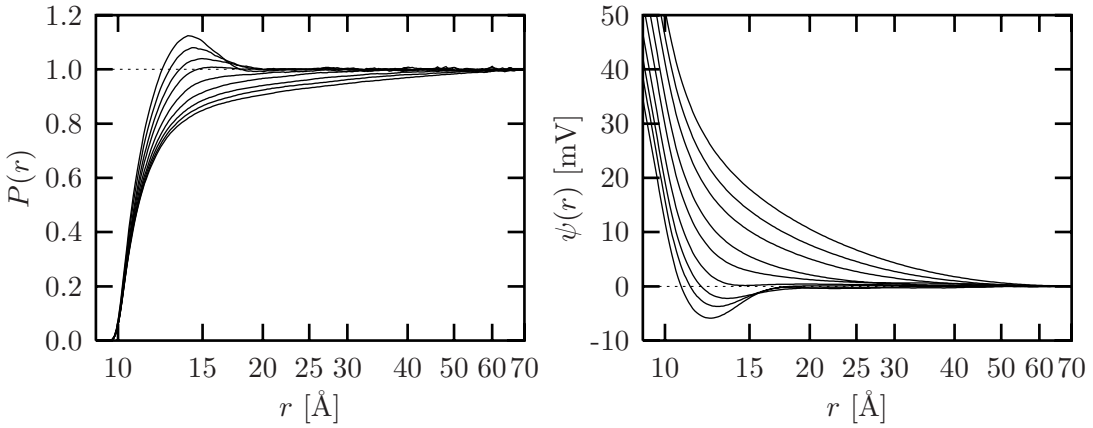

Figure 2.19: Ion distribution function $P(r)$ (left) and mean electrostatic potential $\psi(r)$ (right) for the systems from Tab. 2.5 with Manning parameter $\xi = 4.2$. The 9 curves correspond to different number N_s of 2:2 salt molecules added to the box: $N_s \in \{8, 17, 34, 68, 135, 270, 380, 540, 760\}$. In the distribution function the salt content increases from bottom to top, in the mean electrostatic potential it increases from top to bottom.

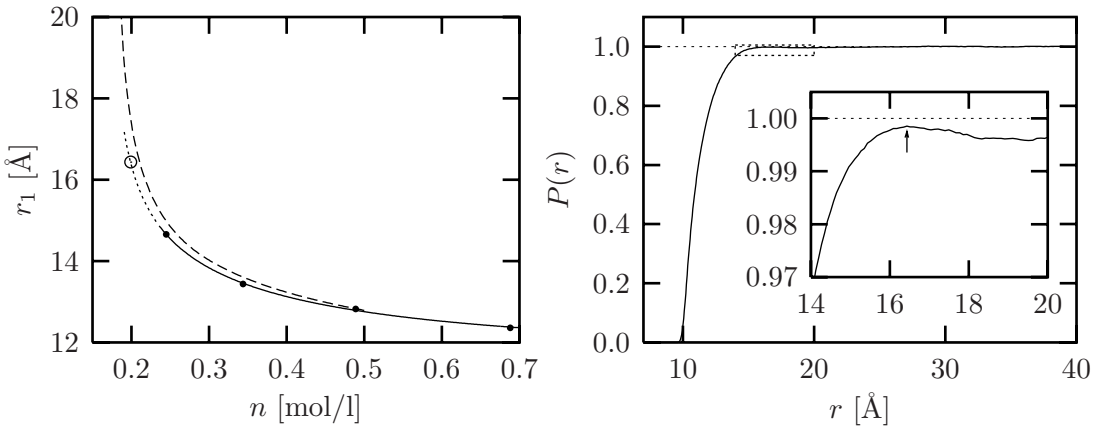

Figure 2.20: Left part: Radius r_1 from Eqn. (2.49) at which overcharging sets in for a DNA-sized and charged rod as a function of salt concentration n. The dots are results of molecular dynamics simulations while the dashed line is the prediction of hypernetted-chain theory (Felipe Jimenez Angeles, personal communication). The open circle results from a very long run ($90\,000\,\tau_{\mathrm{LJ}}$) of a system at 0.199 mol/l, and its $P(r)$ together with a magnification of the relevant part is shown in the right frame. The point where it almost touches the line $P = 1$ is taken as r_1. The solid line and its dotted continuation in the left frame is a fit which merely serves to guide the eye. Given the surprising back-bending of $P(r)$ in the right frame *before* it crosses the electroneutrality line, the dotted part should actually be replaced by a curve, which ceases roughly at 0.2 mol/l.

lead to overcharging. Figure 2.19 shows simulated distribution functions $P(r)$ and mean electrostatic potentials $\psi(r)$ for a cell model with a DNA-sized and -charged rod ($r_0 = 7.86\,\text{Å}$, $\lambda = e_0/1.7\,\text{Å}$), divalent counterions and varying amount of additional 2:2 salt. The phenomenon of overcharging is indeed observed, but only at sufficiently high salt concentration. This may be illustrated by defining r_1 to be the radius at which overcharging sets in, i.e.,

$$r_1 \ = \min \big\{ r : \ P(r) = 1 \big\}. \tag{2.49}$$

Fig. 2.20 illustrates the measured r_1 together with a hypernetted-chain prediction as a function of salt concentration n. Clearly, r_1 must increase with decreasing n, since overcharging is reduced and consequently the size of the charge-compensating layer must increase. In fact, hypernetted-chain theory predicts that $r_1(n)$ diverges at some *finite* density $n^* \approx 0.18$ mol/l corresponding to a salt Debye length of 3.59 Å, or roughly 200 salt molecules within the simulation box. The simulated values lie below the hypernetted-chain prediction, but this is not a feature generally to be expected. In Fig. 2.17 it can be seen that the stronger condensation in hypernetted-chain theory should normally lead to a value of r_1 being smaller than in the simulation. To explain this seeming contradiction, it must be noted that with decreasing density the finite radius of the simulation cell becomes relevant. Indeed, the low-salt distribution functions in Fig. 2.19 reach the value 1 essentially at cell boundary. A reduction of the amount of added salt at fixed cell radius must necessarily lead to values of r_1 being smaller than the hypernetted chain prediction for the bulk, since within a finite cell r_1 cannot diverge. The source of this problem is that a sound comparison with a bulk prediction requires the number of counterions to be much

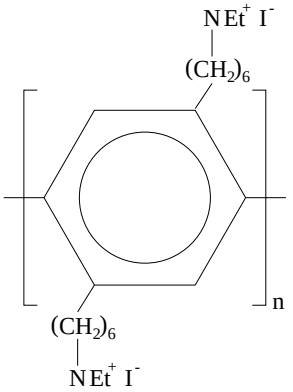

Figure 2.21: Constitution formula for poly(p-phenylene). The fully aromatic backbone exhibits an excellent chemical stability and has a persistence length of approximately 20 nm. The degree of polymerization used in the studies in Ref. [GuBl, BlWi] was located between 20 and 40, so that the contour length equals approximately one persistence length at most. The dominant contribution to the signal in small angle X-ray scattering experiments stems from the iodine ions, since the excess electron density of the backbone is very low.

smaller than the number of salt molecules.

An intriguing phenomenon can be observed in the simulation at the density 0.2 mol/l. This corresponds to 220 salt molecules within the box, which is only 10% larger than the estimation for n^* from hypernetted-chain theory. The distribution function $P(r)$ of this system shows a back-bending clearly before it crosses the line $P = 1$, see right frame in Fig. 2.20. Although Fig. 2.11 suggests that overcharging goes along with damped charge oscillations converging symmetrically towards 1, it may also be that there are asymmetric oscillations, i.e., there is a maximum in $P(r)$ but it remains below 1. If this is true, an alternative scenario for the fate of overcharging upon dilution opens up. There still exists a critical density n^*, but instead of diverging, r_1 remains finite but with an infinite slope at n^*. However, independent on the scenario, the determination of n^* by simulation is rather involved, since close to n^* the distribution function $P(r)$ will intersect the neutrality line $P = 1$ in a very acute angle, leaving the determination of r_1 prone to a fairly large error. In any case, the presented simulations have not been able to unambiguously detect overcharging at densities equal to or lower than 0.2 mol/l.

Observe finally that the very existence of such an n^* predicted by hypernetted-chain theory should be taken with a grain of salt. This is a statement concerning a low density region, for which integral equation theories are not constructed and hence not as trustworthy as for high densities. On the other hand, any potential overcharging remaining at low densities would be of such a tiny degree that for all practical purposes its presence would be irrelevant. Whether or not there is a distance far away from the rod, at which the rod charge is completely neutralized is first and foremost an academic problem.

2.5.2 Distribution functions and osmotic coefficient for salt free poly(p-phenylene) solutions

The Manning limiting laws are claimed to apply in the limit of low density. However, an experimental verification of this effect using DNA as rod-like polyelectrolytes is difficult. This is not just a consequence of the usual contrast problems in scattering experiments or the difficulties of keeping a dilute solution salt-free. Rather, at low ionic strength the double helix starts to unwind. It would therefore be desirable to have a stiff model polyelectrolyte which does not suffer from this problem. One such system belonging to the class of poly(para-phenylenes) (ppp) has recently been investigated in Refs. [GuBl, BlWi]. A constitution formula is given in Fig. 2.21 and Tab. 2.7 lists four systems which have been simulated based on a mapping to ppp.

system	c [g/l]	T [°C]	ξ	σ [Å]	d_{ca} [Å]	R [Å]
1	1.5	40	3.4	7.9	4.4	239.3
2	1.5	40	6.8	8.1	4.4	292.0
3	19.95	25	3.32	7.9	4.4	65.6
4	17.99	25	6.64	8.1	4.4	84.3

Table 2.7: Mapping for four poly(p-phenylene) systems. Tabulated are polyelectrolyte concentration c, temperature T, Manning parameter ξ, ion diameter σ, distance of closest approach d_{ca} between ions and the rod and cell radius R corresponding to the given concentration. The experiments have been performed under salt-free aqueous conditions with monovalent counterions [GuBl].

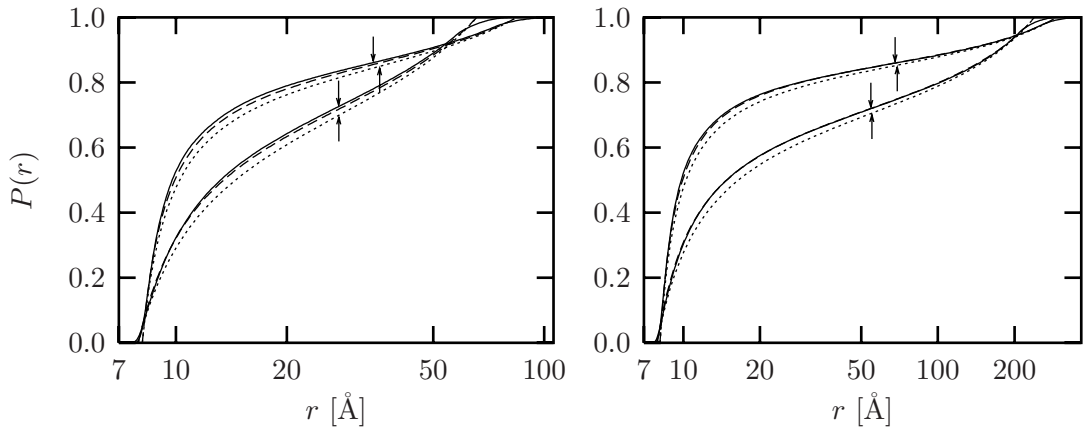

Figure 2.22: Distribution functions for the 4 poly(p-phenylene) systems from Tab. 2.7. Left/right frame correspond to the high/low density systems (3,4)/(1,2), while the upper/lower set of functions correspond to the strongly/weakly charged systems (2,4)/(1,3) respectively. Solid lines are the results of simulation, dotted lines are the Poisson-Boltzmann prediction and dashed lines are from a extended Poisson-Boltzmann theory using the Debye-Hückel-hole-cavity correction from Sec. 1.3.2, computed with the method proposed in Sec. 1.4. The ↑-arrows indicate the inflection points in the Poisson-Boltzmann distributions, while the ↓-arrows mark those points in the simulated distributions. The deviations of the latter from the Poisson-Boltzmann curves at large r originate from the simulation cell having a quadratic instead of a circular cross section.

In a first step the simulated ion distribution functions shall be compared with the Poisson-Boltzmann prediction as well as with an extended Poisson-Boltzmann theory using the Debye-Hückel-hole-cavity correction functional from Sec. 1.3.2. Figure 2.22 shows the corresponding distribution functions for the systems from Tab. 2.7. Qualitatively the Poisson-Boltzmann prediction is already a good description of those systems, if one graciously disregards the inevitable problems at the cell boundary. However, the presence of correlations shifts the distribution functions up in all four cases. Since this shift is rather small, i.e., the correlations are weak, the Debye-Hückel-hole-cavity theory is in fact an excellent description of those systems. Observe, for instance, that in the weakly charged dilute case its prediction can no longer be distinguished from the simulated curve on the

system	$R_{\mathrm{M,PB}}$ [Å]	$f_{\xi,\mathrm{PB}}$	$R_{\mathrm{M,DHHC}}$ [Å]	$f_{\xi,\mathrm{DHHC}}$	$R_{\mathrm{M,MD}}$ [Å]	$f_{\xi,\mathrm{MD}}$	$\xi_{\mathrm{eff,MD}}$
1	55.138	0.7059	53.60	0.718	54.58	0.720	3.67
2	69.263	0.8529	66.38	0.858	67.98	0.860	7.11
3	27.695	0.6988	27.72	0.718	27.63	0.726	3.65
4	35.718	0.8494	35.24	0.858	34.35	0.861	7.19

Table 2.8: Manning radius R_{M} and condensed fraction f_ξ for the four poly(p-phenylene) systems from Tab. 2.7. Shown are the Poisson-Boltzmann (PB), extended Poisson-Boltzmann (DHHC) and molecular dynamics (MD) results. For the latter also an effective Manning parameter $\xi_{\mathrm{eff}} = 1/(1 - f_\xi)$ is displayed. The quantification of counterion condensation has been achieved via the inflection point criterion from Sec. 1.1.3.

chosen scale.

With the help of the condensation criterion from Sec. 1.1.3 the extent of the correlation-enhanced condensation can be further quantified. Table 2.8 thus collects measured values for Manning radii and condensed fractions. The Manning fraction from the molecular dynamics simulation increases only by a fairly small amount. It is at most 4% larger than the Poisson-Boltzmann value. This translates to an effective Manning parameter $\xi_{\mathrm{eff}} = 1/(1 - f_\xi)$ being 5–10% larger than the bare one. This increase is very accurately captured by the Debye-Hückel-hole-cavity theory. Its prediction for f_ξ is at most 1% smaller than the value obtained in the simulation. Interestingly, it is even independent of density. This, however, is not a feature to be generally expected and should therefore not be over-interpreted. Note also that for the dilute systems the molecular dynamics and Debye-Hückel-hole-cavity prediction for the Manning radius is smaller than in the Poisson-Boltzmann case, while for the dense systems the situation is less conclusive. A situation which has been found in the generic systems discussed in Sec. 2.3.1 as well.

In a second step the osmotic coefficients of the four model systems have been computed. Two distinct approaches have been used for analyzing the simulation results: The first one follows Sec. 2.4.1 and computes the pressure from the stress tensor.[15] The second approach exploits the connection from Eqn. (2.45) between osmotic coefficient, Manning parameter and the integration constant γ of the Poisson-Boltzmann equation. The idea is to use the fitting procedure described in Sec. 2.3.2 and from that obtain values $\xi^\star$ and $\gamma^\star$, leading to the osmotic coefficient $(1+\gamma^{\star 2})/2\xi^\star$.[16] For comparison, also the predictions from the Manning limiting law, the full Poisson-Boltzmann expression and results following from the Debye-Hückel-hole-cavity theory are calculated. In the latter case the osmotic coefficient is calculated from the ideal gas contribution at the cell boundary and an additional correlation correction. For this the zero temperature complete screening term in Eqn. (2.44) as derived in TP 2.3 has been used as an approximation to the corresponding Debye-Hückel-hole-cavity expression, which cannot be written down analytically due to the complicated integral involved in the formula for the free energy density. The inclusion

[15] In this case, however, a rotation of the stress tensor is not necessary, since the rods already point in the z-direction. The pressure is thus given by the average of the xx- and yy-components.

[16] The most straightforward approach of measuring the boundary density is less recommendable, since in the simulation the boundary has a quadratic and not a circular cross section, i.e., the merely approximate representation of the cell model becomes most visible and questionable here. In contrast to that, the two other approaches "look" at regions of the cell, which are away from the boundary.

system	$\widehat{p}_{\mathrm{M}}$	$\widehat{p}_{\mathrm{PB}}$	$\widehat{p}_{\mathrm{DHHC}}$	$\widehat{p}_{\mathrm{MD,1}}$	$\widehat{p}_{\mathrm{MD,2}}$	$\widehat{p}_{\mathrm{exp}}$
1	0.1471	0.2128	0.199	0.2005(57)	0.201	0.185(15)
2	0.0735	0.1073	0.101	0.1003(60)	0.102	0.073(15)
3	0.1506	0.2848	0.251	0.2424(57)	0.260	—
4	0.0753	0.1428	0.126	0.1215(56)	0.129	—

Table 2.9: Osmotic coefficient of the four poly(p-phenylene) systems from Tab. 2.7. Shown are the Manning limiting law (M), the Poisson-Boltzmann prediction, the extended Poisson-Boltzmann prediction using the Debye-Hückel-hole-cavity correlation functional with the pressure obtained along the lines of TP 2.3, the simulation result using the stress tensor (MD,1), the simulation result using a Poisson-Boltzmann fit as described in Sec. 2.3.2 (MD,2) and results from measurements on this system using osmometry (exp).

of this correction leads to a further reduction of the osmotic coefficient by 2–6% and should thus be taken into account. For the two dilute systems there also exist measurements[17] of $\widehat{p}$ via osmometry, while for the dense systems this was unfortunately impossible due to counterdiffusion problems. Table 2.9 collects the coefficients for comparison.

The first thing which should be noted is that Poisson-Boltzmann theory gives again a surprisingly good description of the measured coefficients, including the experimentally determined one. A closer look reveals that – as expected – it overestimates $\widehat{p}$, and the deviations are larger for the dense systems. Still, Poisson-Boltzmann theory is off by only 7% or 18% for the dilute or dense systems, respectively, thereby confirming the observation already made when looking at the distribution functions. A further indication of this point is that the Manning limit $1/2\xi$ appears to be a lower boundary, which is also in accord with the pressure measurements on the generic systems with monovalent ions from Sec. 2.4.2. Since there it has also been found that the Manning limit need no longer act as a boundary in the multivalent case, see Fig. 2.13, it would be very interesting to perform experiments on those systems with, e.g., divalent ions. Observe that the experimental value of $\widehat{p}$ for the highly charged dilute system 2 is already at the Manning limit. It must, however, be mentioned that during the measurement of this particular value some problems with counterdiffusion in the membrane osmometer have been suspected, which in effect would make the value appear somewhat to small.

Since the experimentally determined osmotic coefficient appears to be smaller even than the molecular dynamics results, this indicates effects to be relevant which go beyond the model used for simulation. Most obvious candidates for this are the neglect of additional chemical interactions between the ions and the polyelectrolyte as well as solvation effects, i.e., interactions between the ions or the polyelectrolyte with the water molecules from the solution.[18] It is for instance demonstrated in Ref. [BlWi] that the osmotic coefficient also depends on whether on uses chlorine or iodine counterions. While one could certainly account for the different radii of these ions when computing the distance of closest approach entering the Poisson-Boltzmann equation, the implications of the different hydration energies is much less obvious to incorporate and in principle requires very

[17] Jürgen Blaul, personal communication. See also Ref. [BlWi].

[18] Recall that in the simulation the solvent appears only in two places: *(i)* as a viscous thermal background in the Langevin thermostat, see Eqns. (2.10,2.11), and *(ii)* by its value of the dielectric constant, $\varepsilon_{\mathrm{r}} \approx 78.5$ in the aqueous case.

system	ξ	R [Å]	$r_0^\star$ [Å]	R_{M}^* [Å]	γ^*	$\widehat{p}^*$
3	3.32	65.6	8.2	28.19	0.957	0.289
4	6.64	84.3	9.9	39.14	1.014	0.153

Table 2.10: Fit evaluation of small angle X-ray scattering experiments on the systems 3 and 4 from Tab. 2.8. ξ is the Manning parameter, R the cell radius implied by the polyelectrolyte concentration, and $r_0^\star$ the rod radius, which had been the only fitting parameter. From this, the integration constant γ^* and the Manning radius R_{M}^* is determined from the solution of the Poisson-Boltzmann equation. $\widehat{p}^* = (1+\gamma^{*2})/2\xi$ is the attempt to predict the osmotic coefficient of the solution with the help of the Poisson-Boltzmann formula.

expensive all-atom simulations.[19]

Finally it should be noted that the two different methods of analyzing the molecular dynamics data lead to very similar results. While this fact is not particularly useful in a simulation, its consequences for the analysis of experimental data seem promising. In Ref. [GuBl] poly(p-phenylene)-solutions are investigated by means of small angle X-ray scattering, which due to the rod-like geometry turns out to be sensitive to the radial ion distribution function. Therefore, the measured structure factors can be related to Poisson-Boltzmann distribution functions with effective values of ξ, γ etc. Fitting the scattering intensity and thereby determining those values permits in principle a measurement of the osmotic coefficient along the lines already described above. What makes this approach so attractive is that it could ideally complement osmometry. If the density becomes too large, the latter suffers from severe problems with counterdiffusion, but it is exactly this high density which meets the requirements of good contrast necessary for scattering.

A similar fitting procedure has been applied to the measured data from small angle X-ray scattering experiments on the systems 3 and 4 from Tab. 2.8.[20] From a fit to the structure factor the radius $r_0^\star$ of the rod has been determined. The integration constant γ^* and the Manning parameter R_{M}^* then follow from the Poisson-Boltzmann theory. The obtained values are listed in Tab. 2.10. The resulting Manning radius is surprisingly close to the one determined by simulation, particularly for the system with $\xi = 3.32$. The osmotic coefficients constructed from the Poisson-Boltzmann formula are less accurate, 10-20% too large. It would be interesting to observe the effects of introducing more free parameters, similar to the procedure described above, in order to reduce the "Poisson-Boltzmann-bias".

2.6 The quest for correlations

With the complete knowledge of the microstate within a molecular dynamics simulation one can in principle determine arbitrary correlation functions. This permits an identification of the deeper reasons underlying the failure of Poisson-Boltzmann theory.

Up to now the following observation repeatedly turned up from the simulations. The nonlinear Poisson-Boltzmann equation provides a fairly good description of the cell model,

[19] On such a detailed level of description even measuring the solvation energy within a simulation can be a tricky thing, since the computed numbers are sensitive to the boundary conditions and approximations made in the treatment of electrostatic interactions, see for instance Ref. [HüMc99].

[20] Birgit Guilleaume, personal communication; see also Ref. [GuBl].

but it suffers from systematic deviations in strongly coupled or dense systems. It underestimates the extent of counterion condensation and at the same time overestimates the osmotic coefficient. As the common reason for both problems the neglect of correlations has been proposed, basically for two reasons:

1. The circumstances of the failure – strong coupling and high density – are the situations in which correlations are expected to be important. Furthermore, the effects are just what one would intuitively be inclined to ascribe to correlations.[21]

2. More elaborate theories [GoLo85, DaBr95, BaDe] which try to incorporate correlations reproduce the trends of the simulations. Observe for instance that the correlation corrections for the free energy discussed in Sec. 1.3 favor an increase in density. At the presence of a charged macroion this will preferably take place close to its surface, thereby leading to a stronger condensation and a concomitant drop in the boundary density and thus pressure.

However, the present situation is at a halfway stage. On the one hand there is general agreement about the presence of correlations being liable for the failure of Poisson-Boltzmann theory. On the other hand, this insight does not shed any light onto the question, which kind of correlations are important. All one knows from Poisson-Boltzmann theory is that it incorporates *none* of them, since it makes no difference between the potential and the potential of mean force, see Rem. 1.1.1.1. The purpose of integral equation theories is to derive analytic expressions for higher order correlation functions. However, there is no prior prescription for the "correct" closure equation to be used for decoupling the hierarchy of n-point correlation functions, see, e.g., Chapter 13 in Ref. [McQ76]. Therefore the underlying physics is often shrouded in mystery. The correlation correction from Sec. 1.3 uses a one-component plasma model and its Debye-Hückel approximation as an additional contribution to the free energy resulting from individual ion-ion interactions. Yet, in the present version it is unable, even after the inclusion of a hard core, to predict ionic layering in situations in which the simulation proves them to be present. Above that, it gives no access to ionic correlation functions.

In such a situation computer simulations can be enormously helpful. One of their main advantages is that they do not just produce statistical averages of tremendously coarse-grained thermodynamic observables, e.g., energy or pressure. Rather, a simulation often has *complete* knowledge of the microstate of a system, sometimes even as a function of time. If one knows where all ions are and if one has ways to average, on has access to basically all kinds of correlation functions. This section discusses two of them.

2.6.1 The condensed layer as a strongly coupled liquid

If the surface charge density of the rod is high, a fairly large number of counterions will stay within a condensed layer of small radial extent. Addition of salt will further increase the ionic density in this layer. It is clear that beyond a certain point (high λ, high ℓ_B or enough salt) the ions will no longer distribute independently of each other but get locally

[21] At high density also the neglect of an ionic hard core is definitely on the agenda. However, one would rather believe that its presence tends to reduce condensation and increase the pressure. This is also suggested by the hard core correction for the pressure in density functional theories, see TP. 1.3.3.

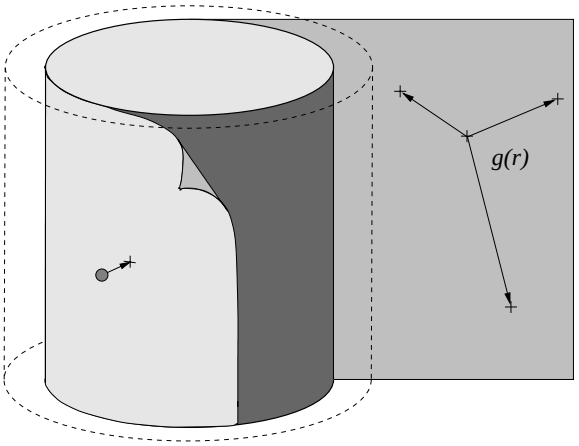

Figure 2.23: Illustration of the computation of surface correlations. Counterions within a certain small distance from the rod constitute the innermost condensed layer. Their coordinates are radially projected onto the surface, which after that is unrolled to a flat plane. The two-dimensional pair correlation function $g(r)$ is then determined from the projected points.

correlated. This effect will now be measured for the DNA-sized models from Sec. 2.5.1, for which 0.5 mol/l of a 2:2 salt has been added in excess to the divalent counterions.

The first issue is to define the innermost layer. For this, a distance from the rod is chosen which contains many counterions but virtually no coions. A distance of roughly 11.5 Å from the rod axis turned out to be quite suitable. This is about a third ion diameter farther out than the distance of closest approach. To avoid difficulties with remaining coions, only the counterions within this distance are taken into account in all what follows. In a second step the coordinates of those ions are radially projected onto the surface of the cylinder of closest approach, and this surface is then rolled out to a flat plane, see Fig. 2.23 for an illustration of this procedure. Finally, the two-dimensional pair correlation function $g(r)$ of these projected points is computed.

One might object that the unrolled flat plane leads one to believe that the pair correlation function does only depend on distance, while in reality such a rotational symmetry cannot be expected, due to the anisotropic rod curvature. However, an investigation of $g(\boldsymbol{r})$ revealed that the pair correlation function is in fact rotationally symmetric up to essentially a distance which corresponds to half the circumference of the cylinder of closest approach, which is roughly 30 Å. Larger distances can of course only be realized along the rod instead of around it. A possible reason for this surprising symmetry is that at short distances the curvature is not yet perceptible while at large distances the particles are already uncorrelated.

Figure 2.24 shows the thus measured $g(r)$ for the four most strongly charged systems from Fig. 2.16 and Tab. 2.11 summarizes a few characteristics of it. The most important thing to observe is that for the strongly charged systems $g(r)$ shows definite signs of correlations. Apart from the trivial correlation hole at small r there is a distance $r_{\max}$ at which ions are more likely to be found than under the assumption of independent distribution. Notice that the maximum in $g(r)$ is not located at $r \approx \sigma$ but much farther out. Hence, its existence is not merely an artifact of close packing of repulsive Lennard-Jones spheres. However, if the condensed ions are assumed to form a triangular lattice on the surface in order to maximize their mutual repulsion, the resulting distance $d_\triangle$ is markedly larger than $r_{\max}$. Together with the only weakly pronounced oscillations in $g(r)$ this proves the correlation induced interactions to be rather short-ranged, yet less local than a pure hard core. In any case, the range is several times larger than the average salt Debye length $\ell_{\mathrm{D}} \approx 0.5\,\sigma$.

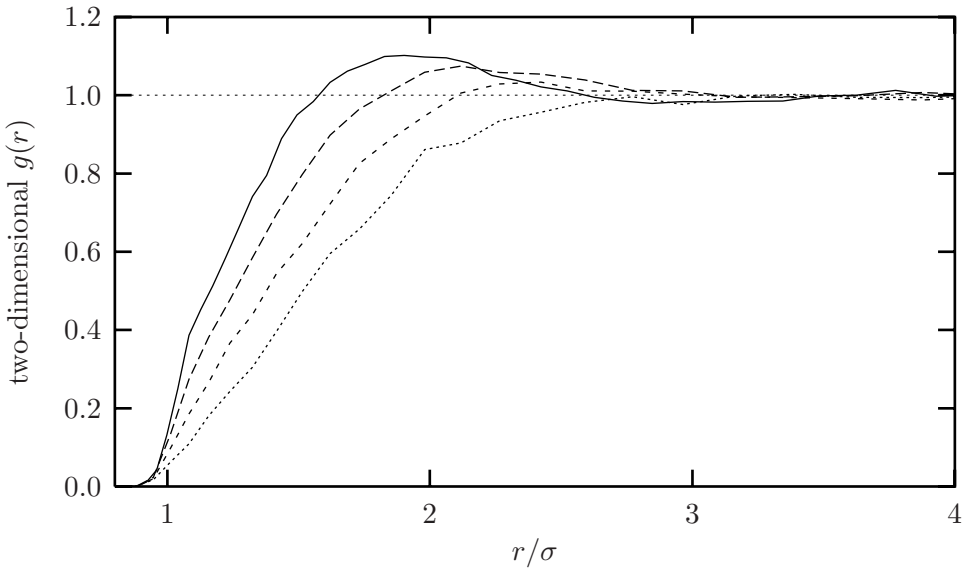

Figure 2.24: Two-dimensional pair correlation function $g(r)$ for the projection of counterions within a close condensed layer onto the cylinder of closest approach, see text and Fig. 2.23. The four functions belong to the most strongly charged systems in Fig. 2.16. From solid to dotted the Manning parameter decreases as 10.5, 8.4, 6.3 and 4.2. The last value corresponds to DNA.

ξ	r_l/σ	$N_+(r_\mathrm{l})$	$N_-(r_\mathrm{l})$	N_+^0	$d_\triangle/\sigma$	d_ς/σ	r_max/σ	$\bar{n}_+$ [mol/l]
4.2	2.75	29.5	0.69	36	4.120	3.473	—	3.1
6.3	2.70	47.7	0.32	54	3.244	2.836	2.4	5.7
8.4	2.65	66.0	0.15	72	2.757	2.456	2.2	9.1
10.5	2.65	88.3	0.08	90	2.383	2.197	1.9	12

Table 2.11: Some specifications of the condensed layer of the four systems from Fig. 2.24. The length r_l is the radial extend of the layer, $N_+(r_\mathrm{l})$ the average number of enclosed positive counterions, $N_-(r_\mathrm{l})$ the average number of negative coions and N_+^0 is the number of positive ions required for neutralizing the rod, always assuming valence $v = 2$. If the positive ions were to form a triangular lattice, the corresponding lattice constant would be $d_\triangle$, and $d_\varsigma = (2e_0/\varsigma)^{1/2}$ is the average distance of N_+^0 positive and 2-valent ions on the surface with surface charge density ς. Those two should be compared to r_max, which is the actual position of the maximum in $g(r)$. For the system with $\xi = 4.2$ this value is immeasurable. The last column lists the average molar counterion concentration $\bar{n}_+$ within the layer. Note that in these systems the Debye length of the salt is $\ell_\mathrm{D} \approx 0.5\,\sigma \approx 2.2\,\text{Å}$.

Such two-dimensional pair correlation functions for mobile ions adsorbed on charged planes have recently been investigated theoretically in Ref. [RoBl96]. The mean separation $d_\varsigma = (ve_0/\varsigma)^{1/2}$ of v-valent ions on the completely neutralized plane of surface charge density ς is identified as the important scaling length. The main predictions for the strongly coupled regime $\Gamma_2 := \ell_\mathrm{B} v^2/d_\varsigma > 1$ are: *(i)*, $g(r)$ should have a single first peak at a distance about the size d_ς of the correlation hole. *(ii)*, the breadth of this peak should decrease with Γ_2 while its maximum should increase. This trend is indeed seen to be true for the functions in Fig. 2.24, only d_ς is roughly 10–20% larger than the actual peak position.

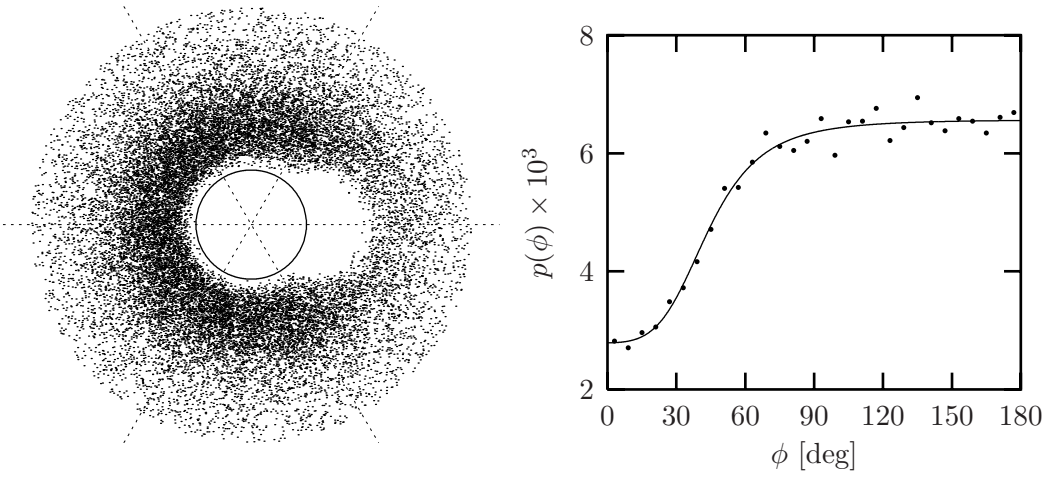

Figure 2.25: Left part: Density plot of the 3-point correlation function $g_{\rightarrow}(\boldsymbol{r})$ for the highest charged system from Fig. 2.24 with Manning parameter $\xi = 10.5$. If an ion is located at the origin and its *nearest* neighbor is on the right side and not further away than $1.3\,\sigma$, its *next nearest* neighbor is shown as a dot. The circle around the origin has radius σ and corresponds to the distance of closest approach imposed by the Lennard-Jones hard core. The right frame plots the probability distribution of finding the next nearest neighbor at an angle ϕ with respect to line joining nearest neighbor and origin. The solid line is a guide to the eye.

One might want to argue that the presence of much salt entails a further increase of the layer density on top of the usual Gouy-Chapman prediction, see TP. 1.8, but the results obtained in Ref. [RoBl96] are claimed to be independent of the bulk ionic strength $\frac{1}{2}\sum_i n_i v_i^2$, if the latter is smaller than the layer density $\bar{n}_+$. Tab. 2.11 shows this to be the case, even though not always by an order of magnitude. An alternative explanation may be based on the presence of coions: Although there reside very few of them within the innermost condensed layer, there will be an appreciable amount beyond and possibly very close to r_1. Those ions can act as "bridges", they attract counterions and thereby reduce the average closest distance between them.

Although $r_{\max} < d_{\triangle}$, this does not exclude a local hexatic ordering of the counterions. But since $g(\boldsymbol{r})$ is on average rotationally symmetric, establishing signs for this requires the investigation of a suitable 3-point correlation function. The trick is to break the rotational symmetry, which suggests the following procedure: $g(r)$ is proportional to the probability of finding a particle at a distance r, given that there is also a particle at the origin. Now define $g_{\rightarrow}(\boldsymbol{r})$ to be proportional to the probability of finding a particle at position $\boldsymbol{r}$, given that there is also a particle at the origin *and* given that the particle which is closest to the origin is situated to the right side. This definition is further restricted to be sensitive only for next nearest neighbors and not arbitrary other particles. Thence, it answers the question: "If the nearest neighbor is on the right side, where is the next nearest neighbor?" A density plot of this observable is shown in the left part of Fig. 2.25. For this, the most highly charged DNA-sized system with Manning parameter $\xi = 10.5$ has been used. Clearly visible are the two correlation holes around the origin and the nearest neighbor as well as a tendency of the next nearest neighbor to be on the side opposing the nearest neighbor. All those effects are trivially explained. However, on top of that no preferential ion accumulations in the "hexatic directions" indicated as dotted lines is

perceptible. The right part of Fig. 2.25 shows the probability distribution of finding the next nearest neighbor at an angle ϕ with respect to the line joining nearest neighbor and origin. The correlation hole generated by the nearest neighbor is visible, but no increase in $p(\phi)$ at 60°, 120° or 180°. Rather, the measured data are compatible with a fairly structureless distribution, as indicated by the solid line.

Since the most strongly charged system does not show hexatic order, it will certainly be absent in the other ones. However, the coupling constant Γ_2 introduced above has a value only about 3 in the system with Manning parameter $\xi = 10.5$. For larger values of Γ_2 one would not only expect much stronger correlations and hexatic ordering but even crystallization of the adsorbed counterions into a two-dimensional Wigner crystal [RoBl96, Shk99].

2.6.2 The three-dimensional $\mathbf{g(r)}$

If the radius r_0 of the charged rod is small, its surface is bent very much and renders the formation of a two-dimensional correlated layer rather doubtful. In fact, Ref. [Shk99] suggests that in the case $r_0\lambda \ll ve_0$, or alternatively $r_0/\ell_B \ll v/\xi$, ions will more likely form a three-dimensional correlated structure on the background of the rods, which for high enough coupling can be described as a Wigner crystal. For the generic models investigated in Sec. 2.3 this will be tested here by computing the usual three-dimensional pair correlation function $g(r)$. Before that, a few general remarks are appropriate.

If the ions form a three-dimensional crystal structure, there will be a typical minimum distance between ions depending on density. Assuming hexagonal closed packing[22], the volume per ion is given by $d_{\mathrm{hcp}}^3/\sqrt{2}$, where d_{hcp} is the minimum ion distance. As a function of density it is therefore given by

$$d_{\mathrm{hcp}} = (\sqrt{2}/n)^{1/3} \tag{2.50}$$

and varies with the *third* root of density. There is, however, another important length scale in the system, which is the separation of the rods. Assuming a system like in Fig. 2.4 with one rod of line charge density λ placed along the main diagonal of a cubic box of length L_b, the following relations hold. In TP. 2.1 the separation of rods is shown to be $d_{\mathrm{rod}} = L_b\sqrt{2/3}$. Furthermore, the total number of ions is $\sqrt{3}L\lambda/ve_0$, giving a density $\sqrt{3}\lambda/L^2ve_0$ which varies inversely to L^2 instead of L^3. As a consequence, the separation of the rods as a function of ionic density is given by

$$d_{\mathrm{rod}} = (2\lambda/\sqrt{3}ve_0n)^{1/2}, \tag{2.51}$$

which varies with the *second* root of density. Hence, whatever the details of the actual structure are, if one measures a new characteristic length varying like $n^{1/3}$, it can be viewed as a bulk crystal property, while a length varying with $n^{1/2}$ is rod-imposed.

Since the correlations are expected for dense systems, only those have been investigated. Moreover, in the dilute case the three-dimensional $g(r)$ would be too much dominated by the one-dimensional contribution resulting from the strong condensation along

[22] For the generic models this would be compatible with the hexagonal symmetry along one direction imposed by the rods, with which the Wigner crystal has to arrange.

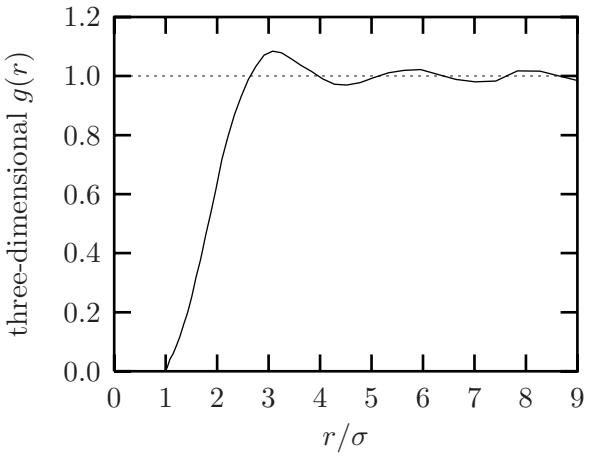

Figure 2.26: Three-dimensional $g(r)$ for the generic system from Tab. 2.4 with trivalent counterions at a density of $0.04247\,\sigma^{-3}$. Clearly visible is a structure pointing to local arrangements of the ions, for which the position of the first maximum is taken as a characteristic length.

$v = 2$			$v = 3$		
N, p	$n\,\sigma^3$	$r_{\max}/\sigma$	N, p	$n\,\sigma^3$	$r_{\max}/\sigma$
4.5, 4	1.133×10^{-1}	2.35	4.5, 4	7.550×10^{-2}	2.42
5, 4	9.174×10^{-2}	2.59	5, 6	6.116×10^{-2}	2.65
6, 4	6.371×10^{-2}	3.15	6, 4	4.247×10^{-2}	3.13
7, 4	4.680×10^{-2}	3.72	6.5, 6	3.619×10^{-2}	3.39
8, 3	3.583×10^{-2}	4.33	7, 3	3.120×10^{-2}	3.71
			8, 3	2.389×10^{-2}	4.14
			9, 4	1.888×10^{-2}	4.56

Table 2.12: Measured positions $r_{\max}$ of the first maximum in the three-dimensional $g(r)$ for the dense multivalent systems from Tab. 2.4. The errors are estimated to be less than 5%. A graphical visualization is given in Fig. 2.27.

the rod, which first would have to be corrected.[23] Hence, in the following only the divalent and trivalent systems from Tab. 2.4 with a density larger than $0.03\,\sigma^{-3}$ (divalent) or $0.02\,\sigma^{-3}$ (trivalent) have been investigated. As an example, Fig. 2.26 shows the $g(r)$ for the trivalent system with the lowest, i.e., most negative, osmotic coefficient, which has a density of $0.04247\,\sigma^{-3}$ The visible structure is quantified by the position $r_{\max}$ of the first maximum, and the important question to be answered is its origin. Table 2.12 lists the measured values of $r_{\max}$ and Fig. 2.27 gives a graphical representation on a log-log scale. The interesting thing to note is that the density dependence is compatible with a slope $-1/2$. In Eqn. 2.51 this has been seen to be the exponent expected for a rod-imposed structure.

At first sight this finding might appear inevitable. Nevertheless, since $r_0\lambda < ve_0$ for the investigated cases, the inequality from the beginning of this section does in fact hold, albeit not in the strong "$\ll$" version. For this specific situation ve_0/λ is 1.9 for the divalent systems and 2.9 for the trivalent ones. Observe that the inequality does not specify the density of counterions or rods, at which the three-dimensional Wigner crystal is to appear. Rather, Ref. [Shk99] assumes only that a bundle of rods has formed and that the inequality

[23] A suitable way would be to normalize the probability of finding an ion by the Poisson-Boltzmann prediction instead of the usual ideal gas scaling $4\pi r^2$. This has, however, not been pursued further.

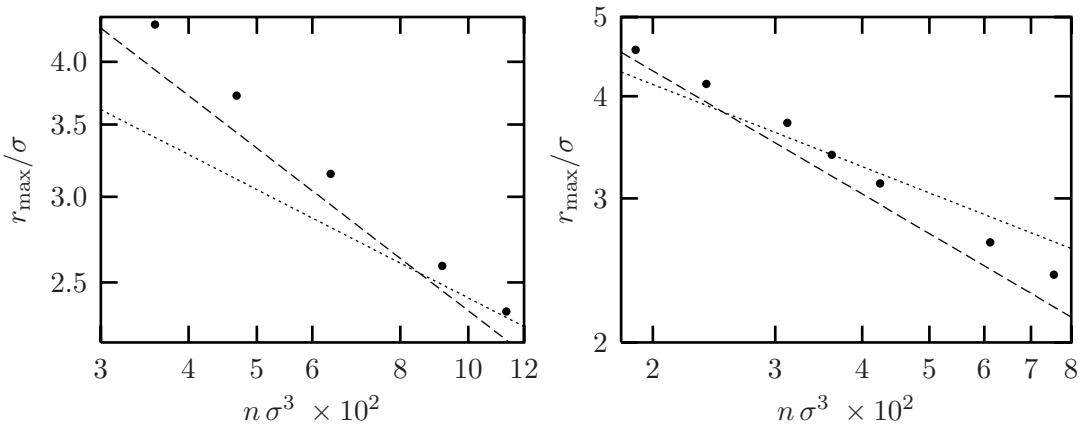

Figure 2.27: Double-logarithmic plot of the position $r_{\max}$ of the first maximum in the three-dimensional pair correlation function for the dense divalent (left) and trivalent (right) generic systems from Tab. 2.4 as a function of density. The dashed line is the separation of the rods in those systems and the dotted line is the minimum ion distance in an hcp crystal.

holds. In view of the fact that the simulations suggest rod-imposed correlations instead of a self-organized Wigner crystal on the background of a homogeneously smeared rod charge, one might want to save the idea by restricting it to higher densities than the ones investigated in the simulation. The reasoning behind this is that the strong localization of ions in the vicinity of the rods gets reduced and the system will appear more homogeneous. However, for the densest systems under investigation the separation of the rods is roughly $2.2\,\sigma$. Hence the ions can just about pass between the rods. For even higher densities the ions become trapped in the one-dimensional channels between the rods and the system ceases to be ergodic. Anyway, Tab. 2.4 and Fig. 2.13 show that the osmotic coefficient for those high density systems would be very large, while the interesting phenomenon of negative pressure in the trivalent system is observed exactly for the densities, at which a ion-rod coupling for $g(r)$ has been found. In other words: Whatever kind of correlations are responsible for the attractive interactions, the dominant contribution is not the formation of a three-dimensional Wigner crystal.

3 Efficient electrostatics: Ewald Sum and Particle Mesh Ewald Algorithms

A challenging task in every computer simulation of particles subject to periodic boundary conditions and long-range interactions is the efficient calculation of inter-particle forces and interaction energies. The famous Ewald sum [Ewa21, Hey80, LePe80^a, LePe80^b] does a remarkable job in splitting the very slowly converging sum over the Coulomb potential into two exponentially converging sums. Still, this method suffers from two deficits. First, it is computationally demanding. This is due to the fact that one part of the problem is solved in reciprocal space implying the need for several Fourier transformations. Second, the algorithm scales like N^2 with N being the number of charged particles in the primary box, or at best like $N^{3/2}$, if one uses cutoffs which are optimized with respect to the splitting parameter [PePe88].

This chapter is devoted to a thorough discussion of the Ewald sum and some of its improved versions using Fast-Fourier routines.

Section 3.1 briefly reviews the notion of periodic boundary conditions.

Section 3.2 gives an introduction to Ewald summation. The important formulæ for energy and forces are collected and the Fourier space notation is discussed for later use.

Section 3.3 presents for the first time a unified mathematical description of three important Particle Mesh algorithms. A detailed discussion of the four steps necessary in each of these algorithms is given: charge assignment onto a mesh, solving the Poisson equation on this mesh, differentiation of the potential to obtain the force and back-interpolation of the forces to the particles.

Section 3.4 summarizes extensive numerical accuracy tests of the three mesh algorithms. Based on the results, an optimal method is suggested, mostly based on the so-called P^{3}M routine.

Section 3.5 constructs an analytical error estimate for the Particle Mesh algorithm, which has been identified as the most accurate one in Sec. 3.4. A numerically convenient analytic approximation is presented in 3.5.3 and it is shown to give very reliable results. No such error estimate was known until now. Its introduction in this work provides for the first time the possibility of knowing about the algorithmic accuracy in advance. It therefore permits an optimal and straightforward tuning of the P^{3}M algorithm.

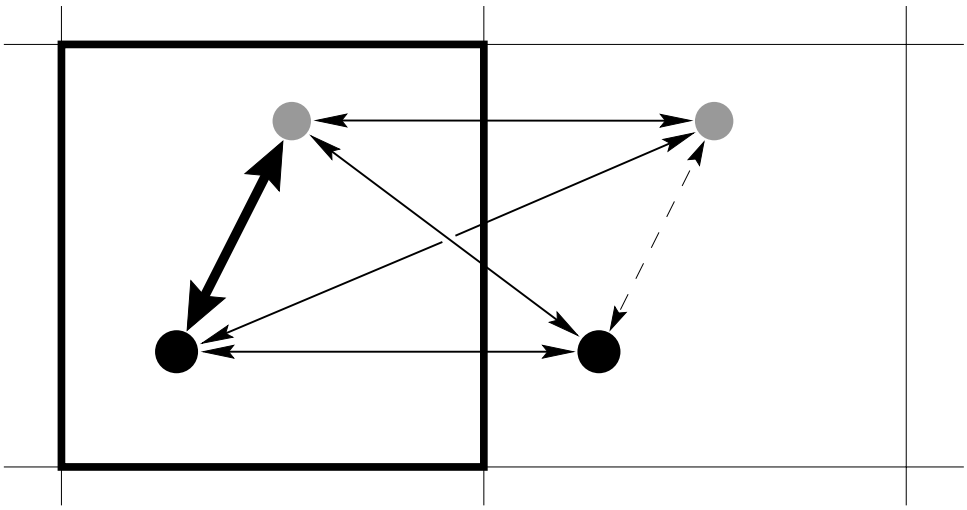

Figure 3.1: Counting interactions in periodic boundary conditions: Bold, normal and dashed arrows indicate interactions weighted with a factor 1, $\frac{1}{2}$ and 0, respectively.

3.1 Interactions within periodic boundary conditions

Periodic boundary conditions yield a boundary free but finite system with, possibly, an infinite number of self interactions. These have to be identified and weighted correctly in order to finally conform to the true bulk limit.

Periodic boundary conditions are a standard way of imitating a bulk system with only a finite number of particles at hand. A primary box is taken as the unit cell (or "base") of a space-filling "crystal" of such boxes (actually, a Bravais lattice), and all particles in this infinite and periodic universe interact with each other [BoKa12, Hai92, FrSm96, AlTi97].[1] Since these infinitely many interactions generally render all extensive observables infinite, the latter must be calculated per periodic box.[2] This poses two problems:

1. All interactions must be distributed, and possibly weighted, in a unique way between boxes such that each box gets its "fair share".

2. Even the interactions belonging to just one box might be infinitely many, if they have infinite range. This can give rise to convergence problems.

From now on the discussion will be limited to interactions that can be represented by a pair potential $U(i, j; \boldsymbol{r})$. Assume a three-dimensional system modeled by a cubic unit cell with length L. The problem of correctly weighting the interactions can be solved in the following way, see also Fig. 3.1:

- Choose a unit cell.

- Count all interactions of particles within this cell in the usual way.

[1] Topologically this amounts to a toroidally closed system.

[2] Note that the thermodynamic limit, in which the artificial periodicity must be removed, corresponds to the primary box expanding to infinity.

- Scale interactions of particles in the unit cell with particles in another replicated cell with a factor $\frac{1}{2}$.
- Do not count interactions of two particles which are both outside the unit cell.

If there are N particles with coordinates $\boldsymbol{r}_i \in [0; L[^{\times 3}$, it can be verified that the following computation of the total interaction energy complies with all these points:

$$E := \frac{1}{2} \sum_{i,j=1}^{N} {\sum_{\boldsymbol{n}\in\mathbb{Z}^3}}' U(i, j; \boldsymbol{r}_i - \boldsymbol{r}_j + \boldsymbol{n}L) \tag{3.1}$$

The prime on the second sum indicates that for $i = j$ the lattice vector $\boldsymbol{n} = \boldsymbol{0}$ must be omitted.

Remarks 3.1.1

1. $\frac{1}{2}\sum_{i,j}$ can not be replaced by $\sum_{i<j}$. The latter does not take into account interactions of a particle with one of its own images.
2. For interactions which do not extend beyond a distance of $L/2$ the minimum image convention can be used. Each particle interacts only with the nearest copy of another particle. Stated differently: for each pair (i, j) there is exactly one $\boldsymbol{n}_{ij}$, namely, the one which minimizes $|\boldsymbol{r}_i - \boldsymbol{r}_j + \boldsymbol{n}_{ij}L|$.
3. The lattice sum over $\mathbb{Z}^3$ and the plain pair potential U can be combined to an effective pair potential U_{eff}, for which the minimum image convention is used. For the Coulomb interaction this procedure will be discussed later in TP 3.2.
4. Even if the pair potential U is isotropic, the effective potential U_{eff} is not. It carries the symmetry group of the Bravais lattice.
5. The anisotropy of U_{eff} results from periodic boundary conditions breaking the continuous rotational symmetry. As a consequence, angular momentum is no longer conserved. However, since continuous translational symmetry is unaffected by periodic boundary conditions, linear momentum is still conserved.
6. If the asymptotic decay of the pair potential U is r^{-3} or slower, the convergence of the interaction energy in Eqn. (3.1) is not guaranteed. For example, it may be conditionally convergent requiring a further specification of the infinite $\mathbb{Z}^3$-sum. This is exactly what happens in the Coulomb problem.

3.2 The Ewald sum

After agreeing upon a limit of the conditionally convergent Coulombic lattice sum, a clever re-summation yields two exponentially converging sums.

There are many examples of long-range interactions which can be treated by Ewald techniques [AlTi97]. Here, however, only the case of Coulomb point charges will be discussed, i.e., an interaction potential $1/r$. Consider therefore a system of N particles with charges q_i at positions $\boldsymbol{r}_i$ in an overall neutral and, for simplicity, cubic simulation box of length

Technical Point 3.1 *(Units)*

Different people and communities prefer different conventions for units, especially when it comes to electrostatics. The choice for this chapter is the following: The Coulomb potential generated by a point particle with charge q located at the position $\boldsymbol{r}_0$ is written as $\phi(\boldsymbol{r}) = q/|\boldsymbol{r}-\boldsymbol{r}_0|$. Thus, its dimension is charge divided by length. In other words, measuring all lengths in multiples of some unit length $\mathscr{L}$ and all charges in multiples of some unit charge $\mathscr{C}$, gives the electrostatic potential in $\mathscr{C}/\mathscr{L}$, the electrostatic energy in $\mathscr{C}^2/\mathscr{L}$ and the electrostatic force in $\mathscr{C}^2/\mathscr{L}^2$.

In this chapter there is no need for specifying $\mathscr{C}$ or $\mathscr{L}$, and when it comes to the final result (be it formulas or numbers), it can always be embellished with prefactors like $1/4\pi\varepsilon_0$.

Example: If one chooses $\mathscr{L} = 1\,\text{Å} = 10^{-10}\,\text{m}$, $\mathscr{C} = e_0 \approx 1.6022 \times 10^{-19}\,\text{C}$, and includes the standard-SI-prefactor $1/4\pi\varepsilon_0$, the numerical value of the original expression q_1q_2/r^2 gives the force in units of $2.3071 \times 10^{-8}\,\text{N}$. Another common unit of force – especially in atomistic simulations – is kcal mol^{-1} Å^{-1}. Obviously,

$$\frac{\text{kcal}}{\text{mol Å}} \approx \frac{4.186 \times 10^3\,\text{J}}{6.02217 \times 10^{23}\ 10^{-10}\,\text{m}} \approx 6.9510 \times 10^{-10}\,\text{N}$$

Thus, if one prefers to measure forces in units of kcal mol^{-1} Å^{-1}, one only has to multiply the numerical value of the original q_1q_2/r^2 by a factor of approximately 331.9.

L. If periodic boundary conditions are applied, the total electrostatic energy of the box follows from Eqn. (3.1) and is given by

$$E \;=\; \frac{1}{2}\sum_{i,j=1}^{N}{\sum_{\boldsymbol{n}\in\mathbb{Z}^3}}' \frac{q_iq_j}{|\boldsymbol{r}_{ij}+\boldsymbol{n}L|}, \tag{3.2}$$

where $\boldsymbol{r}_{ij} = \boldsymbol{r}_i - \boldsymbol{r}_j$. Since this sum is only conditionally convergent[3], its value is not well-defined unless one specifies the precise way in which the cluster of simulation boxes should fill the $\mathbb{R}^3$, i.e., its *shape*, e.g. approximately spherical[4], and the dielectric conditions outside the cluster. A more detailed discussion of these points can be found in Refs. [LePe80^a, LePe80^b, Cai94, BoSt97]. The unit conventions employed in this chapter are summarized in TP 3.1.

3.2.1 The twofold origin of the problem

It is often stated that the long-range of the Coulomb potential complicates the treatment of electrostatic interactions. This is, however, only one part of the problem. In fact, the Coulomb potential bears *two* intrinsic difficulties. It is

1. slowly decaying at large distances, and
2. strongly varying at small distances.

[3] That is, the sum over the absolute values diverges

[4] The idea, however, that something as symmetric as extending spheres will necessarily converge is deceiving. Ref. [BoBo85] proves that a computation of the Madelung constant of the sodium-chloride structure fails when applying the method of extending spheres.

It is the combination of these two properties which leads to severe problems. If only one of them was present, everything would be comparatively easy:

- A short-range potential could be treated by a simple cutoff, as it is done, e.g., for interactions of the Lennard-Jones type.

- A long-range potential, which is periodic[5] and slowly varying *everywhere*, can accurately be represented by the first few terms of its Fourier series. This is, for instance, a commonly applied technique for taking into account torsional degrees of freedom in atomistic simulations.

Obviously, each of the two complications forbids the simple solution of the other, and the slowly decaying long-range part of the Coulomb potential renders a straightforward summation of Eqn. (3.2) impracticable. The trick is thus to split the problem into two parts by the trivial identity

$$\frac{1}{r} = \frac{f(r)}{r} + \frac{1 - f(r)}{r}. \tag{3.3}$$

The underlying idea is to distribute the two complications between the two terms in Eqn. (3.3) by a suitable choice of the splitting function f. In particular:

- The first part $\frac{f(r)}{r}$ should be negligible, or even zero, beyond some cutoff $r_{\max}$, so that the summation up to the cutoff is a good approximation to (or the exact result of) this contribution to the total electrostatic potential.

- The second part $\frac{1-f(r)}{r}$ should be a slowly varying function for *all* r, so that its Fourier transform can be represented by only a few $\boldsymbol{k}$-vectors with $|\boldsymbol{k}| \leq k_{\max}$. This permits an efficient calculation of this contribution to the total electrostatic potential in reciprocal space.

Since the field equations are linear, the sum of these two contributions gives the solution for the potential of the original problem.

3.2.2 The Ewald formulæ

The two requirements on the splitting function f mentioned above leave a large freedom of choice [Hey80, Ber93]. The traditional selection is the complementary error function

$$\operatorname{erfc}(r) := \frac{2}{\sqrt{\pi}} \int_r^\infty \mathrm{d}t \ \mathrm{e}^{-t^2}. \tag{3.4}$$

This results in the well known Ewald formula for the electrostatic energy of the primary box:

$$E = E^{(r)} + E^{(k)} + E^{(s)} + E^{(d)}, \tag{3.5}$$

[5] Note that the effective electrostatic potential within periodic boundary conditions is of course periodic with period L along the three coordinate directions.

where $E^{(r)}$ is the contribution from real space, $E^{(k)}$ the contribution from reciprocal space, $E^{(s)}$ the self energy and $E^{(d)}$ the dipole correction. They can be written as [AlTi97, FrSm96]

$$E^{(r)} = \frac{1}{2}\sum_{i,j}{}' \sum_{\boldsymbol{m}\in\mathbb{Z}^3} q_i q_j \frac{\operatorname{erfc}(\alpha|\boldsymbol{r}_{ij}+\boldsymbol{m}L|)}{|\boldsymbol{r}_{ij}+\boldsymbol{m}L|} \tag{3.6}$$

$$E^{(k)} = \frac{1}{2}\frac{1}{V}\sum_{\boldsymbol{k}\neq\boldsymbol{0}} \frac{4\pi}{k^2} e^{-k^2/4\alpha^2} |\tilde{\rho}(\boldsymbol{k})|^2 \tag{3.7}$$

$$E^{(s)} = -\frac{\alpha}{\sqrt{\pi}}\sum_i q_i^2 \tag{3.8}$$

$$E^{(d)} = \frac{2\pi}{(1+2\varepsilon')V}\left(\sum_i q_i \boldsymbol{r}_i\right)^2, \tag{3.9}$$

where the Fourier transformed charge density $\tilde{\rho}(\boldsymbol{k})$ is defined as

$$\tilde{\rho}(\boldsymbol{k}) = \int_V \mathrm{d}^3 r\ \rho(\boldsymbol{r})\, e^{-\mathrm{i}\,\boldsymbol{k}\cdot\boldsymbol{r}} = \sum_{j=1}^{N} q_j\ e^{-\mathrm{i}\,\boldsymbol{k}\cdot\boldsymbol{r}_j} \qquad \text{where} \qquad \boldsymbol{k}\in\frac{2\pi}{L}\mathbb{Z}^3. \tag{3.10}$$

Remarks 3.2.1

1. The advantage of rewriting Eqn. (3.2) this way is that the exponentially converging sums over $\boldsymbol{m}$ and $\boldsymbol{k}$ in (3.6,3.7) allow the introduction of comparatively small cutoffs without much loss in accuracy. Typically one chooses α large enough as to employ the minimum image convention in Eqn. (3.6).

2. The inverse length α, which is often referred to as the Ewald parameter, tunes the relative weights of the real space and the reciprocal space contributions. However, the final result is independent of α.

3. The form (3.9) given for the dipole correction assumes that the set of periodic replications of the simulation box tends spherically towards an infinite cluster and that the medium outside this sphere is a homogeneous dielectric with dielectric constant ε' [LePe80[a]]. The derivation of this term is not straightforward and requires an accurate mathematical treatment of the conditional convergence of Eqn. (3.2). Note that the case of a surrounding vacuum corresponds to $\varepsilon' = 1$ and that the dipole correction vanishes for metallic (or "tinfoil") boundary conditions, since then $\varepsilon' = \infty$. A detailed discussion of this term can be found in Ref. [BoSt97].

4. The dipole correction in Eqn. (3.9) is independent of the Ewald parameter α. This again shows that the correction is not specific to the Ewald sum but more generally reflects the problems inherent to the conditional convergence of the $\boldsymbol{n}$-sum in Eqn. (3.2).

5. For the computation of $E^{(d)}$ the particle coordinates must *not* be folded back into the primary unit cell, for otherwise each boundary crossing produces an unphysical jump in the electrostatic energy, see Ref. [Cai94].

6. The cutoffs $r_{\max}$ and $k_{\max}$ can be optimized with respect to α such that the required computer time scales like $N^{3/2}$ [PePe88]. This, however, may require that $r_{\max} > L/2$

Technical Point 3.2 *(effective potential)*

An alternative representation of the Ewald energy, which focuses on the effective potential, is frequently found in the literature:

$$E = \sum_{1\le i<j\le N} q_i q_j \varphi(\boldsymbol{r}_{ij}) + \frac{1}{2}\xi \sum_{i=1}^{N} q_i^2 + E^{(d)} \tag{3.12}$$

with the effective potential φ, sometimes referred to as the Wigner potential, given by

$$\varphi(\boldsymbol{r}) = \sum_{\boldsymbol{n}\in\mathbb{Z}^3} \frac{\mathrm{erfc}(\alpha|\boldsymbol{r}+\boldsymbol{n}L|)}{|\boldsymbol{r}+\boldsymbol{n}L|} + \frac{1}{V}\sum_{\boldsymbol{k}\neq\boldsymbol{0}} \frac{4\pi}{k^2} e^{-k^2/4\alpha^2 + \mathrm{i}\,\boldsymbol{k}\cdot\boldsymbol{r}_j} - \frac{\pi}{V\alpha^2} \tag{3.13}$$

and the numerical constant

$$\xi = \lim_{\boldsymbol{r}\downarrow\boldsymbol{0}} \left[\varphi(\boldsymbol{r}) - \frac{1}{r}\right] = \sum_{\boldsymbol{n}\neq\boldsymbol{0}} \left[\frac{\mathrm{erfc}(\alpha|\boldsymbol{n}|L)}{|\boldsymbol{n}|L} + \frac{1}{\pi n^2 L} e^{-\pi^2 n^2/\alpha^2 L^2}\right] - \frac{2\alpha}{\sqrt{\pi}} - \frac{\pi}{V\alpha^2}. \tag{3.14}$$

The splitting between φ and ξ is done in such a way as to ensure *(i)* the independence of φ on α, i.e., $\partial\varphi/\partial\alpha = 0$, and *(ii)* an average potential of zero, i.e., $\int_V \mathrm{d}^3 r\, \varphi(\boldsymbol{r}) = 0$. The two contributions $-\pi/V\alpha^2$ correspond to the term $E^{(n)}$. The existence of the vectorial limit $\boldsymbol{r} \downarrow \boldsymbol{0}$ is not trivial and dependent on a suitable convergence factor. Details can be found in Refs. [LePe80[a], Hum95, HuPr98].

prohibiting the simple minimum image convention in real space and rendering this procedure less enticing.

7. For given finite real- and reciprocal space cutoffs there exists an optimal α such that the accuracy of the approximated Ewald sum is the highest possible. This optimal value can be determined easily with the help of the excellent estimates for the cutoff errors derived by Kolafa and Perram [KoPe92] – essentially by demanding that the real- and reciprocal space contribution to the error should be equal.

8. If the system under investigation is not electrostatically neutral, the infinite sum in Eqn. (3.2) diverges. It can be made convergent by adding a homogeneously distributed background charge which restores neutrality – a typical situation for one-component plasma simulations. This results in an additional electroneutrality-term $E^{(n)}$ to be included in Eqn. (3.5), which reads (see, e.g., [HuPr98])

$$E^{(n)} = -\frac{\pi}{2\alpha^2 V}\left(\sum_i q_i\right)^2. \tag{3.11}$$

   Since the neutralizing background is homogeneous, the correction term in Eqn. (3.11) is independent of the particle positions.

9. An alternative representation of the Ewald formulæ is summarized in TP 3.2.

The force $\boldsymbol{F}_i$ on particle i is obtained by differentiating the electrostatic potential energy E with respect to $\boldsymbol{r}_i$, i.e.,

$$\boldsymbol{F}_i = -\frac{\partial}{\partial \boldsymbol{r}_i} E. \tag{3.15}$$

Using Eqns. (3.5–3.10) one obtains the following Ewald formula for the forces:

$$\boldsymbol{F}_i = \boldsymbol{F}_i^{(r)} + \boldsymbol{F}_i^{(k)} + \boldsymbol{F}_i^{(d)}, \tag{3.16}$$

with the real space, Fourier space and dipole contributions given by:

$$\begin{aligned} \boldsymbol{F}_i^{(r)} &= q_i \sum_j q_j {\sum_{\boldsymbol{m}\in\mathbb{Z}^3}}' \left(\frac{2\alpha}{\sqrt{\pi}} \exp(-\alpha^2 |\boldsymbol{r}_{ij} + \boldsymbol{m}L|^2) \right. \\ &\qquad \left. + \frac{\operatorname{erfc}(\alpha|\boldsymbol{r}_{ij} + \boldsymbol{m}L|)}{|\boldsymbol{r}_{ij} + \boldsymbol{m}L|} \right) \frac{\boldsymbol{r}_{ij} + \boldsymbol{m}L}{|\boldsymbol{r}_{ij} + \boldsymbol{m}L|^2} \end{aligned} \tag{3.17}$$

$$\boldsymbol{F}_i^{(k)} = q_i \sum_j q_j \frac{1}{V} \sum_{\boldsymbol{k}\neq\boldsymbol{0}} \frac{4\pi\boldsymbol{k}}{k^2} \exp\left(-\frac{k^2}{4\alpha^2}\right) \sin(\boldsymbol{k}\cdot\boldsymbol{r}_{ij}) \tag{3.18}$$

$$\boldsymbol{F}_i^{(d)} = -\frac{4\pi q_i}{(1+2\varepsilon')V} \sum_j q_j \boldsymbol{r}_j. \tag{3.19}$$

Since the self energy in Eqn. (3.8) and the neutralizing contribution in Eqn. (3.11) are independent of particle positions, they do not contribute to the force.

3.2.3 Fourier representation

More insight into the Ewald sum can be gained by the following considerations. Let $\tilde{g}(\boldsymbol{k}) := 4\pi/k^2$ be the Fourier transformed Green function of the Coulomb potential $1/r$ and $\tilde{\gamma}(\boldsymbol{k}) := \exp(-k^2/4\alpha^2)$. With these definitions Eqn. (3.7) can be rewritten as

$$E^{(k)} = \frac{1}{2} \sum_j q_j \left(\frac{1}{V} \sum_{\boldsymbol{k}\neq\boldsymbol{0}} \tilde{g}(\boldsymbol{k})\, \tilde{\gamma}(\boldsymbol{k})\, \tilde{\rho}(\boldsymbol{k})\, e^{\mathrm{i}\,\boldsymbol{k}\cdot\boldsymbol{r}_j} \right) =: \frac{1}{2} \sum_j q_j\, \phi^{(k)}(\boldsymbol{r}_j). \tag{3.20}$$

Here $\phi^{(k)}(\boldsymbol{r}_j)$ is the electrostatic potential at the point $\boldsymbol{r}_j$ due to the *second* term in Eqn. (3.3) and its Fourier transform is given by

$$\tilde{\phi}^{(k)}(\boldsymbol{k}) = \tilde{g}(\boldsymbol{k})\, \tilde{\gamma}(\boldsymbol{k})\, \tilde{\rho}(\boldsymbol{k}). \tag{3.21}$$

As is known, products in reciprocal space correspond to convolutions in real space. Hence Eqn. (3.21) shows that the reciprocal space contribution to the electrostatic potential is created by a charge distribution which is obtained from the original point charge distribution by a convolution with a "smearing function" $\gamma(\boldsymbol{r})$.

For the standard Ewald sum, $\gamma(\boldsymbol{r})$ is a Gaussian, i.e., $\gamma(\boldsymbol{r}) = \alpha^3\pi^{-3/2}\exp(-\alpha^2 r^2)$. This is merely a consequence of choosing the splitting function f in Eqn. (3.3) to be the complementary error function. In fact, an alternative method to motivate the splitting is to replace the point charge distribution ρ by a screened charge distribution $\rho - \rho\star\gamma$ and to compensate this screening by adding the smeared charge distribution $\rho\star\gamma$, see Fig. 3.2.

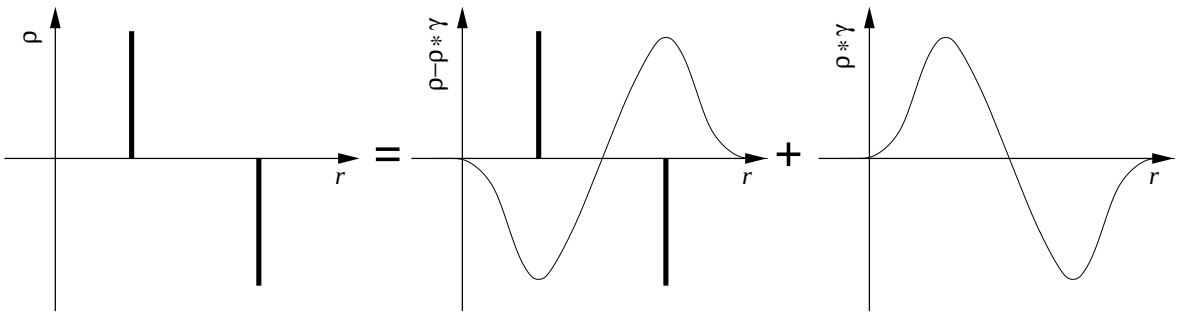

Figure 3.2: Alternative motivation for the Ewald formulæ. A point charge distribution is split into *(i)* a screened point charge distribution and *(ii)* the corresponding screening distribution. Part *(i)* is a superposition of multipole-free charge distributions (whose potential thus decays stronger than algebraically) and leads to short-ranged interactions – it is summed in real space. Part *(ii)* is slowly varying and can be represented by a few Fourier coefficients – it is summed in reciprocal space. Sketched after [AlTi97, FrSm96].

The star denotes the convolution operation. From a mathematical point of view these two interpretations are perfectly equivalent: Instead of splitting the potential one splits the charge density.

At this point a word of caution seems appropriate. Whereas the electrostatic potential depends linearly on the charge density, the electrostatic energy does not. Thus, calculating the energies of the charge densities $\rho - \rho \star \gamma$ and $\rho \star \gamma$, and adding these contributions together would *not* give the energy of the charge density ρ. Consequently, $E^{(k)}$ is not the electrostatic energy of a charge density $\rho \star \gamma$ but the Fourier space contribution to the electrostatic energy of the charge density ρ. This subtle point becomes more transparent by writing down the energy explicitly. If ϕ_ρ denotes the potential originating from ρ, the linear dependence of ϕ_ρ on ρ implies an equation like $\phi_\rho = \phi_{\rho-\rho\star\gamma} + \phi_{\rho\star\gamma}$. The electrostatic energy can thus be rewritten as

$$\begin{aligned} E' &= \frac{1}{2}\int \mathrm{d}^3 r\; \rho(\boldsymbol{r})\,\phi_\rho(\boldsymbol{r}) \;=\; \frac{1}{2}\int \mathrm{d}^3 r\; \rho(\boldsymbol{r})\left[\phi_{\rho-\rho\star\gamma}(\boldsymbol{r}) + \phi_{\rho\star\gamma}(\boldsymbol{r})\right] \\ &= \frac{1}{2}\int \mathrm{d}^3 r\; \rho(\boldsymbol{r})\,\phi_{\rho-\rho\star\gamma}(\boldsymbol{r}) + \frac{1}{2}\int \mathrm{d}^3 r\; \rho(\boldsymbol{r})\,\phi_{\rho\star\gamma}(\boldsymbol{r}). \end{aligned} \tag{3.22}$$

The two terms in the last line are the real space and the Fourier space contribution to the energy, corresponding to Eqns. (3.6) and (3.7) respectively, but neither of them can be interpreted as the energy of a charge distribution $\rho - \rho\star\gamma$ or $\rho\star\gamma$. Moreover, the quantity E' contains unphysical self-energy contributions, i.e., energy due to the interaction of a charge (or γ-smeared charge) with itself. In the actual Ewald sum the self-energy contribution of the real space part is canceled by omitting the term $\boldsymbol{m} = \boldsymbol{0}$ for $i = j$ in Eqn. (3.6), whereas the self energy contribution of $E^{(k)}$ must be subtracted separately. This is the origin of the term $E^{(s)}$.

3.3 Ewald summation on a grid

A finite Fourier transform on a grid of N points can be done in order $N \log N$. This suggests a possibility of significantly reducing the algorithmic cost of the Ewald sum: discretize it.

The Fourier transformations involved in Eqns. (3.7,3.18) are the most time consuming part of the Ewald sum. Several methods have been proposed to address this problem, e.g., tabulation of the complete Ewald potential [SaDi76] or the use of polynomial approximations. A particularly successful approach for the latter is the expansion of the non-spherical contributions to the Ewald potential in cubic harmonics [SaDi76, AdDu86]. Apart from the difficulty of computational overhead which may strongly increase with the desired accuracy, these methods do not solve the additional problem of unfavorable scaling with particle number. At best they scale as $N^{3/2}$ [PePe88], which is more costly than a plain cutoff or reaction field approach.

The essential idea is *not* to avoid the Fourier transformations but to modify the problem in such a way that it permits application of the Fast Fourier Transformation (FFT, see e.g. [PrTe92] and references therein). This reduces the complexity of the reciprocal part of the Ewald sum to $N \log N$. If the real space cutoff is chosen to be small enough, this scaling applies to the complete Ewald sum. Since the FFT is a grid transformation, there are discretization problems to be solved and corresponding discretization errors to be minimized.

At present there exist several mesh implementations of the Ewald sum – similar in spirit but different in detail. In the following the main focus will be on the original particle-particle–particle-mesh (P^3M) method of Hockney and Eastwood [HoEa88] and two of its variants, namely, the Particle Mesh Ewald (PME) method of Darden *et al.* [DaYo93] and an extension of the latter by Essmann *et al.* [EsPe95], which will be referred to as Smooth Particle Mesh Ewald (SPME).

There have been some uncertainties in the literature concerning the relative performance of these methods [ToBo95], and it has been shown previously that the P^3M approach – the oldest of the three – is actually the most accurate one and should be the preferred choice [LuTi95]. However, in this reference the PME method was combined with a disadvantageous charge assignment scheme, and the more recent SPME was not considered. It seems therefore justified to test again these three methods under similar well posed and reproducible conditions and a larger number of tuning parameters.

The original literature on particle mesh routines is usually not easy to digest for the non-specialist. It is obscured by the fact that various authors approach the problem from different directions and use different notations. This chapter tries to present a unified view of the common methods and analyzes in detail the ingredients comprising them. This hopefully uncovers the large number of possibilities for combining the different parts, thus allowing a judicious balance of accuracy, speed and ease of implementation. Moreover, it is shown that due to some subtle interdependencies not all combinations are advantageous, although they might appear promising at first sight. The combinations which have been chosen in the literature are summarized at the end of this section in Table 3.1.

Performing the Fourier transformations in the reciprocal space part of the Ewald sum by FFT routines is by no means straightforward:

1. The point charges with continuous coordinates have to be replaced by a grid based charge density, since the FFT is a discrete and finite transformation.

2. It is neither obvious nor true that the best grid approximation to the continuum solution of the Poisson equation is achieved by using the continuum Green function [HoEa88].

3. There are at least three possibilities for implementing the differentiation needed in Eqn. (3.15). They differ in accuracy and speed.

4. The procedure of assigning the forces calculated on the mesh back to the actual particles can – under certain circumstances – lead to unwanted violations of Newton's third law. They can be anything between harmless and disastrous.

The four steps involved in a particle mesh calculation are sources of various kinds of errors, originating, e.g., from discretization, interpolation or aliasing[6] problems. Since these contributions are not independent of each other (reducing one might enhance another), the only reasonable demand is the minimization of the *total* error at given computational effort.

One aim of this chapter is to compile some of the possibilities for each step, in order to draw a comparison between the three mesh implementations mentioned above, viz, PME, SPME and P^3M. Like the Ewald sum, all these algorithms can be extended to a triclinic simulation cell by reverting to general dual basis vectors, and one can also use a different number of grid points in each direction. In order to keep the notation simple, the following discussion is restricted to the case of a cubic box and the same number of mesh points in each direction. How the generalizations can be done is described, e.g., in the references on PME [DaYo93] and SPME [EsPe95].

3.3.1 Charge Assignment

The purpose of charge assignment is to substitute the actual charge density of point particles with a mesh based charge "density", see Fig. 3.3. The actual procedure can be written down very easily. It will first be discussed in the one-dimensional case, in which particles with coordinates $x \in [0; L] \subset \mathbb{R}$ have to be assigned to the mesh points $x_p \in \mathbb{M} = \{p\,h : p = 0, \ldots, N_\mathrm{M} - 1\}$, where N_M is the number of mesh points and $h := L/N_\mathrm{M}$ is their spacing. For simplicity, the chosen notation restrains from explicitly taking into account that any x-value outside $[0; L[$ has to be folded back into this interval in order to conform with periodic boundary conditions. Rather, it is assumed that this is done when necessary. In short: all calculations are to be understood "modulo L".

Define an even function $W(x)$ such that the fraction of charge which is assigned to the mesh point x_p due to a unit charge at position x is given by $W(x - x_p)$. If the charge density of the system is $\rho(x)$, then the mesh based charge density ρ_M can be written as the convolution

$$\rho_\mathrm{M}(x_p) = \frac{1}{h} \int_0^L \mathrm{d}x\; W(x_p - x)\, \rho(x). \tag{3.23}$$

[6] A finite grid cannot represent arbitrarily large $\boldsymbol{k}$-vectors. Instead, they are folded back into the first "Brillouin zone" and there distort the true spectrum. This effect is usually referred to as "aliasing". See, e.g., Sec. 12.1 in Ref. [PrTe92].

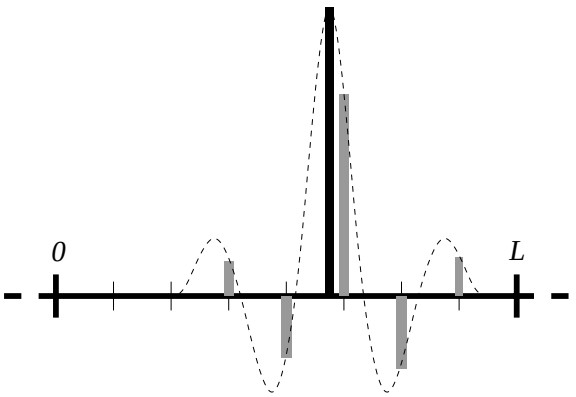

Figure 3.3: Sketch of a one-dimensional charge assignment. A suitable fraction of a charge residing at some (continuous) position within the interval $[0; L[$ is assigned to its five nearest grid points of an 8-mesh. The fractions (gray) are determined by a *charge assignment function* (dashed curve).

The prefactor $1/h$ ensures that ρ_{M} is in fact a density. Henceforth any such function W will be called a charge assignment function.

The important question is: What properties should W have in order to be a suitable choice? The following list summarizes some desirable features:

- Charge conservation, i.e., the fractional charges of one particle, which have been distributed to the surrounding grid points, sum up to the total charge of that particle.
- Finite, and if possible small, support[7], since the computational cost increases with the number of mesh points among which the charge of each particle is distributed.
- Localization of discretization errors, i.e., inaccuracies in the force between two particles due to the discretization should become small with increasing particle separation.
- Large degree of smoothness, i.e., the fractional charge of particle i which is assigned to some mesh point x_p should be a smoothly varying function of the position of particle i.
- Minimization of aliasing errors, i.e., the charge assignment function should decay sufficiently rapidly in Fourier space.
- Easy and transparent implementation.

Remarks 3.3.1

1. Not all of these characteristics can be achieved at the same time. Some properties are indeed positively correlated. A large degree of smoothness implies a fast decay in reciprocal space and thus minimizes aliasing errors. However, some other properties exclude each other. Minimization of aliasing errors implies a sufficient localization in reciprocal space which is incompatible with a small support in real space. Thus, a good charge assignment function is always a compromise between these different demands.

2. The choice of $W(x)$ is not independent of the other decisions made for the mesh implementation. In TP 3.3 it is demonstrated that if one sticks to the continuum Coulomb Green function in the mesh calculation, the requirement for localization

[7] The support of a real-valued function f defined on X is the closure of the set $\{x \in X : f(x) \neq 0\}$. This is essentially the range of values for which the function is nonzero.

of discretization errors is enough to restrict the charge assignment to a Lagrange interpolation scheme [DeHo98[a]]. This is in fact the combination used for PME [DaYo93, Pet95]. Hence, other charge assignment functions can be competitive only if the Coulomb Green function is somehow adjusted at the same time.

The choice for the charge assignment function of Hockney and Eastwood is primarily motivated by smoothness demands. In a P^{th} order assignment scheme, i.e., the charge of one particle is distributed between its P nearest mesh points, they define the Fourier transformed charge assignment function as

$$\tilde{W}^{(P)}(k) := h\left(\frac{\sin(kh/2)}{kh/2}\right)^P. \tag{3.30}$$

Transforming this back to real space via the convolution theorem gives

$$W^{(P)}(x) = \underbrace{(\chi_{[-\frac{1}{2},\frac{1}{2}]} \star \cdots \star \chi_{[-\frac{1}{2},\frac{1}{2}]})}_{P\text{-fold convolution}}(x/h). \tag{3.31}$$

Remarks 3.3.2

1. $\chi_{\mathscr{I}}$ is the characteristic function of the interval $\mathscr{I}$, i.e., the function that is 1 within this interval and 0 outside.

2. The central limit theorem shows that for increasing P the charge assignment function $W^{(P)}$ resembles more and more closely a Gaussian centered at zero. Its variance is P times as large as the variance of $W^{(1)}$.

3. $W^{(P)}$ has finite support $[-\frac{Ph}{2}, \frac{Ph}{2}]$.

4. For large P the function $W^{(P)}$ is very smooth. This is due to the fact that it is actually a spline of order P and thus $P-2$ times differentiable [Sch73].

5. As a matter of convenience the corresponding charge fractions $W_p^{(P)}(x) = W^{(P)}(x - x_p)$ are tabulated for $P \in \{1, \ldots, 7\}$ in Sec. 3.3.5.

In Fig. 3.4 the third order assignment functions for the Lagrange and the spline interpolation scheme are plotted. While the spline function is in general $P-2$ times continuously differentiable, the Lagrange assignment function is not as smooth: Generally, for even assignment order it is continuous, but its derivative is not, while for odd assignment order it is discontinuous right away. Incidentally, for $P = 1$ and $P = 2$ both schemes coincide.

The SPME method uses essentially the same charge assignment functions as the P^3M-method. This is discussed in the next section.

Charge assignment in more than one dimension can be achieved by a simple factorization approach. E.g., the three-dimensional charge assignment function $W(\boldsymbol{r})$ can be written as

$$W(\boldsymbol{r}) = W(x)W(y)W(z). \tag{3.32}$$

This is certainly not the only possibility [HoEa88] but it is computationally advantageous.

Technical Point 3.3 *(Lagrange interpolation)*

The use of the continuum Coulomb Green function suggests a so called Lagrange interpolation scheme, since this leads to a nice cancellation of certain discretization errors. The notation follows Hockney and Eastwood [HoEa88] and only the one-dimensional case is considered.
The electrostatic potential at position x' due to a unit charge residing at position x is *not* just a function of $|x' - x|$ but also depends on the distances of this charge from its neighboring mesh points. Let $g(x)$ be the continuum Coulomb Green function and $W_p(x) = W(x - x_p)$ the charge assigned to mesh point p at position x_p due to a unit charge at position x. The electrostatic potential at position x' can then be written as

$$\phi(x') = \sum_{p=1}^{P} W_p(x)\, g(x' - x_p) \tag{3.24}$$

where the sum is taken over all P mesh points to which the particle at position x contributed some fraction of its charge. Taylor expanding $g(x' - x_p)$ about $(x' - x)$ gives

$$\phi(x') = \sum_{p=1}^{P} W_p(x) \sum_{n=0}^{\infty} \frac{(x - x_p)^n}{n!} g^{(n)}(x - x'). \tag{3.25}$$

One may cancel the terms depending on $x - x_p$ up to order P by choosing $W_p(x)$ such that

$$\sum_{p=1}^{P} W_p(x)\, (x - x_p)^{n-1} = \delta_{1,n} \quad , \quad n = 1, \ldots, P. \tag{3.26}$$

By induction with respect to n one can show that this may equivalently be expressed as

$$\sum_{p=1}^{P} W_p(x)\, x_p^{n-1} = x^{n-1} \quad , \quad n = 1, \ldots, P. \tag{3.27}$$

This system of P linear equations has a unique solution for the $W_p(x)$, since the coefficient matrix $(x_p^{n-1})_{np}$ is a Vandermonde matrix for the distinct points $x_1, \ldots, x_P$ and hence has full rank. The $W_p(x)$ are thus polynomials of degree $P - 1$. In particular, at the mesh points this yields

$$\sum_{p=1}^{P} W_p(x_q)\, x_p^{n-1} = x_q^{n-1} \quad , \quad n, q = 1, \ldots, P \tag{3.28}$$

which – again due to the invertibility of $(x_p^{n-1})_{np}$ – can only be true if

$$W_p(x_q) = \delta_{p,q} \quad , \quad p, q = 1, \ldots, P. \tag{3.29}$$

Equation (3.29) suffices to determine the polynomials $W_p(x)$. They are referred to as the fundamental polynomials for the Lagrange interpolation problem [LaTi85]. Petersen tabulates them for $P = 3, \ldots, 7$ and their implementation is explained in detail [Pet95].

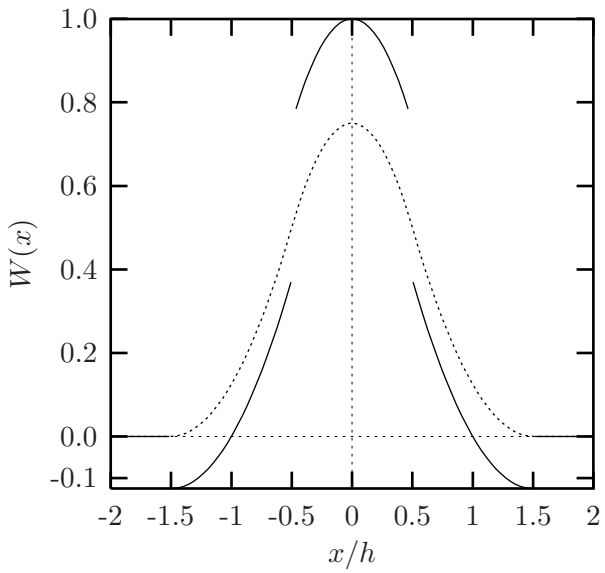

Figure 3.4: Third order charge assignment function for the Lagrange scheme [DaYo93, Pet95] (solid line) and the spline scheme [HoEa88] (dotted line, see also Eqn. (3.31)). Both assignment functions have support $[-\frac{3}{2}h; \frac{3}{2}h]$ and are piecewise quadratic. While for all odd assignment orders the Lagrange assignment function is discontinuous (for even assignment order it is continuous but not differentiable), the spline assignment function is in general $P-2$ times continuously differentiable by construction. Note, however, that the Lagrange assignment function is optimized with respect to a different property, see TP 3.3.

The generalization of Eqn. (3.23) to three dimensions can be written as

$$\rho_{\mathrm{M}}(\boldsymbol{r}_p) = \frac{1}{h^3}\int_{L^3} \mathrm{d}^3 r\; W(\boldsymbol{r}_p - \boldsymbol{r})\,\rho(\boldsymbol{r}) \tag{3.33}$$

$$= \frac{1}{h^3}\sum_{i=1}^{N} q_i W(\boldsymbol{r}_p - \boldsymbol{r}_i). \tag{3.34}$$

In the last equation the reader should not confuse the coordinate of particle i, $\boldsymbol{r}_i$, with the coordinate of mesh point p, $\boldsymbol{r}_p$.

3.3.2 Solving the Poisson equation

For the standard Ewald sum, the Fourier space contribution to the electrostatic energy is given by Eqn. (3.7). This section discusses how this equation has to be modified for the particle mesh version.

The simplest approach is used in the PME method [DaYo93], where it is assumed that this equation is appropriate in the discrete case as well. The only difference is that the Fourier transformed charge density $\tilde{\rho}$ from Eqn. (3.10) is replaced by the finite Fourier transform of the mesh based charge density, $\hat{\rho}_{\mathrm{M}}$, defined as

$$\hat{\rho}_{\mathrm{M}}(\boldsymbol{k}) := h^3 \sum_{\boldsymbol{r}_p \in \mathbb{M}} \rho_{\mathrm{M}}(\boldsymbol{r}_p)\, e^{-\mathrm{i}\,\boldsymbol{k}\cdot\boldsymbol{r}_p}, \tag{3.35}$$

where $\sum_{\boldsymbol{r}_p\in\mathbb{M}}$ is the sum over the three-dimensional mesh in real space and the $\boldsymbol{k}$-vectors are from the corresponding Fourier space mesh. In order to distinguish between the usual and the finite Fourier transform, the latter is indicated by a hat and the former by a tilde. As discussed in the previous subsection and TP 3.3, the use of the continuum Coulomb Green function is best accompanied by a Lagrange interpolation scheme for the charge assignment.

A second algorithm, the SPME method, has been presented by Essmann *et al.* [EsPe95]. It uses a smooth charge assignment scheme and hence an adjusted Green function. The

reasoning is as follows: Starting with Eqns. (3.7, 3.10) it is argued that charge assignment onto the mesh can be viewed as interpolating exponentials of the form $\exp(\mathrm{i}kx)$ at discrete grid points. This problem has a particularly elegant solution, the so-called exponential Euler splines [Sch73]. If x is the continuous particle coordinate and P is even[8], one has

$$e^{\mathrm{i}kx} \approx b(k) \sum_{l\in\mathbb{Z}} M^{(P)}(x-lh)\, e^{\mathrm{i}klh} \qquad \text{with} \qquad b(k) = \frac{e^{\mathrm{i}kPh}}{\sum_{l=1}^{P-1} M^{(P)}(lh)\, e^{\mathrm{i}klh}}. \quad (3.36)$$

Remarks 3.3.3

1. The function $M^{(P)}$ is a cardinal-B-spline of order P [Sch73].

2. Due to the interpolation in Eqn. (3.36) $M^{(P)}$ acts as the charge assignment function.

3. $M^{(1)} = \chi_{[0,1]}$, and higher splines can be generated via the recursion

$$M^{(P)}(x) \;=\; \frac{x}{P-1}\, M^{(P-1)}(x) \;+\; \frac{P-x}{P-1}\, M^{(P-1)}(x-1). \quad (3.37)$$

4. A closed formula for $M^{(P)}$ reads

$$M^{(P)}(x) = (\underbrace{\chi_{[0,1]} \star \cdots \star \chi_{[0,1]}}_{P\text{-fold convolution}})(x). \quad (3.38)$$

   Incidentally, this implies that $M^{(P)}$ is identical to the probability distribution of the sum of P independent random variables each distributed uniformly on the unit interval [EsPe95].

5. A comparison of Eqn. (3.38) with Eqn. (3.31) reveals that the charge assignment functions from the SPME and the P^{3}M method are in fact identical up to a translation: $M^{(P)}(x) = W^{(P)}(x - \frac{Ph}{2})$.

6. The derivative of $M^{(P)}$ can be constructed from $M^{(P-1)}$

$$\frac{\mathrm{d}}{\mathrm{d}x}\, M^{(P)}(x) \;=\; M^{(P-1)}(x) \;-\; M^{(P-1)}(x-1) \quad (3.39)$$

   This also proves $M^{(P)}$ to be $P-2$ times continuously differentiable.

7. $M^{(P)}$ has finite support $[0; Ph]$, so the sum in Eqn. (3.36) is finite.

8. $M^{(P)}$ is not an even function, and in the original reference on SPME the charge assignment differs slightly from Eqn. (3.34). However, the only effect of the translation is that the original system is represented by a shifted mesh system. This is irrelevant from a practical point of view, since the shift is undone in the back-interpolation if accomplished with the same assignment function.

9. The first 7 cardinal-B-splines are sketched in Fig. 3.5.

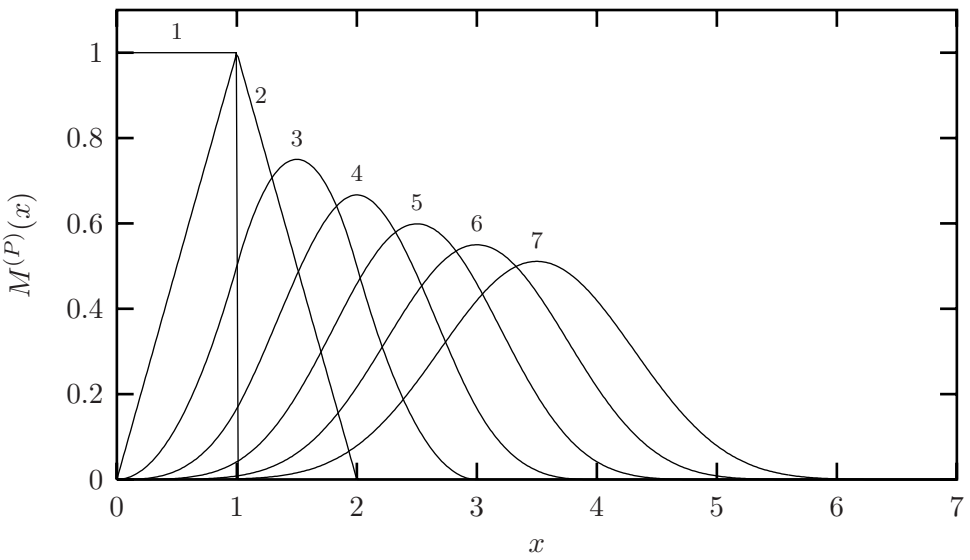

Figure 3.5: Sketch of the first 7 cardinal-B-splines $M^{(P)}(x)$, parameterized by P. Note that the charge assignment functions $W^{(P)}(x)$ for the P^{3}M algorithm are just the "centered" B-splines.

Now the following approximation for $E^{(k)}$ can be derived by inserting Eqn. (3.36) into Eqn. (3.7). The substitution yields

$$E^{(k)} \approx \frac{1}{2} \sum_{\boldsymbol{r}_p \in \mathbb{M}} h^3 \rho_{\mathrm{M}}(\boldsymbol{r}_p) \big[\rho_{\mathrm{M}} \star G\big](\boldsymbol{r}_p), \tag{3.40}$$

where the star "$\star$" denotes the finite convolution

$$\big[\rho_{\mathrm{M}} \star G\big](\boldsymbol{r}_p) = h^3 \sum_{\boldsymbol{r}_q \in \mathbb{M}} \rho_{\mathrm{M}}(\boldsymbol{r}_q) G(\boldsymbol{r}_p - \boldsymbol{r}_q) \tag{3.41}$$

(again, the periodic closure is not written down explicitly), and the function G is given by its finite Fourier transform

$$\hat{G}(\boldsymbol{k}) \quad = \quad B(\boldsymbol{k}) \sum_{\boldsymbol{m} \in \mathbb{Z}^3} \frac{4\pi}{(\boldsymbol{k} + \frac{2\pi}{h}\boldsymbol{m})^2} \, \tilde{\gamma}(\boldsymbol{k} + \frac{2\pi}{h}\boldsymbol{m}) \tag{3.42}$$

$$\text{with} \qquad B(\boldsymbol{k}) \quad := \quad \Big| b(k_x) b(k_y) b(k_z) \Big|^2. \tag{3.43}$$

Following Hockney and Eastwood, G will be termed influence function. The nice thing about G is that it is by construction independent of particle coordinates. It can therefore be computed in advance and stored for later use.

Eqn. (3.40) can be made plausible in the following way: G plays the role of a Coulomb Green function which has incorporated the "smearing" with the Gaussian γ. Hence, its convolution with the mesh based point charge density gives the mesh based electrostatic

[8] A recipe for the treatment of odd P can be found in the original SPME reference [EsPe95].

potential of γ-smeared charges. Multiplying this with the mesh based charge $h^3\rho_{\mathrm{M}}$ and summing over all mesh points gives the Fourier space contribution to the electrostatic energy up to a factor $1/2$, which merely cancels some double counting. This should be compared to Eqn. (3.20) or the second term in Eqn. (3.22).

As pointed out in Rem 3.3.1.2, a charge assignment different from the Lagrange interpolation scheme can be competitive only, if the Coulomb Green function is changed at the same time. The replacement of the usual smeared Green function $g \star \gamma$ with the influence function G, which essentially differs by the additional prefactor B in Fourier space, achieves exactly that. Conversely, PME uses a Lagrange interpolation scheme together with the unchanged Coulomb Green function, i.e., Eqns. (3.40, 3.42) with the function B being identical to 1.

Finally, the alias sum occurring in Eqn. (3.42) is substituted according to the following rule [EsPe95]: If N_{M} is the number of mesh points in each direction and the vector $\boldsymbol{k}$ on the left hand side is given by $\boldsymbol{k} = 2\pi\boldsymbol{n}/L$, with $\boldsymbol{n} \in \{0, \ldots, N_{\mathrm{M}} - 1\}^3$, then define $\hat{G}(\boldsymbol{k}) = B(\boldsymbol{k})\tilde{g}(\boldsymbol{k}')\tilde{\gamma}(\boldsymbol{k}')$, where $\boldsymbol{k}' = 2\pi\boldsymbol{n}'/L$ and $n_i' = n_i$ for $0 \leq n_i \leq N_{\mathrm{M}}/2$ and $n_i' = n_i - N_{\mathrm{M}}$ otherwise $(i = x, y, z)$.

A third possibility, the so-called P^{3}M method, has been presented by Hockney and Eastwood [HoEa88]. Their objective was an optimization of the influence function G in Eqn. (3.40), which causes the final result of the mesh calculation to be as close as possible to the original continuum problem. In order to proceed one first has to give the statement "as close as possible" a more quantitative meaning.

Take two particles with coordinates $\boldsymbol{r}_1$ and $\boldsymbol{r}_2$ and define $\boldsymbol{r} := \boldsymbol{r}_1 - \boldsymbol{r}_2$. The true physical force between these particles is a function of $\boldsymbol{r}$ only. However, in any mesh implementation the actually computed force also depends on the positions of the particles relative to the mesh, e.g., on the position of the first particle within its mesh cell. The reason for this is that translational symmetry present in the originally continuous Ewald problem is broken by the mesh. This suggests a measure for the error: Integrate the square of the difference between the calculated force $\boldsymbol{F}$ and the true physical reference force $\boldsymbol{R}$ over all values of $\boldsymbol{r}$, and average this quantity over all positions of, e.g., the first particle within one particular mesh cell

$$Q := \frac{1}{V_c} \int_{V_c} \mathrm{d}^3 r_1 \int_V \mathrm{d}^3 r \left[\boldsymbol{F}(\boldsymbol{r}; \boldsymbol{r}_1) - \boldsymbol{R}(\boldsymbol{r})\right]^2 . \tag{3.44}$$

Here $V_c = h^3$ is the volume of one mesh cell. The solution of the Poisson equation is accomplished by Eqn. (3.40) and the derivative to obtain the force in Eqn. (3.15) is performed by applying finite difference operators to the mesh based electrostatic potential (see below). Since the discretization error Q can be regarded as a functional of $\hat{G}$, the optimal influence function $\hat{G}_{\mathrm{opt}}$ can be obtained by setting the functional derivative of Q with respect to $\hat{G}$ to zero

$$\left.\frac{\delta Q}{\delta \hat{G}}\right|_{\hat{G}=\hat{G}_{\mathrm{opt}}} = 0. \tag{3.45}$$

Starting from this idea, Hockney and Eastwood were able to derive the following expression

for $\hat{G}_{\text{opt}}$ [HoEa88]:

$$\hat{G}_{\text{opt}}(\boldsymbol{k}) = \frac{\tilde{\boldsymbol{D}}(\boldsymbol{k}) \cdot \sum_{\boldsymbol{m}\in\mathbb{Z}^3} \tilde{U}^2(\boldsymbol{k} + \frac{2\pi}{h}\boldsymbol{m}) \tilde{\boldsymbol{R}}(\boldsymbol{k} + \frac{2\pi}{h}\boldsymbol{m})}{|\tilde{\boldsymbol{D}}(\boldsymbol{k})|^2 \left[\sum_{\boldsymbol{m}\in\mathbb{Z}^3} \tilde{U}^2(\boldsymbol{k} + \frac{2\pi}{h}\boldsymbol{m})\right]^2}. \tag{3.46}$$

Here $\tilde{\boldsymbol{D}}(\boldsymbol{k})$ is the Fourier transform of the employed differentiation operator, see next section and TP 3.4, $\tilde{U}(\boldsymbol{k}) = \tilde{W}(\boldsymbol{k})/V_c$ is the Fourier transform of the charge assignment function divided by the volume of one mesh cell, and $\tilde{\boldsymbol{R}}(\boldsymbol{k})$ is the Fourier transform of the true reference force, given by

$$\tilde{\boldsymbol{R}}(\boldsymbol{k}) = -\mathrm{i}\boldsymbol{k}\tilde{g}(\boldsymbol{k})\tilde{\gamma}(\boldsymbol{k}). \tag{3.47}$$

Remarks 3.3.4

1. The optimal influence function in Eqn. (3.46) differs from the expression in the book of Hockney and Eastwood [HoEa88], who use $\tilde{\gamma}^2$ instead of $\tilde{\gamma}$. The reason is that Eqn. (3.47) describes the true reference force between a γ-smeared charge and a point charge, while Hockney and Eastwood choose a slightly different approach in which they need the force between two γ-smeared charges. In addition, the factor 4π is kept in the Fourier transformed Green function $\tilde{g}$.

2. The alias sums over $\boldsymbol{m}$ in Eqn. (3.46) are rapidly convergent. Typically it is sufficient to truncate them at $|\boldsymbol{m}| \leq 2$. The sum in the denominator can even be done analytically, which will later be used in Sec. 3.5.

3. $\hat{G}_{\text{opt}}$ is independent of particle coordinates and thus needs to be computed only once prior to the actual simulation.

4. The expression for the optimal influence function in Eqn. (3.46) differs from the SPME influence function in Eqn. (3.42). Hence, the latter cannot be optimal with respect to rms force accuracy.

A final word concerning the implementation seems appropriate. Although the convolution $\rho_{\text{M}} \star G$ in Eqn. (3.40) is a nice and compact notation, the whole purpose of these particle mesh routines is to employ the convolution theorem and to use efficient FFT routines to calculate $\rho_{\text{M}} \star G$. The central steps are thus:

- Calculate the finite Fourier transform $\hat{\rho}_{\text{M}}$ of the mesh based charge density ρ_{M}.
- Multiply $\hat{\rho}_{\text{M}}$ with the Fourier space representation of the influence function, $\hat{G}$.
- Apply an inverse finite Fourier transform to this product to obtain the finite convolution of ρ_{M} with G. Formally this can be written as

$$\rho_{\text{M}} \star G \;=\; \overleftarrow{\text{FFT}} \left[\overrightarrow{\text{FFT}}\,[\rho_{\text{M}}] \times \overrightarrow{\text{FFT}}\,[G] \right]. \tag{3.48}$$

  In this way one needs only $\hat{G}$ to calculate $\rho_{\text{M}} \star G$, but never G itself.

Equation (3.48) is the important part which all particle mesh algorithms have in common. The various methods differ, e.g., in their choice of G, the assignment function W or the implementation of the derivative in the force equation (3.15).

3.3.3 Differentiation

After the calculation of the electrostatic energy, the forces on the particles are obtained by differentiation according to Eqn. (3.15). For the Fourier space part of particle mesh methods there are, however, several possibilities to implement this procedure. In other words: there exist several possible substitutes for Eqn. (3.18), in particular

1. Differentiation in Fourier space.
2. Analytic differentiation of the assignment function in real space.
3. Discrete differentiation on the mesh in real space.

Differentiation in Fourier space is easy to accomplish, since it merely involves a multiplication of the Fourier transformed potential with the Fourier transformed differentiation operator $\tilde{\boldsymbol{D}}(\boldsymbol{k})$. This is a fast, local and accurate operation. Although one might want to use Fourier transforms of discrete difference operators, allowing for the fact that one is actually working on a mesh, the best results are obtained when the Fourier transform of the continuum differential operator, namely $\mathrm{i}\boldsymbol{k}$, is employed. Therefore this method will be referred to as $\mathrm{i}\boldsymbol{k}$-differentiation. The basic idea is not to calculate the mesh based electrostatic potential $\phi^{(k)}(\boldsymbol{r}_p)$ via Eqn. (3.48), but the mesh based electric field $\boldsymbol{E}(\boldsymbol{r}_p)$ by the following simple modification

$$\underline{\boldsymbol{E}(\boldsymbol{r}_p)} \;\approx\; -\frac{\partial}{\partial \boldsymbol{r}_p}\phi^{(k)}(\boldsymbol{r}_p) = -\frac{\partial}{\partial \boldsymbol{r}_p}\big[\rho_{\mathrm{M}} \star G\big](\boldsymbol{r}_p) = \underline{-\overleftarrow{\mathrm{FFT}}\left[\mathrm{i}\boldsymbol{k} \;\times\; \hat{\rho}_{\mathrm{M}} \;\times\; \hat{G}\right](\boldsymbol{r}_p)}. \quad (3.49)$$

This method is chosen in the PME algorithm. As will be shown later, it leads to the most accurate force calculations when it is used in conjunction with the optimal influence function from Eqn. (3.46). Note that since $\boldsymbol{k}$ is a vector, there are in fact *three* inverse three-dimensional Fourier transforms to be calculated in Eqn. (3.49).

The electrostatic energy calculated on the mesh depends on the particle coordinates through the arguments of the charge assignment function W. As the creators of the SPME method point out, a smooth charge assignment scheme permits an analytic differentiation of the energy. This is due to the fact that the quantity ρ_{M} containing the particle coordinates $\boldsymbol{r}_i$ then depends in a differentiable way on the $\boldsymbol{r}_i$. Using Eqns. (3.15, 3.40) and the fact that G is even and independent of particle coordinates, one can derive

$$\begin{aligned}
\boldsymbol{F}_i &\approx -\frac{\partial}{\partial \boldsymbol{r}_i}\frac{1}{2}\sum_{\boldsymbol{r}_p\in\mathbb{M}} h^3\rho_{\mathrm{M}}(\boldsymbol{r}_p)\big[\rho_{\mathrm{M}}\star G\big](\boldsymbol{r}_p) \\
&= -\frac{1}{2}h^6\sum_{\boldsymbol{r}_p,\boldsymbol{r}_q\in\mathbb{M}}\left(\frac{\partial\rho_{\mathrm{M}}}{\partial \boldsymbol{r}_i}(\boldsymbol{r}_p)\rho_{\mathrm{M}}(\boldsymbol{r}_q) + \rho_{\mathrm{M}}(\boldsymbol{r}_p)\frac{\partial\rho_{\mathrm{M}}}{\partial \boldsymbol{r}_i}(\boldsymbol{r}_q)\right)\times G(\boldsymbol{r}_p-\boldsymbol{r}_q) \\
&= -h^6\sum_{\boldsymbol{r}_p,\boldsymbol{r}_q\in\mathbb{M}}\frac{\partial\rho_{\mathrm{M}}}{\partial \boldsymbol{r}_i}(\boldsymbol{r}_p)\rho_{\mathrm{M}}(\boldsymbol{r}_q)\times\frac{1}{2}\Big(G(\boldsymbol{r}_p-\boldsymbol{r}_q)+G(\boldsymbol{r}_q-\boldsymbol{r}_p)\Big) \\
&= -h^3\sum_{\boldsymbol{r}_p\in\mathbb{M}}\frac{\partial\rho_{\mathrm{M}}}{\partial \boldsymbol{r}_i}(\boldsymbol{r}_p)\big[\rho_{\mathrm{M}}\star G\big](\boldsymbol{r}_p). \qquad (3.50)
\end{aligned}$$

Remarks 3.3.5

1. From the definition of the charge assignment in Eqn. (3.33) it is obvious that the array $[\partial\rho_{\mathrm{M}}/\partial\boldsymbol{r}_i](\boldsymbol{r}_p)$ is obtained by a charge assignment scheme which uses the gradient of the assignment function W. It can thus be calculated conveniently at the same time as ρ_{M}.

2. For computing the derivative, the functional relation from Rem. 3.3.3.6 may be helpful.

3. The procedure is fast since only one inverse Fourier transform is required.

4. Unfortunately, this differentiation scheme leads to a small random particle drift, since momentum is not conserved any more. This is discussed in the next subsection. The total momentum of the simulation box can be kept constant by subtracting the mean force $\frac{1}{N}\sum_i \boldsymbol{F}_i$ from each particle. Nevertheless, the reduction in the accuracy of the particle forces due to these local random force fluctuations can be compensated only marginally by this global correction.

A third possibility for implementing the derivative in Eqn. (3.15) is the use of finite difference operators. They calculate the force on one mesh point from the potential at the neighboring mesh points. This is the method which is favored by Hockney and Eastwood for $\mathrm{P^3M}$. Higher accuracy is achieved by considering not only the nearest neighbors but also mesh points farther away, i.e., using linear combinations of nearest neighbor, next nearest neighbor etc. difference operators. TP 3.4 outlines how these approximations are constructed systematically. In the $\mathrm{P^3M}$-method the Fourier transforms of these operators are needed for the calculation of the optimal influence function in Eqn. (3.46). This approach needs only one inverse Fourier transformation, as in the method of analytic differentiation. But unlike the latter, it conserves momentum if the difference operators are chosen correctly [HoEa88]. It therefore has no problems with spurious particle drifts and resulting errors in the force. However, using the neighboring points is a nonlocal approach, and increasing its accuracy can only be achieved by taking into account more neighbors making it even more nonlocal and costly.

Apparently, there is no unique optimal way for doing the differentiation. Each approach combines advantages and drawbacks which have to be balanced against each other under the constraint of required accuracy and available computational resources. For instance, if the required accuracy is not very high, using only the nearest neighbors for the discrete differentiation on the mesh might be accurate enough. Certainly, multiplication in Fourier space by $\mathrm{i}\boldsymbol{k}$ gives better results, but this approach is usually slower due to the two additional Fourier transformations. However, if higher accuracy is required, the finite difference approximation calls for more neighbors and becomes more and more costly. On the other hand, the $\mathrm{i}\boldsymbol{k}$-approach immediately gives the best result possible by discrete differentiation. This is due to the fact that increasing the order of the differentiation scheme implies the Fourier transformed operators to approximate $\mathrm{i}\boldsymbol{k}$ to higher and higher truncation order. In fact, this is how these approximations are constructed, see TP 3.4. In other words, accepting the two additional Fourier transformations can become competitive. Moreover, the method of analytic differentiation could be faster than the discrete difference method even for $J = 1$. Thus, in cases where the latter is less accurate than analytic differentiation, there is no reason for using it.

Technical Point 3.4 *(difference operators)*

Mesh approximations for the differential operator $\mathrm{d}/\mathrm{d}x$ can systematically be written as convex combinations of difference operators. The idea is described for one dimension, the generalization to higher dimensions can be done easily via the Cartesian components.
Define the j^{th}-neighbor centered difference operator Δ_j by

$$(\Delta_j f)(x) := \frac{f(x+jh) - f(x-jh)}{2jh}, \tag{3.51}$$

where h is the mesh spacing and x some mesh point. Applying this operator to a function f can be written as the convolution $D_j \star f$, with $D_j(x) = \frac{1}{2jh}\{\delta(x+jh) - \delta(x-jh)\}$. From the convolution theorem it follows that in Fourier space the derivative is given by $\tilde{D}_j(k)\tilde{f}(k)$, where it is easily verified that $\tilde{D}_j(k) = \mathrm{i}\,\sin(jkh)/jh$. Note that in the limit $h \downarrow 0$ this reduces to the Fourier representation of $\mathrm{d}/\mathrm{d}x$, namely $\mathrm{i}k$.
Since one can expect to achieve better approximations for the differential operator by using linear combinations of the difference operators Δ_j, define a J^{th}-order difference operator by

$$\Delta^{(J)} := \sum_{j=1}^{J} c_j\,\Delta_j \qquad , \qquad c_j \in \mathbb{R}. \tag{3.52}$$

Using the Fourier representation of the differential and the j^{th}-neighbor centered difference operator, one demands that the linear combinations approximate $\mathrm{i}k$ to as high an order as possible:

$$\sum_{j=1}^{J} c_j\,\mathrm{i}\frac{\sin(jkh)}{jh} = \mathrm{i}k + \mathscr{O}((kh)^{2J+1}) \qquad \text{or} \qquad \sum_{j=1}^{J} c_j\,\cos(jkh) = 1 + \mathscr{O}((kh)^{2J}). \tag{3.53}$$

The second equation follows from differentiating the first with respect to k. Taylor expanding the cosine in Eqn. (3.53ii) and equating coefficients gives J linear equations for the J unknowns c_j. The first few are given in the following table:

order J	c_1	c_2	c_3	c_4	c_5	c_6	c_7
1	1						
2	$4/3$	$-1/3$					
3	$3/2$	$-3/5$	$1/10$				
4	$8/5$	$-4/5$	$8/35$	$-1/35$			
5	$5/3$	$-20/21$	$5/14$	$-5/63$	$1/126$		
6	$12/7$	$-15/14$	$10/21$	$-1/7$	$2/77$	$-1/462$	
7	$7/4$	$-7/6$	$7/12$	$-7/33$	$7/132$	$-7/858$	$1/1716$

Note that in the case of the 2^{nd}-order approximation the weighting $(\frac{4}{3}, -\frac{1}{3})$, which empirically was found to be optimal [HoEa88], is reproduced.

algorithm	charge assignment	Poisson solver	differentiation	reference
PME	Lagrange, TP 3.3	Eqn. (3.42, $B \equiv 1$)	$i\boldsymbol{k}$, Eqn. (3.49)	[DaYo93]
SPME	spline, Eqn. (3.38)	Eqn. (3.42, 3.43)	analytic, Eqn. (3.50)	[EsPe95]
P^3M	spline, Eqn. (3.31)	Eqn. (3.46)	discrete, TP 3.4	[HoEa88]

Table 3.1: Compilation of the "modules" which comprise the original particle mesh routines discussed in this chapter.

Whether there exists a break-even point between these methods and – if yes – where it is located depends on the tuning parameters like mesh size and interpolation order as well as on the details of the implementation or the computational facilities one is working with. A general statement seems to be difficult.

3.3.4 Back-interpolation

At some stage of any particle mesh method a back-interpolation of the mesh based results to the actual particles is necessary. As has been demonstrated in the last subsection, this can be done before or after the Fourier transformation back to real space, i.e., the mesh points can carry either the potential or the components of the electric field.

This back-interpolation is done in a similar way as the distribution of the charges to the mesh at the beginning of the calculation, namely, via some assignment function W. For instance, the force on particle i is given by

$$\boldsymbol{F}_i = q_i \sum_{\boldsymbol{r}_p \in \mathbb{M}} \boldsymbol{E}(\boldsymbol{r}_p) W(\boldsymbol{r}_i - \boldsymbol{r}_p), \tag{3.54}$$

with $\boldsymbol{E}(\boldsymbol{r}_p)$ being the electric field on mesh point $\boldsymbol{r}_p$ in Eqn. (3.49). Eqn. (3.54) can be illustrated in the following way: Due to the discretization each particle is replaced by several "sub-particles" located at the surrounding mesh points and carrying a certain fraction of the charge of the original particle. The force on each sub-particle is given by its charge times the electric field at its mesh point, and the total force acting on the original particle is the sum of the forces acting on its sub-particles.

From a technical point of view it is convenient to use the same function W for the assignment onto and the back-interpolation from the mesh. If in the first step one not only calculates the total charge accumulated at some mesh point but additionally memorizes, to what extend the individual particles contributed to this charge, the interpolation back can be done without a single function call to W.

There is also a more subtle reason suggesting a symmetric interpolation, which is related to the conservation of momentum. As demonstrated by Hockney and Eastwood [HoEa88], *(i)* the force which a particle acts onto itself is zero, and *(ii)* Newton's third law is obeyed, if

- charge assignment and force interpolation are done by the same function W, and
- the approximations to the derivatives are correctly space centered.

The second requirement states that if the electric field at some mesh point $\boldsymbol{r}_p$ can formally be written as $\sum_{\boldsymbol{r}_q} \boldsymbol{d}(\boldsymbol{r}_p, \boldsymbol{r}_q)\rho_{\mathrm{M}}(\boldsymbol{r}_q)$, then $\boldsymbol{d}(\boldsymbol{r}_p, \boldsymbol{r}_q) = -\boldsymbol{d}(\boldsymbol{r}_q, \boldsymbol{r}_p)$.

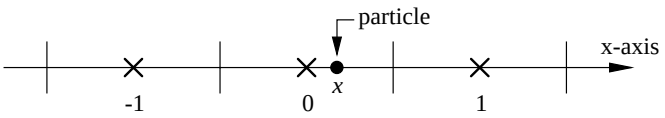

Figure 3.6: Schematic illustration of three-point charge assignment. The crosses are the mesh points and the lines indicate the Wigner-Seitz cell boundaries of each point. The mesh spacing is $h = 1$. All particles with $x \in [-\frac{1}{2}, +\frac{1}{2}]$ distribute their charge between the mesh points at -1, 0 and +1 and the corresponding charge fractions are $W_p(x)$, $p \in \{-1, 0, +1\}$. (After [HoEa88])

The method of analytical differentiation mentioned in the last subsection does not use mesh based derivatives. This is the approach chosen in the implementation of SPME. The inventors of the method state that the sum of the electrostatic forces on the atoms is not zero but a random quantity of the order of the rms error in the force [EsPe95]. It is reasonable to believe that these fluctuations have their origin in a violation of the above conditions, although strictly speaking these are only *sufficient* conditions for momentum conservation.

For a more detailed discussion of related effects and the connection between momentum conserving and energy conserving methods see Hockney and Eastwood [HoEa88].

3.3.5 Charge assignment with B-splines

This section describes the procedure of charge assignment in more detail and tabulates the charge fractions needed for a P^{th} order assignment scheme à la Hockney and Eastwood [HoEa88], see Eqns. (3.30,3.31).

Let the units be chosen such that the grid spacing is 1. For any P consecutive mesh points there exists an interval $\mathscr{I}$ of length 1 such that the charge of a particle with coordinate $x \in \mathscr{I}$ is distributed between these mesh points. By simple shifting one can assume this interval to be $[-\frac{1}{2}, +\frac{1}{2}]$. Then the P mesh points will lie at $-\frac{P-1}{2}, -\frac{P-1}{2} + 1, \ldots, \frac{P-1}{2}$. This is schematically illustrated in Fig. 3.6 for $P = 3$. The charge fraction $W_p(x)$, which will be assigned to the mesh point x_p, is related to the charge assignment function $W(x)$ via $W_p(x) = W(x - x_p)$.

The basic steps which have to be done for a particle with coordinate x, generally not in $[-\frac{1}{2}, +\frac{1}{2}]$, during a P^{th} order charge assignment are thus

1. Define $\bar{x}$ to be the coordinate of the mesh point being closest to the particle if P is odd, or the midpoint between the two closest mesh points if P is even.

2. Find the P mesh points x_p which are closest to x. They will be indexed by their position relative to $\bar{x}$, so $p \in \{-\frac{P-1}{2}, -\frac{P-1}{2} + 1, \ldots, \frac{P-1}{2}\}$.

3. The fraction of charge which is assigned to each of these mesh points is given by $W_p(x - \bar{x})$.

In this way the charge fractions are written as a function of the separation $x - \bar{x} \in [-\frac{1}{2}, +\frac{1}{2}]$. Hockney and Eastwood refer to the cases $P = 1$, 2 and 3 as NGP (nearest grid point), CIC (cloud in cell) and TSC (triangular shaped cloud), respectively. Generally, for $P \in \{1, \ldots, 7\}$ the charge fractions $W_p^{(P)}(x)$ are given by the following polynomials:

$P = 1$:

$$W_0^{(1)}(x) = 1$$

$P = 2$:

$$\begin{aligned} W_{-1/2}^{(2)}(x) &= \frac{1}{2}(1-2x) \\ W_{+1/2}^{(2)}(x) &= \frac{1}{2}(1+2x) \end{aligned}$$

$P = 3$:

$$\begin{aligned} W_{-1}^{(3)}(x) &= \frac{1}{8}(1-4x+4x^2) \\ W_{0}^{(3)}(x) &= \frac{1}{4}(3-4x^2) \\ W_{+1}^{(3)}(x) &= \frac{1}{8}(1+4x+4x^2) \end{aligned}$$

$P = 4$:

$$\begin{aligned} W_{-3/2}^{(4)}(x) &= \frac{1}{48}(1-6x+12x^2-8x^3) \\ W_{-1/2}^{(4)}(x) &= \frac{1}{48}(23-30x-12x^2+24x^3) \\ W_{+1/2}^{(4)}(x) &= \frac{1}{48}(23+30x-12x^2-24x^3) \\ W_{+3/2}^{(4)}(x) &= \frac{1}{48}(1+6x+12x^2+8x^3) \end{aligned}$$

$P = 5$:

$$\begin{aligned} W_{-2}^{(5)}(x) &= \frac{1}{384}(1-8x+24x^2-32x^3+16x^4) \\ W_{-1}^{(5)}(x) &= \frac{1}{96}(19-44x+24x^2+16x^3-16x^4) \\ W_{0}^{(5)}(x) &= \frac{1}{192}(115-120x^2+48x^4) \\ W_{+1}^{(5)}(x) &= \frac{1}{96}(19+44x+24x^2-16x^3-16x^4) \\ W_{+2}^{(5)}(x) &= \frac{1}{384}(1+8x+24x^2+32x^3+16x^4) \end{aligned}$$

$P = 6$:

$$
\begin{aligned}
W^{(6)}_{-5/2}(x) &= \frac{1}{3840}(1 - 10x + 40x^2 - 80x^3 + 80x^4 - 32x^5) \\
W^{(6)}_{-3/2}(x) &= \frac{1}{3840}(237 - 750x + 840x^2 - 240x^3 - 240x^4 + 160x^5) \\
W^{(6)}_{-1/2}(x) &= \frac{1}{1920}(841 - 770x - 440x^2 + 560x^3 + 80x^4 - 160x^5) \\
W^{(6)}_{+1/2}(x) &= \frac{1}{1920}(841 + 770x - 440x^2 - 560x^3 + 80x^4 + 160x^5) \\
W^{(6)}_{+3/2}(x) &= \frac{1}{3840}(237 + 750x + 840x^2 + 240x^3 - 240x^4 - 160x^5) \\
W^{(6)}_{+5/2}(x) &= \frac{1}{3840}(1 + 10x + 40x^2 + 80x^3 + 80x^4 + 32x^5)
\end{aligned}
$$

$P = 7$:

$$
\begin{aligned}
W^{(7)}_{-3}(x) &= \frac{1}{46080}(1 - 12x + 60x^2 - 160x^3 + 240x^4 - 192x^5 + 64x^6) \\
W^{(7)}_{-2}(x) &= \frac{1}{23040}(361 - 1416x + 2220x^2 - 1600x^3 + 240x^4 + 384x^5 - 192x^6) \\
W^{(7)}_{-1}(x) &= \frac{1}{46080}(10543 - 17340x + 4740x^2 + 6880x^3 - 4080x^4 - 960x^5 + 960x^6) \\
W^{(7)}_{0}(x) &= \frac{1}{11520}(5887 - 4620x^2 + 1680x^4 - 320x^6) \\
W^{(7)}_{+1}(x) &= \frac{1}{46080}(10543 + 17340x + 4740x^2 - 6880x^3 - 4080x^4 + 960x^5 + 960x^6) \\
W^{(7)}_{+2}(x) &= \frac{1}{23040}(361 + 1416x + 2220x^2 + 1600x^3 + 240x^4 - 384x^5 - 192x^6) \\
W^{(7)}_{+3}(x) &= \frac{1}{46080}(1 + 12x + 60x^2 + 160x^3 + 240x^4 + 192x^5 + 64x^6)
\end{aligned}
$$

3.4 Investigating the accuracy

The root mean square error in the force provides one way of assessing the quality of different particle mesh algorithms. Using this measure, the P³M algorithm with Fourier space differentiation emerges as the most accurate procedure.

An investigation of the errors connected with particle mesh Ewald methods is important for three reasons:

1. The procedure of discretization introduces new sources of errors in addition to the ones originating from real and reciprocal space cutoffs.

2. Comparing the efficiency of different mesh methods is only fair, if it is done at the same level of accuracy.

3. The tuning parameters should be chosen in such a way as to run the algorithm at its optimal operation point.

However, there is no unique or optimal measure of accuracy. If molecular dynamics simulations are performed, the main interest lies in errors connected with the force, while in Monte-Carlo simulations one is concerned with accurate energies. In the simulation of ensemble averages it is the global accuracy, measured e.g. by root mean square quantities, which is important. In the simulation of rare events local accuracy and maximal errors are relevant as well. Errors in the force can be due to their magnitude or due to their direction. And finally, one might be interested in absolute or relative errors.

Whatever quantity one decides to look at, it can be investigated as a function of *system* parameters like particle separation or distribution, *tuning* parameters like α, mesh size or interpolation order and *components* of the algorithm, e.g., interpolation or differentiation scheme or splitting function $f(r)$. This obviously gives rise to a very large number of combinations. In other words: The corresponding parameter space is large and nontrivial, i.e., general statements concerning the performance of one method can usually not be extracted from low-dimensional cuts through this space, since different methods scale differently with respect to their parameters.

This section nevertheless presents some numerical accuracy measurements at important points of this parameter space for the following reasons: As emphasized before, there are several options for the implementation of each step of a mesh calculation – e.g. three ways for doing the derivative in Eqn. (3.15). This freedom of choice and its impact on the overall accuracy has so far not been systematically investigated in the literature, although a qualitative understanding of at least *typical* influences of the different parts on the performance permits a judicious assessment and comparison of the resulting algorithms, in particular P^3M, PME and SPME. It is shown which combinations are attractive and which should definitely be avoided. And finally, the presented measurements comprise easily reproducible data which should allow the reader a comparison with own implementations of particle mesh Ewald routines. Still, the aim of this section is not a presentation of large accurate tables, claiming to provide an easy way for tuning these algorithms under all circumstances. On the contrary, any potential user is encouraged to perform some of these simple measurements on his/her own, thereby not only gaining insight but also the possibility to optimize the tuning parameters. It must be stressed that parameters which are only roughly estimated or even historically handed down should be taken with great care.

This work will solely be concerned with one measure of accuracy, namely the root mean square (rms) error in the force given by

$$\Delta F := \sqrt{\frac{1}{N}\sum_{i=1}^{N}\left(\boldsymbol{F}_i - \boldsymbol{F}_i^{\mathrm{exa}}\right)^2}, \tag{3.55}$$

where $\boldsymbol{F}_i$ is the force on particle number i calculated via some mesh method and $\boldsymbol{F}_i^{\mathrm{exa}}$ is the *exact* physical force on that particle, calculable e.g. by a well converged standard Ewald sum. There exist error estimates for the real space and Fourier space contribution to this error for the standard Ewald sum [KoPe92] and for the PME method [Pet95]. Their existence greatly simplify the determination of the optimal value of α. For the case of the in particular i$\boldsymbol{k}$-differentiated P^3M method such a formula is derived in Sec. 3.5.

Technical Point 3.5 *(Random model system)*

The model system used for testing the particle mesh routines is easiest described by explaining its generation. The coordinates of 100 particles are constructed by first drawing 300 random numbers $\mathscr{R}_n$ between 0 and 1. If L is the box length then particle 1 gets the coordinates $(L\mathscr{R}_1, L\mathscr{R}_2, L\mathscr{R}_3)$, particle 2 gets $(L\mathscr{R}_4, L\mathscr{R}_5, L\mathscr{R}_6)$ and so on. Moreover, particles with an even/odd number will get a positive/negative unit charge.

The choice of the random number generator is the following: If a_n is a positive integer, define its successor $a_{n+1} := (1103515245\, a_n + 12345) \mod 2^{32}$ and from this construct the pseudo random number $\mathscr{R}_n := [(a_n \div 65536) \mod 32768]/32769$, where "$\div$" should denote an integer division which discards any division rest. Choosing $a_0 = 1$ yields the sequence of random numbers $16838, 5758, 10113, \ldots$, of which the first 300 are used for positioning the particles, e.g. with $L = 10$ the first particle has coordinates $(5.138\ldots, 1.757\ldots, 3.086\ldots)$ and a negative unit charge. The smallest minimum image distance is approximately 0.370264 and occurs between particle 46 and particle 98. This random number generator is not particularly good, but very easy to implement. Many `C` libraries provide a function `rand`, which relies on the described formulæ.

3.4.1 Error as a function of α

The rms error (3.55) is computed for a system of 100 particles (50 carry a positive and 50 a negative unit charge), which were randomly placed within a simulation box of length $L = 10$, as a function of the Ewald parameter α. In order to make the results fully reproducible, the actual random configuration is described in TP 3.5. See TP 3.1 for the conventions on units.

For small α the result of the Ewald sum (or any of the described particle mesh methods) is dominated by the real space contribution in Eqn. (3.17) while for large α the Fourier part (3.18) becomes more important. This is a simple consequence of the fact that in the real space sum the Ewald parameter α occurs in the numerator of the exponential function (or – to be precise – of the complementary error function) while in the Fourier space sum it occurs in the denominator. It therefore influences the decay of both contributions in a converse way. Hence, at given cutoffs the same applies to the errors. Since with increasing α the real space contribution becomes more accurate while the Fourier space contribution degrades in accuracy, one can expect an optimal α to exist at which the *total* error is minimal. This is approximately at the point where real space and Fourier space errors are equal. Since the different mesh methods all coincide in the treatment of the real space part, their errors should all be the same for sufficiently small α.

Fig. 3.7 shows the rms error of the force as a function of α, which was obtained by investigating the model system from TP 3.5 with various mesh methods. They all share a mesh size of $N_\mathrm{M} = 32$ (and thus have 32^3 mesh points in total), an interpolation order $P = 7$ and a real space cutoff $r_\mathrm{max} = 4$. The general features described above, like a low accuracy for very small or very large values of α and an optimal value in-between, are clearly visible. However, the various methods differ considerably in their accuracy. Note that in this and the following figures the vertical scale is logarithmic.

The solid line corresponds to PME. This method comprises two elements which make one think about possible improvements: a not very smooth charge assignment scheme (namely, the Lagrange interpolation) and the use of the plain continuum Green function.

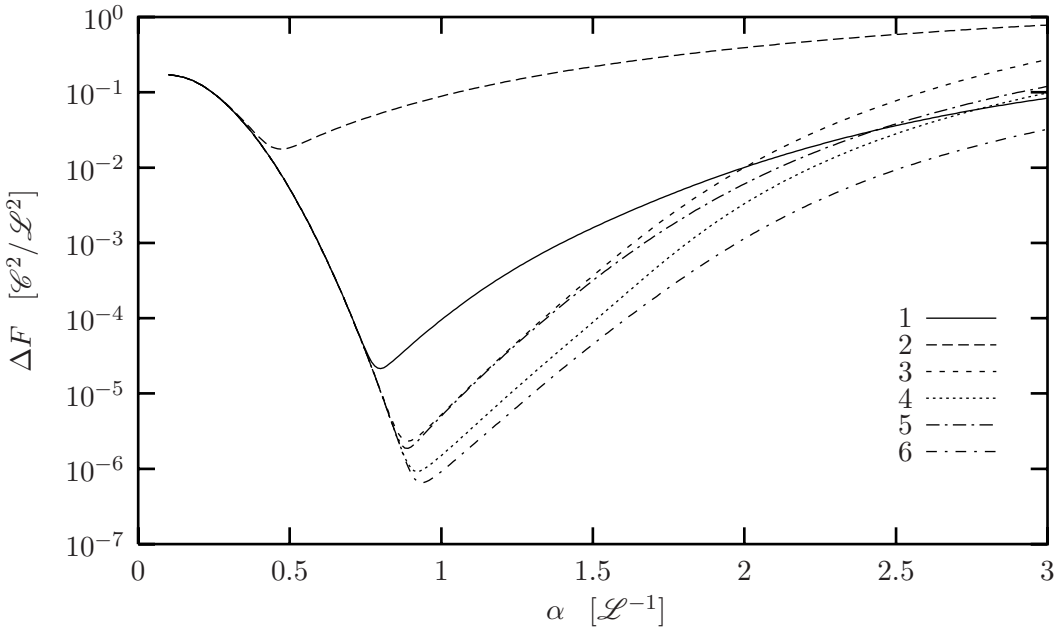

Figure 3.7: Comparison of different mesh methods: The rms error ΔF from Eqn. (3.55) for a system of 100 charged particles randomly distributed within a cubic box of length $L = 10$ (see TP 3.5) is shown as a function of the Ewald parameter α for 6 mesh algorithms, which all share $N_{\mathrm{M}} = 32$, $P = 7$ and $r_{\max} = 4$. Line 1 is PME. Line 2 corresponds to an algorithm which is obtained from PME by retaining the continuum Green function but changing to the spline charge assignment. Lines 3 and 4 are analytically and i$\boldsymbol{k}$-differentiated SPME respectively and line 5 and 6 are analytically and i$\boldsymbol{k}$-differentiated $\mathrm{P^3M}$ respectively. Note the logarithmic vertical scale in this and the following figures.

There is clearly no *obvious* advantageous replacement for the latter, but it is easy to replace the Lagrange scheme by the smooth spline interpolation by just changing the assignment function. Yet, the result of this supposed improvement, shown in line 2, is in fact disappointing. As mentioned in TP 3.3, the continuum Green function is best accompanied by a Lagrange interpolation scheme, since this leads to a cancellation of certain discretization errors. Changing the assignment scheme destroys this effect and the resulting error shatters the desired improvement in accuracy completely.

Improving upon PME requires a proper treatment of both elements – charge assignment and Green function. This is in fact what the remaining two algorithms (SPME and $\mathrm{P^3M}$) accomplish. Since they both use a smooth spline interpolation, they are both potential candidates for analytic differentiation. In fact, the SPME method, as described in the original publication [EsPe95], chooses this implementation of the derivative, because it is very fast (line 3). Nevertheless, the i$\boldsymbol{k}$-method is still possible and leads to an even better result (line 4), which admittedly has to be payed with two additional FFT calls. Analytically differentiated $\mathrm{P^3M}$ gives an error almost identical to analytically differentiated SPME, but if one implements the i$\boldsymbol{k}$-derivative, $\mathrm{P^3M}$ improves slightly on SPME. From a theoretical point of view this is not surprising: After all, if $\mathrm{P^3M}$ uses an optimal differentiation (in view of accuracy) and an optimal influence function, it can be expected to constitute a lower bound for the error. If, however, the optimal differentiation is replaced

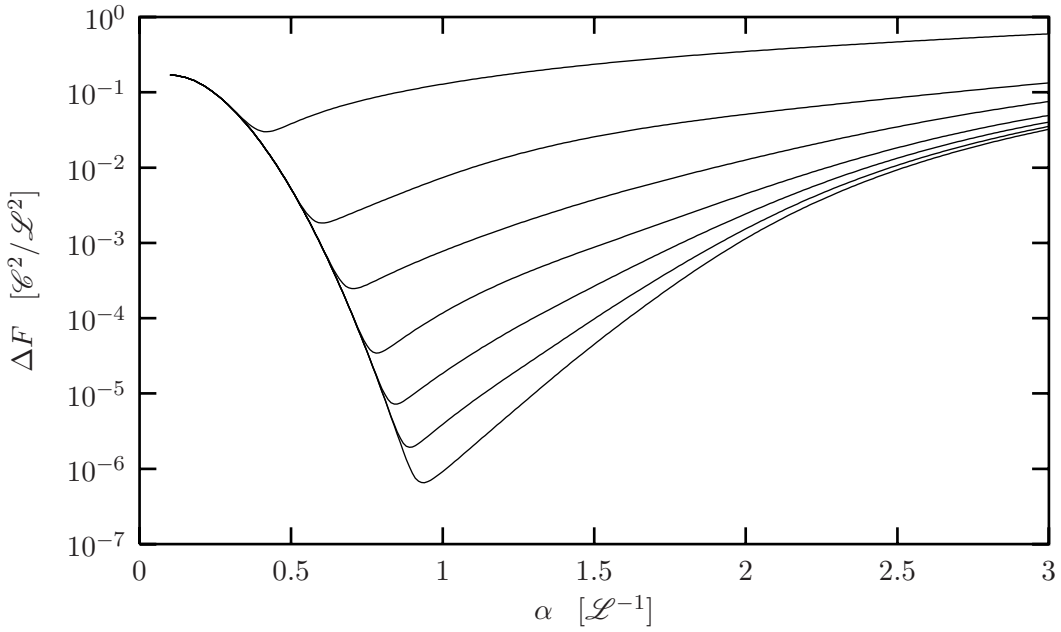

Figure 3.8: Influence of the charge assignment order: The rms error ΔF for the model system from TP 3.5 is calculated for the i$\boldsymbol{k}$-differentiated P^3M method with $N_M = 32$ and $r_{max} = 4$. From top to bottom the order P of the (spline) charge assignment scheme is increased from 1 to 7.

by the analytic differentiation, a new source of error appears (namely, the random force fluctuations described in Rem. 3.3.5.4 and Sec. 3.3.4). If this contribution dominates, the fact that P^3M uses a better influence function than SPME cannot make a large difference. In the present case the analytically differentiated SPME is a factor of 9.2 more accurate than PME, while the i$\boldsymbol{k}$-differentiated P^3M method is more accurate than PME by a factor of about 33. One must however realize that SPME and P^3M have different execution times, since P^3M needs two additional FFT calls compared to SPME. But apart from the analytically differentiated curves all methods summarized in Fig. 3.7 need exactly the same time for a mesh calculation. This comes from the fact that the methods differ only in parts which normally are tabulated anyway like, e.g., the influence function.

There is another surprising thing to note about SPME: For the chosen values of N_M and P the curves for PME and (analytically differentiated) SPME intersect, i.e., the latter is not necessarily more accurate. It could be argued that at least for the optimal value of α SPME is better, but this optimal α of course depends on the real space cutoff r_{max} as well. If this cutoff is decreased, the real space contribution to the error is increased. In fact, using the estimate of Kolafa and Perram [KoPe92] one finds that at the intersection point of PME and SPME this contribution will have the same size as the Fourier space contribution for (in this case) $r_{max} \approx 1$. Thus, for even smaller values of r_{max} PME would actually be more accurate than SPME.

After comparing various particle mesh methods, the next step is to examine in a little more detail some parts of the algorithm. For illustration the P^3M method is used exclusively, since corresponding plots for PME or SPME would look qualitatively very similar.

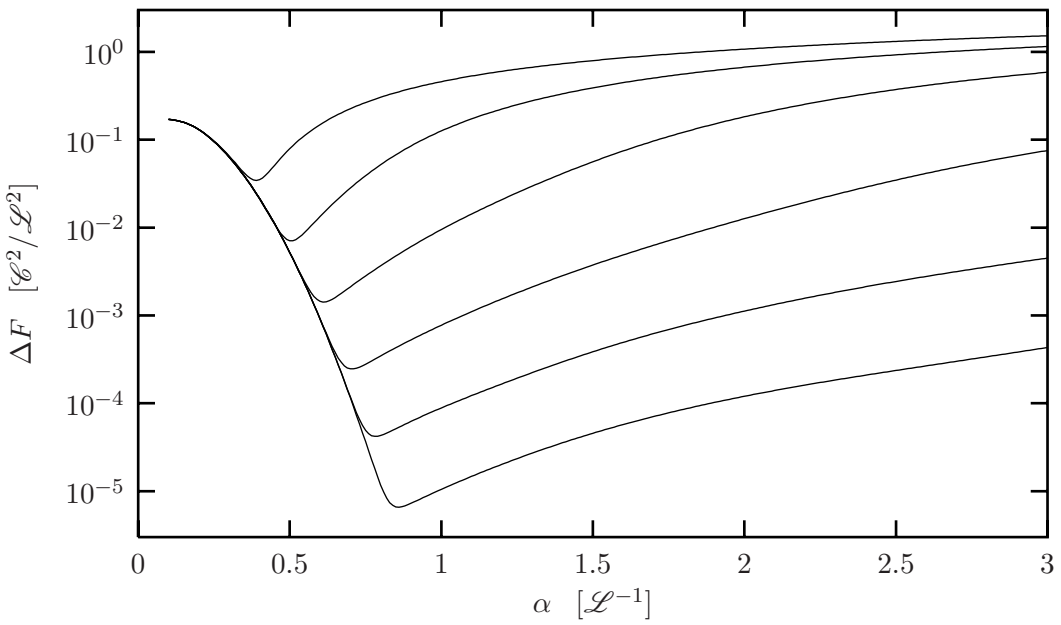

Figure 3.9: Influence of the mesh size: The rms error ΔF for the model system from TP 3.5 is calculated for the i$\boldsymbol{k}$-differentiated P^{3}M method with $P = 3$ and $r_{\max} = 4$. From top to bottom the mesh size N_{M} is given by 4, 8, 16, 32, 64 and 128. (Note that the total number of mesh points in this three-dimensional system is given by $(N_{\mathrm{M}})^3$.)

In Figure 3.8 the parameters of the i$\boldsymbol{k}$-differentiated P^{3}M method from Fig. 3.7 have been taken, but the charge assignment order is varied from $P = 1$ to $P = 7$. Increasing P improves the accuracy by more than three orders of magnitude (from $P = 1$ to $P = 7$), but the reward for going from P to $P + 1$ is larger for small P. Note also that the optimal value of α depends on P.

In Figure 3.9 the order of the charge assignment scheme is fixed at $P = 3$ and the number N_{M} of Fourier mesh points is varied. Qualitatively the behavior is similar to Fig. 3.8: Improving the method reduces the error and shifts the optimal α to the right. Note that from a computational point of view Figs. 3.8 and 3.9 are conjugate in the following sense: The accuracy depends on both N_{M} and P, but increasing one parameter does not influence the performance of the other. In other words, the charge assignment scales as P^3 independent of N_{M} and the FFT scales as $(N_{\mathrm{M}} \log N_{\mathrm{M}})^3$ independent of P. Optimal performance requires a suitable combination of N_{M} and P.

The next investigation concerns the differentiation scheme. To this end the P^{3}M method with $N_{\mathrm{M}} = 32$ and $P = 7$ is used and various orders J of the mesh based approximation to the difference operator (see TP 3.4) are employed.[9] The results are shown in Fig. 3.10, which looks pretty much like Fig. 3.8 but has been generated quite differently. With increasing order of the difference approximation the errors decrease and finally converge towards the result of the i$\boldsymbol{k}$-differentiation scheme, which provides a lower bound to

[9] The actual calculations have been done by a multiplication in Fourier space with the transformed approximations $\tilde{\boldsymbol{D}}^{(J)}$, which is not how the discrete differentiation should be implemented in any real code. Still, it gives the correct results for this comparison.

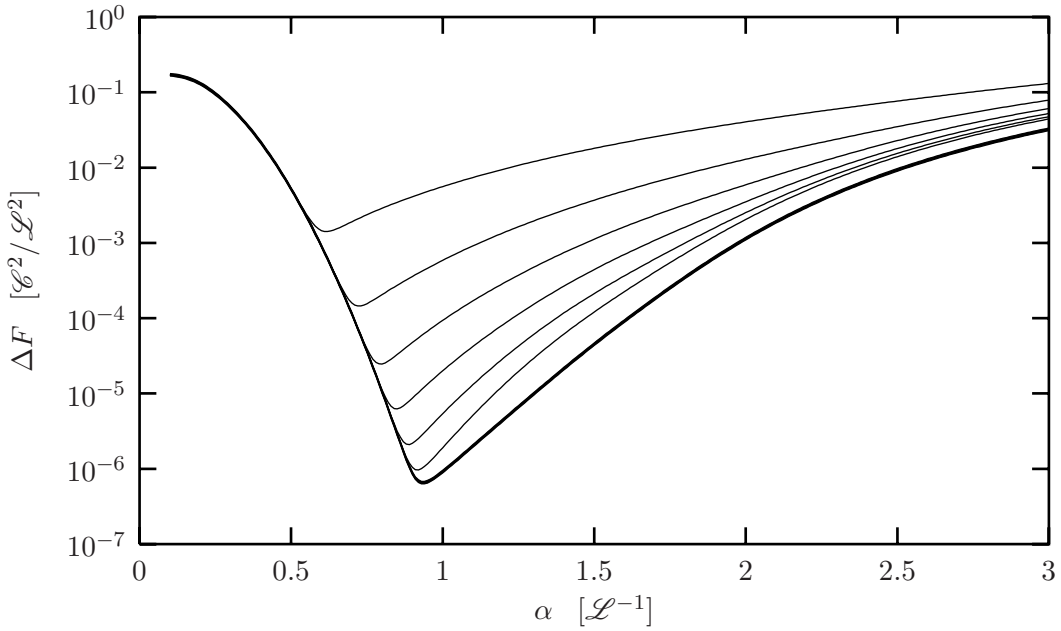

Figure 3.10: Influence of the differentiation scheme: The rms error ΔF for the model system from TP 3.5 is calculated for the P^3M method with $N_M = 32$, $P = 7$ and $r_{max} = 4$. Shown are 6 mesh based approximations to the differentiation operator i$\boldsymbol{k}$ (from top to bottom: $\Delta^{(1)}, \ldots, \Delta^{(6)}$, see TP 3.4) as well as the result for i$\boldsymbol{k}$ itself (lowest curve, bold line).

the error of this method. After all, i$\boldsymbol{k}$ is the Fourier representation of the exact differential operator, and in the standard Ewald sum the differentiation is also done this way, as can be seen in Eqn. (3.18). In Fig. 3.10 the lower bound is reached in the minimum at $J = 7$, so further improving the differentiation order is not useful. Of course, if the accuracy of the lower bound is smaller (since, e.g., the charge assignment order is lower) the i$\boldsymbol{k}$-bound will be reached already by smaller values of J. Note that in this example the method of analytic differentiation gives approximately the same accuracy as a fifth order difference scheme (compare to Fig. 3.7). Since analytic differentiation is much faster, it should be preferred to the finite difference approach in cases where the latter is less accurate anyway.

The last part of this section deals with the determination of the optimal α-value. There exist rather good estimates for the real- and reciprocal space error of the standard Ewald sum [KoPe92] and the reciprocal space error of the PME method [Pet95]. The optimal α-value of these two methods and the corresponding accuracy can be obtained very precisely by simply calculating the intersection point of the real- and corresponding reciprocal space estimates. Their high quality is clearly demonstrated in Fig. 3.11. The existence of these formulas has ever been a big advantage of the PME method, since it permits an a priori determination of the optimal operation point as a function of system specifications (like box length, particle number or valence) or method parameters (like mesh size or assignment order). The derivation of a similar error estimate for the P^3M method is the focus of Sec. 3.5. This is basically the last step which is missing to advocate P^3M as the most accurate and versatile Ewald mesh method.

Some concluding remarks concerning the accuracy of mesh methods compared to the Ewald sum seem appropriate. The optimal α value for a standard Ewald summation of

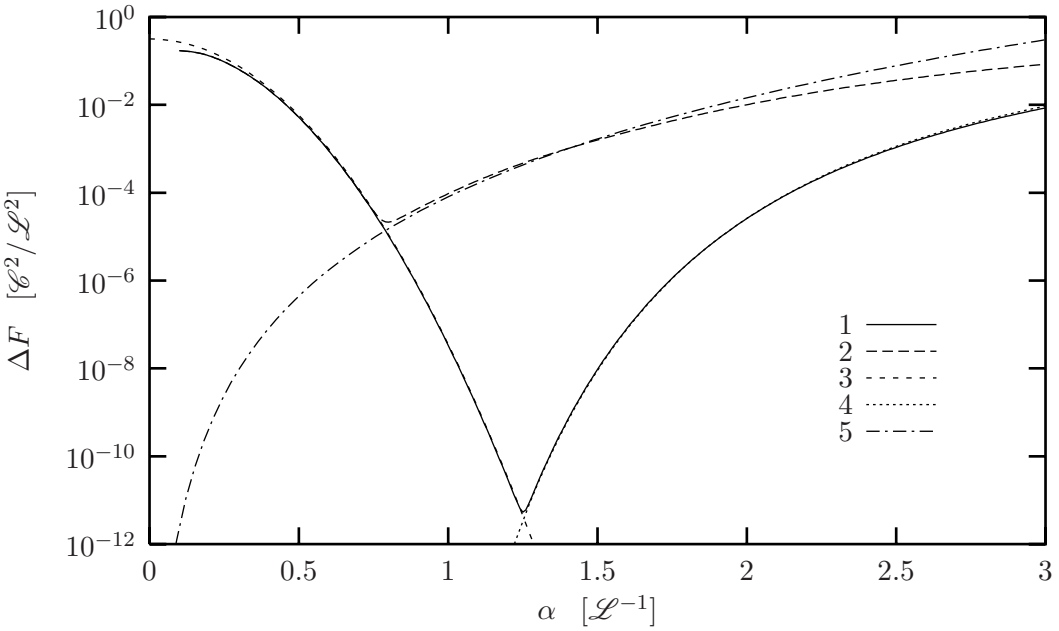

Figure 3.11: Comparison of a mesh method with the standard Ewald sum: The rms error ΔF for the Ewald (line 1) and PME (line 2) method are calculated for the model system from TP 3.5. The parameters for PME are the same as in Fig. 3.7 and the Fourier space cutoff for the Ewald sum is set to $k_{\max} = 20 \times 2\pi/L$. This value is interesting to compare with the PME method, because it corresponds to the same number of $\boldsymbol{k}$-vectors (since $\frac{4}{3}\pi\, 20^3 \approx 32^3$). Also shown is the estimate for the real space error [KoPe92] (line 3), the Fourier space error for Ewald (line 4, the slightly better estimate from Petersen [Pet95] has been used) and the Fourier space error for PME [Pet95] (line 5). Note that the estimates for the Ewald sum can hardly be distinguished from line 1.

the model system with $k_{\max} = 20 \times 2\pi/L$ (which thus has the same number of $\boldsymbol{k}$-vectors, because $\frac{4}{3}\pi\, 20^3 \approx 32^3$) is approximately 1.25 and the corresponding total error is of the order 5×10^{-12} (see Fig. 3.11). Although much optimization effort has been put into mesh methods in order to reduce errors, one must face the fact that one generally loses many orders of magnitude in accuracy due to discretization. If high accuracy is essential but speed is not an issue, the conventional Ewald method is unsurpassed: it is much easier to program and the desired accuracy can be increased up to machine precision without any additional programming effort. It would however be misleading to infer that particle mesh methods sacrifice accuracy in favor of speed, because due to the more advantageous scaling with particle number (essentially $N \log N$ compared to $N^{3/2}$) there will always be a critical number N^*, such that the mesh method will be faster than the Ewald sum for particle numbers $N > N^*$. See e.g. Ref. [Pet95] for a discussion of the break-even value N^* for PME.

3.4.2 Error as a function of minimum image distance

Instead of calculating the rms error for a complete configuration, it is also instructive to investigate it as a function of the minimum image distance r between two particles. This offers a possibility to monitor the distance dependence of the accuracy for the various methods. Thus, pairs of particles have been created randomly inside the simulation box

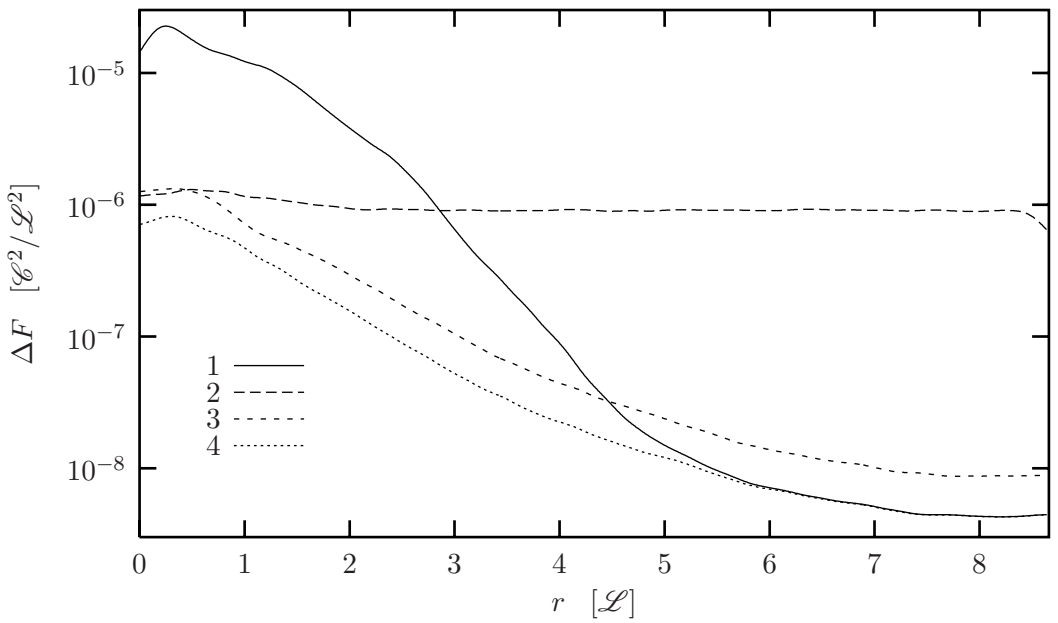

Figure 3.12: Distance dependency: The rms error ΔF as a function of the minimum image separation r between two particles is shown for several mesh methods, which all share $N_{\mathrm{M}} = 32$ and $P = 7$. Line 1 corresponds to PME, line 2 and 3 are analytically and i$\boldsymbol{k}$-differentiated SPME respectively and line 4 is i$\boldsymbol{k}$-differentiated P^{3}M. For each method α is individually set to its optimal value from Fig. 3.7: $\alpha_1 = 0.8$, $\alpha_2 = 0.89$, $\alpha_3 = 0.92$ and $\alpha_4 = 0.94$.

with $L = 10$ with *given* minimum image separation r, and the rms error is computed from Eqn. (3.55). This has been repeated for 5×10^4 separations equally spaced between 0 and $\frac{1}{2}\sqrt{3}L$, which is the largest possible minimum image separation in a cubic box. As this is done at constant α for each method, the real space contribution to the force always cancels when performing the difference in Eqn. (3.55). Hence, this plot is only sensitive to the Fourier contribution, and it is not necessary to specify a real space cutoff. A grid with $N_{\mathrm{M}} = 32$ and a charge assignment order of $P = 7$ was used. However, as can be seen from Fig. 3.7, different methods have their optimal operation point at different values of α. Therefore it is more sensible to compare the different methods at their individual optimal value of α, which can be obtained from Fig. 3.7. Although the curves in Fig. 3.7 correspond to a system which contains 100 particles (and not just 2), this has no influence on the optimal value of α, since real space and Fourier space contribution to ΔF display the same dependence on particle number. See also the general discussion of the scaling of ΔF with particle number and valence in 3.5.1.

The Coulomb problem in the given periodic geometry lacks spherical symmetry and due to the existence of a grid also the translational symmetry is broken. So – strictly speaking – ΔF is not just a function of r but also depends on the relative orientation of the particles and their location within the box. This manifests itself in the fact that the measured points $\Delta F(r)$ do not collapse onto a single smooth curve but show some scatter. Since the present discussion does not focus on this anisotropy effect, the scatter is averaged by binning 50 points together at one time and additionally performing a Gaussian

smoothing (with width 0.1). This makes the data easier to plot and understand.

The result of this measurement is shown in Fig. 3.12. Several interesting things can be observed. All algorithms produce their largest errors at small distances and they become considerably more accurate at larger values of r – with one exception: The analytically differentiated SPME method almost immediately settles to a comparatively large constant error. Since the only difference between lines 2 and 3 is the differentiation scheme, it must be the random force fluctuations discussed in Rem. 3.3.5.4 and Sec. 3.3.4 which are responsible for this effect. Note that PME at some distance gives better results than i$\boldsymbol{k}$-differentiated SPME. Also it is most surprising that at large distances PME and P^3M give identical errors, although they differ considerably in the charge assignment scheme as well as in the employed Coulomb Green function. Finally, the i$\boldsymbol{k}$-differentiated P^3M method is most accurate for all distances. In this case this is not surprising, since the quantity Q from Eqn. (3.44), with respect to which P^3M is optimized, is essentially the integral over any of these curves in Fig. 3.12, weighted with the probability density of the minimum image distance r.

3.5 Error estimate for the P^3M algorithm

The rms force error is proportional to the sum of the square of all charges and inversely proportional to the square root of the number of charged particles. The proportionality constant is known for the P^3M algorithm, which permits the construction of a highly accurate error estimate.

Up to now a unified view on FFT accelerated methods has been presented and detailed accuracy measurements have been carried out. Since, however, all these algorithms contain various free parameters, working at the maximally obtainable accuracy requires the user to tune them very carefully. This is straightforward if there exists a theoretical estimate of the errors involved – as is the case for the standard Ewald sum [KoPe92] as well as for the so-called particle mesh Ewald (PME) method [Pet95] – but rather tedious otherwise.

In this section such an estimate for the root mean square error in the force of the so-called particle-particle–particle-mesh (P^3M) algorithm is constructed by extending an error measure derived by Hockney and Eastwood [HoEa88], and an easy to use analytical approximation to the expression comprising various sums is presented. This allows a straightforward and precise determination of the optimal splitting parameter as a function of system specifications and P^3M parameters and hence knowledge of the force accuracy prior to the actual simulation. The high quality of the estimate is demonstrated in several examples [DeHo98^b].

3.5.1 Scaling of the rms force error

This section addresses the dependence of the root mean square error in the force in Eqn. (3.55) on the number of charged particles and their valence.[10] Since the assumptions and arguments involved are of a rather general nature, the result is not specific to a certain type of Ewald method.

[10] Recall that this is by no means the only interesting measure of accuracy, as has been discussion at the beginning of Sec. 3.4. It is, however, the only one which is considered here.

It is reasonable to assume that the error in the force on particle i can be written as

$$\Delta \boldsymbol{F}_i \;:=\; \boldsymbol{F}_i - \boldsymbol{F}_i^{\mathrm{exa}} \;=\; q_i \sum_{j\neq i} q_j \, \boldsymbol{\chi}_{ij}. \tag{3.56}$$

The idea behind this ansatz is that – just as it is true for $\boldsymbol{F}_i$ – the *error* in $\boldsymbol{F}_i$ originates from the $N-1$ interactions of particle i with the other charged particles, and each contribution should be proportional to the product of the two charges involved. The vector $\boldsymbol{\chi}_{ij}$ gives the direction and magnitude of this error for two unit charges and depends on their separation and orientation as well as on the specific algorithm used for calculating the electrostatic forces. For this term it is further assumed that

$$\left\langle \boldsymbol{\chi}_{ij} \cdot \boldsymbol{\chi}_{ik} \right\rangle \;=\; \delta_{jk} \left\langle \boldsymbol{\chi}_{ij}^2 \right\rangle \;=:\; \delta_{jk}\, \chi^2, \tag{3.57}$$

where averaging over the particle configurations is denoted by the angular brackets $\langle \cdots \rangle$. The underlying assumption that contributions from different particles are uncorrelated is certainly not always true, think, e.g., of highly ordered or strongly inhomogeneous particle distributions. However, it is a sensible one for *random* systems. Obviously, the term $\langle \boldsymbol{\chi}_{ij}^2 \rangle$ – the mean square force error for two unit charges – can no longer depend on i and j and is thus written as χ^2. Using Eqns. (3.56,3.57), it follows

$$\left\langle (\Delta \boldsymbol{F}_i)^2 \right\rangle \;=\; q_i^2 \sum_{j\neq i} \sum_{k\neq i} q_j q_k \langle \boldsymbol{\chi}_{ij} \cdot \boldsymbol{\chi}_{ik} \rangle \;\approx\; q_i^2 \, \chi^2 \, \mathscr{Q}^2, \tag{3.58}$$

where the important quantity $\mathscr{Q}^2$ is defined as

$$\mathscr{Q}^2 \;:=\; \sum_{j=1}^{N} q_j^2. \tag{3.59}$$

Not all particles necessarily have the same charge. More specifically, let there be P subsets $\mathbb{N}_p$, defined by the condition that all $|\mathbb{N}_p|$ particles from the subset $\mathbb{N}_p$ have the same charge c_p. If $|\mathbb{N}_p| \gg 1$, the law of large numbers [Fel57] and Eqn. (3.58) give

$$\frac{1}{|\mathbb{N}_p|} \sum_{i\in\mathbb{N}_p} (\Delta \boldsymbol{F}_i)^2 \;\approx\; \left\langle (\Delta \boldsymbol{F}_i)^2 \right\rangle_{i\in\mathbb{N}_p} \;\approx\; c_p^2 \, \chi^2 \, \mathscr{Q}^2, \tag{3.60}$$

i.e., the arithmetic mean of the $(\Delta \boldsymbol{F}_i)^2$ for all particles $i \in \mathbb{N}_p$ can be approximated by the ensemble average for one particle from $\mathbb{N}_p$. In the case where all $|\mathbb{N}_p|$ are large, it follows

$$\begin{aligned} \frac{1}{N} \sum_{i=1}^{N} (\Delta \boldsymbol{F}_i)^2 \;&=\; \sum_{p=1}^{P} \frac{|\mathbb{N}_p|}{N} \left(\frac{1}{|\mathbb{N}_p|} \sum_{i\in\mathbb{N}_p} (\Delta \boldsymbol{F}_i)^2 \right) \\ &\approx\; \chi^2 \, \frac{\mathscr{Q}^2}{N} \sum_{p=1}^{P} |\mathbb{N}_p| c_p^2 \;=\; \chi^2 \, \frac{\mathscr{Q}^4}{N}. \end{aligned} \tag{3.61}$$

Inserting this into Eqn. (3.55) gives the final relation

$$\Delta F \;\approx\; \chi \, \frac{\mathscr{Q}^2}{\sqrt{N}}. \tag{3.62}$$

Thus, the scaling of the rms error in the force with particle number and valence is given by the factor $\mathscr{Q}^2 N^{-1/2}$, whereas the prefactor χ – which cannot be obtained by such simple arguments – contains the details of the method. Indeed, the estimates for the real and reciprocal space error of the standard Ewald sum [KoPe92] as well as the estimate for the reciprocal space error of the PME method [Pet95] are exactly of the form (3.62). Note that any information on the valence distribution enters only through the value of $\mathscr{Q}^2$.

3.5.2 The error measure of Hockney and Eastwood

The most interesting ingredient of the P^{3}M method is the optimal influence function from Eqn. (3.46). It is constructed such that the result of the mesh calculation is as close as possible to the solution of the original continuum problem. More precisely, the P^{3}M method is derived from the requirement that the resulting Fourier space contribution to the force minimizes the error measure Q from Eqn. (3.44). But in the light of the last section Q is readily recognized as the mean square force error between two unit charges (up to a factor of L^{-3}). This provides a link between the rms error of an N particle system and the error Q from Hockney and Eastwood: Using Eqn. (3.62) one obtains

$$\Delta F \;\approx\; \mathscr{Q}^2 \sqrt{\frac{Q}{NL^3}}. \tag{3.63}$$

It is important to realize that Hockney and Eastwood not only provide a closed expression for the optimal influence function $\hat{G}_{\mathrm{opt}}$, but also a closed expression for the corresponding "optimal error" $Q_{\mathrm{opt}} = Q[\hat{G}_{\mathrm{opt}}]$:

$$\begin{aligned} Q_{\mathrm{opt}} \;=\; \frac{1}{L^3} \sum_{\boldsymbol{k}\in\hat{\mathbb{M}}} \Bigg\{ & \sum_{\boldsymbol{m}\in\mathbb{Z}^3} \left| \tilde{\boldsymbol{R}}(\boldsymbol{k} + \frac{2\pi}{h}\boldsymbol{m}) \right|^2 \\ & - \frac{\left| \tilde{\boldsymbol{D}}(\boldsymbol{k}) \cdot \sum_{\boldsymbol{m}\in\mathbb{Z}^3} \tilde{U}^2(\boldsymbol{k} + \frac{2\pi}{h}\boldsymbol{m}) \tilde{\boldsymbol{R}}^*(\boldsymbol{k} + \frac{2\pi}{h}\boldsymbol{m}) \right|^2}{|\tilde{\boldsymbol{D}}(\boldsymbol{k})|^2 \left[\sum_{\boldsymbol{m}\in\mathbb{Z}^3} \tilde{U}^2(\boldsymbol{k} + \frac{2\pi}{h}\boldsymbol{m}) \right]^2} \Bigg\}. \end{aligned} \tag{3.64}$$

The outer sum extends over all $\boldsymbol{k}$-vectors of the Fourier transformed mesh $\hat{\mathbb{M}}$, and the asterisk denotes the complex conjugate. Once again, in the special case of i$\boldsymbol{k}$-differentiation one has $\tilde{\boldsymbol{D}}(\boldsymbol{k}) = \mathrm{i}\boldsymbol{k}$.

Admittedly, Eqn. (3.64) looks rather complicated. Still, in combination with Eqn. (3.63) it gives the rms force error of the P^{3}M method or – more precisely – of its Fourier space contribution. After all, the computation of Q_{opt} and that of $\hat{G}_{\mathrm{opt}}$ are quite similar. It should be emphasized that the formula (3.64) for the optimal Q-value, just like the one for the optimal influence function in Eqn. (3.46), is of a very general nature. It does also work for different charge assignment functions, reference forces or any differentiation scheme which can be expressed by an operator $\tilde{\boldsymbol{D}}(\boldsymbol{k})$, in particular for the finite difference schemes presented in TP 3.4.

The corresponding rms error in the force from the real space contribution in Eqn (3.17) has been derived by Kolafa and Perram [KoPe92] and is provided here for reference purpose:

$$\Delta F^{(r)} \approx \frac{2\mathscr{Q}^2}{\sqrt{N r_{\max} L^3}} \exp(-\alpha^2 r_{\max}^2). \tag{3.65}$$

With these two estimates at hand it is easy to determine the optimal value of the splitting parameter α via a stand-alone program, which takes the relevant system parameters (N, $\mathcal{Q}^2$, L) and specifications of the algorithm ($r_{\max}$, N_{M}, P) as its input. If real and reciprocal space contribution to the error, $\Delta F^{(r)}$ and $\Delta F^{(k)}$ respectively, are assumed to be statistically independent, the total error is given by

$$\Delta F = \sqrt{\left(\Delta F^{(r)}\right)^2 + \left(\Delta F^{(k)}\right)^2}. \tag{3.66}$$

This quantity has to be minimized with respect to α. In most cases it is, however, accurate enough to use the following approximation: Determine the value of α at which the real and reciprocal space contribution to the rms force error are equal.

3.5.3 Analytic approximation

Although the closed expression for the error from the last section is not complicated, it is somewhat difficult to implement. A possible calculation of the optimal value of α using, e.g., a bisection method needs several computations of Q_{opt}, and for each computation it is necessary to calculate the inner aliasing sums and the outer sum over the $\boldsymbol{k}$-vectors. For large Fourier meshes this can be rather time consuming. To alleviate this problem, an analytic approximation to the error estimate in Eqn. (3.64) is derived in this section, which is essentially an expansion for small $h\alpha$. For ease of notation the discussion will be restricted to a cubic system and the same number N_{M} of mesh points along each direction. Only the case of i$\boldsymbol{k}$-differentiation, as given in Eqn. (3.49), is treated, since this has been found to be the most accurate method, see Sec. 3.4 and Ref. [DeHo98[a]]. The subsequent line of reasoning can, however, be extended to more general cases.

The aim of the following derivation will be a successive approximation of Eqn. (3.64). The first step is to observe that two of the three sums over $\mathbb{Z}^3$ contain $\tilde{\boldsymbol{R}}$ with its exponential factor $\gamma(\boldsymbol{k}) = \exp(-k^2/4\alpha^2)$ (see Eqn. (3.47)). Since near the boundary of $\hat{\mathbb{M}}$ its value is roughly given by $\exp(-(\pi/h\alpha)^2)$, $\tilde{\boldsymbol{R}}$ is exponentially small outside $\hat{\mathbb{M}}$ if $h\alpha$ is small. Thus, it is a good approximation to retain only the term with $\boldsymbol{m} = \boldsymbol{0}$ in these two sums. Inserting $\tilde{\boldsymbol{D}}(\boldsymbol{k}) = \mathrm{i}\boldsymbol{k}$, the Fourier transform of the charge assignment function from Eqn. (3.30) and using the fact that $\sin^2(x + n\pi) = \sin^2(x)$ for integral n, one obtains

$$Q_{\mathrm{opt}} \approx \frac{(4\pi)^2}{L^3} \sum_{\boldsymbol{k}\in\hat{\mathbb{M}}} \frac{e^{-k^2/2\alpha^2}}{k^2} \left\{ 1 - f^{(P)}\Big(\frac{k_x h}{2}\Big) f^{(P)}\Big(\frac{k_y h}{2}\Big) f^{(P)}\Big(\frac{k_z h}{2}\Big) \right\} \tag{3.67}$$

with the function $f^{(P)}$ defined as

$$f^{(P)}(x) := \frac{x^{-4P}}{\Big(\sum_{m\in\mathbb{Z}} (x + m\pi)^{-2P}\Big)^2}. \tag{3.68}$$

In a second step the aliasing sum in the denominator of Eqn. (3.68) is evaluated analytically by exploiting the partial fraction expansion [AbSt72]:

$$\sin^{-2}(x) = \sum_{m\in\mathbb{Z}} (x + m\pi)^{-2} \quad , \quad x \in \mathbb{R}\backslash\pi\mathbb{Z}. \tag{3.69}$$

P	$c_0^{(P)}$	$c_1^{(P)}$	$c_2^{(P)}$	$c_3^{(P)}$	$c_4^{(P)}$	$c_5^{(P)}$	$c_6^{(P)}$
1	$\frac{2}{3}$						
2	$\frac{2}{45}$	$\frac{8}{189}$					
3	$\frac{4}{945}$	$\frac{2}{225}$	$\frac{8}{1\,485}$				
4	$\frac{2}{4\,725}$	$\frac{16}{10\,395}$	$\frac{5\,528}{3\,869\,775}$	$\frac{32}{42\,525}$			
5	$\frac{4}{93\,555}$	$\frac{2\,764}{11\,609\,325}$	$\frac{8}{25\,515}$	$\frac{7\,234}{32\,531\,625}$	$\frac{350\,936}{3\,206\,852\,775}$		
6	$\frac{2\,764}{638\,512\,875}$	$\frac{16}{467\,775}$	$\frac{7\,234}{119\,282\,625}$	$\frac{1\,403\,744}{25\,196\,700\,375}$	$\frac{1\,396\,888}{40\,521\,009\,375}$	$\frac{2\,485\,856}{152\,506\,344\,375}$	
7	$\frac{8}{18\,243\,225}$	$\frac{7\,234}{1\,550\,674\,125}$	$\frac{701\,872}{65\,511\,420\,975}$	$\frac{2\,793\,776}{225\,759\,909\,375}$	$\frac{1\,242\,928}{132\,172\,165\,125}$	$\frac{1\,890\,912\,728}{352\,985\,880\,121\,875}$	$\frac{21\,053\,792}{8\,533\,724\,574\,375}$
1	0.666667						
2	0.444444e-1	0.423280e-1					
3	0.423280e-2	0.888889e-2	0.538721e-2				
4	0.423280e-3	0.153920e-2	0.142851e-2	0.752499e-3			
5	0.427556e-4	0.238084e-3	0.313541e-3	0.222368e-3	0.109433e-3		
6	0.432881e-5	0.342045e-4	0.606459e-4	0.557114e-4	0.344732e-4	0.163000e-4	
7	0.438519e-6	0.466507e-5	0.107137e-4	0.123750e-4	0.940386e-5	0.535691e-5	0.246713e-5

Table 3.2: Expansion coefficients $c_m^{(P)}$ for the functions $f^{(P)}$ from Eqns. (3.68,3.71) as needed in Eqn. (3.72).

Differentiating this expression $2P-2$ times gives

$$\sum_{m\in\mathbb{Z}} (x+m\pi)^{-2P} = \frac{1}{(2P-1)!}\frac{\mathrm{d}^{2P-2}}{\mathrm{d}x^{2P-2}}\sin^{-2}(x). \tag{3.70}$$

This equation leads to a closed expression for the function $f^{(P)}$ from Eqn. (3.68):

$$f^{(P)}(x) \;=\; \frac{\big[(2P-1)!\big]^2}{x^{4P}}\left(\frac{\mathrm{d}^{2P-2}}{\mathrm{d}x^{2P-2}}\sin^{-2}(x)\right)^{-2}. \tag{3.71}$$

Unfortunately, the sum over $\hat{\mathbb{M}}$ is still too complicated to perform, so some further approximations are necessary: $f^{(P)}$ is expanded in a Taylor series up to order $4P-2$. Since *(i)* $f^{(P)}$ is an even function, *(ii)* $f^{(P)}(0)=1$ and *(iii)* the lowest nontrivial term is of order x^{2P}, this expansion can be written as

$$f^{(P)}(x) \;\approx\; f_T^{(P)}(x) \;:=\; 1 - x^{2P}\sum_{m=0}^{P-1} c_m^{(P)}\, x^{2m}. \tag{3.72}$$

The coefficients $c_m^{(P)}$ are easily determined with the help of any mathematical computer program capable of symbolic algebra and are listed in Table 3.2. The term in curly brackets from Eqn. (3.67) can now be approximated as

$$1 - f^{(P)}\Big(\frac{k_x h}{2}\Big) f^{(P)}\Big(\frac{k_y h}{2}\Big) f^{(P)}\Big(\frac{k_z h}{2}\Big) \;\approx$$

$$\left(1 - f_{\mathrm{T}}^{(P)}\Big(\frac{k_x h}{2}\Big)\right) + \left(1 - f_{\mathrm{T}}^{(P)}\Big(\frac{k_y h}{2}\Big)\right) + \left(1 - f_{\mathrm{T}}^{(P)}\Big(\frac{k_z h}{2}\Big)\right). \tag{3.73}$$

The product of the three functions $f^{(P)}$ is computed by multiplying their Taylor expansions term by term. However, the results are only retained up to the truncation order $4P-2$. Note that the first neglected cross term would be of order $4P$.

For symmetry reasons it is evident that all three terms in the last line of (3.73) contribute in the same way to the value of the sum in Eqn. (3.67). It is therefore sufficient to choose one of them – e.g., the z-term – and multiply by 3. Together with the definition of $f_{\mathrm{T}}^{(P)}$ from Eqn. (3.72) this leads to

$$Q_{\mathrm{opt}} \;\approx\; 3\,\frac{(4\pi)^2}{L^3}\sum_{\boldsymbol{k}\in\hat{\mathbb{M}}}\frac{e^{-k^2/2\alpha^2}}{k^2}\sum_{m=0}^{P-1} c_m^{(P)}\left(\frac{k_z h}{2}\right)^{2(P+m)}. \tag{3.74}$$

Finally, the sum is replaced by an integral via

$$\left(\frac{2\pi}{L}\right)^3\sum_{\boldsymbol{k}} \;\longrightarrow\; \int \mathrm{d}^3k. \tag{3.75}$$

If one extends the range of integration to $\mathbb{R}^3$ and changes to spherical polar coordinates, the remaining angular and radial integrals can be performed with the help of

$$\int_0^\pi \mathrm{d}\vartheta\,\sin\vartheta\,\cos^{2n}\vartheta = \frac{2}{2n+1} \quad , \quad n\in\mathbb{N} \tag{3.76}$$

P	$a_0^{(P)}$	$a_1^{(P)}$	$a_2^{(P)}$	$a_3^{(P)}$	$a_4^{(P)}$	$a_5^{(P)}$	$a_6^{(P)}$
1	$\frac{2}{3}$						
2	$\frac{1}{50}$	$\frac{5}{294}$					
3	$\frac{1}{588}$	$\frac{7}{1\,440}$	$\frac{21}{3\,872}$				
4	$\frac{1}{4\,320}$	$\frac{3}{1\,936}$	$\frac{7\,601}{2\,271\,360}$	$\frac{143}{28\,800}$			
5	$\frac{1}{23\,232}$	$\frac{7\,601}{13\,628\,160}$	$\frac{143}{69\,120}$	$\frac{517\,231}{106\,536\,960}$	$\frac{106\,640\,677}{11\,737\,571\,328}$		
6	$\frac{691}{68\,140\,800}$	$\frac{13}{57\,600}$	$\frac{47\,021}{35\,512\,320}$	$\frac{9\,694\,607}{2\,095\,994\,880}$	$\frac{733\,191\,589}{59\,609\,088\,000}$	$\frac{326\,190\,917}{11\,700\,633\,600}$	
7	$\frac{1}{345\,600}$	$\frac{3\,617}{35\,512\,320}$	$\frac{745\,739}{838\,397\,952}$	$\frac{56\,399\,353}{12\,773\,376\,000}$	$\frac{25\,091\,609}{1\,560\,084\,480}$	$\frac{1\,755\,948\,832\,039}{36\,229\,939\,200\,000}$	$\frac{4\,887\,769\,399}{37\,838\,389\,248}$
1	0.666667						
2	0.200000e-1	0.170068e-1					
3	0.170068e-2	0.486111e-2	0.542355e-2				
4	0.231481e-3	0.154959e-2	0.334645e-2	0.496528e-2			
5	0.430441e-4	0.557742e-3	0.206887e-2	0.485494e-2	0.908541e-2		
6	0.101408e-4	0.225694e-3	0.132408e-2	0.462530e-2	0.123000e-1	0.278781e-1	
7	0.289352e-5	0.101852e-3	0.889481e-3	0.441538e-2	0.160835e-1	0.484668e-1	0.129175

Table 3.3: Expansion coefficients $a_m^{(P)}$ from Eqn. (3.79).

and

$$\int_0^\infty \mathrm{d}x\, x^{2n} e^{-x^2} = \frac{\sqrt{\pi}\,(2n-1)!!}{2^{n+1}} \quad , \quad n \in \mathbb{N} \tag{3.77}$$

where $(2n-1)!! = 1 \cdot 3 \cdot 5 \cdots (2n-1)$. Collecting all parts together gives

$$Q_{\mathrm{opt}} \;\approx\; \sqrt{2\pi}\,\alpha\;(h\alpha)^{2P} \sum_{m=0}^{P-1} a_m^{(P)}\,(h\alpha)^{2m} \tag{3.78}$$

with the abbreviation

$$a_m^{(P)} := 12\,\frac{\big(2(P+m)-1\big)!!}{2(P+m)+1}\,2^{-2(P+m)}\,c_m^{(P)}. \tag{3.79}$$

Combining this with Eqn. (3.63) results in the following analytical approximation for the Fourier space contribution to the rms force error of the P^{3}M algorithm:

$$\Delta F \;\approx\; \frac{\mathscr{Q}^2}{L^2}\,(h\alpha)^P \sqrt{\frac{\alpha L}{N}\sqrt{2\pi}\sum_{m=0}^{P-1} a_m^{(P)}\,(h\alpha)^{2m}}. \tag{3.80}$$

The exact expansion coefficients $a_m^{(P)}$, which are rational numbers, are listed in Table 3.3.

Eqn. (3.80) has been derived under the explicit assumption that $h\alpha$ is small. Both the restriction to the term $\boldsymbol{m} = \boldsymbol{0}$ for the two sums in Eqn. (3.64) and the expansion of the function $f^{(P)}$ from Eqns. (3.68,3.71) in powers of $h\alpha$ are questionable when $h\alpha$ becomes large. But in this case it is still safe to go back to the original error estimate, i.e., to the combination of Eqns. (3.63) and (3.64).

3.5.4 Comparison with Petersen's PME estimate

In Ref. [Pet95] Petersen constructs an rms force error estimate for the PME method, which – translated to the notation conventions used in this work – is written as

$$\Big(\Delta F_{\mathrm{PME}}\Big)^2 \;=\; \frac{24\,\mathscr{Q}^4}{NL^4(P!)^2}\langle\phi_P^2\rangle h^{2P} {\sum_{\boldsymbol{k}\in\hat{\mathbb{M}}}}' \frac{\exp\{-k^2/2\alpha^2\}}{k^2}\,k_z^{2P} \tag{3.81}$$

with the numbers $\langle\phi_P^2\rangle$ defined as

$$\langle\phi_P^2\rangle \;:=\; \int_{-1/2}^{1/2}\mathrm{d}x \prod_{s=-(P-1)/2}^{(P-1)/2}(x-s)^2. \tag{3.82}$$

Numerical values of $\langle\phi_P^2\rangle$ for $P \in \{1,\ldots,7\}$ can be found in Table 3.4. Petersen proceeds by replacing the sum over $\hat{\mathbb{M}}$ by an integral over $\mathbb{R}^3$ and changing to polar coordinates. Yet, he performs a Laplace evaluation of the resulting Gaussian integral instead of using Eqn. (3.77). If this unnecessary approximation is avoided, the final result reads

$$\Delta F_{\mathrm{PME}} \;\approx\; \frac{\mathscr{Q}^2}{L^2}\,(h\alpha)^P \sqrt{\frac{\alpha L}{N}\sqrt{2\pi}\,\frac{24\langle\phi_P^2\rangle(2P-1)!!}{(P!)^2(2P+1)}}. \tag{3.83}$$

P	1	2	3	4	5	6	7
$\langle\phi_P^2\rangle$	0.83333e-1	0.33333e-1	0.60566e-1	0.16349	0.90274	0.63170e1	0.70908e2
$\frac{\Delta F_{\mathrm{PME}}}{\Delta F_{\mathrm{P3M}}}$	1.0	2.4495	7.1327	18.528	54.799	151.86	456.72

Table 3.4: Prefactors $\langle\phi_P^2\rangle$ from Eqn. (3.82) as well as the ratio between the PME and P^{3}M rms force error estimates from Eqn. (3.84).

Comparing this to Eqn. (3.80) shows that Petersen's formula looks rather similar to the P^{3}M estimate derived in this work, but it is an expansion in $h\alpha$ which terminates at the lowest nontrivial order. Still, one may try to compare both estimates by restricting the sum over m in the P^{3}M estimate in Eqn. (3.80) to the term $m = 0$. This gives an expression for the ratio of the two errors, which is independent of α and merely a function of the charge assignment order P:

$$\frac{\Delta F_{\mathrm{PME}}}{\Delta F_{\mathrm{P3M}}} \approx \frac{2^P}{P!}\sqrt{\frac{2\,\langle\phi_P^2\rangle}{c_0^{(P)}}}. \tag{3.84}$$

After inserting the numerical values of $\langle\phi_P^2\rangle$ and $c_0^{(P)}$ this ratio proves the PME error to be larger than the P^{3}M error, as is shown in Table 3.4. After the numerical evidence from Sec. 3.4 this is a second – this time analytical – hint that P^{3}M is the more accurate particle mesh algorithm of the two. However, since, for large P the lowest order expansion becomes questionable, this result should not be over-interpreted: Including the terms $m > 0$ in the P^{3}M error will increase ΔF_{P3M}. Yet, it is very clear that the PME error from Eqn. (3.83) also changes upon addition of higher order terms.

3.5.5 Numerical tests

In this section the accuracy of the P^{3}M error estimates is demonstrated by comparing their predictions with the exact rms force error ΔF from Eqn. (3.55). The exact forces $\boldsymbol{F}_i$ needed for computing ΔF are obtained by a standard Ewald sum using large cutoffs. The test system is the one from TP 3.5 and the unit conventions are described in TP 3.1. The estimate which emerges from combining Eqns. (3.63) and (3.64) is referred to as the *full estimate* and Eqn. (3.80) as the *analytical approximation*.

In a first example the number of mesh points is fixed to $N_{\mathrm{M}} = 32$ and the real space cutoff to $r_{\max} = 4$. The charge assignment order varies from $P = 1$ through $P = 7$. In Fig. 3.13 the resulting curves for the rms force error ΔF are plotted together with the full error estimate (left) and the analytical approximation (right). It can be seen very clearly that the full estimate accurately predicts the Fourier space contribution to ΔF for all values of α and P. Since the real space contribution is also known [KoPe92] (see also Eqn. (3.65)), this permits an easy determination of the optimal value of the splitting parameter α. The analytical approximation is almost as accurate as the full formula, however, for large P it diminishes in accuracy if α becomes large. This is due to the fact that Eqn. (3.80) has been derived under the assumption that $h\alpha$ is small. Note that the expansion coefficients $a_m^{(P)}$ needed in Eqn. (3.80) strongly increase with increasing m if P becomes larger, see

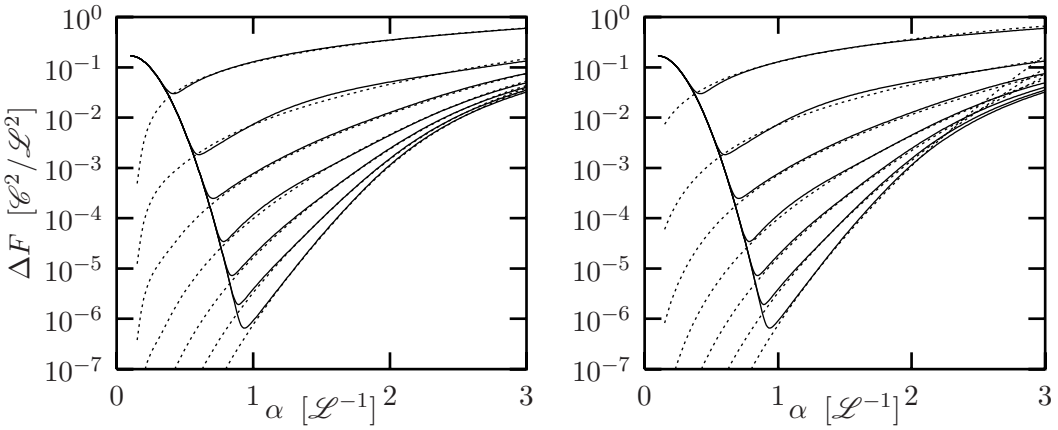

Figure 3.13: The rms error ΔF (solid lines) for the system from TP 3.5 is calculated for the i$\boldsymbol{k}$-differentiated P^3M method with $N_M = 32$ mesh points and real space cutoff $r_{max} = 4$. From top to bottom the order of the charge assignment function is increased from 1 to 7. In the left part the dotted lines are the corresponding full estimates, while in the right part they correspond to the analytical approximation.

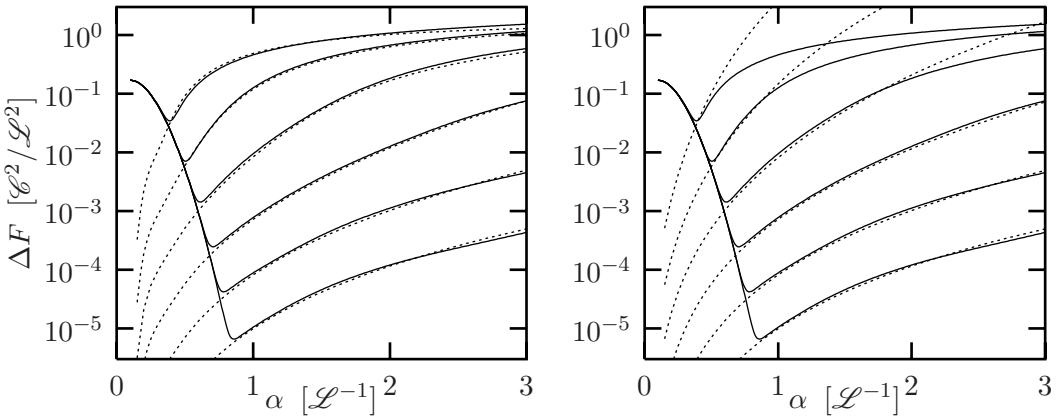

Figure 3.14: ΔF (solid lines) for the same system as in the previous figure is calculated for the i$\boldsymbol{k}$-differentiated P^3M method with charge assignment order $P = 3$ and real space cutoff $r_{max} = 4$. From top to bottom the number of mesh points varies like 4, 8, 16, 32, 64, 128. The dotted lines are the full error estimates (left) or the analytical approximation (right).

Tab. 3.3. Still, both estimates are useful for determining the optimal operation point, and Eqn. (3.80) can be calculated much faster than the sums from Eqn. (3.64).

The next test studies at fixed charge assignment order $P = 3$ different mesh sizes $h = L/N_M$ by investigating $N_M \in \{4, 8, 16, 32, 64, 128\}$. Fig. 3.14 shows ΔF in comparison with the full and the approximated error estimate respectively. Again, it can be seen that the former predicts very accurately the Fourier space contribution to ΔF. As expected, the analytical approximation has problems at small N_M. This is due to the fact that a small number of mesh points results in a large mesh size h. However, for large N_M the analytical estimate is very useful. Essentially, one has to check the value of $h\alpha$: If this is of the order unity or even larger, care is called for. Observe that the value of $h\alpha$ is

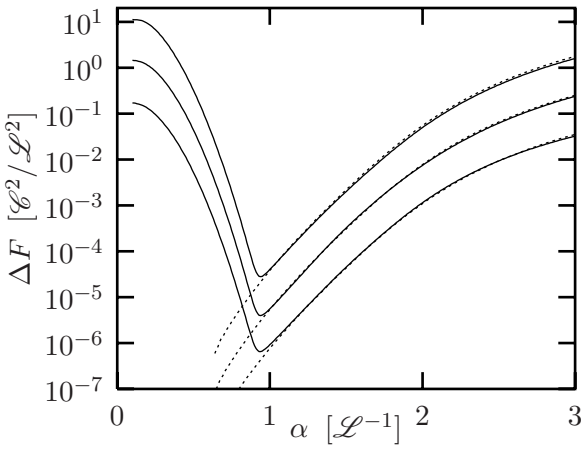

Figure 3.15: Test of the $\mathscr{Q}^2 N^{-1/2}$ scaling of ΔF. The three solid lines show the rms force error ΔF for systems, which differ in their $(\mathscr{Q}^2, N)$ values ($r_{\max} = 4$, $N_{\mathrm{M}} = 32$ and $P = 7$). From top to bottom they are characterized by $(10000, 400)$, $(1000, 200)$ and $(100, 100)$ (the last system is the same as the one in Figs. 3.13,3.14). The dotted curves are the corresponding full error estimates.

approximately 1 at the points where the analytical approximation starts to deviate from the true curve.

Next it is demonstrated that the scaling of the rms force error with particle number and valence distribution is in fact correctly given by $\Delta F \propto \mathscr{Q}^2 N^{-1/2}$. To this end three systems which differ only in the values of $\mathscr{Q}^2$ and N are investigated. The first system is the same as the one investigated in Figs. 3.13,3.14. A second system contains 200 particles, namely, 50 monovalent and 50 trivalent pairs. Finally, a third system contains 400 particles: 50 pairs with charge ± 1, 100 pairs with charge ± 5 and 50 pairs with charge ± 7. Hence, their $(\mathscr{Q}^2, N)$ values are given by $(100, 100)$, $(1000, 200)$ and $(10000, 400)$, respectively, and the ratio of their scaling prefactors is thus $1 : \sqrt{50} : 50$. In Fig. 3.15 this is clearly visible in the constant shift of the three curves with respect to one another. Also shown is the full error estimate, which again predicts the Fourier space contribution to ΔF in all three cases very precisely.

So far only homogeneous random systems have been used for testing the error estimates. This, however, does not necessarily reflect the situation encountered in all computer experiments. As a last numerical test it is shown that deviations from a random distribution, as they frequently occur in charged systems, in fact have a noticeable influence on the rms error. To demonstrate this, a simple model of a solution of flexible polyelectrolytes is used. 106 Lennard-Jones particles were joined to build up a polymer chain. Every third "monomer" was monovalently charged and 8 such chains together with 96 trivalent and oppositely charged counterions, which make the complete system electrically neutral, were put in a cubic simulation box of length $L \approx 179$. The system was brought into the canonical state by means of a Molecular Dynamics simulation and a Langevin thermostat.

Under certain circumstances (e.g., at sufficiently low temperature and the appropriate density range) such polyelectrolyte chains collapse, and this happened to the described system. The chain sizes shrunk to much smaller values than for comparable neutral polymers and 90% of the counterions were condensed within a distance of only two Lennard–Jones radii from the nearest chain.

The various phenomena leading to this transition, the influence of the system parameters or the dynamics are only a few of the interesting physical questions. Yet, the only thing which is important now is the fact that after the transition the system has developed local inhomogeneities. To demonstrate this, Fig. 3.16 shows the measured relative frequency

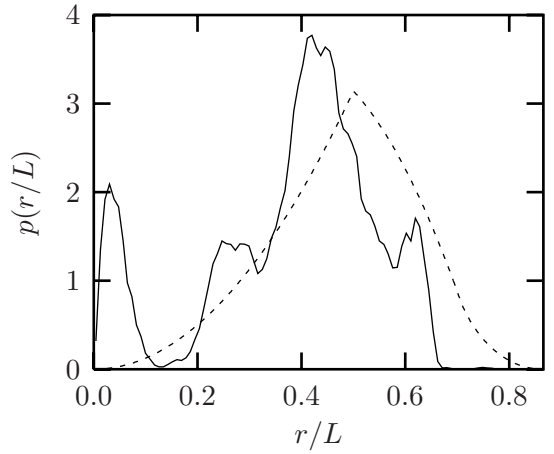

Figure 3.16: Measured relative frequency $p(r/L)$ for the scaled minimum image separation r/L between two charges of the polyelectrolyte system described in the text (solid line). For comparison, the probability density of r/L for a random system is also shown (dashed line).

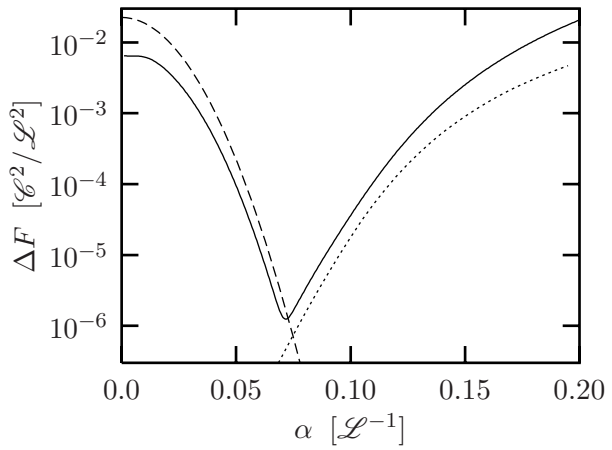

Figure 3.17: rms force error ΔF for the polyelectrolyte system described in the text (solid line). The dotted curve is the full P^{3}M estimate for the reciprocal space contribution, the dashed curve is the estimate for the real space contribution. Note that due to the strong inhomogeneities in the charge distribution (see Fig. 3.16) both estimates show systematic deviations from the true error curve.

$p(r/L)$ of the scaled minimum image distance $r/L \in [0; \sqrt{3}/2]$ between two charges, irrespective of their valence, and compares this to the probability density of r/L for a random system. The differences are very pronounced. Apart from the more complicated structure of the measured curve, note that small separations are more frequent at the expense of larger ones. For this system the rms force error ΔF and the corresponding estimates for the real and reciprocal space contribution (Eqns. (3.65;3.63,3.64)) have been computed. Since the simulation box comprises 288 monovalent and 96 trivalent charges, this gives $N = 384$ and $\mathscr{Q} = 1152$. The result is shown in Fig. 3.17. No longer do the estimates correctly predict the two branches of ΔF. Rather, at small values of α the algorithm gives better results than expected from Eqn. (3.65), while at large values of α the estimated ΔF is smaller than the actual one. This trend can be explained qualitatively in the following way: At small values of α the force, and also its error, is dominated by the real space contribution from Eqn. (3.17). This error originates from neglected contributions beyond the real space cutoff $r_{\max}$. In the case of Fig 3.17 $r_{\max}/L \approx 0.243$ has been used and from Fig. 3.16 it can be seen that there are more particles within this cutoff (and thus less beyond) than in the case of a random particle distribution. This should lead to an enhanced real space accuracy. On the other hand, Fig. 3.12 demonstrates that the rms error of the P^{3}M method strongly increases with decreasing minimum image distance. The general shift towards smaller r, which can be observed in the polyelectrolyte system, should thus

lead to an enlarged reciprocal space error. Observable effects will occur at large values of α, where this contribution to ΔF dominates.

Although the systematic deviations of the error estimates from the true curve are easily detectable, they are less dramatic than one could have expected from Fig. 3.16. The optimal splitting parameter from Fig. 3.17 is given by $\alpha_{\text{opt}} \approx 0.0715$ with a corresponding $\Delta F_{\text{opt}} \approx 1.2 \times 10^{-6}$, while the intersection point of real and reciprocal space estimate occurs at $\alpha \approx 0.0740$, predicting an error of $\Delta F \approx 9.3 \times 10^{-7}$. If the estimated value of α had been used, this would have resulted in an error of $\Delta F \approx 1.5 \times 10^{-6}$, which is roughly 25% larger than at the optimal value of α. If such a safety margin is considered already at the beginning, the *a priori* determination of the "optimal" value of α by means of Eqns. (3.63,3.64,3.65) together with an *a posteriori* validity check is still a good approach. In any case, if one knows, or at least has reasons to suspect, that the investigated system is susceptible to the development of inhomogeneities, one should always be aware of a potential failure of the presented error formulæ. In case of doubt, some simple numerical tests should be performed.

Conclusion

Theoretical and numerical studies of stiff linear polyelectrolytes within the framework of a cell model have been presented. A novel criterion for quantifying the phenomenon of counterion condensation was introduced, which turned out to provide a fruitful base for understanding many interesting effects. For instance, it was used to illuminate the transition from counterion condensation to screening, when salt is gradually added to the system. In the presence of excluded volume interactions it revealed that the layer of condensed ions must be distinguished from the smaller layer of closely packed ions. The screening ability of a mixture of ions having different valences was readily seen to increase compared to single-valent solutions. The enhanced counterion condensation caused by ionic correlations and its dependence on parameters such as density, Bjerrum length, valence and ionic strength was measured. These examples prove the condensation criterion to be a suitable tool for analyzing linear polyelectrolytes. Its application to further problems, such as hydrophobic or structured counterions and its extension to flexible polyelectrolytes appears promising.

The important issue of understanding ion-ion correlations remains a fascinating but difficult problem. For weakly coupled systems correction terms to the Poisson-Boltzmann free energy density together with a local density approximation have been shown to be very successful in this work. However, they are incapable of describing many effects which qualitatively go beyond mean-field theory, e.g., charge reversal, a non-monotonic zeta-potential and attractive interactions between like-charged macroions. Recently attempts have been made to relate such phenomena to the formation of various kinds of Wigner crystals. To assess these theoretical ideas, computer simulations will certainly be indispensable, since they are presently the only practicable way of obtaining sufficiently detailed information on ionic distributions and correlation functions. The original numerical investigations presented in this work and the correlation analysis of the obtained data are a step in this direction.

The study of large ionic systems is always limited by the computationally demanding treatment of long-range interactions. The Particle Mesh Ewald algorithms discussed and used in this work offer an elegant solution to this problem due to their almost linear scaling with the number of charged particles. However, a judicious choice of the relevant tuning parameters is imperative. The analytic error estimate for the P^3M method derived in this work should be an important step towards a straightforward and yet accuracy controlled application of this algorithm.

List of technical points

Acknowledgments

I would like to thank Prof. Kurt Kremer for suggesting the exciting field of polyelectrolytes for my thesis and for his continuing interest in my progress. I am grateful to Christian Holm for inspiring supervision and judicious guidance. He encouraged me to pursue my scientific interests and always devoted time to a clarifying discussion. His confidence meant a lot to me.

I have met new colleagues and friends during my time in Mainz and I owe much to them. My room-mate Oliver Biermann filled me with enthusiasm for mountain-biking and put up with me on office-weekdays. Thomas Soddemann enjoyed with me a camping-holiday in rainy California and taught me about the huge importance of tiny details. Roland Faller taught me how to cook, at least he tried his very best. Dirk Reith made me become a Comedian Harmonist, at least for one year. Mikko Karttunen carefully read the entire manuscript despite only a short time being available. His many valuable remarks added a lot to the readability of the text. Hans Jörg Limbach and René Messina always had time when I needed a technical advice. Burkhard Dünweg readily shared his profound knowledge of physics. Marcia Barbosa showed to me how physics is done the lighthearted way. Uwe Micka shared his knowledge of polyelectrolytes and Particle Mesh Ewald routines. Doris Kirsch always had an encouraging smile for me when I dropped by her office. Jürgen Blaul, Birgit Guilleaume, Felipe Jimenez Angeles and Sylvio May kindly provided results of experiments and computations.

This work had never been written without the invaluable help, clear criticism and constant support of many people. How could I ever acknowledge all the things they have done for me?

Finally, I thank my family for their love and support.

Bibliography

[Abe59] R. Abe, *Prog. Theory Phys.*, **22**, 213 (1959).

[AbSt72] M. Abramowitz and I. A. Stegun, editors, *Handbook of mathematical functions*, Dover, New York, 9th edition (1972).

[AdDu86] D. J. Adams and G. S. Dubey, *J. Comp. Phys.*, **72**, 156 (1987).

[AlCh84] S. Alexander, P. M. Chaikin, P. Grant, G. J. Morales, P. Pincus and D. Hone, *J. Chem. Phys.*, **80**, 5776 (1984).

[AlBe51] T. Alfrey, P. Berg and H. J. Morawetz, *J. Polym. Sci.*, **7**, 543 (1951).

[AlTi97] M. P. Allen and D. J. Tildesley, *Computer Simulation of Liquids*, Oxford Science Publications, Clarendon Press, first edition (1997).

[BaJo96] J.-L. Barat and J.-F. Joanny, in *Advances in Chemical Physics* (Edited by I. Prigogine and S. A. Rice), volume 94, pp. 1–66, John Wiley & Sons (1996).

[BaDe] M. C. Barbosa, M. Deserno and C. Holm, *Europhys. Lett.* (submitted).

[BaHa80] M. Baus and J.-P. Hansen, *Phys. Rep.*, **59**(1), 1 (1980).

[Bel98] L. Belloni, *Colloids and Surfaces*, **A 140**, 227 (1998).

[BeDr84] L. Belloni, M. Drifford and P. Turq, *Chem. Phys.*, **83**, 147 (1984).

[Ber93] H. J. C. Berendsen, in *Computer Simulation of Biomolecular Systems* (Edited by W. F. van Gunsteren, P. K. Weiner and A. J. Wilkinson), volume 2, pp. 161–81, The Netherlands (1993), ESCOM.

[BlWi] J. Blaul, M. Wittemann, M. Ballauff and M. Rehahn, *J. Phys. Chem. B* (submitted).

[BoSt97] S. Boresch and O. Steinhauser, *Ber. Bunsenges. Phys. Chem.*, **101**(7), 1019 (1997).

[BoKa12] M. Born and T. von Karman, *Physik. Z.*, **13**, 297 (1912).

[BoAn97] I. Borukhov, D. Andelman and H. Orland, *Phys. Rev. Lett.*, **79**(3), 435 (1997).

[BoBo85] D. Borwein, J. M. Borwein and K. F. Taylor, *J. Math. Phys.*, **26**(1), 2999 (November 1985).

[BrSa66] S. G. Brysh, H. L. Sahlin and E. Teller, *J. Chem. Phys.*, **45**, 2102 (1966).

[Cai94] J.-M. Caillol, *J. Chem. Phys.*, **101**(7), 6080 (1994).

[Cal85] H. B. Callen, *Thermodynamics and an Introduction to Thermostatistics*, Wiley, New York, second edition (1985).

[Cha13] D. L. Chapman, *Phil. Mag.*, **25**, 475 (1913).

[DaYo93] T. Darden, D. York and L. Pedersen, *J. Chem. Phys.*, **98**(12), 10089 (June 1993).

[DaBr95] T. Das, D. Bratko, L. B. Bhuiyan and C. W. Outhwaite, *J. Phys. Chem.*, **99**, 410 (1995).

[DaBr97] T. Das, D. Bratko, L. B. Bhuiyan and C. W. Outhwaite, *J. Chem. Phys.*, **107**(21), 9197 (1997).

[LePe80^a] S. W. De Leeuw, J. W. Perram and E. R. Smith, *Proc. R. Soc. Lond. A*, **373**, 27 (1980).

[LePe80^b] S. W. De Leeuw, J. W. Perram and E. R. Smith, *Proc. R. Soc. Lond. A*, **373**, 57 (1980).

[DeHü23] P. Debye and E. Hückel, *Phys. Z.*, **24**(9), 185 (1923).

[Des00] M. Deserno, *Physica A*, **278**, 405 (2000).

[DeHo98^a] M. Deserno and C. Holm, *J. Chem. Phys.*, **109**(18), 7678 (1998).

[DeHo98^b] M. Deserno and C. Holm, *J. Chem. Phys.*, **109**(18), 7694 (1998).

[DeHo00] M. Deserno, C. Holm and S. May, *Macromolecules*, **33**, 199 (2000).

[Dün93] B. Dünweg, *J. Chem. Phys.*, **99**(9), 6977 (1993).

[DüPa91] B. Dünweg and W. Paul, *Int. J. Mod. Phys. C*, **2**, 817 (1991).

[Dwi61] H. B. Dwight, *Tables of Integrals and other Mathematical Data*, MacMillan, New York, fourth edition (1961).

[EsWa95] P. Español and P. Warren, *Europhys. Lett.*, **30**, 191 (1995).

[EsPe95] U. Essmann, L. Perera, M. L. Berkowitz, T. Darden, H. Lee and L. G. Pedersen, *J. Chem. Phys.*, **103**(19), 8577 (November 1995).

[Ewa21] P. Ewald, *Ann. Phys.*, **64**, 253 (1921).

[Fel57] W. Feller, *An Introduction to Probability Theory and Its Applications*, John Wiley & Sons, New York, second edition (1957).

[FrSm96] D. Frenkel and B. Smit, *Understanding Molecular Simulation*, Academic Press, San Diego (1996).

[FuKa51] R. M. Fuoss, A. Katchalsky and S. Lifson, *Proc. Natl. Acad. Sci. USA*, **37**, 579 (1951).

[GoLo85] E. Gonzales-Tovar, M. Lozada-Cassou and D. Henderson, *J. Chem. Phys.*, **83**(1), 361 (1985).

[Gou10] G. L. Gouy, *J. Phys.*, **9**, 457 (1910).

[GrKr86] G. S. Grest and K. Kremer, *Phys. Rev. A*, **33**(5), 3628 (1986).

[GrMa97] N. Grønbech-Jensen, R. J. Mashl, R. F. Bruinsma and W. M. Gelbart, *Phys. Rev. Lett.*, **78**(12), 2477 (1997).

[Gro91] R. D. Groot, *J. Chem. Phys.*, **95**(12), 9191 (1991).

[GuWe80] M. Gueron and G. Weisbuch, *Biopolymers*, **19**, 353 (1980).

[GuBl] B. Guilleaume, J. Blaul, M. Wittemann, M. Rehahn and M. Ballauff, *J. Phys.: Cond. Matt.* (in press).

[Gul89] L. Guldbrand, *Mol. Phys.*, **67**(1), 217 (1989).

[Hai92] J. M. Haile, *Molecular Dynamics Simulation: Elementary methods*, John Wiley & Sons, New York (1992).

[HeBo96] D. Henwood and J. Bonet, *Finite Elements. A Gentle Introduction*, MacMillan, London (1996).

[Hey80] D. M. Heyes, *J. Chem. Phys.*, **74**(3), 1924 (February 1981).

[Hil55] T. L. Hill, *Archives of biochemistry and biophysics*, **57**, 229 (1995).

[HoEa88] R. W. Hockney and J. W. Eastwood, *Computer simulation using particles*, IOP Ltd (1988).

[Hum95] G. Hummer, *Chem. Phys. Lett.*, **235**, 297 (1995).

[HuGr98] G. Hummer, N. Grønbech-Jensen and M. Neumann, *J. Chem. Phys.*, **109**(7), 2791 (1998).

[HuPr98] G. Hummer, L. R. Pratt and A. E. García, *J. Phys. Chem. A*, **102**(41), 7885 (1998).

[HüMc99] P. H. Hünenberger and J. A. McCammon, *J. Chem. Phys.*, **110**(4), 1856 (1999).

[Hun87] R. J. Hunter, *Foundations of Colloid Science, Volume 1*, Oxford Science Publications, Clarendon Press, Oxford (1987).

[KoPe92] J. Kolafa and J. W. Perram, *Mol. Sim.*, **9**(5), 351 (1992).

[KrRo86] K. Kremer, M. O. Robbins and G. S. Grest, *Phys. Rev. Lett.*, **57**, 2694 (1986).

[KuLe98] P. S. Kuhn, Y. Levin and M. C. Barbosa, *Macromolecules*, **31**, 8347 (1998).

[LaWo94] G. Lamm, L. Wong and G. R. Pack, *Biopolymers*, **34**, 227 (1994).

[LaTi85] P. Lancaster and M. Tismenetsky, *The Theory of Matrices*, Academic Press, second edition (1985).

[LaMa85] A. Lasota and M. C. Mackey, *Probabilistic properties of deterministic systems*, Cambridge University Press, Cambridge (1985).

[LeZi84^b] M. Le Bret and B. H. Zimm, *Biopolymers*, **23**, 287 (1984).

[LeZi84^a] M. Le Bret and B. H. Zimm, *Biopolymers*, **23**, 271 (1984).

[LeBa98] Y. Levin, M. C. Barbosa and M. N. Tamashiro, *Europhys. Lett.*, **41**, 123 (1998).

[LeFi96] Y. Levin and M. E. Fisher, *Physica A*, **225**, 164 (1996).

[LiNa75] E. H. Lieb and H. Narnhofer, *J. Stat. Phys.*, **12**, 291 (1975).

[LiNa76] E. H. Lieb and H. Narnhofer, *J. Stat. Phys.*, **14**, 465 (1976).

[LuTi95] B. A. Luty, I. G. Tironi and W. F. van Gunsteren, *J. Chem. Phys.*, **103**(8), 3014 (1995).

[LyNo97] A. P. Lyubartsev and L. Nordenskiöld, *J. Phys. Chem.*, **101**, 4335 (1997).

[LyTa98] A. P. Lyubartsev, J. X. Tang, P. A. Janmey and N. Lars, *Phys. Rev. Lett.*, **81**(24), 5465 (1998).

[Man92] M. Mandel, *J. Phys. Chem.*, **96**(10), 3934 (1992).

[Man69] G. S. Manning, *J. Chem. Phys.*, **51**, 954 (1969).

[McQ76] D. A. McQuarrie, *Statistical Mechanics*, Harper's chemistry series, Harper Collins, New York (1976).

[Min87] P. Minnhagen, *Rev. Mod. Phys.*, **59**, 1001 (1987).

[NeJo98] R. R. Netz and J.-F. Joanny, *Macromolecules*, **31**, 5123 (1998).

[NeOr99] R. R. Netz and H. Orland, *cond-mat/9902220* (1999).

[Neu99] J. C. Neu, *Phys. Rev. Lett.*, **82**(5), 1072 (1999).

[Ng74] K.-C. Ng, *J. Chem. Phys.*, **61**, 2680 (1974).

[NiGu91] L. G. Nilsson, L. Guldbrand and Nordenskiöld, *Mol. Phys.*, **72**(1), 177 (1991).

[Nor84] S. Nordholm, *Chem. Phys. Lett.*, **105**(3), 302 (1984).

[Oos70] F. Oosawa, *Polyelectrolytes*, Marcel Decker, New York (1970).

[PaLa93] G. R. Pack and G. Lamm, *Int. J. Quant. Chem.*, **20**, 213 (1993).

[PaHa98] I. Pagonabarraga, M. H. J. Hagen and D. Frenkel, *Europhys. Lett.*, **42**(4), 377 (1998).

[PaYe99] C. N. Patra and A. Yethiraj, *J. Chem. Phys.*, **103**, 6080 (1999).

[PeJö93] R. Penfold, B. Jönsson and S. Nordholm, *J. Chem. Phys.*, **99**(1), 497 (1993).

[PeNo90] R. Penfold, S. Nordholm, B. Jönsson and C. E. Woodward, *J. Chem. Phys.*, **92**(3), 1915 (1990).

[PePe88] J. W. Perram, H. G. Petersen and S. W. De Leeuw, *Mol Phys*, **65**(4), 875 (1988).

[Pet95] H. A. Petersen, *J. Chem. Phys.*, **103**(9), 3668 (1995).

[PrTe92] W. H. Press, S. A. Teukolsky, W. T. Vetterling and B. P. Flannery, *Numerical Recipes in C*, Cambridge University Press, Cambridge, second edition (1992).

[RaWo85] G. V. Ramanathan and C. P. Woodbury, Jr., *J. Chem. Phys.*, **82**(3), 1482 (1985).

[Ris89] H. Risken, *The Fokker-Planck Equation*, Springer, Berlin, second edition (1989).

[RoDe87] F. J. Rogers and H. E. DeWitt, editors, *Strongly Coupled Plasmas*, Plenum Press, New York (1987).

[Ros96] Y. Rosenfeld, *Phys. Rev. E*, **54**, 2827 (1996).

[RoBl96] I. Rouzina and V. A. Bloomfield, *J. Phys. Chem.*, **100**, 9977 (1996).

[Sal58] E. E. Salpeter, *Ann. Phys.*, **5**, 183 (1958).

[SaDi76] M. J. L. Sangester and M. Dixon, *Adv. Phys.*, **63**, 247 (1976).

[Sch73] I. J. Schoenberg, *Cardinal Spline Interpolation*, Society for Industrial and Applied Mathematics, Philadelphia (1973).

[Shk99] B. I. Shklovskii, *Phys. Rev. Lett.*, **82**(16), 3268 (1999).

[SkFi78] J. Skolnick and M. Fixman, *Macromolecules*, **11**, 867 (1978).

[Spr96] M. Sprik, in *Monte Carlo and Molecular Dynamics of Condensed Matter Systems* (Edited by K. Binder and G. Ciccotti), volume 49, p. 43, Bologna (1996), SIF.

[SpPo73] J. F. Springer, M.-A. Porkrant and F. A. Stevens, *J. Chem. Phys.*, **58**, 4863 (1973).

[StRo90] M. J. Stevens and M. O. Robbins, *Europhys. Lett.*, **12**, 81 (1990).

[Sti75] D. Stigter, *Journal of Colloid and Interface Science*, **53**(2), 296 (1975).

[TaLe98] M. N. Tamashiro, Y. Levin and M. C. Barbosa, *Physica A*, **258**, 341 (1998).

[TaLe99] M. N. Tamashiro, Y. Levin and M. C. Barbosa, *Physica A*, **268**, 24 (1999).

[ToBo95] A. Y. Toukmaji and J. A. Board Jr., *Comp. Phys. Comm.*, **95**, 73 (1996).

[TrWi97] C. A. Tracy and H. Widom, *Physica A*, **244**, 402 (1997).

[TrRa] E. Trizac and J.-L. Raimbault, *Phys. Rev. E* (in press).

[WeJö82] H. Wennerström, B. Jönsson and P. Linse, *J. Chem. Phys.*, **76**(9), 4665 (1982).

[ZeCl92] G. Zerah, J. Clerouin and E. L. Pollock, *Phys. Rev. Lett.*, **69**, 446 (1992).